ORIENTATION DYNAMICS AND MICROSCOPE IMAGING OF COLLOIDAL SUSPENSIONS

A Dissertation

Presented to the Faculty of the Graduate School

of Cornell University

in Partial Fulfillment of the Requirements for the Degree of

Doctor of Philosophy

by

Brian David Leahy

August 2016

ORIENTATION DYNAMICS AND MICROSCOPE IMAGING OF COLLOIDAL SUSPENSIONS

Brian David Leahy, Ph.D.

Cornell University 2016

Micron-sized colloidal particles provide a unique window into the workings of statistical mechanics. These particles are large enough to be easily imaged with a microscope, allowing for detailed, mechanistic testing of statistical theories, yet small enough to still feel the effects of Brownian motion and thermal forces. Moreover, these thermal forces result in dynamics that are controlled by energy scales at room temperature and time scales on the order of seconds. In addition to allowing detailed control over a colloidal suspension, these accessible scales allow for the possibility of driving the suspension far from equilibrium and the exploration of non-equilibrium statistical mechanics. Much work has focused on the behavior of spherical colloidal particles, which lack an orientational degree of freedom and have simpler dynamics. However, many real suspensions are composed of particles with an orientational degree of freedom. In this thesis I explore the dynamics of dilute suspensions of nonspherical colloidal particles far from equilibrium. First, using an experiment I show that the rotational diffusivity of rodlike colloidal particles is enhanced under shear. Second, using a simplified theory I analytically solve for these dynamics far from equilibrium (in the limit of large Péclet numbers). The diffusivity is enhanced at a rate proportional to the square of the particle's aspect ratio. Interestingly, this solution also provides insight into the oscillatory shear dynamics of these particles, and into the continuous and oscillatory shear rheology of these suspensions. Third, I use this solution to control the alignment and rheology

of a suspension of particles. Finally, I close by improving the microscope's resolution by 10-100× through image analysis alone, without modifying the microscope itself. By improving the resolution we expect to be able to see new dynamics of colloidal particles at unprecedented scales.

BIOGRAPHICAL SKETCH

In the rude hours of a warm summer night in June 1987, Brian experienced his first taste of the excitement of physics when the delivering doctor knocked him off the table. While supposedly no head injuries were sustained during this fall, it imparted Brian with the realization that the physics of everyday life was interesting and useful. Armed with this conviction, Brian enrolled in the University of Chicago for undergraduate studies, where he first learned a Lagrangian formulation of babies falling off tables and eventually graduated with honors in 2009. From 2007-2010 Brian worked as a research assistant at the University of Chicago and at Argonne National Laboratory; in this time Brian first learned how to do research and realized he enjoyed it. Brian then enrolled in the Physics Department at Cornell University, where he is currently finishing his six-year tour.

To Luka Pocivavsek, Mati Meron, and Binhua Lin. The seeds for the enthusiasm I have for studying science was first planted in me by Luka, for my desire to understand it deeper by Mati, and my ability to do the research and design an experiment by Binhua. If It were not for those three people I would never have started or finished graduate school.

ACKNOWLEDGEMENTS

In addition to the numerous coauthors and people I have acknowledged throughout my papers, I would like to take a few sentences to acknowledge specific individuals. First, I would like to acknowledge my committee. Don Koch's tremendous knowledge on all things related to suspensions of rods and fibers has helped me tremendously in my PhD. When I am unable to convice Don, then I know that I do not understand the science sufficiently. Jim Sethna's incredible intellect and deep understanding of science has been of enormous help in solving technical and conceptual problems and has encouraged me to understand all my areas of research more deeply. And Itai Cohen's relentless dedication to finding the core of the scientific problem, answering it rigorously and completely, and communicating it clearly have defined my time at Cornell. If I have communicated anything clearly in this thesis or during the course of my PhD it is because of Itai. The students – graduate and undergraduate – and postdocs in the Cohen lab have been a pleasure to work with and a helpful resource throughout my time at Cornell. In no particular order – Xiang Cheng encouraged and helped me in my first project and inspired me with his tireless dedication to doing excelleng science. John C. Mergo was and is always a help in both the design and execution of everything from computer programming to machining. Without John I would have had much more difficulty doing the science and certainly much more difficulty in navigating the lab and graduate school. Tsevi Beatus has always been eager to provide insight or just to help me work through a problem. His insights into programming, image processing, experimental design, and choosing a scientific project have helped me mature as a scientist, and his emotional support has helped me stay alive while doing it. Lena Bartell and Sam Whitehead have always been equally eager to contribute scientific and structural ideas to my research, whether in the lab or over

a beer. Without frequent discussions with Lena, both my papers on Controlling Suspensions of Rodlike Particles and my 2015 JFM would be in much worse shape than they are now. Neil Lin has always been around for discussions on colloids and science, starting from when we were neighbors in our first year offices throughout all the years in the Cohen Lab at adjacent desks. Muxin Zhang was a brilliant undergraduate student whose help with the (mostly unpublished) liquid crystal project was invaluable to me. In addition, I have been fortunate to have excellent collaborators. The collaboration with Matt Bierbaum on our Light Microscopy at Maximal Precision paper has been extremely helpful. The frequent, almost daily discussions we had helped hone the PERI code into a precise, highly-engineered machine. Working this closely with Matt has forced me to understand the details of microscopy much more precisely and has transformed me into a better programmer. Oleg Lavrentovich and Shuang Zhang provided me with their extensive, practical knowledge on liquid crystals to me, despite the lack of a publication from that collaboration. Nathan Ellis has taught me how to machine and how to design and machine an apparatus well. Without Nate I would never have been able to fabricate the several major apparati and the dozens of small parts that I used throughout my PhD, and I certainly would have been much less sane without Nate's personal advice and support. Cornell University and the Physics Department have always been an excellent, collegial place to work, where dozens of people are eager to give you scientific advice. Without people like Dave Moore, Jessica Killian, Yariv Yanay, Ben Savitsky, Megan Comins, Zach Lamberty, Ethan Kassner, John Stout, Cody Long, Andy Bohn, Marc Miskin, Peter Rose, Prof. Carl Franck, Prof. Roseanna Zia, Prof. Lynden Archer, and Prof. Paul McEuen, my research at Cornell would have progressed much more slowly and certainly much less enjoyably.

I would also like to acknowledge my funding sources. Three years of my PhD were paid for my and National Defense Science and Engineering Graduate (NDSEG) fellowship. In addition to allowing me to eat, the NDSEG gave me the freedom to chase down projects that I thought were more interesting without fear of losing funding. I would also like to acknowledge the NSF (CBET-PMP Award No. 1232666) and DOE for support during my time at Cornell.

TABLE OF CONTENTS

LIST OF TABLES

LIST OF FIGURES

CHAPTER 1

INTRODUCTION

The alarm's soft bleating awakens you. Your hand mechanically fumbles for your phone, as the soft glow from its LCD screen illuminates the paint's mountainous texture on your wall. Rote hands grasp at clothes as rote feet carry you towards the shower. The hot water trickles down your neck in the same rivulets it always has while the shampoo oozes its way out of the bottle to spiral on your palm. The bubbly lather of soap and shampoo drips on the shower floor at your feet. Awake, you step out and grab a fresh piece of toast. The butter runs smoothly over its hot surface, joined by the slow drizzle of thick honey and the uneven spreading of strawberry jam. Soon, the last tastes of honey and jam are joined by the minty taste of the rod of toothpaste that your right hand extrudes from the tube. The key turns in the ignition; the engine's mellifluous rumble greets your ears. The smooth feel of the shifter in your right hand mirrors the smooth surface of the latte in your left. The morning sun glistens off the closing car door as you stride towards the office to begin your day.

As you recall your morning, the wide array of fluid behaviors that you have witnessed astounds you. Water and honey flowed simply, but the jam and shampoo did not, instead holding their form after they stop flowing. The toothpaste leaves the tube as a giant plug, without changing shape like a normal fluid. These complex flow behaviors arise due to structured elements in the fluid – added polymers, small colloidal particles, and surfactants. These additives allow for a tuning of the fluid's rheology beyond what is possible with simple liquids. Additives in your motor oil and transmission fluid allow them to remain inviscid enough to allow the engine to turn over at low temperatures, yet viscous enough to function as a lubricant at

high temperatures. The paint on your wall has colloidal particles added to make it shear-thin, making it easy to apply to the wall with your roller at high shear rates but preventing it from flowing off the wall at low shear rates, which creates the mottled texture on the wall. The glistenting spray paint on your car door also has colloidal particles added to it to change the film's rheology and prevent it from slipping off as it dries. Even objects whose use does not directly depend on their flow properties are frequently made of structured fluids – your LCD screen utilizes the orientational structure of a nematic liquid crystal, and your bar of soap is composed of mesogenic molecules that form nematic and smectic phases when mixed with water.

In most of these examples, the material consists of a suspending fluid phase and a dispersed phase – micellar surfactants in the oil, coffee particles in the latte, polymeric additives in the shampoo. The dispersed phase tends to be made up of small (10 nm - 10 μm) particles. Due to their small size, these particles behave qualitatively different from more macroscopic objects. First, they undergo Brownian motion and are randomly kicked in all directions due to thermal collisions with the solvent molecules. Second, interparticle interactions are important. Frequently the interaction strength is on the scale of thermal energy or the strength of the applied flow, which results in a rich phase behavior of the suspension as it flows or as the temperature changes slightly – think of the butter's solid-like behavior as you cut it with a knife but liquid-like flowing as you spread it over the hot toast.

One of the simplest model systems for these substances is nondeformable colloidal particles suspended in a fluid. For many of the systems – the milk and coffee in your latte – the particles are mostly spherical. For other systems, the particles have an orientational degree of freedom – polymer orientations in the shampoo or

disc-like clay particles which can be added to the spray paint on your car. Occasionally these particles have nearly no interactions, and occassionally they attract or repel one another. For simplicity, much work in colloidal science has focused on hard colloidal spheres suspended in Newtonian solvents. However, spheres lack an orientation degree of freedom. As a result, their rheology in the dilute limit is trivial, and their behavior in denser suspensions is difficult to understand from first principles.

In this thesis, I discuss the flow and static behavior of colloidal dispersions. In the next three chapters of this thesis, I describe the orientational dynamics of dilute suspensions of axisymmetric particles under flow, through experiments, theory, and simulation. In chapter 2 I demonstrate experimentally that rotational Brownian motion is effectively enhanced under shear flows, due to a Taylor-dispersion-like coupling between the varying, deterministic rotation of the particle in a shear flow (Jeffery orbit) and the random rotational Brownian motion of the particle. In chapter 3, I analytically solve for the particle's orientation dynamics in the simple case of a particle confined to rotate in the flow-gradient plane at high Péclet numbers, under both simple shear flow and under an arbitrary periodic shear. I use this analytical solution to shed insight on the experimental measurements in chapter 2. Since the particle orientations couple to the suspension rheology, I then use this solution to discuss the transient and oscillatory shear rheology of a dilute suspension of axisymmetric particls. Since the system is a physical system with an analytical solution, it provides new insight into the types of nonlinear and non-Newtonian rheological responses of suspensions. In chapter 4 I use the exact solution from chapter 3 for an arbitrary oscillatory shear waveform to find an optimal waveform for a desired set of properties. I show that particle alignment and suspension rheology are highly tunable, including the creation of large, non-

transient hydrodynamic normal stresses in dilute suspensions. Surprisingly, the optimal waveforms are simple, allowing for them to be easily understood in the framework of chapter 3. Finally, I change gears and create a featuring algorithm that precisely identifies colloidal particle positions and sizes in a confocal microscope image, which are frequently used in the studying of colloidal suspensions. This algorithm relies on a detailed physical model of the image formation in a confocal microscope, which I (briefly) explain and implement. Since this method identifies particle positions and sizes to nanometer resolution, we use this method to measure interparticle interaction potentials in systems of colloidal spheres.

CHAPTER 2

ENHANCING ROTATIONAL DIFFUSION USING OSCILLATORY SHEAR

Taylor dispersion – shear-induced enhancement of translational diffusion – is an important phenomenon with applications ranging from pharmacology to geology. Through experiments and simulations, we show rotational diffusion is also enhanced for anisotropic particles in oscillatory shear. This enhancement arises from variations in the particle's rotation (Jeffery orbit) and depends on the strain amplitude, rate, and particle aspect ratio in a distinct manner from the translational diffusion. This separate tunability of translational and rotational diffusion opens the door to new techniques for controlling positions and orientations of suspended anisotropic colloids. [1]

[1] This work has already been published; see ref. [88].

2.1 Main Text

G. I. Taylor [145] was the first to point out that a Brownian particle in a pipe diffuses faster when the suspension is flowing. Qualitatively, this behavior arises because diffusion along the radius of the pipe allows the particle to be advected with the flow at different speeds [145, 7]. This effect on translational diffusion is general. As such, Taylor dispersion has become a useful paradigm for understanding diverse phenomena ranging from fluid transport in rock strata [137, 19], nutrient distribution in farm soils [23], controlling drug delivery [44], and measuring the diffusion constants of slowly-diffusing substances [2, 12].

Given the importance of enhanced translational diffusion, we ask whether dispersant *orientations* are also affected by shear. Colloidal particle orientations are randomized by thermal motion via rotational diffusion [43]. However, the effect of flows on orientational diffusion remains poorly understood. Enhanced translational diffusion under shear results from the particle accessing streamlines with different flow velocities. Similarly, we expect that a particle with access to rotational trajectories with different angular velocities might display enhanced rotational diffusion. Particles with axial symmetry "tumble" with an unsteady rotation in what are known as Jeffery orbits. The orientation of these particles is completely specified by a unit normal $\vec{n}$. For a particle with effective aspect ratio p in a flow with strain rate $\dot{\gamma}$, the periodic tumbling is described by [73, 24]

$$\begin{aligned} \tan\phi(t) &= p\tan\left(\tfrac{\dot{\gamma}t}{p+1/p}\right) \\ \tan^2\theta &= \left[\kappa^2\left(p\cos^2\phi + 1/p\sin^2\phi\right)\right]^{-1} \quad , \end{aligned} \tag{2.1}$$

where ϕ is the azimuthal angle from the gradient direction, θ is the polar angle between the vorticity direction and the particle's orientation, and κ^2 is an orbit constant set by the initial conditions. For isotropic particles $p = 1$ and the particle

tumbles uniformly. However, if $p \neq 1$, a particle's orientation is advected with different angular velocities depending on its position in the periodic orbit. Thus, in analogy with results for translational Taylor dispersion, we would expect enhanced rotational diffusion for nonspherical particles under shear.

Here we report experiments and simulations addressing rotational and translational diffusion of colloid dimers under oscillatory shear. We find the rotational diffusion is enhanced and depends on the dimensionless strain rate or Péclet number Pe, effective aspect ratio p, and shear strain γ. Moreover, the dependence of rotational diffusion on these three parameters differs markedly from the translational diffusion. With the advent of new techniques for synthesizing nonspherical particles and their increasing importance in novel materials [27, 58], separate tunability of rotations and orientations promises important applications in mixing and self-assembly.

To explore rotational diffusion under shear, we used hollow silica colloidal dimers whose lobes are $\approx$1 μm in diameter [94] suspended in an index-matched but density-mismatched 80:20 glycerol:water solution dyed with fluorescein salt. The dimers are slightly elongated, with a length-to-width aspect ratio of 2.5. In addition, we determined the dimer hydrodynamic aspect ratio by fitting 200 measured Jeffery orbits to Eq. 2.1. We measure a median aspect ratio 2.3 $\pm$0.9, consistent with previous predictions and measurements for true dimers [154, 153].

Previous studies demonstrated that dense suspensions of rod-like particles under shear display enhanced translational or rotational diffusion, which can arise from many-body hydrodynamic effects [115], collisions [49], or particle-particle interactions [114]. To focus solely on coupling between Brownian motion and shear, we use suspensions at very dilute volume fractions $\approx 10^{-4}$. Consequently, to ob-

tain statistical power each particle must be tracked for days at a time. While such measurements are challenging due to limitations in apparatus stability, they cleanly eliminate many body effects and clarify the interpretation of our results.

The suspension is loaded in a shear cell consisting of 4 mm $\times$ 4 mm silicon wafer positioned above a glass cover slip and held parallel with less than 1 μm variation over the length of the wafer. The gap separation was tuned from 7 to 12 μm in order to vary the strain amplitude. While the plate separation could be set accurately, over the duration of our long experiments we measured that the gap size could drift by up to 20%, which in turn affected the applied strain. The silicon wafer is held stationary, while the glass cover slip is sheared by a piezo controller under oscillatory triangle-wave shear. Our setup mounts on a fast confocal microscope allowing us to accurately image the three-dimensional position and orientation of a colloidal dimer at peak-to-peak shear strains up to $\gamma = 3.4$ and frequencies up to 0.2 Hz.

We image the dimer's position and orientation with a full three-dimensional scan, oversampling in all three directions to increase measurement precision (Fig. 2.1a). After accounting for optical distortion [63], we use a custom featuring code to reconstruct the particle voxels (Fig. 2.1b). Principal component analysis is used to determine the particle orientation [21]. Using this method we can determine the particle orientation to within $\approx 5^\circ$ as well as locate the particle's position with subpixel resolution - within 30nm in the flow x and vorticity z directions, and within 100 nm in the gradient direction y.

Under shear, the dimer's position is advected with the flow, while its orientation tumbles in a Jeffery orbit. Translational and rotational Brownian motion addition-

[21] Code is available online at cohengroup.ccmr.cornell.edu

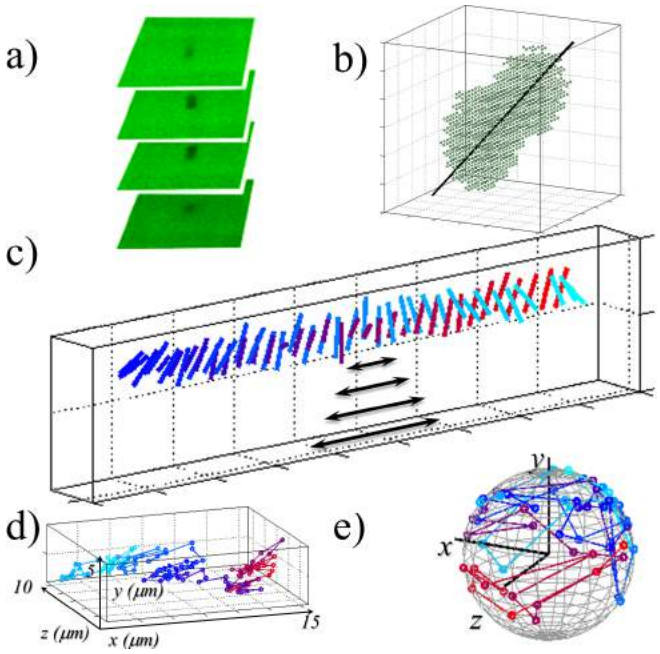

Figure 2.1: a) Representative confocal microscope images of a dimer. b) The reconstructed voxels and orientation of the dimer. c) Reconstructed trajectory of dimer under triangle-wave shear. The flow direction is indicated by arrows. The peak-to-peak strain is $\gamma = 3.4$ and the period T=100 seconds. The dimer's position and orientation are represented by the rod, and the color variation represents the time. In our analysis, we record the dimer position and orientation at the cycle extrema, corresponding to the cyan, blue, and red rods. d) A trajectory of 250 strobed positions, color coded in time. e) The corresponding orientations, plotted on the unit sphere.

ally randomize the position and orientation, resulting in a net displacement after each cycle (Fig. 2.1c). To track the long-time behavior of the dimer under shear, we take a strobed image at both ends of the triangular cycle (Fig. 2.1d,e) and reconstruct its trajectory [36]. From these trajectories we extract the orientational distributions (Fig. 2.2). The effective translational diffusion tensor $\mathbf{D}_{\text{eff}}$, and the effective rotational diffusion constant D^r_{eff} are extracted using the time correlations:

$$\begin{aligned} \langle \vec{n}(t) \cdot \vec{n}(t+\Delta t) \rangle &= e^{-2D^r_{\text{eff}}\Delta t} \\ \langle x_i(t) x_j(t+\Delta t) \rangle &= 2(D^T_{\text{eff}})_{ij}\Delta t \,, \end{aligned} \tag{2.2}$$

where Δt is an integer number of periods T (Fig. 2.3a,b). While we find that

the rotational data in 3b are well-fit by a single exponential decay, we note that rotational diffusion is strictly speaking a tensorial quantity that can in principle vary with orientation.

To complement our experimental investigations, we model a colloidal dimer in a shear flow with a Langevin equation. The particle orientation $\vec{n}$ evolves as:

$$\frac{d\vec{n}}{dt} = \left\{ \mathbf{\Omega} \cdot \vec{n} + \frac{p^2 - 1}{p^2 + 1} \left[\mathbf{E} \cdot \vec{n} - \vec{n}(\vec{n} \cdot \mathbf{E} \cdot \vec{n}) \right] \right\} + (2D_0^r)^{1/2} \vec{\Gamma}(t) \tag{2.3}$$

The first term in the brackets describes a uniform rotation due to a shear flow, and the second term accounts for the effects arising from particle shape and orientation relative to the imposed shear strain [73]. The final term on the right hand side accounts for rotational Brownian motion. Here D_0^r is the rotational diffusion constant of the particle and $\vec{\Gamma}$ is a diffusive white-noise term. $\mathbf{\Omega}$ is the vorticity tensor and $\mathbf{E}$ is the rate-of-strain tensor for triangle-wave oscillatory shear: $\mathbf{\Omega}_{ij} = \frac{1}{2}(\partial_i u_j - \partial_j u_i)$, $\mathbf{E}_{ij} = \frac{1}{2}(\partial_i u_j + \partial_j u_i)$.

Our experiment consists of suspension of sedimenting spheroids in a shear flow bounded by rigid surfaces, whereas our simulation models the rotation of a single spheroid in an infinite fluid. While our experiment minimizes interparticle hydrodynamic interactions [150, 1, 115, 127] by using extremely dilute volume fractions, due to the geometry of the experiment we cannot avoid interactions with the wall [111, 139]. Nevertheless, we find similar behavior between our experiments and simulations, despite the fact that the walls considerably influence the translational dynamics. We posit the reason for this agreement is, as simulations have shown, the wall's effect is only at the few percent level on the Jeffery orbits [111], which is what ultimately affects the rotational diffusion.

Three dimensionless parameters control the particle's distribution and diffusiv-

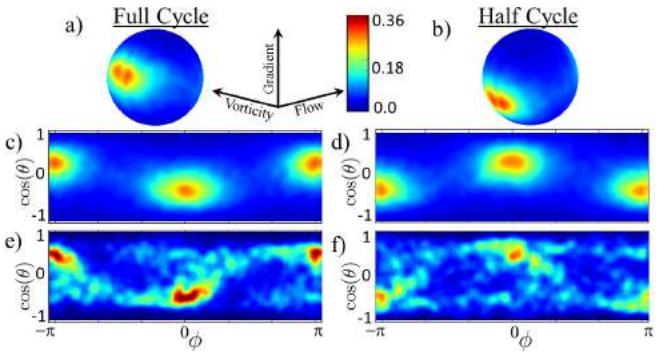

Figure 2.2: a,b) Measured orientation distribution from 12,000 simulation cycles at $p = 2.3$, Pe $= 600$, and $\gamma = 3.4$, plotted on the unit sphere. The distribution oscillates with the flow. Thus different orientations are observed at integer versus half-integer cycles. c,d) The same distribution as in (a & b), but plotted with an equiareal mapping where θ is the polar angle measured from the gradient direction, and ϕ is the azimuthal angle measured from the flow direction. e,f) The orientation distribution from experiment, separated by full (e) versus half(f) cycles, measured at the same Pe, γ. All images share the same color scale.

ities: the aspect ratio p, the dimensionless strain rate or Péclet number Pe$=\dot{\gamma}/D_0^r$, and the peak-to-peak strain amplitude $\gamma = \dot{\gamma}T/2$ (Eq. 2.3). Previous works [66] have shown that Eq. 2.3 leads to an inhomogeneous steady-state distribution of particle orientations under continuous shear. In contrast, our experiments and simulations for oscillatory shear show the orientational distribution oscillates with the flow (Fig. 2.2 b,d versus c,e). While the distributions show the $\vec{n} \rightarrow -\vec{n}$ symmetry required by Eq. 2.3, they are not symmetric about either the gradient or flow axes separately [2]. At low Pe, γ, or near $p = 1$, the orientational distribution becomes isotropic. Interestingly, increasing Pe at fixed γ strengthens the alignment, whereas increasing γ at fixed Pe both strengthens the alignment and alters its direction. We find excellent agreement between simulations and experiments. Moreover, at high amplitude and high Pe the simulated distributions approach previous calculations for rods under continuous shear [66].

[2] See EPAPS for details about the experimental setup and additional data, including movies of the orientational distributions over a range of shear parameters and enhanced rotational diffusion as a function of aspect ratio.

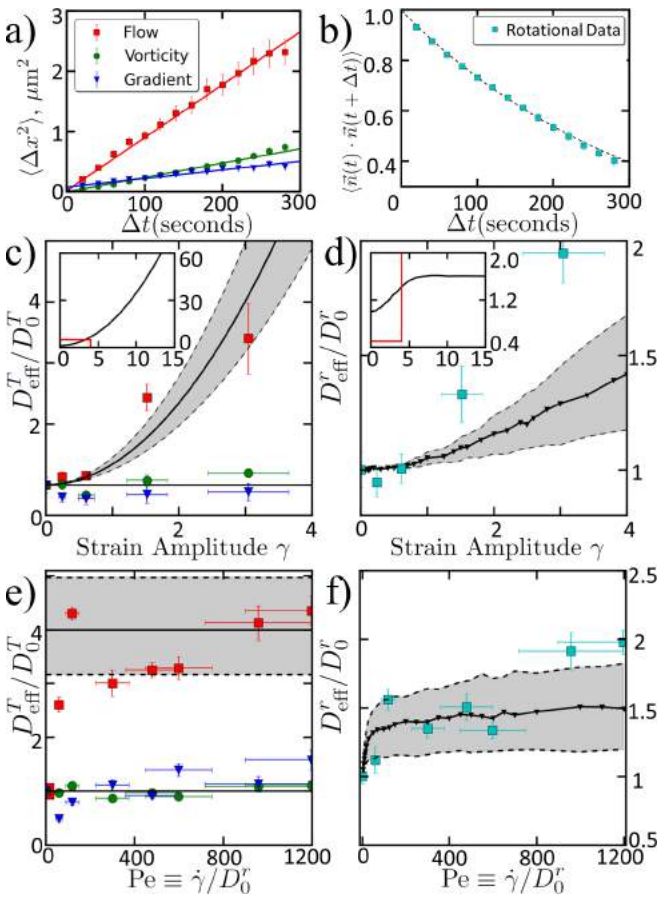

Figure 2.3: a) Measured mean-square displacement along flow (red squares), vorticity (green circles), and gradient (blue triangles) directions. b) Measured correlation of the corresponding orientations. c) Normalized translational diffusion $\mathbf{D}^T_{\rm eff}/D^T_0$, along all three axes versus γ at fixed Pe = 80. Symbols correspond to measurements while the black lines correspond to predicted values (Eq. 2.4). The gray band indicates the effects of experimental uncertainty in γ on the prediction. Inset: The predicted diffusion along the flow direction for $0 < \gamma < 15$. Red box illustrates range in main panel. d) $D^r_{\rm eff}/D^r_0$ for the same dataset as (c), as measured from experiment (cyan squares) and simulation at $p = 2.3$ (black points). Shaded band indicates the effect of experimental uncertainty in aspect ratio. Inset: simulated rotational diffusion for $0 < \gamma < 15$. Red box illustrates range in main panel. e,f) Translational (e) and rotational (f) diffusion at constant $\gamma = 3.4$ and varying Pe. Overlaid in black lines are the expected values from theory (c) and simulation (d).

In addition to distributions, we simultaneously measure the particle's rotational and translational diffusion after an integer number of cycles. We find the particle's translational [114, 95] and rotational motions are well fit by diffusive trajectories of Eq. 2.2. The translational mean-square displacement, shown in Fig. 2.3a, increases linearly with time while the time-correlation of particle orientations, shown in Fig. 2.3b, exponentially decays. From these curves we extract effective diffusion constants, which depend on the dimensionless parameters Pe, γ, and p.

The experimental data in Fig. 2.3c show the translational diffusion along the flow direction $(D^T_{\text{eff}})_{xx}$ increasing with γ. $(D^T_{\text{eff}})_{xx}$ ranges from its equilibrium value at $\gamma = 0$ to $\approx 3.5\times$ its equilibrium value at $\gamma = 3$. In contrast, the diffusion constants along the gradient and vorticity directions $(D^T_{\text{eff}})_{yy}$ and $(D^T_{\text{eff}})_{zz}$ remain at the equilibrium value. Theory predicts that for spherical particles in triangle wave shear the diffusivity is [95]:

$$\langle x^2 \rangle = 2D_x t + \tfrac{2}{3} D_y \gamma^2 t \quad \langle y^2 \rangle = 2D_y t \quad \langle z^2 \rangle = 2D_z t \tag{2.4}$$

where x, y, and z are the flow, gradient, and vorticity directions and t is taken at integer multiples of the cycle period. Clearly, an anisotropic particle has different diffusivities along its different axes [61, 108]. Since the particle's orientation couples to the flow, D_x, D_y, and D_z in Eq. 2.4 will depend on the applied shear flow. Building on results for continuous shear [52], however, we calculate this change to be at the few percent level in our experiments. We thus compare our data with Eq. 2.4 in Fig. 2.3 using equilibrium values for D_x, D_y, D_z. We find excellent agreement between theory (black lines) and experiments (data points) for all the effective diffusion constants. As predicted, only $(D^T_{\text{eff}})_{xx}$ increases with γ. As shown in Fig. 2.3 inset the effective diffusion along the flow direction increases quadratically with γ indefinitely.

Since at fixed γ $\mathbf{D}^T_{\text{eff}}$ depends on Pe only through D_x, D_y, D_z,we predict an enhanced $(D^T_{\text{eff}})_{xx}$ even as Pe $\to 0$ and no measurable dependence of D^T_{eff} on Pe. As expected, we observe that $(D^T_{\text{eff}})_{yy}$ and $(D^T_{\text{eff}})_{zz}$ remain constant while $(D^T_{\text{eff}})_{xx}$ is significantly enhanced even at the lowest Pe measured (Fig. 2.3e). However, there is a weak trend in the $(D^T_{\text{eff}})_{xx}$ data. We attribute this trend to experimental effects from fluctuations in the shear cell gap (gray band) and gravitational settling that can affect data at low Pe [3]2.

We find that D^r_{eff} is also enhanced by shear, nearly doubling by $\gamma = 3$ (Fig 2.3d). A similar trend is observed in our simulations (black line; gray band accounts for uncertainty in p). However, simulations at larger γ than those accessible in experiments show that D^r_{eff} saturates at a value that depends on Pe and p (Fig. 2.3d inset). Because Jeffery orbits are periodic with strain, after the orientation has completed 1/2 a period ($\gamma = \pi(p + 1/p)$) no new rotational dynamics appear. Since larger strain does not provide access to new changes in the streamlines, the rotational diffusion saturates. In contrast, the translational diffusion increases indefinitely, as there is no strain scale for translations.

The Pe dependence of D^r_{eff} contrasts with translational diffusion. While $(D^T_{\text{eff}})_{xx}$ remains enhanced at low Pe, in both experiment and simulation D^r_{eff} increases continuously with Pe (Fig. 2.3f). Our simulations also suggest that for large Pe D^r_{eff} still increases, albeit slowly [4]2.

A more complete map of the dependence of D^r_{eff} on Pe and γ for $p = 2.8$ is shown in Fig. 2.4a. This figure summarises 778 simulations of D^r_{eff} in the range $0 < \gamma < 30$ and $0 <$ Pe < 1400. The heat maps show that both trends - D^r_{eff} increasing slowly with Pe and saturating at high γ - are general over a large range of parameters. In addition, they illustrate two unexpected trends. First, the slight

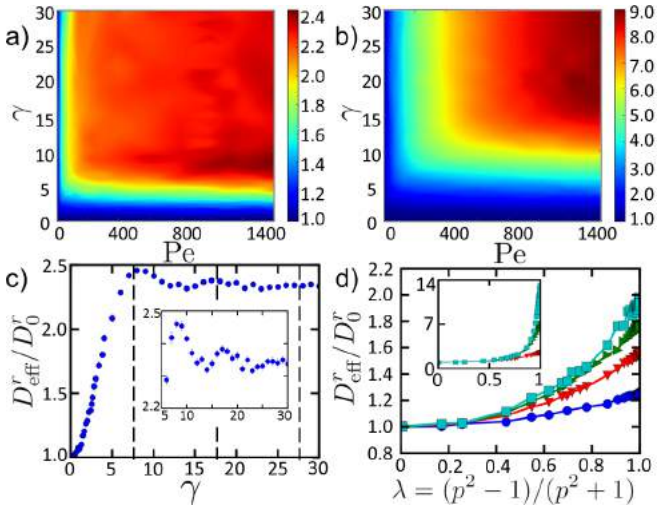

Figure 2.4: $D^r_{\rm eff}/D^r_0$, plotted against both Pe and γ at $p = 2.83$ (a) and $p = 7.0$ (b). c) Data from (a) at Pe=1400 demonstrating oscillations in $D^r_{\rm eff}$ with γ. d) $D^r_{\rm eff}/D^r_0$ vs. $\lambda = (p^2-1)/(p^2+1)$, taken at fixed $\gamma = 2.83$ and at four separate Pe: 10 (blue circles), 40 (red vertical triangles), 289 (green horizontal triangles), and 1000 (cyan squares). Inset: $D^r_{\rm eff}/D^r_0$ versus λ at Pe =10,40,1000 and $\gamma = 15$.

slopes observed for the contours of $D^r_{\rm eff}$ indicate that the dependence on Pe and γ is coupled. Second, we find multiple resonances in $D^r_{\rm eff}$ with increasing γ, visible as the dark red "bumps" at high Pe in Fig. 2.4a and the peaks in Fig. 2.4c. These oscillations result from the Jeffery orbit periodicity. Particle rotation under triangle wave shear maps onto rotation under continuous shear when γ corresponds to an integer number of half Jeffery orbits (distance between vertical dashed lines in Fig.2.4c).

While it is known increasing aspect ratio can at most vary translational diffusion anisotropy by a factor of 2 for rods in bulk fluids [86], here we find a much stronger dependence of the rotational diffusion on aspect ratio. Although it is difficult to alter the aspect ratio in experiments, we can examine the dependence of $D^r_{\rm eff}$ on p in simulation. To this end, we evaluated $D^r_{\rm eff}$ at 537 different γ and Pe values and at fixed $p = 7.0$ (Fig. 2.4b). At large Pe the rotational diffusion again saturates when $\gamma \sim \pi(p + 1/p)$. However, while $D^r_{\rm eff}$ at $p = 2.83$ was enhanced by 2.4, we

find that D^r_{eff} at $p = 7$ is enhanced by a factor of 9. The general trends in the data for the dependence of D^r_{eff} on p can be examined by plotting D^r_{eff} versus the Jeffery coefficient $\lambda = (p^2-1)/(p^2+1)$ at fixed Pe and γ (Fig. 2.4d). We find that D^r_{eff} remains finite as $p \to \infty$. For $\gamma = 2.8$ this value is roughly 2 at Pe = 1000 (cyan squares, main panel) whereas for $\gamma = 15$ this value increases to 14 at Pe = 1000 (inset). Finally, for all simulated Pe and γ, we find no enhanced diffusion in the limit of spherical particles and uniform rotation ($p \to 1$). Just as enhanced diffusion due to Taylor dispersion requires access to a gradient in the real-space streamlines, enhanced rotational diffusion requires access to nonuniform rotational trajectories.

Overall, the diffusion of a colloidal dimer shows a complex dependence on the shear flow and the particle aspect ratio. Simply by changing the applied shear, the rotational diffusion of a colloidal particle can be tuned absolutely and relative to the translational diffusion. In particular, by changing γ the translational diffusion increases indefinitely, whereas the rotational diffusion saturates. This separate tunability of orientations and positions opens the door to new techniques for manipulating self-assembly, particle separation, and suspension rheology. Moreover, the formulation of these results extends to two and even three axis shear flows, allowing an additional handle for manipulating particle orientations and positions. Further measurements with larger data sets may be able to look for anisotropy in the rotational diffusion. Nearly 60 years after Taylor originally showed that translational diffusion could be enhanced by flow, new techniques in particle synthesis and measurement of orientational trajectories show that these general principles can be extended to rotational diffusion.

Acknowledgments

We thank D. Koch, Y. Lin, and T. Beatus for useful discussions, and M. Solomon for useful discussions on particle synthesis & featuring. This publication is based on work supported in part by Award No. KUS-C1-018-02, made by King Abdullah University of Science and Technology (KAUST), the U.S. Department of Energy, Office of Basic Energy Sciences, Division of Materials Sciences and Engineering under Award (ER46517) (XC, DO & CLW) and DoD, Air Force Office of Scientific Research, National Defense Science and Engineering Graduate (NDSEG) Fellowship, 32 CFR 168a (BL).

2.2 Appendix: Supplementary Materials

2.3 Experimental Setup & Featuring Method

Our shear cell consists of a homebuilt "confocal rheometer" that is described elsewhere [30]. The shear cell consists of two macroscopic (≈20 cm) machined objects which are precisely positioned within several microns of each other. Over the course of the long experiments, the temperature in the room drifts by a degree or two Celsius. The small changes from thermal expansion of these parts is enough to change the gap size by several microns, which can be a large relative change in the gap size and thus the strain rate. We have measured a 20% change in the gap size - corresponding to only a 2 micron drift - for some of our experiments, which is what set the size of the shaded regions in Fig. 3 c&e. Achieving more stable gaps over the course of the week that is necessary to collect enough statistics for an experiment will require substantially better temperature control and therefore a redesign of the apparatus.

We use a fast confocal z-stack to image our dimers under shear. The z-stack consists of 50 512× 128 pixel (at .12 μm/pixel) slices, separated by 0.165 μm in z and taken at a slice rate of 216 frames per second, or 1/4 of a second for the entire z-stack. This allows the particle to be completely imaged before it has significantly moved due to the shear flow. A typical reconstructed dimer thus has ≈1500 voxels in its reconstruction. We identify the particle by noise-filtering and carefully thresholding the image. After accounting for stretching along the confocal's vertical axis (the gradient axis of the shear) due to optical distortion, [63], we use a custom featuring code to reconstruct the entire particle from the image. We then determine the particle's position and orientation by taking the brightness-weighted mean and brightness-weighted covariance matrix of the particle's voxels. The eigenvector of the covariance matrix with the largest eigenvalue is identified as

the particle's orientation; we avoided the ambiguity in the sign of the particle's orientation by selecting the orientation closest to the particle's previous orientation. We checked that this method accurately identifies the particle orientation by testing the method on generated images of colloidal dimers at arbitrary orientations and with a noise level similar to that in our experimental images.

We determined the uncertainty in our particle positions by extrapolating the experimentally measured correlations ($\langle xx \rangle, \langle yy \rangle, \langle zz \rangle,$ and $\langle \vec{n}(t) \cdot \vec{n}(t + \Delta t) \rangle$) to $\Delta t = 0$ and finding the intercept. From this we find that we can measure particle orientation to within 5°, and the particle position to within 30 nm in the flow and vorticity directions and 100 nm in the gradient direction. Our resolution in the gradient direction is dominated by lack of precision in the confocal's vertical positioning relative to the shear cell.

In addition to checking the uncertainty in our particle locations, we also checked to see whether sedimentation could play a strong role. Since our dimers are hollow silica shells and since the solvent is viscous, they do sediment, although more slowly than a solid particle in water would. From looking at the mean-square vertical position $\langle z^2 \rangle$ of quiescent dimers, we estimate that the sedimentation time of our dimer is approximately 150 seconds. While this is faster than $1/D_0^r$, which is about 1000 seconds, for all but the lowest shear frequencies the sedimentation time is considerably larger than the time for one shear cycle and is much larger than $1/\dot{\gamma}$. In addition, the particle can also rotate freely in all directions. The Brownian height $\sqrt{\langle z^2 \rangle}$ of the particle is about 1 particle size, allowing rotations in the gradient-flow plane. Moreover, even particles near the walls exhibit full 3D Jeffery orbits – the necessary criterion for the enhancement of rotational diffusion. Furthermore, as mentioned above, we can measure angular displacements

corresponding to times much less than the sedimentation time so that even if sedimentation were hindering the full motion of the particle we can still measure its diffusive displacements. Thus we do not think that the density-mismatch has a strong influence on the experimental results.

2.4 Diffusion under Oscillatory Shear

The effect of continuous shear on translational diffusion is well-understood. Like a purely diffusive particle, the mean displacement $\langle \vec{x} \rangle = 0$ in the reference frame where the particle starts at $z = 0$. However, the mean square displacement tensor $\langle x_i x_j \rangle$ no longer increases linearly in time. Instead, it is given by [32, 76, 101, 95]

$$\begin{array}{lll} \langle x^2 \rangle = 2Dt + 2/3D\dot{\gamma}^2 t^3 & \langle y^2 \rangle = 2Dt & \langle z^2 \rangle = 2Dt \\ \langle xy \rangle = 0 & \langle xz \rangle = D\dot{\gamma} t^2 & \langle yz \rangle = 0 \end{array} \tag{2.5}$$

where x, y, and z are the flow, gradient, and vorticity directions, respectively. For $\langle x^2 \rangle$, the linear term $2Dt$ arises from ordinary diffusion, while the nonlinear term $2/3D\dot{\gamma}^2 t^3$ arises from the Taylor dispersion mechanism, sampling different trajectories in z. Note also that unlike in ordinary diffusion, there is a correlation between the motion in the flow direction and the gradient direction: $\langle xz \rangle \neq 0$.

For a particle under triangle-wave oscillatory shear, we can view its probability distribution after an integer number of cycles as the sum of two random variables: a displacement after shearing at constant strain rate $\dot{\gamma}$ for a time $T/2$, and a second displacement after shearing with $-\dot{\gamma}$ for a time $T/2$. Since the mean and variance of the sum of two random variables is the sum of each random variable's mean and variance, we can simply add the values for $\langle \vec{x} \rangle$ and $\langle x_i x_j \rangle$ from Eq 2.5, one with

$\dot{\gamma}T/2$ and one with $-\dot{\gamma}T/2$:

$$\begin{array}{lll} \langle x^2 \rangle = 2D_t + 2/3D\gamma^2 t & \langle y^2 \rangle = 2Dt & \langle z^2 \rangle = 2Dt \\ \langle xy \rangle = 0 & \langle xz \rangle = 0 & \langle yz \rangle = 0 \end{array} \tag{2.6}$$

where $\gamma = \dot{\gamma}T/2$ is the strain amplitude and t is measured after an integer number of cycles ($t = nT$). Alternatively, one can follow the derivation presented D. Leighton [95]. When evaluated at a cycle extrema, it provides the same result. For all our experimental data, we find that $\langle xx \rangle, \langle yy \rangle, \langle zz \rangle$ increase linearly with time, and that the cross terms $\langle xy \rangle, \langle xz \rangle, \langle yz \rangle$ are zero to within our experimental precision.

2.5 Effect of changing p on diffusion

With our current particle synthesis methods we are unable to probe experimentally the behavior of large aspect ratio particles; however, we can estimate these effects. The only effect of Pe on diffusion is through the orientation of the particle. The reason the orientational distribution matters is that the particle has different diffusion constants along different axes. Coupled to the particle orientation, this anisotropic diffusion affects the average diffusion constants along the flow, vorticity, and gradient directions. However, even at long aspect ratios, the anisotropic translational diffusion is at most a factor of 2 different between diffusions along the perpendicular and long particle axis [86]. Thus at most there would be a factor of 2 difference between a very long and very short rod.

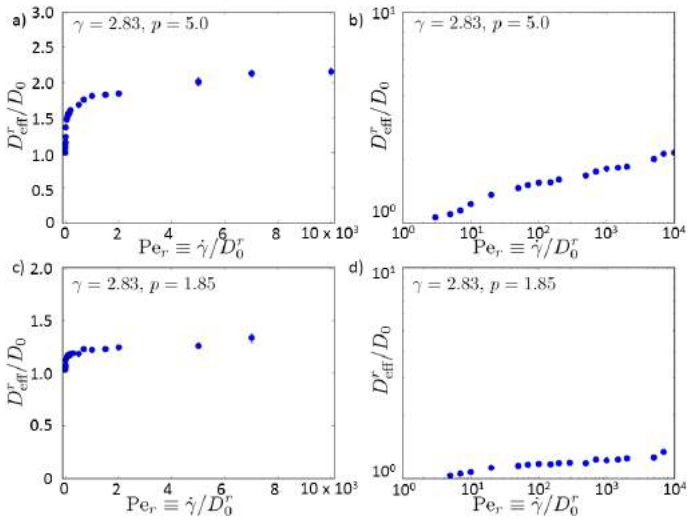

Figure 2.5: $D^r_{\rm eff}$ vs. Pe at $\gamma = 2.83$, for $p = 5.0$ (linear scale, (a) and log scale, (b)) and $p = 1.85$ (linear scale, (a) and log scale, (b)). Intermediate values of p show similar trends.

2.6 Simulated $D^r_{\rm eff}$ at large Pe

As mentioned in the text and shown in the figure below, we observe that $D^r_{\rm eff}$ increases with Pe for as far as we have simulated. Shown below is $D^r_{\rm eff}$ vs. Pe for two separate aspect ratios; intermediate aspect ratios show similar behavior. The effect is not an artifact of of a finite simulation timestep; decreasing the timestep by a factor of 2 at the highest Pe produces no change within statistical uncertainty.

2.7 Simulated $D^r_{\rm eff}$ for continuous shear

While our main text discusses rotational diffusion under oscillatory shear, we also note that the same qualitative effect can happen in continuous shear. Instead of strobing after an integer number of cycles, we can strobe at integer multiples of the particle Jeffery orbit's period. Similar to the rotaitonal diffusion under oscillatory shear, under continuous shear the rotational diffusion is also enhanced with Pe and

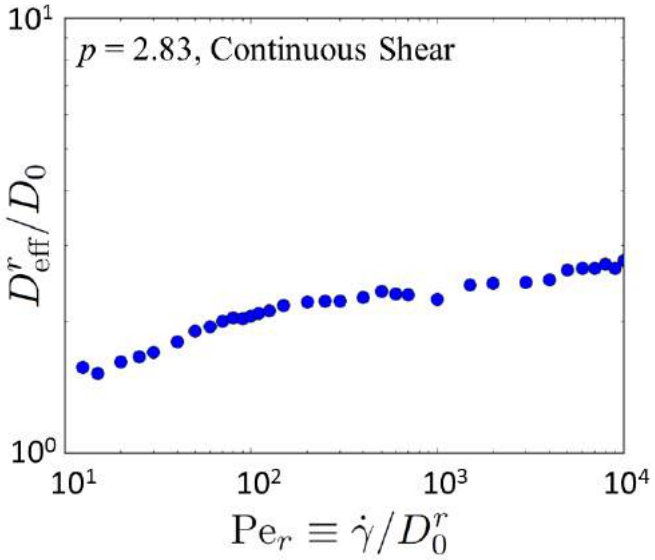

Figure 2.6: D^r_{eff} vs. Pe at $p = 2.83$ for continuous shear. Like oscillatory shear, we observe an increase in the rotational diffusion, when measured after an integer number of Jeffery Orbits.

p. Figure S2 below shows a log-log plot of D^r_{eff}/D^r_0 vs. Pe for a fixed aspect ratio $p = 2.83$.

2.8 Discussion & Future Work

In the past three years since this paper has been published [88], new techniques and knowledge have suggested better future experiments. In this section, I would like to briefly review what these new techniques and knowledge suggest about new experiments. First, I will talk about re-analyzing the same or very similar data, collected on a confocal microscope with the same dimer particles and the same shear cell apparatus. Second, I will discuss how a similar but new experiment should be designed. I will not mention what new directions could be included in a totally new experiment, as these are briefly discussed in chapter 3 and 4.

2.8.1 Re-analyzing the same data

While in chapter 2 we had shown experimentally that rotational diffusion is enhanced under shear, we did not experimentally determine the full orientation dynamics. As shown in recent theoretical analyses [89], at high Pe the orientation relaxation are better described in terms of the particle's phase angle κ and possibly the orbit constant C. It would be interesting to re-examine the experimental dynamics in ref. [88] and see if they are well-described by the theory in ref. [89]. At high Pe the orientational dynamics should follow the theory. However as Pe decreases, there should be deviations from the theory. It would be interesting to see how these deviations scale with Pe and what they look like experimentally.

The particle orientations and positions were extracted using the heuristic algorithm described in section 2.2. In light of the rest of the work in this thesis (*i.e* chapter 5), it would be interesting to extract particle positions and orientations with a physical reconstruction of the image. This would especially matter for the

orientations. The algorithm in section 2.2 functions by thresholding an image and identifying voxels of the image that correspond to the particle. The particle's orientation is defined as the principle eigenvector of the covariance matrix of the voxel positions, either weighted or not weighted by the image intensity. Empirically, I was able to determine that this produces a fairly unbiased measurement of particle orientation by looking at orientation distributions under zero shear. However, the asymmetric point-spread function of the microscope slightly elongates particles along the optical axis. This effect must produce a bias in the measured particle orientations, although the bias must in turn be small.

In principle, featuring the images with a physical reconstruction (PERI) will eliminate this bias. However, PERI functions by creating a generative model of the image, which requires a detailed knowledge of the particle shape. While this knowledge is easy to acquire for colloidal spheres – only the radius needs to be fit, and the functional form is known to be a sphere – for the dimers used in ref. [88] creating this generative model is more difficult. The dimers are not simply two osculating spheres, but are somewhat "peanut" shaped. In addition, both the size and the shape of the dimers varies from dimer to dimer. Since both the shape and the mode of variations of this shape are unknown, parameterizing these dimers is not simple.

However, PERI not only extracts parameters from an image, but it also creates maximally-realistic generated data. Thus, instead of using PERI directly to feature the images, PERI could be used indirectly to calibrate a heuristic algorithm. In addition to allowing for estimation of featuring errors, PERI could be used to compare different heuristic algorithms on realistic generated data (such as the one in ref. [13]) or even to guide design of accurate heuristic algorithms.

2.8.2 Re-doing an experiment

The experiment in chapter 2 was done using a line-scanning confocal microscope to acquire the data. While fast, this microscope still required about 0.25 s to complete a scan, restricting the range of strain rates usable. To image with this microscope, the suspending fluid needs to be index-matched to the particle, and to be able to suspend the particles, the fluid must be compatible with the particle. This severely restricts the range of suspending fluids that can be used, essentially leaving only a mixture of $\approx 80\%$ glycerol and 20% water. As a result of the restricted strain rates and viscous samples, only a moderate range of Pe is accessible, with data at low Pe requiring very slow imaging with very long times between frames. As a result, collecting the data in ref. [88] required 10 days of continuous imaging on the confocal microscope. However, as the microscope is in an ordinary room, the temperature in the room fluctuates by several degrees over the course of a few hours, as people enter and exit the room and other microscopes and lights are turned on and off. These temperature changes are on the scale of a 1-2 K and do not significantly affect the diffusion constant or viscosity of the solvent. However, since the shear cell (described in ref. [97]) is a macroscopic machined piece of equipment with a microscopic gap, these small changes in temperature result in a large change in the microscopic gap, due to differential thermal expansion of the shear cell apparatus. Since the displacement and frequency of the motion of the bottom plate are controlled, this change in the gap results in a large change in both the strain amplitude and the strain rate of the applied flow. This results in the large uncertainty in the applied flow and some of the large uncertainty in the measured parameters visible in figure 2.3. Moreover, since the confocal operates by taking a three-dimensional image stack as opposed to a single two-dimensional image, the memory and hard-disk space on the computer rapidly fill

up. To partially circumvent this, I attempted to image the particle only at the start and end of the shear cycle. At fast shear frequencies there is some small error in this, due to a lag between sending the signal for the confocal to image and the confocal actually responding, although by attempting many times and timing the delay it is possible to narrow this phase mismatch to $\approx 5\%$ of a cycle. However, by only imaging at the start and end of a cycle, information about the dynamics during a cycle are lost. Finally, since the dimers are polydisperse, I attempted to continuously image one dimer to reduce systematic noise due to different sizes of dimers. (Since rotational diffusion scales with the size a as $\sim 1/a^3$, a 10% change in particle size results in a 30% change in the particle diameter. And there were many different sized particles in the sub-par sample I was provided with. While I did my best to only include dimers that were the same size, it is impossible to do this, resulting in more errors.) However, by continually including one dimer over a long period of time, the dye photobleaches. This photobleaching results in seriously decreased contrast in the image, making the feature extraction significantly more difficult. As a result of these issues, confocal microscopy is probably not the best way to re-collect this data.

Instead, I would recommend the usage of holographic imaging. In holographic imaging, a coherent laser is used to illuminate the sample. This laser scatters off particles in the field of view. The scattered field and incident field interfere to produce a scattering pattern on the detector in the image plane of the microscope. Fitting this interference pattern provides information about the particle size and particle position, including its position along the optical axis. For anisotropic particles, the scattering pattern also gives information about the particle orientation. Since the scattering pattern is only collected at one plane, the resulting data is two-dimensional. As a result, holographic imaging both (1) is very fast – the frame

rate is only limited by the frame rate of the camera, and fast cameras with 100,000 frames per second are easy to purchase – and (2) has a low memory and disk-space footprint. In addition, reported fit errors in holographic imaging are very small – typically around a few nm for spherical particle positions. The laser could be easily ported through a the modified shear cell I machined from scratch with both a top and bottom glass plate for imaging liquid crystals (briefly mentiond in ref. [97]). Finally, holographic imaging relies on there being some index contrast between the particle and the fluid, as opposed to confocal microscopy which requires that they be exactly index matched. As a result, the range of available suspending fluids and hence fluid viscosities is much, much greater with holographic imaging. Finally, since the imaging is scattering-based, holographic imaging does not suffer from photobleaching. Holographic imaging would thus overcome many of the limitations of the confocal microscopy used – acquisition speed, range of Pe accessible, duration of experiment and temperature and gap-size drift, quantity of data, dynamics within one oscillation and phase shifts from imaging vs. shearing, photobleaching. In addition, holographic microscopy is fairly simple to set up as compared to a complex confocal.

However, holographic microscopy is not a panacea. The technique functions by fitting a known scattering distribution to the data. In general, these scattering distributions are complicated to calculate for all but one particle and for any shape but spheres. Complications due to multiple-particle scattering will not affect a new experiment, since the experiment concerned single particles. However, difficulties will arise from the lack of a scattering solution for the peanut-shaped particles. Nevertheless, this is a problem with a defined, conceptually straightforward solution – calculate a scattering matrix – and any techniques developed in solving this problem are likely to be useful for other systems.

Finally, there are a few small things that could now also be improved about the experiment. In the past few years, new particle synthesis techniques have been developed that allow for synthesis of colloidal rods or bullets [85]. These particles seem easier to synthesize and seem easier to stabilize, which was another source of problems for the dimers. Moreover, their simpler shape would allow for a parameterized description of them either for PERI or for fitting holography images. They also would provide a validation of the measurements at a different aspect ratio than that of the dimers. Finally, a better temperature control box could be designed for the shear cell, reducing the drift in the gap and providing better measurements.

CHAPTER 3

THE EFFECT OF SHEAR FLOW ON THE ROTATIONAL DIFFUSION OF A SINGLE AXISYMMETRIC PARTICLE

Understanding the orientation dynamics of anisotropic colloidal particles is important for suspension rheology and particle self-assembly. However, even for the simplest case of dilute suspensions in shear flow, the orientation dynamics of nonspherical Brownian particles are poorly understood. Here we analytically calculate the time-dependent orientation distributions for nonspherical axisymmetric particles confined to rotate in the flow-gradient plane, in the limit of small but nonzero Brownian diffusivity. For continuous shear, despite the complicated dynamics arising from the particle rotations, we find a coordinate change that maps the orientation dynamics to a diffusion equation with a remarkably simple ratio of the enhanced rotary diffusivity to the zero shear diffusion: $D^r_{\text{eff}}/D^r_0 = \frac{3}{8}(p - 1/p)^2 + 1$. For oscillatory shear, the enhanced diffusion becomes orientation dependent and drastically alters the long-time orientation distributions. We describe a general method for solving the time dependent oscillatory shear distributions and finding the effective diffusion constant. As an illustration, we use this method to solve for the diffusion and distributions in the case of triangle wave oscillatory shear and find that they depend strongly on the strain amplitude and particle aspect ratio. These results provide new insight into the time dependent rheology of suspensions of anisotropic particles. For continuous shear, we find two distinct diffusive time scales in the rheology that scale separately with aspect ratio p, as $1/D^r_0 p^4$ and as $1/D^r_0 p^2$ for $p \gg 1$. For oscillatory shear flows, the intrinsic viscosity oscillates with the strain amplitude. Finally, we show the relevance of our results to real suspensions in which particles can rotate freely. Collectively, the interplay between shear induced rotations and diffusion has rich structure and strong effects: for a particle

with aspect ratio 10, the oscillatory shear intrinsic viscosity varies by a factor of ≈ 2 and the rotational diffusion by a factor of ≈ 40. [1]

[1] This work has already been published; see ref. [89].

3.1 Introduction

Stir a solution and the solute will mix faster than when the solution is left quiescent. This mixing is enhanced even at low Reynold's numbers due to the coupling of random Brownian motion and spatially-varying fluid velocities. Brownian motion causes solute particles to access different fluid streamlines, which in turn differentially advect the solute particles. On long times, this combination of diffusion and advection looks the same as an enhanced translational diffusion. This mechanism, known as Taylor dispersion, occurs in a wide variety of natural and industrial processes ranging from drug delivery in the bloodstream [44] to microfluidic lab-on-a-chip setups [38], with high Reynolds number analogs even determining mixing in streams and rivers [47]. Taylor dispersion is only one example of the broader coupling that occurs between advection and diffusion that is used to manipulate mass transport across many scales, ranging from chaotic mixing in microchannels [141] through particle clustering in turbulent fluids [9].

Anisotropic particles allow for more complex coupling between diffusion and convection, due to the additional orientational degrees of freedom they possess. Under shear, an isolated ellipsoid's orientation is not constant, but instead rotates with the flow in an unsteady motion known as a Jeffery orbit [73]. In colloidal suspensions, rotational Brownian motion also changes the particles' orientations, creating the possibility of a coupling between the Jeffery orbit and rotational diffusion. Recently, through experiments and simulations Leahy *et al* [88] observed an enhancement of the rotational diffusion for colloidal dimers under shear, suggesting that such a coupling does exist. However, little is known about this coupling compared to its translational counterparts.

In this paper, we take the first steps towards calculating analytically the effects

of rotary diffusion coupled with Jeffery orbits. In the rest of section 3.1, we first review previous work on the effects of rotational diffusion coupled with Jeffery orbits. In section 3.2, we find the time-dependent orientation distribution for a dilute suspension of axisymmetric particles subjected to continuous shear. To make the analysis tractable, we examine the limit where the shear rate is large (*i.e.* $Pe \gg 1$, where the Péclet number $Pe \equiv \dot{\gamma}/D_0^r$ is the ratio of the shear rate to the zero-shear rotary diffusion constant), and we restrict the particle orientations to reside in the flow-gradient plane, which is a representative Jeffery orbit. Remarkably, we find that the complicated convection-diffusion equation describing the particle's orientations maps to a simple diffusion equation in a new coordinate with an enhanced diffusion constant. In section 3.3, we generalize these results to derive the time-dependent evolution of nonspherical particle orientations under *oscillatory* shear. Even in the limit of large shear rates, the oscillatory shear distributions and diffusive dynamics differ considerably from the continuous shear distributions. In section 3.4, we examine particular solutions of the oscillatory shear equations, taking triangle-wave shear as an analytically tractable example. In section 3.5, we use our results to explore how rotational diffusion affects the rheology of a suspension of nonspherical particles at large shear rates. Finally, in section 3.6, we close by comparing our results to traditional Taylor dispersion and demonstrating their relevance to real three-dimensional particle orientations.

While Jeffery explained the rotation of an ellipsoid, his solution does not address particles of other shapes. However, symmetry and group theory arguments can be used to ascertain how a general particle rotates [62]. For an axisymmetric particle, the orientation is completely specified by a unit normal $\boldsymbol{n}$. As shown by Bretherton [24], any axisymmetric particle in Stokes flow rotates in a Jeffery orbit

as:

$$\frac{d\boldsymbol{n}}{dt} = \boldsymbol{n}\cdot\boldsymbol{\Omega} + \lambda\left[\mathbf{E}\cdot\boldsymbol{n} - \boldsymbol{n}\left(\boldsymbol{n}\cdot\mathbf{E}\cdot\boldsymbol{n}\right)\right] \tag{3.1}$$

Here $\boldsymbol{\Omega}$ and $\mathbf{E}$ are the fluid vorticity and rate-of-strain tensors, $\Omega_{ij} \equiv (\partial_i u_j - \partial_j u_i)/2$ and $E_{ij} \equiv (\partial_i u_j + \partial_j u_i)/2$. The coefficient λ is a scalar constant which depends on the particle geometry and can be found from solving the full Stokes equations. Jeffery [73] showed for an ellipsoid of revolution that $\lambda \equiv (p^2-1)/(p^2+1)$, where p is the particle aspect ratio. For simple, continuous shear with strain rate $\dot{\gamma}$, equation (3.1) simplifies considerably. If $|\lambda| < 1$, which is usually the case, then the magnitude of the second term is always less than the first term, and the particle rotates indefinitely. Denoting θ as the polar angle measured from the vorticity direction and ϕ as the azimuthal angle from the gradient direction in the flow-gradient plane, (3.1) admits the solution

$$\begin{aligned} \tan\phi &= p\tan\left(\frac{\dot{\gamma}t}{p+1/p} + \kappa\right) \\ \tan\theta &= C\left(p\cos^2\phi + \frac{1}{p}\sin^2\phi\right)^{-1/2} \end{aligned}, \tag{3.2}$$

where p is an effective aspect ratio and the phase angle κ and orbit constant C capture the particle's initial orientation. Equations (3.1) and (3.2) show a symmetry under the transformation $p \to 1/p$, $\phi \to \phi + \pi/2$; thus, the motion of disc-like and rodlike particles are the same up to a change of axes. Note that (3.2) employs different definition of C than usual in the literature to emphasize the $p \to 1/p$ symmetry. The particle rotates in one of an infinite number of Jeffery orbits, each of which is described by an orbit constant C determined by the particle's initial orientation. Since the orbits are periodic, there is no mechanism to select a unique long-time distribution of orientations.

In colloids, rotational diffusion also affects the particles' orientations. The probability distribution ρ of finding a rod at orientation (θ, ϕ) is given by a Fokker-

Planck equation:

$$\frac{\partial \rho}{\partial t} = D_0^r \nabla^2 \rho - \nabla \cdot (\rho \boldsymbol{u}) \ , \tag{3.3}$$

$$\boldsymbol{u} = \hat{\boldsymbol{\phi}} \frac{\dot{\gamma}}{p + 1/p} \left(p \cos^2 \phi + \frac{1}{p} \sin^2 \phi \right) \sin \theta + \hat{\boldsymbol{\theta}} \frac{\dot{\gamma}(p^2 - 1)}{4(p^2 + 1)} \sin 2\phi \sin 2\theta \ . \tag{3.4}$$

Here t is the time, D_0^r is the rotary diffusion constant, $\boldsymbol{u}$ is the Jeffery orbit's rotary velocity field from (3.1), $\hat{\boldsymbol{\phi}}$ and $\hat{\boldsymbol{\theta}}$ are unit vectors in the ϕ and θ directions, and the divergence and Laplacian operators act in orientation space (θ, ϕ). The relative strength of the diffusive term $D_0^r \nabla^2 \rho$ to the advective term $\nabla \cdot (\rho \boldsymbol{u})$ is quantified by a rotary Péclet number $Pe = \dot{\gamma}/D_0^r$. While ordinarily the diffusion in (3.3) is due to Brownian motion, equation (3.3) has also been used to capture the effects of random hydrodynamic interactions in non-Brownian fibre suspensions at finite concentrations [48, 115]. As a result, (3.3) has been analysed in many different limiting values of the Péclet number, which we now describe.

Low shear rates, $Pe \ll 1$: When there is no shear, (3.3) reduces to a simple diffusion equation, and the particle orientations become isotropically distributed on times longer than $1/D_0^r$. When Pe is small but nonzero, the distribution can be found through a straightforward perturbation approach. If the particle is elongated ($p > 1$), to first order in Pe the steady-state orientation distribution is enhanced along the flow's extensional axis, where the Jeffery orbit has a negative divergence, and the distribution is suppressed along the flow's compressive axis, where the Jeffery orbit has a positive divergence. This perturbation expansion can be extended to yield a power series in $Pe = \dot{\gamma}/D_0^r$ [109, 136, 140] and has been evaluated numerically up to many orders in Pe. However, the series does not converge for $Pe \gtrsim 1$, and other methods must be used to find the distribution for such flows [81].

High shear rates, $Pe \gg 1$: Early attempts to calculate the distributions in

the limit of weak diffusion simply looked for a steady-state solution to (3.3) with $D_0^r = 0$. However, this procedure produces an apparent indeterminacy in ρ, since without diffusion there is no mechanism to select a steady-state distribution of orbit constants. Leal and Hinch realized that weak diffusion primarily acts to select a distribution of the particles' phase angles κ and orbit constants C [92, 66]. When $p \gg 1$ the mode of the steady-state distribution has an orbit constant $C \approx \sqrt{p/8}$, corresponding to an orbit that bends strongly towards the flow direction when $\phi = \pi/2$ but returns to a moderate distance away from the gradient direction when $\phi = 0$. Diffusion also randomizes κ and orients most particles near the flow direction, where the orbit's rotational velocity is slow. As a result, the steady-state distribution is strongly aligned with the flow for large p.

Intermediate shear rates, $1 \ll Pe \ll (p+1/p)^3$*:* When the particle aspect ratio is large $p \gg 1$, equation (3.4) shows that the particle rotates extremely slowly when oriented near the flow direction. As a result, for large p it is possible for the Jeffery orbit to be dominant compared to diffusion over most of the orbit, but for diffusion to be important in a small orientational boundary layer of size $\sim 1/p$ near $\phi = \pi/2$. Hinch and Leahy [66] showed that in this intermediate regime ($1 \ll Pe \ll p^3$), the fraction of particles oriented away from the flow direction decreases as $\sim 1/Pe^{1/3}$. These predictions at high and intermediate Pe have been verified experimentally, both quantitatively [151] and qualitatively [53, 74, 57, 25, 113, 88].

Dynamics. The time evolution of ρ is of interest since it determines the startup rheology of a suspension of rodlike particles. At low Pe, the time dynamics are determined by rotational diffusion, and there is only one time scale of interest. At $Pe = 0$, the evolution of the particle orientations is described by a simple diffusion equation, which has been studied extensively [56, 152, 69]. At low but nonzero

Pe, the dynamics of (3.3) have been studied since the 1930s [109] through series expansions in Pe, partly as a model polymeric solutions under startup flows. At second order and higher in Pe, the orientation transients in a suspension cause a stress overshoot, followed by an undershoot [16, 136, 140].

At high Pe the time variation due to the Jeffery orbit becomes important. However, since the rotation is periodic, the Jeffery orbit by itself does not lead to a steady-state distribution. The distribution in (3.3) instead approaches steady-state due to diffusion, which occurs on a longer time scale. Thus, in contrast to the low Pe case, at high Pe there are two time scales which determine the evolution of ρ. The time-dependence of ρ due to the Jeffery orbit at high Pe has been well-studied. At short times, the Jeffery orbit causes oscillations in ρ, which have been observed experimentally through direct imaging [106, 105], flow dichroism [53, 118], and suspension rheology [72].

Comparatively less work has focused on the approach of ρ to steady-state due to diffusion. Hinch and Leal [67] attempted to solve (3.3) exactly by separation of variables. While they were not able to obtain an exact solution, they made scaling arguments based on the orthogonality of the eigenfunctions of the convection-diffusion operator to qualitatively understand the time evolution of ρ, arguing that at high Pe there were two diffusive time scales in the rheology. Recently, through a combination of experiments and simulation Leahy *et al* [88] showed that oscillatory shear at high Pe enhances rotational diffusion, as measured from the orientational correlations. This enhancement was attributed to a mechanism where rotational diffusion allows different particles to access regions of different rotational velocity, leading to an enhanced effective diffusion. An analytical solution of the rotational dynamics under shear would provide additional insight into the effect of shear on

rotational diffusion.

3.2 Orientation dynamics under continuous shear

A full time-dependent solution to (3.3) has not been found for over seventy years. Even in the limit of large shear rates ($Pe \gg 1$), a uniformly valid time-dependent solution does not exist. Rather than attempt to solve (3.3) exactly, then, we examine the case where the particle is restricted to the most extreme Jeffery orbit along the flow-gradient plane (i.e. $\theta = \pi/2$). Equation (3.3) then simplifies to

$$\begin{aligned} \frac{\partial \rho}{\partial t} &= D_0^r \frac{\partial^2 \rho}{\partial \phi^2} - \frac{\partial}{\partial \phi}\left[\rho u(\phi)\right] \\ u(\phi) &= \frac{\dot{\gamma}}{p + 1/p}\left(p\cos^2\phi + \frac{1}{p}\sin^2\phi\right) \end{aligned} \tag{3.5}$$

Since this Jeffery orbit has the largest variation in angular velocities and is representative of the Jeffery orbit's ϕ dynamics, we expect that it captures the essence of the orientation dynamics along the Jeffery orbits in three dimensions; we defer a discussion of three-dimensional orientation dynamics to section 3.6.

At high Pe, the complicated advective term is dominant, while the much simpler diffusive term is weak. The reverse case would be easier to treat: If the advective term were simple and the diffusion term complicated, we could hope to solve the dominant advective portion exactly and to treat the weak diffusion with a singular perturbation scheme. When written in the ϕ coordinate, the advective term is complicated due to the rotation of the Jeffery orbit. This suggests that we parameterize the particle's orientation by a coordinate that does not change due

to the Jeffery orbit. We define new coordinates (κ, t') such that

$$\begin{aligned} \frac{\partial \kappa}{\partial \phi} &= \frac{\bar{u}}{u(\phi)} & \frac{\partial \kappa}{\partial t} &= -\bar{u} \\ \frac{\partial t'}{\partial \phi} &= 0 & \frac{\partial t'}{\partial t} &= 1 \end{aligned} \tag{3.6}$$

where $\bar{u}$ is the mean velocity over an entire Jeffery orbit, *i.e.* $\bar{u} \equiv \Delta\phi / T_{\mathrm{JO}} = \dot{\gamma}/(p + 1/p)$ where $\Delta\phi = 2\pi$ and T_{JO} is the Jeffery orbit period from (3.2). The constant $\bar{u}$ non-dimensionalizes the velocity; the reason for this choice is discussed in section 3.3. For a Jeffery orbit, the new coordinates are the same as the phase angle defined in (3.2):

$$p \tan(\bar{u}t' + \kappa) \equiv \tan\phi \tag{3.7}$$

$$t' \equiv t\,; \tag{3.8}$$

the definition in (3.6) gives a construction of κ for arbitrary rotary velocity fields. These coordinates are illustrated schematically in figure 3.1. Under the angular portion of the coordinate change, lines spaced by constant ϕ (panel 3.1a) get bunched in κ (3.1b) to reflect the velocity differences along the orbit, causing the particles' motion (red arrows) to look like a uniform rotation. This angular portion of the coordinate change is the coordinate space used by Leal and Hinch [92] to determine the steady-state distributions under continuous shear. The t dependence of κ in (3.6) removes this uniform rotation (3.1c).

In this new phase-angle coordinate κ, advection due to the Jeffery orbit is completely removed. The probability of finding a particle with a phase angle in $(\kappa, \kappa + d\kappa)$ evolves solely due to diffusion. Thus, instead of writing (3.5) with the distribution $\rho(\phi)$, we recast equation (3.5) in terms of an ancillary distribution $f(\kappa)$ that describes the probability of finding a particle in the region $(\kappa, \kappa + d\kappa)$:

$$f(\kappa) \equiv \rho \frac{\partial \phi}{\partial \kappa} = \rho \frac{u}{\bar{u}}\,. \tag{3.9}$$

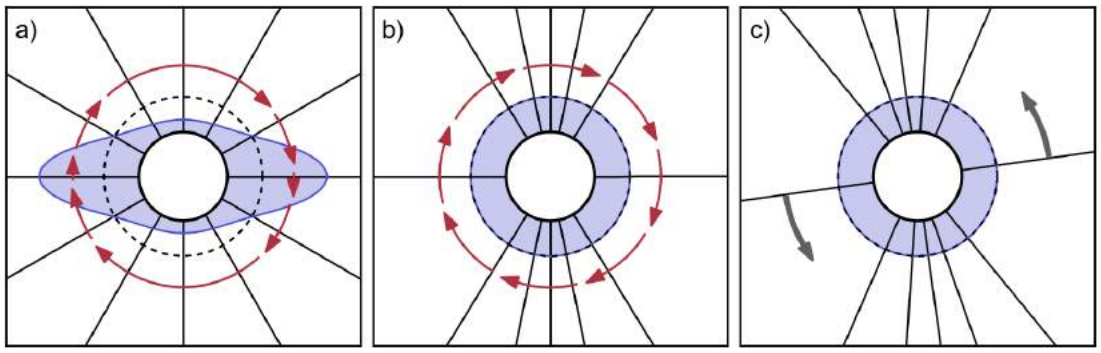

Figure 3.1: The continuous-shear distributions $\rho(\phi)$ from (3.18) for a particle with aspect ratio $p \approx 2.83$. (a) $\rho(\phi)$ in steady-state. Here the value of ρ is shown by the distance from the central black ring; the dotted black line shows the zero-shear equilibrium distribution ($\rho = 1/2\pi$). The solid black lines correspond to 12 equally-spaced angles at $\phi = n\pi/6$. The red arrows indicate the Jeffery orbit velocity (3.1). (b,c) The ancillary distribution f in the stretched space. The angular portion of (3.8), shown in (b), stretches the space significantly, visible from the bunched ϕ gridlines, and turns the Jeffery orbit into a uniform rotation. By transforming to a rotating reference frame (c), the uniform rotation in (b) is removed.

With the new coordinates (κ, t') and the ancillary distribution f, equation (3.5) can be recast into a simpler form. Direct substitution of the definition of f into (3.5) gives

$$\frac{\bar{u}}{u(\phi)}\frac{\partial f}{\partial t} = D_0^r \frac{\partial^2}{\partial \phi^2}\left(\frac{\bar{u}}{u(\phi)} f\right) - \bar{u}\frac{\partial f}{\partial \phi} \tag{3.10}$$

Transforming the derivatives to the new coordinates, equation (3.10) can be written after some simple rearrangements as

$$\begin{aligned} \frac{\partial f}{\partial t'} &= D_0^r \frac{\partial}{\partial \kappa}\left[\frac{\bar{u}}{u}\frac{\partial}{\partial \kappa}\left(\frac{\bar{u}}{u} f\right)\right], \text{ where} \\ \frac{\bar{u}}{u(\phi)} &= \left[p\cos^2\phi + \frac{1}{p}\sin^2\phi\right]^{-1} = \frac{1}{p}\cos^2(\kappa + \bar{u}t) + p\sin^2(\kappa + \bar{u}t) \end{aligned} \tag{3.11}$$

This construction of κ and $f(\kappa)$ results in an ancillary distribution f that does not move with the Jeffery orbit; all the time evolution of $f(\kappa)$ arises from diffusion, as visible from (3.11). The initial equation (3.5) is a complicated partial differential equation in simple coordinates. By making the coordinate change $\phi \to \kappa$, (3.5) has been transformed into a more tractable partial differential equation in compli-

cated coordinates. Since the coordinate change is straightforward, we can analyse equation (3.11) in the stretched coordinates to understand the rod's dynamics, and easily transform back to ϕ afterward.

Equation (3.11) is exact, describing both the significant long-time diffusion of the particle orientations and the small, less important short-time changes due to coupling between the Jeffery orbits and diffusion. To understand the orientation distribution when diffusion is small, we introduce a dimensionless advective time $\mathfrak{t} = \bar{u}t'$ and the dimensionless diffusion or inverse Pe number $\epsilon \equiv D_0^r/\bar{u}$. In dimensionless form, (3.11) then becomes

$$\frac{\partial f}{\partial \mathfrak{t}} = \epsilon \frac{\partial}{\partial \kappa}\left[\frac{\bar{u}}{u}\frac{\partial}{\partial \kappa}\left(\frac{\bar{u}}{u}f\right)\right] \ . \tag{3.12}$$

We wish to understand the evolution of f on long times $\mathfrak{t} \gtrsim 1/\epsilon$, in the limit $\epsilon \to 0$. To isolate the long-time behaviour, we find the net change of f after a full Jeffery orbit by integrating (3.11) over a period of a Jeffery orbit, $\bar{u}T_{JO} = 2\pi$. Expanding the derivatives in (3.12) and integrating gives

$$\begin{aligned} f(\kappa, \mathfrak{t}+2\pi) = f(\kappa,\mathfrak{t}) + \epsilon\Bigg\{ & \int_{\mathfrak{t}}^{\mathfrak{t}+2\pi} \left(\frac{\bar{u}}{u(\phi(\kappa,\tau))}\right)^2 \frac{\partial^2 f}{\partial \kappa^2}\, d\tau + \\ & \frac{3}{2}\int_{\mathfrak{t}}^{\mathfrak{t}+2\pi} \frac{\partial}{\partial \kappa}\left(\frac{\bar{u}}{u(\phi(\kappa,\tau))}\right)^2 \frac{\partial f}{\partial \kappa}\, d\tau + \\ & \frac{1}{2}\int_{\mathfrak{t}}^{\mathfrak{t}+2\pi} \frac{\partial^2}{\partial \kappa^2}\left(\frac{\bar{u}}{u(\phi(\kappa,\tau))}\right)^2 f\, d\tau \Bigg\} \end{aligned} \tag{3.13}$$

where τ is a dummy variable of the integration.

By assuming that the diffusion is weak (*i.e.* the dimensionless diffusion $\epsilon \equiv D_0^r/\bar{u} \ll 1$), these integrals can be simplified considerably. Since f changes slowly with time, cf. (3.12), f and its derivatives in κ can be Taylor expanded in $\mathfrak{t}$ about $\mathfrak{t} = 0$: $f(\kappa,\mathfrak{t}) = f(\kappa,0) + \mathfrak{t}\partial f/\partial \mathfrak{t}(t=0) + O(\mathfrak{t}^2)$. But by construction $\partial f/\partial \mathfrak{t} = O(\epsilon)$, so $f(\kappa,\mathfrak{t})$ can be approximated by $f(\kappa,0)$, with a correction to (3.13) of $O(\epsilon^2)$. In

contrast, the function $u(\kappa + \mathfrak{t})$ cannot be approximated by $u(\kappa)$, since $\partial u/\partial \mathfrak{t}$ is $O(1)$. Thus, to first order in ϵ, equation (3.13) can be written as

$$\begin{aligned} f(\kappa, \mathfrak{t} + 2\pi) - f(\kappa, \tau) = \epsilon \Bigg\{ & \frac{\partial^2 f}{\partial \kappa^2} \int_{\mathfrak{t}}^{\mathfrak{t}+2\pi} \left(\frac{\bar{u}}{u(\kappa + \tau)} \right)^2 d\tau + \\ & \frac{3}{2} \frac{\partial f}{\partial \kappa} \int_{\mathfrak{t}}^{\mathfrak{t}+2\pi} \frac{\partial}{\partial \kappa} \left(\frac{\bar{u}}{u(\kappa + \tau)} \right)^2 d\tau + \\ & \frac{1}{2} f \frac{\partial^2}{\partial \kappa^2} \int_{\mathfrak{t}}^{\mathfrak{t}+2\pi} \left(\frac{\bar{u}}{u(\kappa + \tau)} \right)^2 d\tau \Bigg\} + O(\epsilon^2) \end{aligned} \tag{3.14}$$

This finite-time update equation can be recast as a differential equation in the limit $\epsilon \to 0$. Define a new dimensionless time $\tau \equiv \epsilon \mathfrak{t} \equiv D_0^r t$. Rewriting the integrals in (3.14) as averages gives

$$\frac{f(\kappa, \tau + 2\pi\epsilon) - f(\kappa, \tau)}{2\pi\epsilon} = \left\langle \left(\frac{\bar{u}}{u} \right)^2 \right\rangle \frac{\partial^2 f}{\partial \kappa^2} + \frac{3}{2} \frac{\partial}{\partial \kappa} \left\langle \left(\frac{\bar{u}}{u} \right)^2 \right\rangle \frac{\partial f}{\partial \kappa} + \frac{1}{2} \frac{\partial^2}{\partial \kappa^2} \left\langle \left(\frac{\bar{u}}{u} \right)^2 \right\rangle f \tag{3.15}$$

where $\langle \cdot \rangle$ denotes the average over a Jeffery orbit period. In the limit of large shear rates $\epsilon \to 0$, and this update equation becomes a differential equation. Re-casting back to the dimensional (κ, t') coordinates, (3.14) can be written as the differential equation:

$$\frac{\partial f}{\partial t'} = D_0^r \left[\left\langle \left(\frac{\bar{u}}{u} \right)^2 \right\rangle \frac{\partial^2 f}{\partial \kappa^2} + \frac{3}{2} \left\langle \frac{\partial}{\partial \kappa} \left(\frac{\bar{u}}{u} \right)^2 \right\rangle \frac{\partial f}{\partial \kappa} + \frac{1}{2} \left\langle \frac{\partial^2}{\partial \kappa^2} \left(\frac{\bar{u}}{u} \right)^2 \right\rangle f + O(\epsilon) \right] \tag{3.16}$$

In addition, the second and third integrals on the right hand side of (3.16) can be simplified. Since the rotation rate u is a function of $\kappa + \bar{u}t'$ only, cf. (3.11), the derivatives of u can be rewritten as $\partial u/\partial \kappa = \bar{u} \partial u/\partial t'$. Consequently, the second and third terms become integrals of a derivative, and vanish since u and its derivative are periodic. As a result, only the first of the three integrals in (3.16) is nonzero.

Remarkably, in the limit $\epsilon \to 0$ these manipulations transform the complex ori-

entation dynamics in (3.5) into a simple diffusion equation with a uniform diffusion constant:

$$\frac{\partial f}{\partial t'} = D_0^r \left\langle \left(\frac{\bar{u}}{u}\right)^2 \right\rangle \frac{\partial^2 f}{\partial \kappa^2} \tag{3.17}$$

where the angle brackets denote a time-average over one orbit. On long times, the rod's orientation moves diffusively in the stretched space with an effective diffusion constant $D^r_{\text{eff}} = D^r_0 \langle (\bar{u}/u)^2 \rangle$. When diffusion is small, it acts to randomize the phase angle κ of the rod's Jeffery orbit. While the randomizing kicks of diffusion coupled to the Jeffery orbit do *not* produce diffusive behaviour in real ϕ space, their combined effect results in an emergent simple diffusion in the stretched κ space.

Up to this point, none of the results depend on the specific form of the Jeffery orbit. All that is required to proceed up to (3.17) is a rotary velocity field $u(\phi)$ that is non-zero and gives rise to periodic orbits, allowing for an appropriate coordinate change. The details of the Jeffery orbit only enter into the value of the effective diffusion constant D^r_{eff} and in the definition of κ and $f(\kappa)$. At long times, $f(\kappa) = 1/2\pi$ and κ is completely randomized, giving a steady-state distribution

$$\rho(\phi) = \frac{1}{2\pi} \left[p \cos^2 \phi + 1/p \sin^2 \phi \right]^{-1}, \tag{3.18}$$

i.e. rods with $p > 1$ mostly orient along the flow direction ($\phi \approx \pi/2$), where the Jeffery orbit velocity is slowest, cf. figure 3.1. This long-time distribution is the 2D version of Leal and Hinch's solution.

More importantly, our derivation also allows us to calculate an analytical solution for the orientation dynamics. Evaluating the average $\langle (\bar{u}/u)^2 \rangle$ we find a simple form for the effective diffusion constant D^r_{eff}:

$$D^r_{\text{eff}}/D^r_0 = \frac{3}{8}(p - 1/p)^2 + 1 \tag{3.19}$$

Equation (3.19) states that the effective diffusion of rodlike particles is enhanced under shear, in agreement with experiments in three dimensions [88]. The effective diffusion constant D^r_{eff} is symmetric with respect to $p \to 1/p$, respecting the symmetry of the Jeffery orbits. For spherical particles, which have $p = 1$ and undergo uniform rotation, the rotational diffusion is not enhanced: $D^r_{\text{eff}}(p = 1)/D^r_0 = 1$. Just as Taylor dispersion requires nonuniform translational velocities to enhance the diffusion, a nonuniform Jeffery orbit is required to enhance the rotational diffusion.

The $\sim p^2$ enhancement of the diffusion for $p \gg 1$ can be understood from the structure of the Jeffery orbit. As can be seen from (3.5), for most of the rod's possible orientations the Jeffery orbit's rotation scales as $u \sim \dot{\gamma}$, independent of aspect ratio. Thus, over most of the Jeffery orbit, the relative effect of diffusion compared to advection is $D^r_0/u \sim D^r_0/\dot{\gamma}$. However, when the particle is aligned with the flow ($\phi \approx \pi/2$), the particle's rotation is considerably slower, of order $\sim \dot{\gamma}/p^2$ when p is large. Thus, near the flow direction, the relative effect of diffusion is $D^r_0/u \sim D^r_0 p^2/\dot{\gamma}$, larger by a factor of p^2. This p^2 enhancement of the effect of diffusion produces the p^2 scaling of the effective diffusion in (3.19).

Since (3.17) is a simple diffusion equation in the phase angle coordinate κ, a solution for $f(\kappa, t')$ is easy to obtain by separation of variables. For a particle with phase angle κ_0 at time $t' = 0$, the ancillary distribution f evolves as

$$f(\kappa, t') = \frac{1}{2\pi} + \frac{1}{\pi} \sum_{m=1}^{\infty} \cos[m(\kappa - \kappa_0)] e^{-m^2 D^r_{\text{eff}} t'} \ . \tag{3.20}$$

In practice, however, the orientation dynamics in the original ϕ space are of interest, not the dynamics in κ space. In principle, the dynamics of any distribution in ϕ space can be calculated by substituting the relation between κ and ϕ, given in (3.8), into a solution of (3.17) such as (3.20). Alternatively, the evolution of a

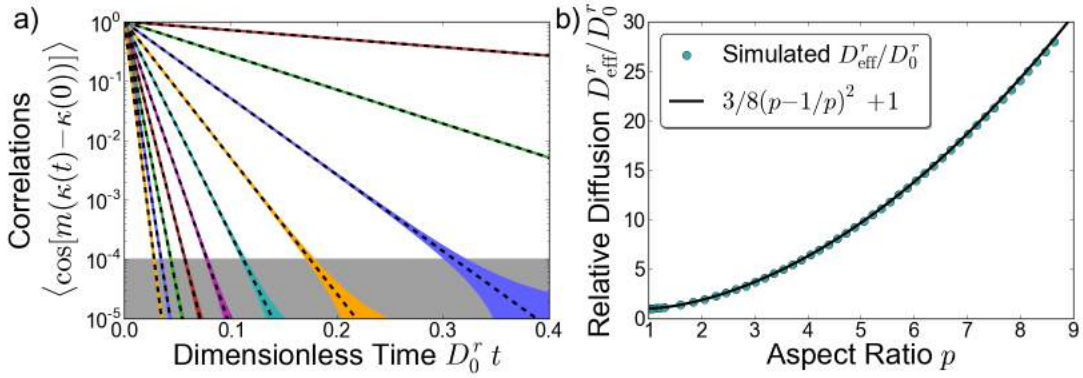

Figure 3.2: Rotational diffusion under continuous shear in the stretched κ-space. (a) Semi-log plot of the correlations $\langle\cos(m\Delta\kappa)\rangle$ vs. time for an aspect ratio $p \approx 2.83$ and $Pe = 10^4$. The black dotted lines correspond to diffusive correlations with the diffusion constant from (3.19); the colored lines correspond to the simulated correlations. There is excellent agreement with no adjustable parameters. At long times, higher-order corrections in $1/Pe$ are visible as the broadening into bands when the correlations decrease below $\approx 10^{-4}$ (grey shaded region). (b) The diffusion constant $D_{\rm eff}^r$, extracted from simulated $m = 1$ correlations, plotted vs. aspect ratio (cyan circles), alongside the prediction from (3.19) (black line).

rod's orientation in κ space can be measured instead. Correlations in κ, such as $\langle\cos m(\kappa - \kappa_0)\rangle = e^{-m^2 D_{\rm eff}^r t}$ suggested by (3.20), provide direct information about the enhanced diffusion constant. Additionally, any function of ϕ also can be written in terms of κ and t', allowing for any expectation value to be evaluated in κ space.

Nevertheless, even without this substitution, many details of the orientation dynamics in ϕ can be gleaned from the solutions for $f(\kappa)$ in (3.20). In particular, the distributions ρ or f relax to their steady-state values with a spectrum of exponential decays superimposed on the Jeffery orbit's oscillation. The spectrum of decay times for these exponentials is $1/m^2 D_{\rm eff}^r$ for integer m – the same decay times as the zero-shear diffusion equation, but with an enhanced diffusion constant $D_{\rm eff}^r$ instead of D_0^r. The slowest of these time scales, $1/D_{\rm eff}^r$, will determine how fast a generic expectation value relaxes to its steady state, including the correlations determining the rheology discussed in section 3.5.

To test our solution (3.19) for the orientation dynamics, we simulated (3.5) over a large range of aspect ratios at a large Péclet of $Pe \equiv \dot{\gamma}/D_0^r = 10^4$, as described in appendix 3.7. The ϕ correlations $\langle \cos m(\phi - \phi_0) \rangle$ are not diffusive but instead exhibit oscillations with complicated damping and orientational dependence. In contrast, the theory described above predicts that the correlations in κ-space follow a diffusive behaviour with correlations that decay as simple exponentials. We test this prediction by fitting the κ correlations in our simulations to the exponential decay $\langle \cos[m(\kappa(t) - \kappa(0))] \rangle = e^{-m^2 D_{\text{eff}}^r t}$ suggested by (3.20), as shown in figure 3.2. We find excellent agreement over a wide range of particle aspect ratios, with diffusion constants given by (3.19).

Equation (3.11) only describes the singular contribution of diffusion to the distribution and is not correct to $O(\epsilon)$ at long times. Indeed, the steady-state solution $\rho \propto 1/u$ in (3.18) only satisfies the $\nabla \cdot (\rho \boldsymbol{u})$ portion of (3.5); the $\epsilon \nabla^2 \rho$ term remains. Thus our solution is not a full solution to $O(\epsilon)$ but only captures the cumulative effects of the small diffusion that accrue over long times. It is this $O(\epsilon)$ discrepancy which appears as the broadening of the bands in figure 3.2a. The true steady-state distribution $\rho(\phi)$ can be written as $\rho(\phi) = \rho_0(\phi) + \epsilon \rho_1(\phi)$, where $\rho_0(\phi)$ is the solution given in (3.18). After long times, the correlations $\langle \cos m\Delta\kappa \rangle$ are then

$$\langle \cos m\Delta\kappa \rangle = \int_0^{2\pi} \cos(m\Delta\kappa)\rho_0 \, d\phi + \epsilon \int_0^{2\pi} \cos m(\Delta\kappa)\rho_1 \, d\phi \tag{3.21}$$

While the first term is zero by construction of κ, in general the second term is nonzero and gives an $O(\epsilon)$ correction to the correlations at long times. Since $\phi = \phi(\kappa + \bar{u}t)$, the function $\cos m\Delta\kappa$ oscillates in time, in turn creating a residual $O(\epsilon)$ long-time oscillation in the correlations. This oscillation is visible in figure 3.2 at correlation values below $\sim 1/Pe$, appearing as solid bands due to the many Jeffery orbits spanned by the x-axis.

3.3 Oscillatory shear equations

The success of equations (3.17) and (3.19) at accurately describing the dynamics of rodlike particles subjected to continuous shear suggests that we use a similar framework to examine the dynamics of rods in intrinsically unsteady flows. To this end, we derive an equation analogous to (3.17) that describes the distribution's evolution under an arbitrary oscillatory shear waveform. We show a general method for its solution, which we then implement in section 3.4.

To find the distributions under oscillatory shear, we follow the spirit of the derivation in section 3.2 for continuous shear. Under oscillatory shear, the distribution ρ is described by a convection-diffusion equation similar to (3.5), except that the magnitude of the rotational velocity changes with time. If $\dot{\Gamma}(t)$ is the dimensionless waveform describing the oscillatory shear, such that the instantaneous shear rate is $\dot{\Gamma}(t)\dot{\gamma}$, then the convection-diffusion equation for the particle's orientation takes the form

$$\frac{\partial \rho}{\partial t} = D_0^r \frac{\partial^2 \rho}{\partial \phi^2} - \frac{\partial}{\partial \phi}\left[\rho \dot{\Gamma}(t) u(\phi)\right] \ . \tag{3.22}$$

When written in the coordinate ϕ, the advective portion is exceptionally complicated since the rotational velocity field itself oscillates with the flow through $\dot{\Gamma}(t)$, in addition to the change of ϕ with time. Like the case for continuous shear, the advective term will be considerably simpler when written in terms of the phase angle κ. Thus, we define new coordinates (κ, t') such that κ changes only due to diffusion:

$$\begin{aligned} \frac{\partial \kappa}{\partial \phi} &= \frac{\bar{u}}{u(\phi)} & \frac{\partial \kappa}{\partial t} &= -\dot{\Gamma}(t)\bar{u} \\ \frac{\partial t'}{\partial \phi} &= 0 & \frac{\partial t'}{\partial t} &= 1 \, , \end{aligned} \tag{3.23}$$

where $\bar{u}$ and $u(\phi)$ are defined as before. These coordinates are defined the same way as for continuous shear, except that there is an additional factor of $\dot{\Gamma}(t)$ in

$\partial\kappa/\partial t$ to capture the shear flow's oscillation. Continuing to follow the continuous shear derivation, we recast (3.22) in terms of the ancillary distribution f. Since the angular part of the coordinate change $\partial\kappa/\partial\phi$ remains the same as for continuous shear, $f(\kappa)$ again takes the form (3.9).

With the new oscillatory shear coordinates (κ, t') and the ancillary distribution f, (3.22) can be cast into a simpler differential equation, following the continuous shear argument. Direct substitution of the definition of f gives

$$\frac{\bar{u}}{u(\phi)}\frac{\partial f}{\partial t} = D_0^r \frac{\partial^2}{\partial \phi^2}\left(\frac{\bar{u}}{u(\phi)} f\right) - \dot{\Gamma}(t)\bar{u}\frac{\partial f}{\partial \phi} \tag{3.24}$$

By transforming the derivatives to the new coordinates, (3.24) can be written as

$$\frac{\partial f}{\partial t'} = D_0^r \frac{\partial}{\partial \kappa}\left[\frac{\bar{u}}{u}\frac{\partial}{\partial \kappa}\left(\frac{\bar{u}}{u} f\right)\right] . \tag{3.25}$$

Once again, the construction of κ and $f(\kappa)$ results in an ancillary distribution f that only evolves due to diffusion. Equation (3.25) exactly describes this evolution in the new coordinates for all Pe.

Equation (3.25) is the same form as (3.11) for continuous shear, but it has a hidden difference in the value of $u(\phi(\kappa, t'))$ which we now elucidate. Rearranging the coordinate derivatives (3.23) to find $\partial\phi/\partial t'$ and $\partial\phi/\partial\kappa$ gives an equation for ϕ in terms of κ and t':

$$\frac{\partial \phi}{\partial t'} = \dot{\Gamma}(t)\bar{u}\frac{\partial \phi}{\partial \kappa}$$

Thus, ϕ is a function of $\kappa + \bar{u}\Gamma(t')$, where $\Gamma(t')$ is the antiderivative of $\dot{\Gamma}(t')$. In comparison, under continuous shear ϕ has a simpler dependence on $\kappa + \bar{u}t'$, without the complication due to the functional form of $\Gamma(t')$. For the particular case of a Jeffery orbit, $\bar{u}/u$ is

$$\frac{\bar{u}}{u(\phi)} = \left[p\cos^2\phi + \frac{1}{p}\sin^2\phi\right]^{-1} = \frac{1}{p}\cos^2[\kappa + \bar{u}\Gamma(t')] + p\sin^2[\kappa + \bar{u}\Gamma(t')] \tag{3.26}$$

which is similar to (3.11) for continuous shear but contains a different t' dependence.

Since equation (3.25) is the same form as its continuous shear counterpart (3.11), it can be analysed in the same manner in the limit of large Pe. In particular, we can find the change in f after one cycle of oscillatory shear, instead of after one Jeffery orbit, by following the steps in (3.12-3.14). An update equation similar to (3.14) can be obtained by writing (3.25) with dimensionless variables $\epsilon \equiv D_0^r/\bar{u}$ and $\mathfrak{t} \equiv \bar{u}t$ and integrating over the period of one oscillation $(\mathfrak{t}, \mathfrak{t} + \bar{u}T_{\text{cyc}})$, where T_{cyc} is the period of the oscillatory shear waveform $\Gamma(t)$. The same argument in (3.15-3.16) then recasts this update equation into a differential equation for the time evolution of f, valid in the limit that f does not change significantly over a cycle $\epsilon\bar{u}T_{\text{cyc}} \to 0$:

$$\frac{\partial f}{\partial t'} = \mathfrak{D}(\kappa)\frac{\partial^2 f}{\partial \kappa^2} + \frac{3}{2}\frac{\partial \mathfrak{D}}{\partial \kappa}\frac{\partial f}{\partial \kappa} + \frac{1}{2}\frac{\partial^2 \mathfrak{D}}{\partial \kappa^2} f \quad \text{, where} \tag{3.27}$$

$$\mathfrak{D}(\kappa)/D_0^r \equiv \left\langle \left(\frac{\bar{u}}{u(\kappa + \bar{u}\Gamma(\tau))} \right)^2 \right\rangle \equiv \frac{1}{T_{\text{cyc}}} \int_0^{T_{\text{cyc}}} \left(\frac{\bar{u}}{u(\kappa + \bar{u}\Gamma(\tau))} \right)^2 d\tau \, . \tag{3.28}$$

Equation (3.27) is similar to (3.17), but with an angularly-varying diffusion coefficient $\mathfrak{D}(\kappa)$. For continuous shear, the effective diffusion constant arises from averaging the rotary velocity field over the entire Jeffery orbit. Since the Jeffery orbit is periodic, after a fixed time a particle at any initial orientation has sampled the entire rotary velocity field, leading to an effective diffusion which is independent of starting orientation. For oscillatory shear, a particle does not in general sample an entire Jeffery orbit. The particle's effective diffusion instead results from an average over the portions of the orbit which the particle does sample, and particles at different orientations experience an angularly varying diffusion coefficient $\mathfrak{D}(\kappa)$.

There are salient differences between the oscillatory shear equation (3.27) and

the continuous shear equation (3.17). Equation (3.27) is not a simple diffusion equation in the κ coordinate: terms proportional to both f and $\partial f/\partial\kappa$ appear, and the coefficient $\mathfrak{D}(\kappa)$ of the second derivative term $\partial^2 f/\partial\kappa^2$ is not constant. Even more striking, the long-time solution to (3.27) is not constant in κ, evidently depending on the effective diffusivity $\mathfrak{D}(\kappa)$. The variation of $\mathfrak{D}(\kappa)$ with orientation causes particles to drift away from an isotropic distribution in κ, similar to the mechanisms driving concentration gradients induced by turbophoresis [9, 119], orientation gradients of rods flowing through a fixed bed [128], or the creation of absorbing states observed in dense suspensions of non-Brownian spheres and rods under oscillatory shear [35, 77, 49].

The difference between the oscillatory shear and the continuous shear distributions arises from diffusion. While the continuous shear distribution in the limit $D_0^r/\bar{u} = 0$ is the same for forward and backward shear, there are higher-order corrections in $D_0^r/\bar{u}$ to the distribution that break this symmetry [66]. Under oscillatory shear at large strain rates, these small corrections to the distribution oscillate with the flow, building up after many cycles to create a long-time distribution that differs from the continuous shear distribution, even in the limit of infinitesimal diffusion.

Rearranging (3.27) provides additional insights into the oscillatory shear distributions' evolution. Writing (3.27) in the form $\partial f/\partial t' = -\partial J/\partial\kappa$, where J is a probability flux, explicitly shows the conservation of probability:

$$\frac{\partial f}{\partial t'} = -\frac{\partial}{\partial\kappa}\left[-\mathfrak{D}\frac{\partial f}{\partial\kappa} - \frac{1}{2}\frac{\partial\mathfrak{D}}{\partial\kappa}f\right] \tag{3.29}$$

Here the flux J consists of two terms: one reminiscent of a diffusive term with a diffusion constant $\mathfrak{D}$ and one reminiscent of a drift term with a drift velocity $-1/2 \times \partial\mathfrak{D}/\partial\kappa$. It is this latter effective drift velocity, arising from the spatially-

varying diffusion in (3.28), that causes the particle orientations to drift away from the continuous shear steady-state distribution. Setting $\partial f/\partial t' = 0$ gives the distribution at long times as

$$f(\kappa) \propto (\mathfrak{D}/D_0^r)^{-1/2} \quad \rho(\phi) \propto \frac{\bar{u}}{u}(\mathfrak{D}/D_0^r)^{-1/2} \; . \tag{3.30}$$

To obtain a simple description of the dynamics of the orientation distribution, we follow a procedure similar to that in section 3.2 and transform into a coordinate z yielding a simple diffusion equation. First, we define another ancillary distribution $g(z)$ such that the probability of finding a particle in the region $(z, z+dz)$ is $g(z)dz$, in analogy to the original definition of f:

$$g(z) = f(\kappa(z))\frac{\partial \kappa}{\partial z} \; . \tag{3.31}$$

Next, we choose the coordinate z such that $g(z)$ is constant at long times. Rearranging (3.31) and steady-state f in (3.30) immediately gives one possible definition of z as:

$$\frac{\partial z}{\partial \kappa} = (\mathfrak{D}/D_0^r)^{-1/2} \; . \tag{3.32}$$

When these definitions of z and $g(z)$ are substituted into (3.29), the factors of $\mathfrak{D}$ in the diffusive term and $\partial\mathfrak{D}/\partial\kappa$ in the diffusive drift velocity term are cancelled, resulting in a simple diffusion equation for g:

$$\frac{\partial g}{\partial t'} = D_0^r \frac{\partial^2 g}{\partial z^2} \; . \tag{3.33}$$

Interestingly, recasting (3.29) into a simple diffusion equation requires the relationship between the diffusive flux term and the diffusive drift velocity term to be what it is in (3.29). In general, a convection-diffusion equation with a drift velocity that is not related to a spatially-varying diffusion constant cannot be recast into a simple diffusion equation via the line of reasoning presented here.

While the coordinate change specified by (3.32) recasts (3.27) into a diffusion equation, any other coordinate $\tilde{z}$ related to z by $\tilde{z} \equiv \alpha z$ will also do so, with a different diffusion constant $\tilde{D} = D_0^r/\alpha^2$ – indeed, this is simply a restatement of the scaling symmetries in a diffusion equation. However, while changing coordinates can produce any numerical value of $\tilde{D}$, the physical spectrum of time scales will be independent of these coordinate changes. To find the effective diffusion constant, we return to the specific case of diffusion on a circle. Equation (3.33) can then be solved by separation of variables to give

$$g(z,t) = \sum_m a_m e^{\mathrm{i}mz} e^{-D_0^r m^2 t'} \ . \tag{3.34}$$

Imposing a single-valuedness condition on g, $g(z(\kappa)) = g(z(\kappa + 2\pi))$, constrains m such that $mz(\kappa = 2\pi) = 2\pi n$, where n is an integer, or $m = 2\pi n/z(\kappa = 2\pi)$. With this constraint, equation (3.34) becomes

$$g(z,t') = \sum_{n \in Z} A_n e^{-D_0^r n^2 t' [2\pi/z(\kappa=2\pi)]^2} e^{inz[2\pi/z(\kappa=2\pi)]} \ . \tag{3.35}$$

This solution has the same form as the solution to a diffusion equation on a circle, in a new coordinate $\tilde{z} \equiv z \times 2\pi/z(\kappa{=}2\pi)$. In particular, the spectrum of the decay times is the same as that for diffusion on a circle with diffusion constant:

$$D_{\mathrm{eff}}^r/D_0^r = \left(\frac{2\pi}{z(\kappa{=}2\pi)} \right)^2 \ . \tag{3.36}$$

Incidentally, this same argument provides the reason for choosing the factor of $\bar{u}$ in the definition of the continuous shear κ in (3.6), since it is the factor of $\bar{u}$ that sets $\kappa(\phi{=}\,2\pi, t{=}0) = 2\pi$ and gives the correct spectrum of time scales.

Making this coordinate change $\kappa \to z$ transforms (3.27) into a simple diffusion equation in a more complicated coordinate system. The recast form allows for an exact solution if the new coordinate z is known and provides additional intuition into the evolution of the orientation distribution. In general, the new coordinate

$z(\kappa)$ is difficult to find analytically. However, the coordinate change is simpler to solve numerically than the full partial differential equation, and (3.28), (3.30), and (3.36) allow for a direct calculation of the effective diffusion constant and the long-time distributions without a full determination of $z(\kappa)$. Moreover, for certain strain amplitudes and oscillatory waveforms the distribution and effective diffusion can be solved for analytically. We provide the results of these solutions for triangle-wave shear in the next section.

3.4 Triangle-wave oscillatory shear solutions

As visible from equations (3.32-3.36), the strain amplitude affects both the dynamics and the distributions under oscillatory shear. To gain intuition for the role played by oscillatory strain amplitude, we examine analytically-tractable triangle-wave shear. We solve for three limiting cases – low amplitudes, large amplitudes, and intermediate resonant amplitudes – and compare the calculations with simulations. Finally, we compare numerical solutions for D^r_{eff} and ρ at arbitrary amplitudes with the results from our simulation before discussing similarities between changing the strain amplitude and changing the shear rate. We find that changing the strain amplitude allows for significant control over both the particle orientations and diffusion.

Triangle-wave oscillatory shear $\mathfrak{D}$: The solutions of (3.32-3.36) depend on the particular waveform $\dot{\Gamma}(t)$ through $\mathfrak{D}(\kappa)$. To gain intuition for the distributions under oscillatory shear, we solve for the simplest possible waveform, triangle-wave oscillatory shear. Here the waveform is $\dot{\Gamma}(t) = 1$ for the first half of a cycle, $0 < t < T_{\text{cyc}}/2$, and is $\dot{\Gamma}(t) = -1$ for the second half, $T_{\text{cyc}}/2 < t < T_{\text{cyc}}$. If the

peak-to-peak strain amplitude is γ, then $T_{\rm cyc} = \gamma/\dot{\gamma}$ and $\mathfrak{D}$ from (3.28) can be written as

$$\mathfrak{D}(\kappa)/D_0^r = \frac{\dot{\gamma}}{\gamma}\int_0^{\gamma/\dot{\gamma}} \left(\frac{\bar{u}}{u(\kappa+\bar{u}\tau)}\right)^2 d\tau \ . \tag{3.37}$$

Since $\dot{\Gamma}(t)$ has the same form for the first and second half of each cycle, the contribution to $\mathfrak{D}$ from shearing forward is the same as from shearing backward, and $\mathfrak{D}$ takes the simple form given above. For the particular rotational velocity field $u(\phi)$ from a Jeffery orbit, $\mathfrak{D}$ for triangle-wave shear can be solved exactly using (3.26):

$$\begin{aligned}\mathfrak{D}(\kappa)/D_0^r =& \frac{3}{8}(p-1/p)^2 + 1 + \frac{1}{4\gamma}(p^2-1/p^2)\Bigg\{\frac{1}{8}(p-1/p)\left[\sin 4\left(\kappa+\frac{\gamma}{p+1/p}\right)-\sin 4\kappa\right] \\ & -(p+1/p)\left[\sin 2\left(\kappa+\frac{\gamma}{p+1/p}\right)-\sin 2\kappa\right]\Bigg\} \ ;\end{aligned} \tag{3.38}$$

however, in what follows we will not need to use the complete form of $\mathfrak{D}$.

Small strain amplitudes: We begin by solving equations (3.32-3.36) for both the distributions and the diffusion in the limit of small strain amplitudes $\gamma \ll 1$, while the strain rate is still large ($Pe \gg 1$). By Taylor expanding the integrands in (3.37) about $\tau = 0$ and integrating, the coordinate change $\partial z/\partial\kappa = \sqrt{D_0^r/\mathfrak{D}(\kappa)}$ can be written as

$$\frac{\partial z}{\partial \kappa} = \frac{u}{\bar{u}}\left[1 + \frac{\gamma}{2\dot{\gamma}}\frac{\bar{u}}{u}\frac{\partial u}{\partial \kappa} + O(\gamma^2)\right] \ , \tag{3.39}$$

where we have also Taylor expanded the inverse square root and truncated both Taylor series to $O(\gamma^2)$. Following (3.30) & (3.36) above, we use this coordinate transformation $\partial z/\partial\kappa$ to find both the distributions and the effective diffusion.

To find the distribution $\rho(\phi)$, we substitute $(\mathfrak{D}/D_0^r)^{-1/2}$ from (3.39) above into (3.30):

$$\rho(\phi) \propto 1 + \frac{\gamma}{2\dot{\gamma}}\frac{\bar{u}}{u}\frac{\partial u}{\partial \kappa} + O(\gamma^2) \ . \tag{3.40}$$

Further manipulation can eliminate the κ dependence in this equation. The derivative $\bar{u}/u \times \partial u/\partial\kappa$ can be written in terms of the divergence of the velocity by writing $\partial u/\partial\kappa = \partial u/\partial\phi \times \partial\phi/\partial\kappa$ and using $\partial\phi/\partial\kappa = u/\bar{u}$, cf. (3.23). Since $\partial u/\partial\phi = \nabla \cdot \mathbf{u}$, this substitution with the appropriate normalization constant gives ρ at the start of a cycle as:

$$\rho(\phi) = \frac{1}{2\pi}\left[1 + \frac{\gamma}{2\dot{\gamma}}\nabla \cdot \mathbf{u}\right] = \frac{1}{2\pi}\left[1 - \frac{\gamma}{2}\frac{p^2-1}{p^2+1}\sin 2\phi\right] + O(\gamma^2)\ . \tag{3.41}$$

where we have used the definition of u from the Jeffery orbit, equation (3.5).

To find the effective diffusion, we first find $z(\kappa{=}2\pi)$ by integrating (3.39) over $\kappa = (0, 2\pi)$. The $O(1)$ term in $z(2\pi)$ is simply 2π, since the integral of u over a period is $2\pi\bar{u}$ by definition. For the $O(\gamma)$ correction to $z(2\pi)$ from (3.39) and (3.36), the additional integral is $\sim \int_0^{2\pi} \partial u/\partial\kappa\, d\kappa$, which is zero since u is periodic in κ. Substituting these values of $z(\kappa = 2\pi)$ into equation (3.36) shows that to $O(\gamma)$, the diffusion is not enhanced:

$$D^r_{\text{eff}} = D^r_0 + O(\gamma^2)\ . \tag{3.42}$$

In the limit of $\gamma \to 0$, both the distributions and the diffusion remain unchanged from their zero-shear value, despite the strain rate dominating over diffusion ($\dot{\gamma} \gg D^r_0$). In this limit, the frequency of the shear is large compared to the rotary diffusion. The distribution remains isotropic because the flow oscillates so rapidly that diffusion cannot alter the distribution at all over a cycle. Similarly, since the portion of the Jeffery orbit traversed by a given particle is so small, over one cycle the particle does not explore the varying rotary velocities needed to enhance the diffusion. As a result, the diffusion remains at its equilibrium value and is not enhanced.

As γ is increased, the particles start to sample more of the Jeffery orbit. At

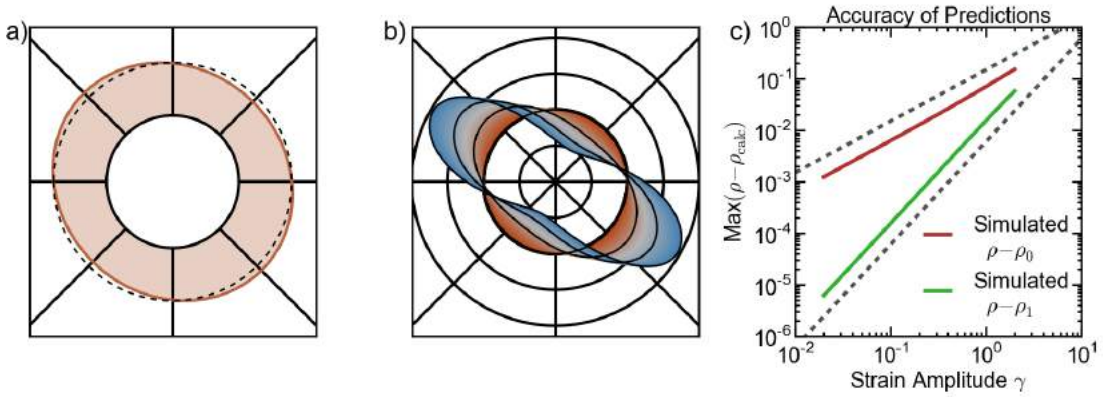

Figure 3.3: Small-amplitude oscillatory shear orientation distributions, for particles with aspect ratio $p = 2.83$ at $Pe = 10^4$. (a) The distribution $\rho(\phi)$ from simulation at a strain amplitude of $\gamma = 0.3$. (b) The corrections to the distribution $\delta\rho \equiv \rho(\phi) - 1/2\pi$ as measured from simulation, for strain amplitudes ranging from $\gamma = 0.02$ (red) to $\gamma = 2.0$ (blue), with four curves equally spaced in γ highlighted in black. At amplitudes near $\gamma = 2$, higher-order corrections cause the distribution to move away from 45° extensional axes. The circular gridlines are spaced at separations of $\delta\rho = 0.5/2\pi$, with the second gridline corresponding to $\delta\rho = 0$; the radial gridlines are equally spaced in ϕ. (c) Log-log plot showing the maximal deviation $\rho - \rho_0$ of the simulated distributions from the zero-amplitude distribution (red) and the maximal deviation $\rho - \rho_1$ from the first-order correction (green), as a function of γ. The second-order corrections are about 20% of the first-order correction at $\gamma = 1$.

these larger amplitudes, enough of the Jeffery orbit is traversed where it can interact with diffusion. This interplay results in an $O(\gamma)$ correction to the distributions, (3.41). Physically, the form of the distribution arises because the Jeffery orbit starts to align the distribution. Since the flow oscillates too fast for the distribution to align completely, the result is a partial alignment along the extensional axis, where the stretching due to the Jeffery orbit is largest. Interestingly, this $\propto \sin 2\phi$ correction to the distributions for large Pe and low γ is the same form as the correction to the continuous shear distribution at low Pe and large γ, cf. [109, 81, 136, 140]. However, this similarity is somewhat coincidental as it depends on the form of $\boldsymbol{u}$. There is excellent agreement between the predictions

for the distributions and our simulations, as shown in figure 3.3.

In contrast, due to symmetry the diffusion constant is only enhanced at $O(\gamma^2)$, cf. (3.42). The diffusion constant D^r_{eff} describes the long-time orientation dynamics; thus D^r_{eff} must be symmetric under a reversal in the flow direction. Since reversing the flow direction corresponds to changing $\gamma \to -\gamma$ and $\phi \to -\phi$, D^r_{eff} cannot be enhanced at $O(\gamma)$; the quadratic increase of D^r_{eff} with γ is shown in the inset to figure 3.5a. The distributions, on the other hand, depend on both γ and ϕ and therefore can have an $O(\gamma)$ correction while still respecting this symmetry.

Intermediate resonant amplitudes: By noting other symmetries of oscillatory shear and the Jeffery orbits, we can find another solution to the oscillatory shear equations. The Jeffery rotary velocity field repeats itself after half an orbit, as visible from (3.1) and figure 3.1. Thus, a particle starting at a given orientation samples the same velocities whether it is sheared forwards or backwards for half an orbit. This symmetry is reflected in the triangle-wave $\mathfrak{D}(\kappa)$ in (3.38): at resonant strain amplitudes $\gamma_r \equiv n\pi(p + 1/p)$ corresponding to half a Jeffery orbit, $\mathfrak{D}(\kappa)$ takes its constant continuous shear value. As a result, at half-integer Jeffery orbit amplitudes, triangle-wave oscillatory shear is exactly the same as continuous shear, with the same distributions and diffusion constant.

Since (3.27) and (3.37) are considerably simplified at resonance under triangle-wave shear, they allow for a perturbative treatment near γ_r. The procedure is similar to the low-amplitude strain treatment outlined above, except here the small parameter is the difference $\delta\gamma$ from a resonant strain amplitude γ_r; *i.e.* $\gamma = \gamma_r + \delta\gamma$. Since resonant amplitude shear is similar to continuous shear, the distribution is simplest in the continuous shear coordinate κ. To first order in $\delta\gamma$, the ancillary

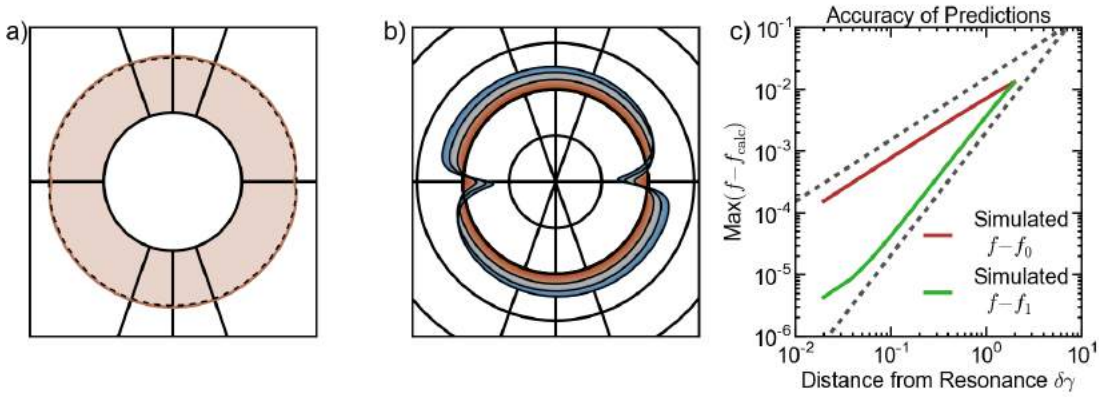

Figure 3.4: Oscillatory shear orientation distributions for particles with aspect ratio $p = 2.83$ (*i.e.* Jeffery orbit period $\dot{\gamma}T_{\mathrm{JO}} = 20$) at $Pe = 10^4$ and a strain amplitude near the first resonance. (a) The ancillary distribution $f(\kappa)$ from simulation at a strain amplitude of $\gamma = 10.6$; note the small bias away from the flow direction. (b) The difference between the continuous shear f and that measured from simulation, for positive distances from resonance $\delta\gamma = 0$ (red) to $\delta\gamma = 1.0$ (blue), with four curves equally spaced in $\delta\gamma$ highlighted in black. The circular gridlines are spaced at intervals of $\delta f = 0.15/2\pi$, with the second gridline corresponding to $\delta f = 0$. The radial gridlines are equally-spaced in ϕ (not κ). (c) Log-log plot showing the maximal deviation $f - f_0$ of the ancillary distribution from the continuous shear f (red) and the maximal deviation $f - f_1$ from the first-order correction (green), as a function of $\delta\gamma$. The second-order corrections are about 20% of the first-order correction at $\delta\gamma = 0.4$.

distribution $f(\kappa)$ and the diffusion are

$$f(\kappa) = \frac{1}{2\pi}\left\{1 + \frac{\delta\gamma}{\gamma_r}\left[\frac{\lambda}{1+\lambda^2/2}\cos(2\kappa) - \frac{\lambda^2}{4(1+\lambda^2/2)}\cos(4\kappa)\right]\right\} + O(\delta\gamma^2) \quad (3.43)$$

$$D^r_{\mathrm{eff}}/D^r_0 = \frac{3}{8}(p - 1/p)^2 + 1 + O(\delta\gamma^2)\ . \quad (3.44)$$

Like the low-amplitude case, the distributions change to first order in $\delta\gamma$, and the diffusion does not change until $O(\delta\gamma^2)$. However, unlike the low-amplitude case, the correction to the distribution is not a single harmonic, but it is composed of two harmonics in the stretched κ space. These predictions are compared against simulation results in figure 3.4 for the distributions and figure 3.5a for the diffusion. While figure 3.4 only compares the simulated and predicted distributions near the first resonant peak for a single aspect ratio, we find good agreement between

equations (3.43) & (3.44) and the simulation over a range of both aspect ratios and resonant amplitudes.

Very large amplitudes: Since continuous shear can be thought of as triangle-wave oscillatory shear with infinite strain amplitude, we expect that at very large amplitudes the distributions only vary slightly from the continuous-shear distributions. This approach to continuous shear can be seen directly from (3.37) & (3.38). The function $\mathfrak{D}(\kappa;\gamma)$, which determines both D^r_{eff} and ρ, is an average value of a periodic function where the strain amplitude γ sets the range of the integration. As γ is increased, more and more periods of the integrand are averaged over, and $\mathfrak{D}(\kappa)$ approaches its infinite-period average value of the continuous shear D^r_{eff} from (3.19). In the limit of infinite amplitude, the oscillatory shear equation (3.27) becomes the continuous shear equation (3.17). Examining the many-cycle averages in (3.28) shows that the difference between $\mathfrak{D}(\kappa;\gamma)$ and the continuous shear limit decreases as $\sim 1/\gamma$, which is echoed by the distributions near resonance in (3.43). Both empirically and by evaluating the many-cycle averages, we find that D^r_{eff} approaches its continuous shear value like $\sim 1/\gamma^2$, faster than the distributions do.

Arbitrary amplitudes: The oscillatory shear equations (3.32-3.36) give predictions for D^r_{eff} and the distributions at all amplitudes, not just at the ones treated perturbatively above. We find the effective diffusion and distributions at arbitrary amplitudes by evaluating (3.30) and (3.36) numerically for triangle-wave shear. Since oscillatory shear can also be used to control the alignment of colloidal rods, we quantify ρ via the liquid crystal scalar order parameter S which captures the degree of total alignment irrespective of the direction. The order parameter S is defined as the largest eigenvalue of the traceless orientation tensor $\mathbf{Q}$; in two dimensions $\mathbf{Q}$ is defined as $\mathbf{Q} = 2\langle \boldsymbol{n}\boldsymbol{n}\rangle - \delta$, where δ is the identity tensor and $\boldsymbol{n}$

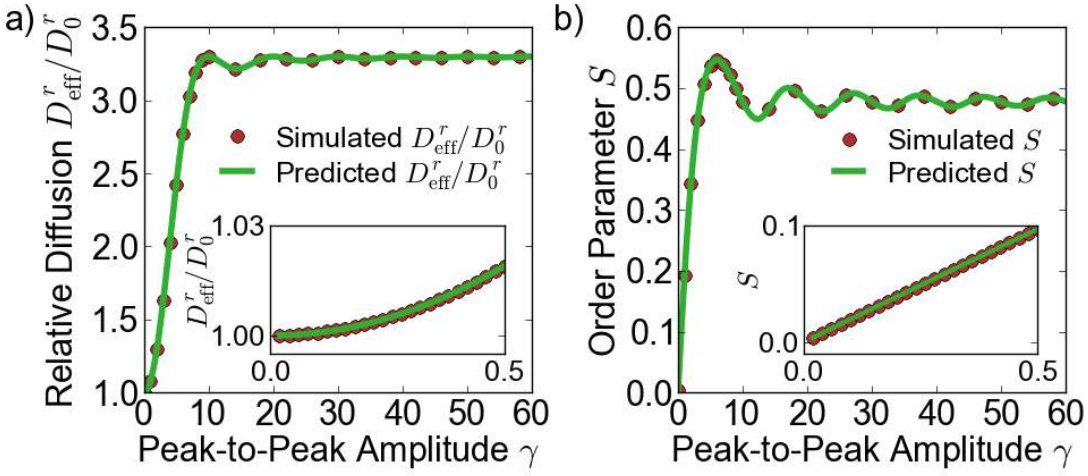

Figure 3.5: (a) Oscillatory shear diffusion D^r_{eff} vs. γ for particles with aspect ratio $p \approx 2.83$, as calculated from (3.36) (green line) and as measured from simulation at $Pe = 10^4$ (red circles). The results from simulation and from (3.36) are the same to the resolution of the plot. The oscillations in the diffusion constant with increasing strain amplitude are clearly visible. Inset: D^r_{eff}/D^r_0 at low amplitudes. (b) The liquid crystal order parameter S vs. γ at the start of a shear cycle for particles $p \approx 2.83$, as predicted from (3.30), green line, and measured from simulation at $Pe = 10^4$, red dots. At zero strain amplitude the distribution is randomly aligned ($S = 0$); with increasing strain amplitude the distribution becomes more aligned, with maximum alignment at $\gamma = 6$. Inset: S at low amplitudes. In the main panels of both (a) and (b) only 1% of the simulated points are plotted to avoid overcrowding.

the orientation unit normal. For an isotropic distribution, $S = 0$; for a perfectly aligned distribution, $S = 1$. Figure 3.5 compares these predicted values (green lines) of D^r_{eff}, panel (a), and S, panel (b), vs. γ against those measured from simulation (red dots). We find excellent agreement between this semi-analytic theory and full numerical simulations for both the diffusion coefficients and distributions, both for the aspect ratio $p = 2.83$ shown in figure 3.5 and over a range of aspect ratios (not shown). The diffusion increases gradually from its zero-amplitude value $D^r_{\text{eff}}/D^r_0 = 1$, reaching the continuous shear value at the resonant amplitude γ_r. At higher amplitudes, the diffusion undergoes damped oscillations with γ, asymptotically approaching its continuous shear value at large strains. In contrast, the

order parameter S increases from 0 linearly with γ when γ is small. Moreover, S is *not* maximal at the resonant amplitudes, but is instead maximal at an amplitude slightly below the first resonance. The order parameter then decreases slightly to its continuous shear value, with damped oscillations at larger γ.

3.5 Rheology

The orientation distribution of axisymmetric particles affects the suspension rheology. In the dilute limit, the additional deviatoric stress $\sigma^{\mathbf{p}}$ due to the particles is

$$\begin{aligned}\sigma^{\mathbf{p}} = 2\eta c\Big\{ & 2A_H\left(\mathbf{E} : \langle \boldsymbol{nnnn}\rangle - \delta\mathbf{E} : \langle \boldsymbol{nn}\rangle\right) \\ & + 2B_H\left(\mathbf{E}\cdot\langle \boldsymbol{nn}\rangle + \langle \boldsymbol{nn}\rangle\cdot\mathbf{E} - \frac{2}{3}\delta\mathbf{E} : \langle \boldsymbol{nn}\rangle\right) \\ & + C_H\mathbf{E} + F_H D_0^r\left(\langle \boldsymbol{nn}\rangle - \frac{1}{3}\delta\right)\Big\}\end{aligned} \tag{3.45}$$

where η is the solvent viscosity, c is the volume fraction of particles, $\mathbf{E}$ is the far-field rate-of-strain tensor of the fluid, δ is the identity tensor, and A_H, B_H, C_H, and F_H are hydrodynamic coefficients [73, 11, 82, 66, 127, 20]. The terms $\propto \mathbf{E}$ result from the additional hydrodynamic resistance due to the particles, which depends on the particles' specific orientations through the average tensors $\langle \boldsymbol{nn}\rangle$ and $\langle \boldsymbol{nnnn}\rangle$. The final term $\propto F_H D_0^r$ is an additional stress due to Brownian rotations of the rods. If the distribution of rods is not isotropic, these Brownian rotations result in a net stress. As the particle orientations and thus the tensors $\langle \boldsymbol{nn}\rangle$ and $\langle \boldsymbol{nnnn}\rangle$ couple to the flow, even a dilute suspension of elongated particles has a non-Newtonian rheology. Since $\langle \boldsymbol{nn}\rangle$ and $\langle \boldsymbol{nnnn}\rangle$ are in general not multiples of the identity, equation (3.45) generically predicts normal stresses. Moreover, both the normal stresses and shear stresses display transients before reaching their steady-state

values, which in turn depend on the shear rate.

These effects have been well-studied for *steady-state* distributions, over a range of Péclet numbers and particle aspect ratios from theory [109, 92, 66, 93, 68, 136, 140], experiments [15, 110, 26, 25, 74], and simulations [125, 140, 138]. Less is known about the rheology of rod suspensions in time-dependent flows at high Pe. Hinch and Leal [67] made qualitative arguments describing the stress oscillations with time in a rod suspension; there have also been several simulations of the time-dependent orientation distributions, *e.g.* [41, 45], that also examined transient stresses. Our theory of rod dynamics builds on these results by providing a quantitative physical picture of the unsteady rheology of a suspension of rods at high Pe, albeit with orientations confined to the flow-gradient plane.

Rheological transients during startup shear: From (3.17) and (3.45) we calculate the shear stress of the suspension of ellipsoidal particles during the startup of shear, for two suspensions with aspect ratios $p = 2.83$ and $p = 5.00$ at $Pe = 10^4$. The orientation distribution starts out isotropically oriented. When the flow starts, the ellipsoids start to tumble in periodic Jeffery orbits, resulting in the large-scale periodic oscillations in the shear stress (figure 3.6a). These oscillations slowly damp out with time as the enhanced rotational diffusion brings the orientation distribution to steady-state. Since the diffusion is enhanced $\sim p^2$ for large p, the oscillating stress for $p = 5.00$ damps faster than the oscillating stress for $p = 2.83$. At very short times, two additional small peaks in the stress are visible in these oscillations. However, this stress feature decays extremely rapidly – even at a large $Pe = 10^4$, it disappears before half a Jeffery orbit for $p = 5.00$.

To understand the origins of these two types of temporal oscillations in the shear stress shown in figure 3.6a, we examine equation (3.45) term by term. For

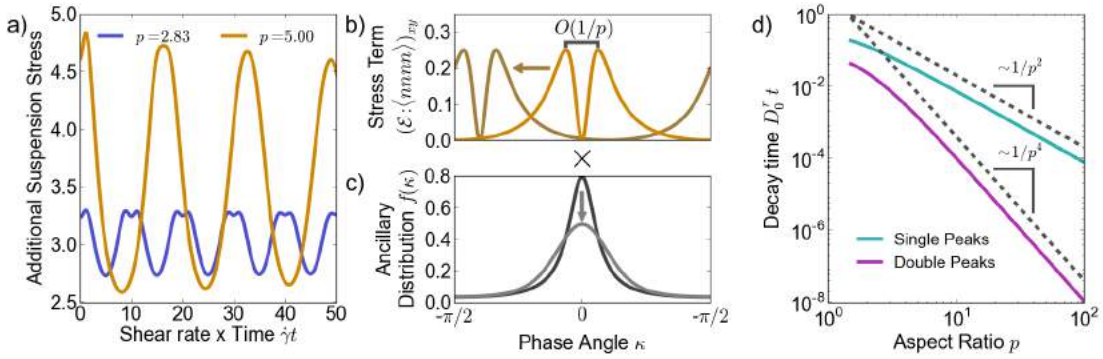

Figure 3.6: (a) The additional suspension stress $\sigma^{\mathbf{P}}{}_{xy}/\eta_0 c\dot{\gamma}$ under continuous shear, normalized by the solvent viscosity, shear rate magnitude, and aspect ratio, as a function of dimensionless time $\dot{\gamma}t$. The stress for two suspensions at $Pe = 10^4$ are shown: with aspect ratios $p = 2.83$ (blue) and $p = 5.00$ (orange). (b) The orientation-dependent stress term $(1 - \cos 4\phi)/8$ as a function of κ for $p = 5.00$. The stress term translates with time, as shown by the bright orange curve at $\bar{u}t = 0$ and the drab orange curve at $\bar{u}t = 0.4\pi$. The double-peaks in the stress term are separated in κ by a distance that scales as $\sim 1/p$ when p is large. (c) The ancillary distribution $f(\kappa)$, at two times: immediately after startup (black line) and at a time slightly after the double peaks have disappeared (grey line). (d) The times for the double peaks (magenta) and single peaks (cyan) to decay, as a function of aspect ratio. The decay times follow the $\sim 1/D_0^r p^4$ and $\sim 1/D_0^r p^2$ large-p scalings, respectively, shown in the dotted lines.

large shear rates, the last term $\propto D_0^r$ is negligible compared to the other terms $\propto \mathbf{E}$, being smaller by a factor of $1/Pe$. The third term $C_H\mathbf{E}$ is independent of time, since the strain rate $\mathbf{E}$ is fixed. For orientations confined to the flow-gradient plane, the second term's contribution to the shear stress is also independent of time, since $2\left(\mathbf{E}\cdot\langle\boldsymbol{nn}\rangle + \langle\boldsymbol{nn}\rangle\cdot\mathbf{E}\right)_{xy} = \langle n_x^2 + n_y^2\rangle = 1$. Thus, at high Pe, only the first term $\propto \mathbf{E} : \langle\boldsymbol{nnnn}\rangle$ in (3.45) contributes significantly to the time-dependent shear stress. This term provides an additional shear stress $(\langle\boldsymbol{nnnn}\rangle : \mathbf{E})_{xy} = \langle 1 - \cos 4\phi\rangle/8$ that is largest at the four orientations along the principle strain axes, $\phi = (n/2 + 1/4)\pi$. Likewise, the stress term is minimal at four orientations that occur when the particle is either aligned with the flow or perpendicular to the flow, $\phi = n\pi/2$. Thus the time varying suspension stress arises from the interplay

between the time-varying distributions and the orientation-dependent stress term $(1 - \cos 4\phi)/8$.

As discussed in section 3.2, the evolution of the orientations is simplest in the stretched coordinate κ. In this coordinate space, the orientation-dependent stress term $(1 - \cos 4\phi)/8$ is bunched in κ and moves with a constant velocity $\bar{u} = \dot{\gamma}/(p + 1/p)$. The four maximal stress orientations $\phi = (n/2 + 1/4)\pi$ are mapped to $\kappa + \bar{u}t = \tan(\pm 1/p)$ and $\tan(\pm 1/p) + \pi$, creating a double-peak in the stress term whose separation decreases as $1/p$ when p is large, cf. (3.6) and figure 3.6b. For an initially isotropic suspension, the ancillary distribution $f(\kappa)$ starts out tightly peaked and evolves diffusively to a constant value, figure 3.6c. The resulting suspension stress arises from the average of the product of the κ- and t-dependent stress term and the time-dependent distribution $f(\kappa)$.

On short times, the ancillary distribution f remains essentially constant while the stress term translates in κ. At time $t = 0$, the double peaks in the stress term are centered around the highly peaked initial distribution, which creates a relatively high stress as illustrated by figure 3.6a-c. After a short time $\sim 1/\dot{\gamma}$, the stress term has moved to the left by the small amount $\sim 1/p$, and f centers on one peak of the stress term. This large overlap produces the short-lived increase in the suspension stress occurring immediately after startup in panel a. At a slightly later time $\sim p/\dot{\gamma}$, the stress term progresses further to the left by an amount $\sim O(1)$, as shown by the drab orange curves, and the troughs in the stress term align with the peaks of $f(\kappa)$, giving rise to the large single troughs in the suspension stress. As the shear continues, the double peak of the stress term moves half a period and realigns with $f(\kappa)$. This realignment produces the observed double peaks in the stress, and the cycle repeats.

On longer time scales, the enhanced diffusion starts to broaden the ancillary distribution. As $f(\kappa)$ broadens, it simultaneously samples multiple regions of the orientation-dependent stress term, and features in ${\sigma^{\mathbf{P}}}_{xy}(t)$ start to disappear. The first to disappear is the double-peak in the suspension stress. When f has broadened by the $\sim 1/p$ separation between the double-peaks in the stress term, figure 3.6c, both the double peaks and the single trough between them are sampled simultaneously, and the double-peaks in ${\sigma^{\mathbf{P}}}_{xy}(t)$ become blurred into a single peak. Diffusion broadens $f(\kappa)$ by this $\sim 1/p$ amount after a time $\sim (1/p)^2/D^r_{\text{eff}} \sim 1/D^r_0 p^4$ for large p. Even with moderate aspect ratios at high Pe, the decay of the double-peaks in the suspension stress onsets extremely quickly: at $Pe = 10^4$ and $p = 5.0$ in figure 3.6a, the peaks have disappeared before the first half Jeffery orbit. Beyond this time scale, the suspension stress continues to oscillate but only with a single-peaked structure. These single peaks in turn disappear after $f(\kappa)$ broadens by an $O(1)$ amount and samples the entirety of the stress term simultaneously. This $O(1)$ broadening only occurs after a much longer time $\sim 1/D^r_{\text{eff}} \sim 1/D^r_0 p^2$ for large p.

The aspect ratio dependence of these two decay times is shown in figure 3.6d. To verify the predicted large aspect ratio scaling, we evaluated the stress from (3.45) using the distributions predicted by the continuous shear theory, equation (3.17) and section 3.2. We define the double-peak disappearance time as the time when the stress at a half-integer Jeffery orbit switches from a local minima to a local maxima, and we define the single-peak disappearance time as the time when the amplitude of the double peaks decays to $1/e$ of its initial value, as described in detail in appendix 3.8. We find good agreement between the simulated time scales and those predicted from the scaling argument above (figure 3.6d). These two timescales $\sim 1/D^r_0 p^4$ and $\sim 1/D^r_0 p^2$, first noticed by Hinch and Leal [67], *both*

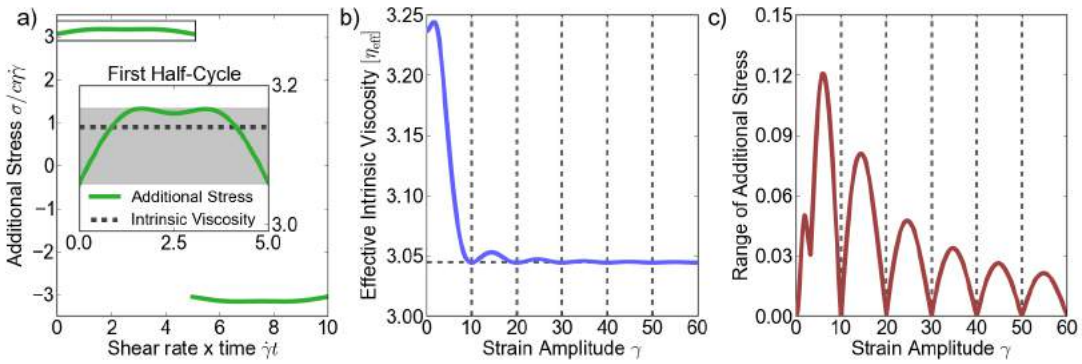

Figure 3.7: (a) The normalized additional suspension shear stress $\sigma^{\mathbf{P}}{}_{xy}/\eta_0 c\dot{\gamma}$ as a function of time for triangle-wave oscillatory shear at amplitude $\gamma = 5.0$. We define the effective viscosity $[\eta_{\text{eff}}]$ as the average of this varying stress over one cycle (dashed black line in inset); the additional variation in the stress we quantify by range of the normalized stress over one-half cycle (grey band in inset). (b) The oscillatory shear effective viscosity $[\eta_{\text{eff}}]$ as a function of γ. (c) The range of the normalized suspension stress as a function of γ; it is always small compared to $[\eta_{\text{eff}}]$.

arise from the mixing of the phase angle in the Jeffery orbit. For orientations in three dimensions, there will be additional time scales associated with the relaxation of the orbit constants.

Overview of triangle-wave oscillatory shear rheology at long times $t \gg 1/D^r_{\text{eff}}$: A representative shear stress signal during one cycle of oscillatory shear is plotted in figure 3.7a, for spheroids with aspect ratio $p = 2.83$ and peak-to-peak strain amplitude $\gamma = 5$, after $f(\kappa)$ has reached steady-state. Although the transients of the orientation distribution have decayed, ρ still oscillates with the period of one cycle. This oscillation in ρ modulates the stress over one half-cycle (figure 3.7a inset), and strictly there is no effective viscosity for a rodlike suspension under oscillatory shear. Nevertheless, since the variations in the stress are small, it is convenient to describe the stress response under oscillatory shear with its value averaged over a half-cycle. To this end, we define the "effective intrinsic viscosity" $[\eta_{\text{eff}}]$ of the suspension as the additional shear stress due to the ellipsoids normalized

by the solvent viscosity, particle volume fraction, and shear rate, $\sigma^{\mathbf{p}}{}_{xy}/(\eta c\dot{\gamma})$, and averaged over a half cycle. The slight variation of the suspension stress we quantify by the range of the normalized stress over one-half cycle, shown in panel 3.7c.

As is the case for continuous shear, the interplay between the orientation distribution and the stress term $(\mathbf{E} : \boldsymbol{nnnn})_{xy} = (1 - \cos 4\phi)/8$ determines the oscillatory shear rheology. However, there are a few differences between the procedure for understanding the suspension stress under oscillatory shear and under continuous shear. First, the stresses in the first and second half-cycle have the same magnitude, so we only examine the stress during the first half cycle. Second, since diffusion is weak ($D^r_{\text{eff}}\gamma/\dot{\gamma} \ll 1$), $f(\kappa)$ is constant throughout a cycle, and only the motion in κ of the stress term produces a time-dependent suspension stress. Third, the change in the long-time $f(\kappa)$ with strain amplitude effects a change in the suspension stress with γ. Fourth, due to its amplitude-dependent displacement $\bar{u}\gamma/\dot{\gamma}$ the motion of the stress term $(1 - \cos 4\phi)/8$ produces an additional γ dependence in the suspension stress. By examining in this way the overlap between the ancillary distribution $f(\kappa)$ and the orientation-dependent stress term $(\mathbf{E} : \boldsymbol{nnnn})_{xy}(\kappa + \bar{u}t)$, we can reconstruct the suspension stress during one cycle of triangle-wave oscillatory shear and understand the oscillatory shear rheology shown in figure 3.7. Rather than laboriously examine each amplitude in the figure, we now examine three salient amplitude regions of interest: (1) low amplitudes $\gamma \ll 1$, (2) the strain amplitude with the maximal viscosity $\gamma \approx 1.7$, and (3) amplitudes near resonance $\gamma \approx \gamma_r$.

Low amplitude [η_{eff}]*:* For $\gamma \to 0$, the orientation distribution is isotropic, cf. (3.41), and $\sigma^{\mathbf{p}}(t)$ is the same as in an isotropic distribution at shear startup. For finite but low amplitudes, the suspension stress is constant during each half

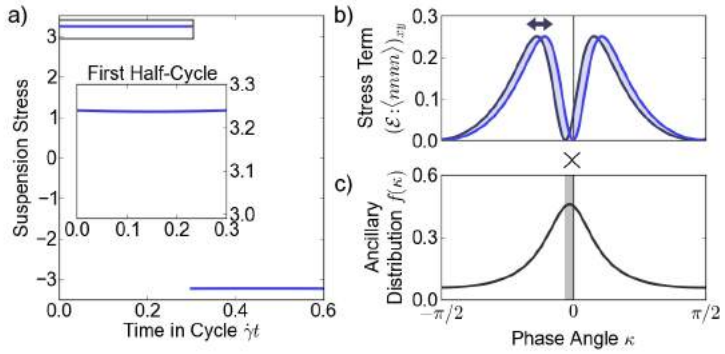

Figure 3.8: Low-amplitude $\gamma = 0.3$ oscillatory shear rheology for a dilute suspension of particles with aspect ratio $p = 2.83$ confined to the flow-gradient plane. (a) The normalized additional suspension stress $\sigma^{\mathbf{p}}{}_{xy}/\eta_0 c\dot{\gamma}$ as a function of dimensionless time $\dot{\gamma}t$ throughout one cycle of oscillatory shear, with a closeup of the stress during the first half cycle in the inset. (b) The orientation-dependent stress term $(\mathbf{E} : \boldsymbol{nnnn})_{xy}$ as a function of κ. The stress term starts with its minimum centered at $\kappa = 0$, shown in light blue. During the cycle, the Jeffery orbit advects the stress term through the lightly shaded region. At the end of the half-cycle, the stress term reaches its final position, shown in dark blue. (c) The ancillary distribution $f(\kappa)$. The shaded region denotes the area swept out by the centre of the stress term. The peak of $f(\kappa)$ is shifted from $\kappa = 0$ to the centre of the region the stress term sweep out during a cycle.

cycle at $O(\gamma)$, figure 3.8a. During each half-cycle of shear, the stress term moves by a small displacement $\bar{u}t = \bar{u}\gamma/\dot{\gamma}$, as shown in panel b. In addition, $f(\kappa)$ shifts from its zero-amplitude value (vertical line) as γ increases, panel c. This shift can be seen from (3.30) and (3.39): f at small amplitudes is the first-order term in a Taylor series in γ of an initially isotropic distribution $f_0(\kappa)$ shifted in κ by half the displacement of the stress term:

$$f(\kappa) = f_0\left(\kappa + \frac{\gamma\bar{u}}{2\dot{\gamma}}\right) + O(\gamma^2)\ , \tag{3.46}$$

Thus, to first order in γ the centre of the stress term oscillates about the centre of f. Since both f and the stress term are constant to first order in κ about their centres, $\sigma^{\mathbf{p}}(t)$ changes from its zero-amplitude value only at $O(\gamma^2)$ during the cycle. The displacement of f in κ space corresponds to a distribution $\rho(\phi)$ at the start

of a cycle that is larger along the flow's compressional axis and is smaller along the extensional axis, reversing as the flow oscillates, cf. figure 3.3. The increase in the stress from orienting particles along the extensional axis at $\phi = \pi/4$ is exactly cancelled by the particle reorientation away from the compressional axis.

Amplitude resulting in maximal $[\eta_{\mathit{eff}}]$*:* Despite the lack of an exact analytical solution for the distributions at arbitrary amplitudes, we can qualitatively understand the existence of a maximum in $[\eta_{\text{eff}}]$. As shown above, for small amplitudes $f(\kappa)$ shifts as γ increases but is otherwise unchanged. This shift suggests a mechanism for the maximal $[\eta_{\mathit{eff}}]$. As $f(\kappa)$ is shifted by a larger amount, eventually its peak is centered on one peak in the stress term, producing a large suspension stress at the cycle's start. During the cycle, the stress term translates until its trough and then second peak overlap with f, creating first a slightly lower before another large stress again at the end of the half-cycle, similar to the double-peaks in the stress under continuous shear. This translation of f corresponds to a distribution $\rho(\phi)$ that is isotropic at the centre of the cycle, but is nonlinearly distorted by the Jeffery orbit to orient more particles along the flow's extensional axis than are removed from the compressional axis, cf. the $\gamma \approx 2$ contours in figure 3.3. This double-peak structure in the suspension stress and the shifted $f(\kappa)$ are borne out in figure 3.9a & b. Since $\sigma^{\mathbf{p}}(t)$ increases at the ends of the cycle, $[\eta_{\text{eff}}]$ increases from its zero-amplitude value, and the stress' range is nonzero. While the argument captures the essence of the occurrence of a maximal viscosity, there are higher-order corrections in γ to f that cause the suspension stress to deviate slightly from the expected results.

The argument above suggests a scaling with aspect ratio for the strain amplitude resulting in a maximal viscosity. As visible from the definition of κ in (3.8),

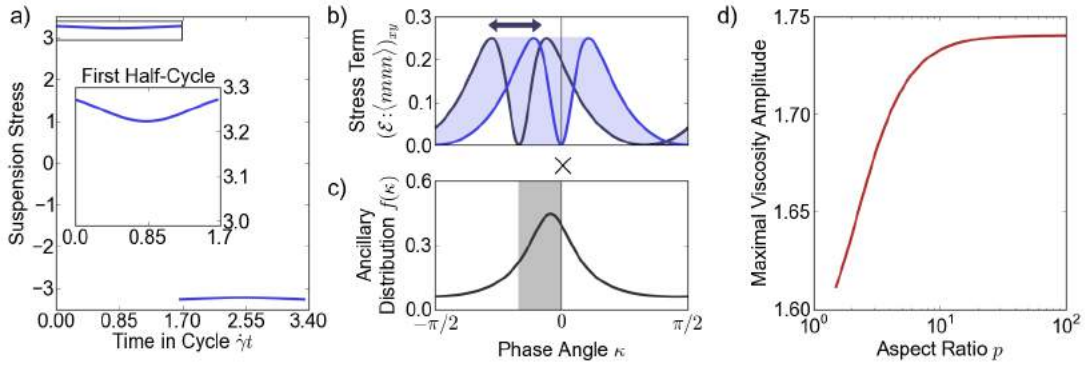

Figure 3.9: Oscillatory shear rheology at the strain amplitude $\gamma = 1.67$ resulting in maximal viscosity for a dilute suspension of particles with aspect ratio $p = 2.83$. (a) The additional suspension stress as a function of dimensionless time $\dot{\gamma}t$ throughout the cycle. (b) The stress term $(\mathbf{E} : \boldsymbol{nnnn})_{xy}$ as a function of κ. The stress term starts with its minimum centered at $\kappa = 0$, shown in light blue. During the first half-cycle, the Jeffery orbit advects the stress term through the lightly shaded region until it reaches final position, shown in dark blue. (c) The ancillary distribution $f(\kappa)$; the shaded region denotes the area swept out by the centre of the stress term. (d) Semi-log plot of the strain amplitude resulting in the maximal viscosity vs. p.

the separation between the double-peaks in the stress term scales as $\sim 1/p$ for large p. From (3.46), the small-amplitude correction to the ancillary distribution shifts f by an amount $\sim \gamma/p$, since $\bar{u}/\dot{\gamma} = 1/(p+1/p)$. Thus, at a strain amplitude $\gamma \sim 1$ independent of p, the peak of f is roughly centered on one of the peaks in the stress term. As a result, the amplitude producing the maximal viscosity should be independent of the particle aspect ratio p. This prediction is verified in figure 3.9d. The amplitude resulting in the maximal viscosity is practically constant with p, varying by less than 10% from $\gamma \approx 1.6$ at an aspect ratio $p = 2$ to its asymptotic value $\gamma \approx 1.74$ at $p = 100$.

Resonant amplitude $[\eta_{eff}]$*:* For resonant amplitudes $\gamma = \gamma_r$ corresponding to half a Jeffery orbit period, the ancillary distribution does not vary with κ: $f(\kappa) = 1/2\pi$. As the stress term moves during the cycle, its overlap with the

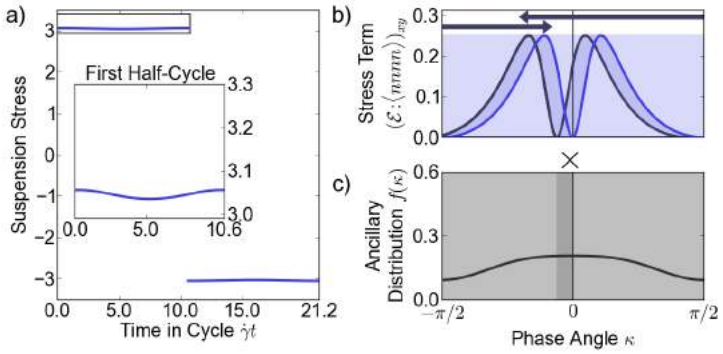

Figure 3.10: Oscillatory shear rheology for an aspect ratio $p = 2.83$ and an amplitude $\gamma = 10.6$ slightly above resonance. (a) The normalized additional suspension stress $\sigma^{\mathbf{P}}{}_{xy}/\eta_0 c\dot{\gamma}$ as a function of dimensionless time $\dot{\gamma}t$ throughout one cycle of oscillatory shear. (b) $(\mathbf{E} : \boldsymbol{nnnn})_{xy}$ as a function of κ. The stress term starts with its minimum centered at $\kappa = 0$, shown in light blue, and is advected by the Jeffery orbit through the lightly shaded region. Since $\gamma = 10.6$ is slightly above resonance, the stress term translates by more than half a period and ends at the final position shown in dark blue. (c) The ancillary distribution $f(\kappa)$. The shaded region denotes the area swept out by the centre of the stress term; with the darkly shaded region illustrating the regions where the minimum in the stress term has traversed twice.

constant f does not change, and the suspension stress remains constant during the cycle. A constant $f(\kappa)$ corresponds to a distribution $\rho(\phi)$ that does not change with time due to the Jeffery orbit, resulting in a suspension stress that is constant during a cycle. Thus, the resonant $f(\kappa)$ yields the same suspension stress and $[\eta_{\text{eff}}]$ as for continuous shear at long times.

For amplitudes slightly away from resonance $\gamma = \gamma_r + \delta\gamma$, the suspension stress changes at $O(\delta\gamma)$, as shown in figure 3.10. The first-order correction to $f(\kappa)$ indicates additional particles are oriented along the maximal stress directions. As a result, the suspension stress at the start of a cycle for amplitudes near resonance is $O(\delta\gamma)$ larger than the suspension stress at resonant amplitudes γ_r. As the stress term moves, at the centre of the cycle it centers on regions where $f(\kappa)$ is less than its resonant-amplitude value, which decreases the suspension stress. Thus, the range

of the stress increases linearly with $\delta\gamma$, figure 3.7c. However, since the effective intrinsic viscosity $[\eta_{\text{eff}}]$ is an average of the suspension stress, the oscillations during one half cycle cancel out, and $[\eta_{\text{eff}}]$ remains the same as at resonance, as shown by the smooth minima in figure 3.7b.

3.6 Conclusion and discussion

In the preceding pages, we have solved for the time-dependent orientation distribution of rodlike particles under shear. Under continuous shear, the convection-diffusion equation is greatly simplified by a change of coordinates $\phi \to \kappa$ that removes the rotation of the Jeffery orbit. This coordinate transformation complicates the diffusion term, but allows it to be treated perturbatively with a method of averages, similar to that used for certain nonlinear ordinary differential equations [124] or for homogenization methods for effective medium properties [8, 31]. The convection-diffusion equation cleanly maps to a simple diffusion equation in the new coordinate, with an enhanced diffusion that depends on averages of the rotational velocity field: $D^r_{\text{eff}} = D^r_0\langle(\bar{u}/u)^2\rangle$. For particles rotating in a Jeffery orbit, the diffusion under continuous shear is enhanced as $\sim p^2$ when p is large. Since the orientation dynamics are an exact diffusion equation in the stretched κ-coordinate at high Pe, a complete solution for any initial distribution can be easily constructed, and all initial distributions relax to a constant ancillary distribution in the κ-coordinate. This steady-state ancillary distribution is the two-dimensional analogue of the three-dimensional steady-state solution found by Leal and Hinch [92].

Under oscillatory shear, a particle does not sample all orientations during each

cycle. As a result, the effective diffusion in the κ-coordinate is an average over the regions the particle does sample, instead of an average over the entire Jeffery orbit. Since different particles sample different regions during a cycle, the effective diffusion changes with orientation κ. This varying diffusion causes particles to drift away from the continuous shear distribution, changing f from its continuous shear form. As a result of the orientationally dependent diffusion, the orientation dynamics in κ-space become complicated. However, it is always possible to map the κ-dynamics under oscillatory shear to a simple diffusion equation in a new coordinate z. Once this mapping is known, a full time-dependent solution for the distributions under oscillatory shear is easily constructed. While the coordinate change $\kappa \rightarrow z$ cannot in general be solved analytically, it can be treated perturbatively at certain amplitudes, particularly for triangle-wave shear, or solved numerically. The solutions for triangle-wave shear show that, for small strain amplitudes $\gamma \ll 1$, the orientation distribution remains isotropic and the rotational diffusion is not enhanced. Moreover, the distributions when $\gamma \ll 1$ at large Pe take the same form as the distributions when $Pe \ll 1$ at large γ. At resonant amplitudes corresponding to half integer Jeffery orbits, the orientation dynamics map exactly to the continuous shear orientation dynamics, providing the same effective diffusion constant and orientation distribution.

Since the moments of the orientation distribution determine the suspension rheology, the solutions for the orientation distributions allow for a detailed understanding of the suspension shear stresses. Examining the time evolution of the overlap between the orientation dependent stress term $\mathbf{E} : \boldsymbol{nnnn}$ and the ancillary distribution $f(\kappa)$ quantitatively explains all the features in both the continuous and oscillatory shear suspension rheology. In particular, our formalism demonstrates the existence of two diffusive time scales in the continuous shear

rheology, and predicts an amplitude-dependent effective intrinsic viscosity under oscillatory shear.

3.6.1 Comparison to Taylor dispersion

Our approach of mapping the rod dynamics to an effective diffusion equation is reminiscent of Taylor dispersion. The canonical Taylor dispersion was calculated by G. I. Taylor for Poiseuille flow in a circular pipe [145, 146]. As the nonuniform flow in the pipe moves different solute parcels at different speeds, the solute spreads out along the axial direction while diffusion erases the flow-induced radial inhomogeneity. Taylor realized that this combination of diffusion and differential advection maps to a simple diffusion equation along the pipe's axis, with a greatly enhanced effective diffusion constant. This result is reminiscent of the rotational dynamics discussed above – the combination of diffusion and differential rotation due to the Jeffery orbit maps to a simple diffusion equation. A natural question to ask is whether the enhanced rotational diffusion *is* simply a modified Taylor dispersion, or whether it is only similar.

The most general formulation of Taylor dispersion was realized by Howard Brenner and others in the 1980s [50]. He viewed the essence of Taylor's method as examining long times where the distribution is equilibrated in a small subspace $\boldsymbol{q}$ (*e.g.* the cross-section of the pipe) to allow for simple calculations of behaviour in other, larger subspaces $\boldsymbol{Q}$ (*e.g.* along the axis of the pipe). This abstraction of Taylor dispersion to arbitrary spaces allows for a rigorous, clean calculation of long-time behaviors. In addition to describing the original Taylor dispersion problem, Brenner and others used this insight to understand the dynamics of seemingly disparate systems, such as the sedimentation velocity of a nonspherical particle

[21] or of a cluster of particles [22], as well as for more intractable problems such as Brownian motion of particles under shear flow [51, 95, 52].

However, the orientation dynamics described in the current paper do not fit simply into the canonical generalized Taylor dispersion picture. In the generalized Taylor dispersion picture, there are two separate positional subspaces $\boldsymbol{q}$ and $\boldsymbol{Q}$. In the rotational dynamics calculated in this paper, there is only *one* positional subspace, corresponding to the angular coordinate ϕ or κ. Thus, Brenner's approach will not work for the problem of rotational diffusion. In part, this limitation arises from the nature of the rotary velocity field and the diffusion. In Taylor dispersion, the enhanced diffusion arises from Brownian motion *perpendicular* to the rotary velocity field. In the enhanced rotational diffusion calculated here, the enhancement arises from Brownian motion *parallel* to the rotary velocity field, and the varying velocity along the streamline enhances the rotational diffusion. In contrast, in traditional Taylor dispersion diffusion parallel to streamlines does not enhance dispersion, since the fluid flow is presumed incompressible.

While our analysis for the evolution of the orientation distribution equations does not fit neatly into Brenner's generalized Taylor dispersion, there are still some mathematical similarities between the two. Instead of integrating over a small positional subspace $\boldsymbol{q}$, the analysis in this paper proceeds by integrating over a short *time*, either one period of a Jeffery orbit or one oscillatory cycle. It is this step that allows for a mapping to a diffusion equation, as it is the small subspace step that allows generalized Taylor dispersion to map complicated dynamics to simpler equations.

3.6.2 Applicability to particle orientations in three dimensions

The analysis presented above is for particle orientations confined to the flow-gradient plane. A natural question to ask is how relevant these results are for real particle orientations in three dimensions. Previous work by Hinch and Leal [67] has investigated theoretically how the orientation dynamics of a suspension of rodlike particles changes due to shear. While the analysis of the full three-dimensional problem proved intractable, they were able to make scaling arguments based on generic properties of the orthogonal eigenfunctions of the convection-diffusion operator. From these arguments, they surmised that there were two timescales in the orientation dynamics: a $\sim 1/D_0^r p^2$ time for the orbit constant relaxation and a $\sim 1/D_0^r p^4$ time for the phase angle relaxation. In section 3.5, we find the same two timescales for the orientation dynamics in the continuous shear rheology but strictly for the phase angle relaxation, as the orbit constant is fixed for particles in the flow-gradient plane. There is one timescale, $\sim 1/D_0^r p^2$, for the phase angle to relax over the full range of the κ coordinate. However, a secondary time scale $\sim 1/D_0^r p^4$ is produced since the κ coordinate stretches the ϕ coordinate by an amount $\sim p$ near the flow direction. Thus, our solution shows there are *two* time scales in the phase angle dynamics, instead of the one suggested by Hinch and Leal [67]. This nuance in the two-dimensional dynamics suggests that a full solution for freely rotating particles would provide additional insight into the orientation dynamics.

When the orientations are not confined to the flow-gradient plane, diffusion randomizes both the Jeffery orbit's phase angle and its orbit constant. If the orbit constant is fixed, diffusion randomizes the phase angle via the same mechanism

described in this paper for particles confined to the flow-gradient plane. Indeed, simply substituting the Jeffery orbit velocity u for a fixed orbit constant into (3.17) provides an effective phase-angle diffusion for any Jeffery orbit. It might be hoped that a full three-dimensional solution could be created by combining this enhanced phase angle diffusion with a diffusive mixing among orbit constants. However, equation (3.2) shows that, for large p, the distance between two Jeffery orbits decreases near the flow direction by a factor $\sim 1/p$ compared with their distance near the gradient direction. This bunching of orbit constants results in an enhanced orbit constant diffusion that increases with p, creating an additional set of time scales for diffusion across orbits. Moreover, the diffusion across orbit constants could be coupled to the diffusion along an orbit, preventing a simple piecewise analysis.

To test the relevance of our predictions to three-dimensional orientations, we have explored the suspension rheology through a Langevin simulation of three-dimensional particle orientations under continuous shear. As discussed above, there should be two sets of time scales in the suspension rheology: one set for the phase angle relaxation, discussed in section 3.5, and a second set of time scales for the orbit constant relaxation. To discern the origins of the simulated rheology time scales, we ran two sets of Langevin simulations with initial particle orientations (θ, ϕ) drawn from two separate distributions.

The first set of simulations consists of particles drawn from an initial distribution with an equilibrated orbit constant, but with a single phase angle in the flow-vorticity plane (*i.e.* from the steady-state distribution in Leal and Hinch [92] with ϕ restricted to $\pi/2$). Since the orbit constants start completely relaxed, any change in the suspension rheology arises solely from the phase angle dynamics.

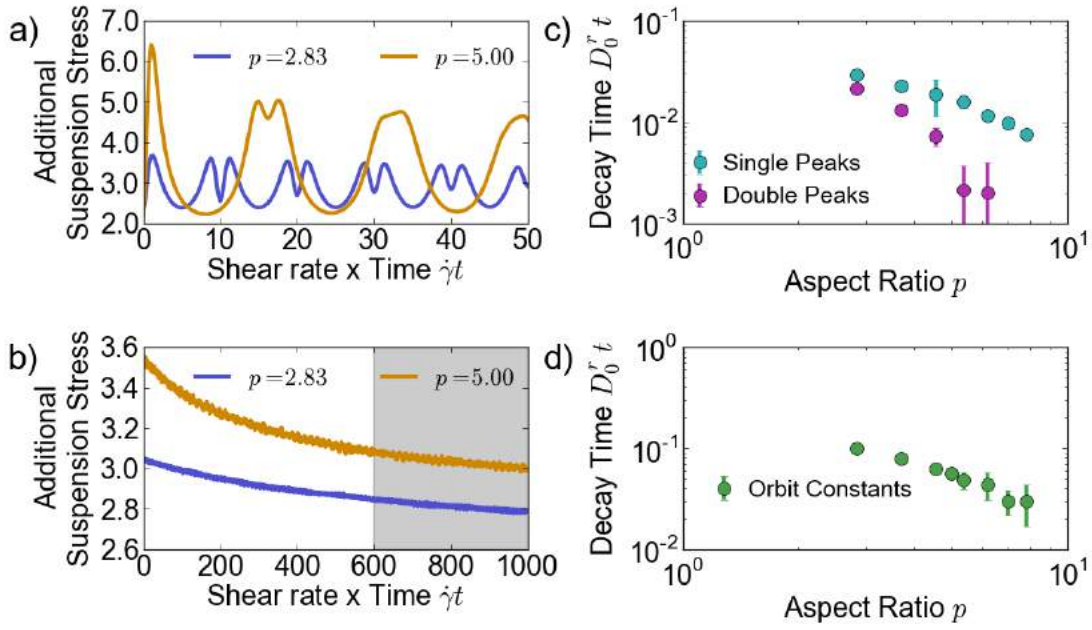

Figure 3.11: Rheology of a suspension of rodlike particles with orientations allowed to rotate freely in three dimensions, for particle aspect ratios $p = 2.83$ and $p = 5.00$ and $Pe = 10^4$, drawn from two separate initial distributions: (a) equilibrated orbit constant but a single phase angle, and (b) equilibrated phase angle but single orbit constant. Note the difference in scale for both axes. (c) The decay times of the single- and double-peak structures in the suspension stress, from simulations over a range of aspect ratios. Since the double-peak structure decays extremely rapidly, our simulation cannot resolve the double-peak decay time for the last two aspect ratios $p \approx 7$ and $p \approx 8$. (d) The decay time of the suspension stress at intermediate times due to the orbit constant relaxation, as fit over the shaded time window in (b).

The suspension rheology for this initial distribution is shown for two aspect ratios $p = 2.83$ and $p = 5.00$ at $Pe = 10^4$ in figure 3.11a. The qualitative features of the suspension shear stress are the same as for the two-dimensional continuous shear rheology in figure 3.6a. There is a distinct double-peak structure in the suspension stress for both aspect ratios at short times. At slightly longer times, the double-peaks fade into single peaks with period of one-half a Jeffery orbit. These single peaks appear to decay more slowly. Note that, since the initial distribution starts from a single phase angle, the double-peaks in the suspension stress start more

pronounced than for the initially isotropic distribution in figure 3.6a.

The second set of simulations consists of particles drawn from an initial distribution with an equilibrated phase angle, but with a single orbit constant in the flow-gradient plane (*i.e* $\theta = \pi/2$ but ϕ drawn from the continuous-shear distribution in (3.18)). Since the phase angle starts completely relaxed, any change in the suspension rheology arises solely from the diffusive relaxation of the orbit constant. The suspension rheology for this initial distribution is shown for two aspect ratios $p = 2.83$ and $p = 5.00$ at $Pe = 10^4$ in figure 3.11b. Since the phase angle starts completely relaxed, the suspension rheology does not change on the time scale of the Jeffery orbit. Instead, the suspension stress only changes on the much longer diffusive time for the orbit constant relaxation, decaying monotonically to its steady-state value.

These time scales for the rheology are shown over a range of aspect ratios in figure 3.11c&d. The time scales are extracted from Langevin simulations of 4000 particles at $Pe = 10^4$, as described in appendix 3.8. The two phase angle time scales are defined similarly to those in section 3.5. The orbit constant time scales shown are defined by fitting the stress at intermediate times to an exponential decay. If the picture for phase angle dynamics laid out in this paper is relevant for three dimensions, then for large p the double peak should decay quickly on a time scale of $\sim 1/D_0^r p^4$ while the single peak should decay more slowly on a time scale of $\sim 1/D_0^r p^2$. To check for this dependence we plot these two time scales for the phase angle relaxation as a function of aspect ratio on a log-log scale in figure 3.11c. There are clearly two separate aspect ratio dependences for the two phase-angle time scales, which seem to be consistent over the limited range with the $\sim 1/D_0^r p^4$ and $\sim 1/D_0^r p^2$ scaling for particles confined to the flow-gradient

plane. Thus the two-dimensional analysis presented in this paper captures much of the three dimensional orientation dynamics. The decay of the stress due to the orbit constants also shows a time scale that scales with p. By fitting the simulated suspension stress to an exponential decay, we find that the orbit constant relaxation time scale is consistent with the $1/D_0^r p^2$ scale argued by Hinch and Leal [67]. These orbit constant time scales are similar in magnitude to the phase angle time scales, suggesting that the distribution's for freely rotating particles is strongly affected by diffusion both along and across orbits.

Under oscillatory shear, we also expect qualitative features of the two-dimensional solutions to be present in three dimensions. As shown by Leahy *et al* [88], in three dimensions the orientation distributions change with strain amplitude under oscillatory shear in a manner similar to the two-dimensional oscillatory shear distributions in section 3.4. The oscillatory shear diffusion D^r_{eff} as measured from correlations in three dimensions also showed oscillations at the resonant Jeffery orbit amplitudes. Thus, the qualitative features of orientation dynamics for particles confined to the flow-gradient plane are present for the full three-dimensional dynamics under oscillatory shear.

3.6.3 Proposed experiments and possible applications

The results presented above suggest several experiments that are possible with current particle synthesis techniques. The detailed predictions in this manuscript could be tested by confining particles to rotate in a single Jeffery orbits, preferably in the flow-gradient plane. This confinement could be accomplished either via a magnetic field [3] or by shearing particles adsorbed to a liquid-liquid interface [135]. Moreover, as discussed in section 3.6.2 many of the scalings and qualitative pre-

dictions of this paper should be relevant for particles rotating in three dimensions. Precise single-particle measurements via confocal or holographic microscopy of D^r_{eff} over a range of aspect ratios and strain amplitudes could further verify the orientation dynamics described above. Alternatively, the average degree of alignment of an anisotropic particle suspension under oscillatory shear could be measured with flow dichroism or a similar technique. Our rheological predictions could be most easily checked for $[\eta_{\text{eff}}]$ as a function of γ, as this measurement allows averaging the stress signal over many cycles to reduce noise. Moreover, the strain amplitude at which $[\eta_{\text{eff}}]$ is maximal is roughly independent of p and thus will be robust to a suspension with aspect ratio polydispersity.

Our results could also be extended to other regimes and applications. Since the analysis in sections 3.2 and 3.3 does not depend on the details of the Jeffery orbit, it could be easily extended to velocity fields other than a Jeffery orbit, such as for weakly inertial particles [142] or for particles in weakly non-Newtonian suspending fluids [90, 91, 139, 70, 71]. On a practical level, oscillatory shear could be used to align rod suspensions for colloidal self-assembly or for 3D printed inks with fibres embedded in them [130, 33]. As shown in figure 3.5b, the maximal orientational alignment is *not* obtained under continuous shear but is at a resonant amplitude that depends on the aspect ratio. By using the arbitrary-waveform oscillatory shear equations (3.27) and (3.28), it might be possible to design a specific waveform for a desired degree of particle alignment. Over ninety years after Jeffery's solution for particle rotations in a viscous fluid, rodlike particles still have intellectually interesting and practically applicable features worthy of discovery.

Acknowledgements

We would like to thank L. Bartell, T. Beatus, and J. Sethna for useful discussions.

We acknowledge support from the National Science Foundation (CBET-1435013) (D.L.K.), from the U. S. Department of Energy, Office of Basic Energy Sciences, Division of Materials Science and Engineering under Award No. ER46517 (I.C.), and from National Defense Science and Engineering Graduate (NDSEG) Fellowship 32 CFR 168a (B.L.).

3.7 Appendix 1: Continuous and oscillatory shear numerical solutions

3.7.1 Continuous shear simulation

We numerically solved the Fokker-Planck equation for the distribution's time evolution (3.5) by expanding the distribution ρ in Fourier space and transforming (3.5) into a sparse matrix equation. For our simulations, we truncated the Fourier series to the first 301 terms (*i.e.* $m \in [-150, 150]$ for basis functions $e^{im\phi}$); the resulting coupled ordinary differential equations were solved with a fourth-order Runge-Kutta integration scheme with a time step of $dt = 5 \times 10^{-4}/\dot{\gamma}$. Either increasing or decreasing the number of terms or the time step had little effect on the simulation results. Rather than simulate a specific set of initial conditions, we evolve 301 separate initial conditions corresponding to $\rho_m(\phi, t=0) = e^{im\phi}$. Using the linearity of (3.5), we can then reconstruct an arbitrary distribution from this set of initial distributions. We can also use these simulation results to rapidly numerically solve for triangle-wave oscillatory shear, as described below.

3.7.2 Construction of oscillatory shear propagators

Rather than numerically integrate equation (3.22) for triangle-wave oscillatory shear at each strain amplitude, we instead opted to numerically create a set of oscillatory shear propagators and find the oscillatory distribution from these propagators. The propagators can be constructed rapidly from the continuous shear solutions and allow for rapid evaluation of the oscillatory shear distributions after an arbitrary time.

To find these propagators, we first find the change in ρ after one full cycle from the continuous shear simulations. One cycle of triangle-wave oscillatory shear can be viewed as two separate pieces: continuous shear going forward for a time $\gamma/\dot{\gamma}$, followed by continuous shear going backward for the same time. Let the probability distribution $\rho_F = \rho_F(\phi, t \,|\, \phi_0)$ be the probability density of finding a particle with orientation ϕ after undergoing forward shear for a time t, given that the particle started at an orientation ϕ_0. Similarly, let $\rho_B(\phi, t \,|\, \phi_0)$ be the probability density of finding a particle at orientation ϕ after undergoing backward shear for a time t. The orientation of the particle ϕ after a full cycle is a two-step process: after the first half of a cycle, the particle rotates to an intermediate orientation $\phi_{1/2}$ with some probability $\rho_F(\phi_{1/2}, t = T_{\text{cyc}}/2 \,|\, \phi_0)$, then rotates during the second half of the cycle from $\phi_{1/2}$ to its final orientation ϕ_1 with some other probability $\rho_B(\phi_1, t \,|\, \phi_{1/2})$. We integrate over $\phi_{1/2}$ to find the conditional probability distribution $\rho(\phi_1, t = T_{\text{cyc}} \,|\, \phi_0)$ of the particle's final orientation after a full cycle:

$$\rho(\phi_1, T_{\text{cyc}} \,|\, \phi_0) = \int \rho_F(\phi_{1/2}, T_{\text{cyc}}/2 \,|\, \phi_0) \rho_B(\phi_1, T_{\text{cyc}}/2 \,|\, \phi_{1/2}) \, d\phi_{1/2} \tag{3.47}$$

Now, we Fourier expand $\rho_F(\phi_{1/2}, T_{\text{cyc}}/2 \,|\, \phi_0)$ in both $\phi_{1/2}$ and ϕ_0, and similarly for

ρ_B:

$$\rho_F(\phi_{1/2}, T_{\rm cyc}/2 \,|\, \phi_0) = \sum_{kl} A^F_{kl} e^{ik\phi_{1/2}} e^{il\phi_0} \tag{3.48}$$

$$\rho_B(\phi_1, T_{\rm cyc}/2 \,|\, \phi_{1/2}) = \sum_{mn} A^B_{mn} e^{im\phi_1} e^{in\phi_{1/2}} \tag{3.49}$$

Substituting into (3.47) and integrating gives a Fourier expansion of $\rho(\phi_1, T_{\rm cyc} \,|\, \phi_0)$ as

$$\begin{aligned} \rho(\phi_1, T_{\rm cyc} \,|\, \phi_0) &= \sum_{ml} B^1_{ml} e^{im\phi_1} e^{il\phi_0} \ , \\ \text{where} \ \ B^1_{ml} &\equiv 2\pi \sum_n A^F_{-n,l} A^B_{mn} \end{aligned} \tag{3.50}$$

Thus, we can calculate the distribution after one cycle of triangle-wave oscillatory shear from the continuous shear distributions by using matrix multiplication. In contrast, most other waveforms require a full numerical solution for ρ at each strain amplitude.

To find the distribution after $N+1$ cycles, we follow a similar argument. We can view the probability of finding the particle at an orientation ϕ_{N+1} after $N+1$ cycles as a two-step process: The particle started at ϕ_0 and rotated to ϕ_N after N cycles with some probability $\rho(\phi_N, NT_{\rm cyc} \,|\, \phi_0)$, followed by a rotation from ϕ_N to ϕ_{N+1} with probability $\rho(\phi_{N+1}, T_{\rm cyc} \,|\, \phi_N)$ after the final cycle. Following the same argument as above, the distribution $\rho(\phi_{N+1}, (N+1)T_{\rm cyc} \,|\, \phi_0)$ can be written as

$$\begin{aligned} \rho(\phi_{N+1}, (N+1)T_{\rm cyc} \,|\, \phi_0) &= \sum_{lm} B^{N+1}_{ml} e^{im\phi_{N+1}} e^{il\phi_0} \ , \\ \text{where} \ \ B^{N+1}_{ml} &\equiv 2\pi \sum_n B^N_{-n,l} B^1_{mn} \end{aligned} \tag{3.51}$$

Thus the distribution after an arbitrary number of triangle-wave oscillation cycles can be reconstructed from the simulated forward and backward probability distributions, once the coefficients A^F_{kl}, A^B_{mn} are known.

The coefficient matrices A^F_{kl}, A^B_{mn} can in turn be calculated from the continuous shear solutions. Let

$$\rho_k(\phi, t) = \sum_l a_{kl}(t) e^{il\phi} \tag{3.52}$$

be the continuous-shear solution of (3.5) subject to the initial condition $\rho_k(\phi, 0) = e^{ik\phi}$, *i.e.* $a_{kl}(0) = \delta_{kl}$. Due to linearity, any distribution $\rho(\phi, t)$ can be written as a sum over the ρ_k. In particular, we can write $\rho_F(\phi, t \,|\, \phi_0)$ in this way:

$$\rho_F(\phi, t \,|\, \phi_0) = \sum_k q_k(\phi_0) \rho_k(\phi, T_{\text{cyc}}/2) \tag{3.53}$$

where $q_k(\phi_0)$ are the coefficients of the Fourier expansion whose values depend on ϕ_0. Substituting the definition of $\rho_k \equiv \sum_k a_{kl} e^{il\phi}$, we can write this as

$$\begin{aligned} \rho_F(\phi, t \,|\, \phi_0) &= \sum_k q_k(\phi_0) \sum_l a_{kl}(t) e^{il\phi} \\ &= \sum_{kl} q_k(\phi_0) a_{kl}(t) e^{il\phi} \end{aligned} \tag{3.54}$$

The distribution $\rho(\phi, t \,|\, \phi_0)$ is defined such that $\rho(\phi, 0 \,|\, \phi_0) = \delta(\phi - \phi_0) \equiv 1/2\pi \sum_k e^{ik(\phi - \phi_0)}$. Substituting this into (3.54) at $t = 0$ and using the definition of A^F_{kl} from (3.48), the forward shear propagator A^F_{kl} and the continuous shear coefficients a_{kl} can be related as

$$A^F_{kl} = \frac{1}{2\pi} a_{-l,k}(T_{\text{cyc}}/2) \; . \tag{3.55}$$

To obtain the coefficients for backward shear A^B_{kl}, we note that shearing backwards is the same as taking $\phi \to -\phi$, $\phi_0 \to -\phi_0$, as visible from (3.5). This is in turn the same as switching the signs of the indices, so the backward shear propagator A^B_{kl} is

$$A^B_{kl} = \frac{1}{2\pi} a_{l,-k} \; . \tag{3.56}$$

Thus, from our simulation for continuous shear in one direction only, we can quickly recreate the time-dependent distribution ρ under triangle-wave oscillatory shear

for strains of arbitrary amplitude. This same procedure can be used to solve the convection-diffusion equation after a time t in $O(\ln t)$ steps instead of the normal $O(t)$ steps needed for direct numerical integration; we use this procedure to rapidly find the long-time distributions under oscillatory shear. We used this fast method to find both ρ and D^r_{eff} numerically at ≈ 3000 separate amplitudes, equally spaced from $\gamma = 0.02 - 60.00$.

3.7.3 Extracting diffusion constants from simulation

For continuous shear, the diffusion coefficients shown in figure 3.2 were calculated by fitting exponentials to correlations $\langle \cos m(\kappa - \kappa_0) \rangle$ from 20 separate initial orientations κ_0 which were sampled from the steady-state distributions. As mentioned in the text, the fitted correlations in κ-space are independent of the starting orientation, while the correlations in the unstretched ϕ-space do depend on the starting orientation.

For oscillatory shear, the situation is slightly more complicated since the orientations are diffusive in a new, stretched z-space. Rather than fitting correlations in the new z-coordinate, which must be computed for each strain amplitude, we examine the long-time decay of an arbitrary correlation. Since the ancillary distribution $g(z)$ evolves according to a diffusion equation in z space with an effective diffusion D^r_{eff}, any correlation $C(\Delta t)$ will decay as a sum of exponentials:

$$C(\Delta t) = \sum_m C_m e^{-m^2 D^r_{\text{eff}} \Delta t} \tag{3.57}$$

At long times $D^r_{\text{eff}} \Delta t \gg 1$, only the term with the smallest m ($m = 1$) remains; the others have decayed. To find the effective diffusion under oscillatory shear, we examine the decay of a correlation C after a long time such that $C(t) \sim$

10^{-3}. For diffusive correlations, the further decay is entirely due to the $m = 1$ term; the terms $m = 2$ and higher are exponentially smaller, approximately $C^4 \sim 10^{-12}$ as can be seen from (3.57), and do not contribute to the decay. From these long time decays of the correlation C, we extract the oscillatory shear diffusion constant D^r_{eff}. To check the robustness of this technique, we evaluate two separate correlations, $\langle \cos \Delta\phi \rangle$ and $\langle \cos \Delta\kappa \rangle$, for 20 separate initial orientations sampled from the long-time distribution. Empirically, the value of D^r_{eff} obtained from the long-time correlations is independent of either the particle's starting orientation or the type of correlation fitted. In contrast, at short and intermediate times the extracted D^r_{eff} varies with both the initial particle orientation and the type of correlation fitted. This difference at short times arises because the orientation is in general *not* diffusive in either the original ϕ space or the continuous-shear stretched κ space, but is diffusive in the (uncalculated) z space for oscillatory shear.

3.8 Appendix 2: Rheology calculations and rheological timescale definitions

Calculating the rheology: To calculate the suspension rheology for the two-dimensional particle orientations under continuous shear, we used the theory of two-dimensional rod dynamics presented in section 3.2 to find the time-dependent ancillary distribution $f(\kappa, t)$ at $Pe = 10^4$. Once the ancillary distribution is known, the suspension stress can be calculated from (3.45). To find the rheology for orientations in three dimensions, we numerically integrated a Langevin equation for 4000 separate initial particle orientations at $Pe = 10^4$, by integrating (3.1) with an additional noise term using an Euler method. The time step size $dt = 5 \times 10^{-4}/\dot{\gamma}$

gives an integration error after each time step that is 10^{-3} that of the random motion. The orientation moment tensors $\langle \boldsymbol{nn} \rangle$ and $\langle \boldsymbol{nnnn} \rangle$ are evaluated from direct averages of the particle orientations.

To calculate the triangle-wave oscillatory shear rheology for two-dimensional particle orientations, we first obtained the oscillatory shear distributions at long times. The ancillary distribution $f(\kappa)$ can be found from (3.30). While the coordinate derivative $\partial z/\partial \kappa$ and thus the functional form of f can be exactly evaluated analytically, the distribution's normalization must be evaluated numerically. Alternatively, the distribution ρ can be found from the simulations at $Pe = 10^4$; we find that both procedures produce the same rheology to within $\approx 1/Pe$. To find the stress during one-half cycle, we evolved the distributions in the limit of no diffusion for the duration of the half-cycle; since our theory describes the limit of large strain rates the ancillary distribution does not diffusively evolve during a cycle. The maximal $[\eta_{\text{eff}}]$ amplitudes are found only from (3.30) which is orders of magnitude faster than simulating the orientation distributions; we use a Nelder-Mead simplex algorithm we find the maximal $[\eta_{\text{eff}}]$ amplitudes for the 1000 aspect ratios logarithmically spaced from $p = 1.5 - 100.0$ shown in figure 3.9c.

Definitions of rheological time scales: The double-peak decay time scale in figure 3.6c is defined as the time when the suspension stress at half-integer Jeffery orbits switches from a local minimum to a local maximum. To find this time scale, we examined the second derivative of the suspension stress via our analytical solution after a fixed time corresponding to 200 half-integer Jeffery orbits and varied the rotary diffusion D_0^r. Examining the stress after these long times prevents the decaying envelope of the suspension stress from biasing the second derivative. Traces of the single peaks are always present, in contrast to the double peaks which

completely disappear after a well-defined time. To minimize short-time transients in the single peak decay time, we looked for the time when the magnitude of the single peaks decayed to 1% of their initial value, by examining the stress at a fixed time corresponding to the first trough after 200 half-integer Jeffery orbits (*i.e.* $\dot{\gamma}t = 200.5\pi(p + 1/p)$) and varying D_0^r. Since the double-peak structure obscures the height of the suspension stress's initial peak at $t = 0$, we examine the decay of the minimum of the troughs in the stress, occurring every $(n + 1/2)/2$ Jeffery orbits. We then rescaled this time to give the corresponding $1/e$ decay time of the single peaks.

We extracted the double-peak and single-peak decay times for the three-dimensional suspension rheology in a similar manner. However, since there is no closed-form solution for three-dimensional rod orientations, we looked at a single set of simulations at $Pe = 10^4$ for each aspect ratio and initial distribution. The double-peak decay time shown in figure 3.11c is the time at which the (smoothed) second derivative of the stress at each half-integer Jeffery orbit is zero, interpolated between half-integer Jeffery orbits to improve temporal resolution. For all but the lowest aspect ratios, this zero occurs after only a few half Jeffery orbits. The single-peak decay times are measured from the same set of simulations. To minimize the effects of noise inherent in a Langevin simulation, we calculated the $1/e$ decay time for the three-dimensional orientations from when the troughs in the stress decayed to 10% of their initial value, instead of 1%.

The orbit constant decay times shown in figure 3.11d are also taken from a single set of simulations for each aspect ratio at $Pe = 10^4$. We defined the time scale for the orbit constant decay by fitting the shear stress at times $0.06 < D_0^r t < 0.1$ to an exponential decay, after subtracting off the steady-state shear stress. To minimize

the effects of noise inherent in the Langevin simulation, we smoothed the simulated shear stress by convolving with a boxcar filter with a width of half a Jeffery orbit; the data shown in figure 3.11b are not smoothed. While there are some transients in the suspension stress at shorter times, empirically we find that the suspension stress is well-described by an exponential decay for all the aspect ratios measured, within the limited resolution of our simulations.

CHAPTER 4

CONTROLLING SUSPENSIONS OF RODLIKE COLLOIDAL PARTICLES

While colloidal suspensions of nonspherical particles have been studied for decades, most work has focused on describing their behavior in simple flows with simple time behavior. Little is known about their behavior in flows with complex variations in time, and in particular the possibility of varying the flow with time to control the suspension's properties. Here we take advantage of a recent solution for the orientation dynamics of a dilute suspension under an *arbitrary* periodic shear flow to control particle alignment and suspension rheology. We use a periodic shear waveform to align particle orientations significantly stronger than under continuous simple shear, increasing the alignment by an amount proportional to the particle aspect ratio. Since particle orientations couple to the suspension stress, we can strongly control the rheology, maximizing and minimizing the viscosity and creating large normal stress signals. Surprisingly, the optimal waveforms are extremely simple, providing a simple understanding of the mechanisms for controlling particle alignment and suspension rheology.

4.1 Introduction

Colloidal suspensions of axisymmetric particles are of considerable interest both as a model system and for their practical applications in engineering. Since nonspherical particles possess an extra, orientational degree of freedom that couples to the rheology, suspensions of these particles exhibit interesting rheological properties such as viscoelasticity and shear-thinning, even in the dilute regime. In addition to being an excellent model system, suspensions of axisymmetric particles arise in numerous biological and engineering applications – from microtubules and red blood cells to nanoparticle metamaterials and extruded fiber composites.

As a result, much work has focused on the flow behavior of suspensions of axisymmetric particles. Jeffery [73] was the first to investigate suspensions of ellipsoidal particles under shear. He found that the particles rotate in an unsteady motion known as a Jeffery orbit. For a particle of aspect ratio p in a simple shear flow, the particle's unit normal $\boldsymbol{n}(\theta, \phi)$ evolves with time t as

$$\begin{aligned} \tan\phi &= p \tan\left(\frac{\Gamma(t)}{p + 1/p} + \kappa\right) \\ \tan\theta &= C\left(p\cos^2\phi + \frac{1}{p}\sin^2\phi\right)^{-1/2} \end{aligned} \tag{4.1}$$

where $\Gamma(t)$ is the accumulated shear strain of the applied flow and the phase angle κ and orbit constant C are constants of integration. The particle's orientation $\boldsymbol{n}(\theta, \phi)$ is parameterized by the polar angle from the vorticity direction θ and the azimuthal angle from the gradient direction ϕ. For most particles [131] the Jeffery orbits are periodic, and thus hydrodynamics alone does not determine the particle orientations at long times under a simple shear flow.

In colloidal suspensions, rotational diffusion acts to randomize particle orientations. In a shear flow, both the deterministic Jeffery orbits and the random

rotational diffusion determine the final orientation distribution ρ as described by a Fokker-Planck equation in orientation space:

$$\frac{\partial \rho}{\partial t} = D\nabla^2\rho - \vec{\nabla}\cdot(\rho\vec{u}) \tag{4.2}$$

where D is the rotational diffusivity. For dilute suspensions in a time-varying simple shear flow, the rotational velocity $\vec{u}$ is the Jeffery orbit rotational velocity. Either Jeffery's solution or symmetry considerations [24] give this rotational velocity as

$$\begin{aligned}\vec{u} &= \boldsymbol{n}\cdot\boldsymbol{\Omega} + \frac{p^2-1}{p^2+1}\left[\boldsymbol{E}\cdot\boldsymbol{n} - \boldsymbol{n}(\boldsymbol{n}\cdot\boldsymbol{E}\cdot\boldsymbol{n})\right] \\ &= \hat{\phi}\frac{\dot{\gamma}(t)}{p+1/p}\left(p\cos^2\phi + \frac{1}{p}\sin^2\phi\right)\sin\theta + \hat{\theta}\frac{\dot{\gamma}(t)(p^2-1)}{4(p^2+1)}\sin 2\phi\sin 2\theta \quad ,\end{aligned} \tag{4.3}$$

where $\boldsymbol{\Omega}$ and $\boldsymbol{E}$ are the instantaneous vorticity and rate-of-strain tensors and $\dot{\gamma}(t)$ the instantaneous strain rate of the flow. The combined effects of diffusion and Jeffery orbits produce an interesting array of orientation distributions and suspension rheology that are fairly well understood for continuous shear at long times. The Péclet number Pe, the ratio of the flow's shear rate to the particle's rotational diffusivity, determines the relative importance of diffusion versus particle reorientation by the Jeffery orbit. At low Pe, diffusion dominates and results in an isotropic orientation distribution and a relatively high suspension viscosity. To first order in Pe the flow creates a slight alignment along the extensional axis, but the suspension viscosity remains the same. Conversely, at high Pe, diffusion causes a randomization of the rod's orientations only insofar as to result in a distribution that does not change in time [92]. Particles tend to align fairly strongly with the flow, where the Jeffery orbit is slowest, which also results in a relatively low suspension viscosity. Interestingly, because the rotational velocity of the Jeffery orbit becomes increasingly varied with increasing aspect ratio p of the particles, there is a third regime at intermediate Pe, where the Jeffery orbit is dominant over

diffusion almost everywhere except in a small region near the flow direction, where diffusion dominates [66].

While extensive research has focused on describing continuous shear of rodlike particle suspensions, much less work has focused on describing their behavior in time-varying flows [67]. The time-dependent convection-diffusion equations for rod orientation dynamics are extremely complicated to solve even in the dilute limit; as yet there is not a complete solution even for the simple case of continuous shear. As a result, an engineer who desires to control a suspension of rodlike particles through shear is essentially limited to either exploring continuous shear at various Pe, or to experimenting through trial-and-error. In this paper, we take the first steps towards creating a theory for *controlling* the flow behavior of suspensions of rodlike particles, instead of *reacting* to it. We take advantage of a recent analytical solution to the orientation dynamics of rodlike particles under an *arbitrary* periodic shear flow, albeit for particles confined to the flow-gradient plane at high Pe [89]. We use this exact solution to optimize desired properties of the suspensions, such as maximizing particle alignment, maximizing and minimizing the suspension shear viscosity, and maximizing the normal stress difference. Surprisingly, the optimal waveforms for controlling suspension behavior are extremely simple and allow for a precise intuition for the mechanism for controlling suspension properties. Along with previous similarities between the restricted and full orientation dynamics [89, 88], this intuition suggests that the qualitative features of the optimal waveforms and results will carry over to real suspensions of particles that can rotate freely in three dimensions.

4.2 Orientations confined to the Flow-Gradient Plane

For particles confined to the flow-gradient plane, the complicated advection-diffusion equation in orientation space $\partial\rho/\partial t = D\nabla^2\rho - \vec{\nabla}\cdot(\rho\vec{u})$ simplifies to

$$\begin{aligned} \frac{\partial\rho}{\partial t} &= D\frac{\partial^2\rho}{\partial\phi^2} - \frac{\partial}{\partial\phi}\left[\dot{\Gamma}(t)u(\phi)\rho\right] \quad , \\ u(\phi) &= \frac{1}{p+1/p}\left(p\cos^2\phi + \frac{1}{p}\sin^2\phi\right) \end{aligned} \tag{4.4}$$

where $\dot{\Gamma}(t)$ is the instantaneous strain rate of the applied flow and $u(\phi)$ the rotational velocity per unit strain rate. As discussed in reference [89], at high Pe the distribution $\rho(\phi,t)$ changes with time in an exceptionally complicated manner. The non-uniform velocity of the Jeffery orbit compresses and expands $\rho(\phi,t)$ and rotates these inhomogeneities with the orbit. These distortions occur on two fast timescales – a flow timescale $\sim 1/\dot{\Gamma}$ and an oscillation timescale associated with time variations in $\dot{\Gamma}(t)$. Diffusion then relaxes the distribution on an additional, diffusive timescale $\sim 1/D$ that is much slower than the flow and oscillation timescales. The distribution does not necessarily relax to a steady state, but may continue to change with the flow's oscillations. At high Pe, $\rho(\phi,t)$ changes rapidly with time because a particle's phase angle κ and orbit constant C in equation 4.1 are roughly constant with time, while its orientation ϕ changes rapidly with time due to the Jeffery orbit.

As a result, at high Pe the orientation dynamics are much simpler when described in terms of the distribution $f(\kappa)$ of the particles' phase angles instead of the distribution $\rho(\phi)$ of their orientations. The phase-angle distribution $f(\kappa)$ and the orientation distribution $\rho(\phi)$ are related by $f(\kappa)\,d\kappa = \rho(\phi)\,d\phi$; using the coordinate relationship between κ and ϕ defined by the Jeffery orbit in equation 4.1

the relation between $f(\kappa)$ and $\rho(\phi)$ simplifies to [89]

$$\begin{aligned}\rho &= \frac{\bar{u}}{u(\phi)} f(\kappa) \\ &= \frac{1}{p\cos^2\phi + 1/p\sin^2\phi} \times f(\kappa) \\ &= \left[1/p\cos^2(\kappa + \bar{u}\Gamma(t)) + p\sin^2(\kappa + \bar{u}\Gamma(t))\right] \times f(\kappa) \quad ,\end{aligned} \tag{4.5}$$

where $\bar{u} = 1/(p + 1/p)$ is the average particle rotation per unit strain. When $D = 0$, the distribution of phase angles $f(\kappa)$ remains constant with time, as the particles only reorient due to their Jeffery orbits. In contrast, the orientation distribution $\rho(\phi)$ changes rapidly, as the Jeffery orbit stretches and advects the distribution. Likewise, when the rotational diffusion is nonzero but weak, the particle orientations are described much more simply in terms of $f(\kappa)$ than $\rho(\phi)$. By construction, $f(\kappa)$ evolves only due to diffusion, and as a result changes only on the long time scale $\sim 1/D$. For an arbitrary periodic strain waveform $\Gamma(t)$, the phase-angle distribution $f(\kappa)$ evolves as [89]

$$\frac{\partial f}{\partial t} = -\frac{\partial}{\partial \kappa}\left[-\mathfrak{D}(\kappa)\frac{\partial f}{\partial \kappa} - \frac{1}{2}\frac{\partial \mathfrak{D}}{\partial \kappa} f\right] \tag{4.6}$$

in the limit that the characteristic diffusion time is large compared to the period of the waveform T_{cyc}: $\mathrm{Pe} \equiv 1/DT_{cyc} \gg 1$. Here $\mathfrak{D}(\kappa)$ is an effective phase-angle dependent rotational diffusion, defined through the inverse-square of the particle's rotational velocity time-averaged over a cycle:

$$\begin{aligned}\mathfrak{D}(\kappa)/D &= \frac{1}{T_{cyc}}\int_0^{T_{cyc}} \left(\frac{\bar{u}}{u(\kappa + \bar{u}\Gamma(t))}\right)^2 dt \\ &= \frac{1}{T_{cyc}}\int_0^{T_{cyc}} \left[\frac{1}{p}\cos^2\left(\kappa + \frac{\Gamma(t)}{p + 1/p}\right) + p\sin^2\left(\kappa + \frac{\Gamma(t)}{p + 1/p}\right)\right]^2 dt \quad .\end{aligned} \tag{4.7}$$

In particular, at long times $f(\kappa)$ has a simple steady-state solution that does not change with time:

$$f(\kappa) \propto (\mathfrak{D}(\kappa)/D)^{-1/2} \, , \tag{4.8}$$

regardless of how complicated the applied shear flow is. In contrast, even at long times $\rho(\phi, t)$ changes rapidly with time for all but the simplest flows. Physically, the orientation distribution is determined through diffusion by a memory of the average applied shear flow through $\mathfrak{D}(\kappa)$. The particles migrate to phase-angle regions of low diffusivity, as is common in systems ranging from the creation of concentration gradients in turbophoreis [119, 9] to absorbing states in dense, non-Brownian suspensions [35, 49]. The memory of the applied flow is only determined by time-averages of functions of the shear strain, independent the strain rate, the frequency of the oscillation, and the orders in which the strains occurred. The particle orientations forget their initial conditions on an enhanced time scale $\propto 1/D$ [89].

Figure 4.1 illustrates these two distinct ways of viewing the evolution of particle orientations with time. Under continuous shear, a steady-state solution for ρ exists, as shown in figure 4.1a for a suspension of particles with $p = 5.0$. The distribution is symmetric with respect to inverting the particle's orientation ($\hat{n} \to -\hat{n}$ or $\phi \to \phi + \pi$), keeping the symmetry of the Jeffery orbit. As $\mathrm{Pe} \to \infty$, the steady-state solution corresponds to an orientation distribution $\rho(\phi)$ that is inversely proportional to $u(\phi)$, resulting in a $\propto 1/p$ suppression of particle orientations near the gradient direction at $\phi = 0, \pi$, where the particles rotate rapidly, and a $\propto p$ enhancement of particle orientations along the flow direction at $\phi = \pi/2, 3\pi/2$, where particles rotate slowly. In contrast, in κ-space the distribution $f(\kappa)$ is constant, as diffusion effectively erases the memory of the starting time of the shear (panel b). Translating from $f(\kappa)$ to $\rho(\phi)$ involves multiplying by the prefactor $\bar{u}/u(\phi)$ in equation 4.5. Since $\phi = \phi(\kappa + \bar{u}\Gamma(t))$ (cf. equation 4.1) and since $\Gamma(t) = \dot{\gamma}t$ for continuous shear, this prefactor $\bar{u}/u$ translates with a fixed velocity in κ space, as illustrated by the lower portion of panel b.

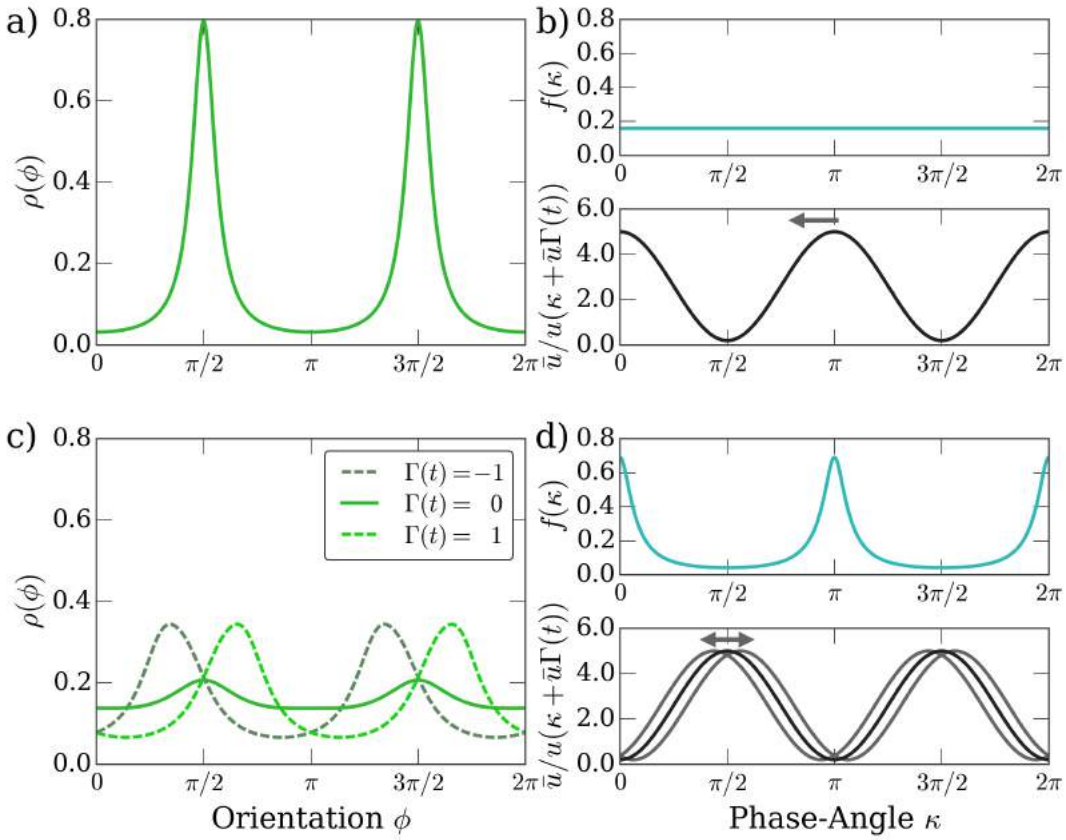

Figure 4.1: (a) $\rho(\phi)$ for particles with aspect ratio $p = 5.0$ under continuous shear is sharply peaked and constant in time. (b) The corresponding phase-angle distribution $f(\kappa)$ (upper panel) is constant in κ and time. The sharp-peaks of $\rho(\phi)$ correspond to the sharp peaks in the prefactor $\bar{u}/u$ which multiply $f(\kappa)$. The prefactor translates as the strain increases, leaving $\rho(\phi)$ unchanged in time as $f(\kappa) = 1/2\pi$ is constant in κ. (c) $\rho(\phi)$ under oscillatory shear $\Gamma(t) = 1.0\sin(t)$ changes in a complicated manner with time, stretching and rotating with the flow. In contrast, the phase-angle picture in (d) is much simpler. $f(\kappa)$ does not change with time (top), and has a peak near $\kappa = 0$ and $\kappa = \pi$. The time-varying $\rho(\phi)$ corresponds to the motion of the prefactor $\bar{u}/u$ in time (bottom, motion indicated by arrows), as its peaks and troughs align with various features in $f(\kappa)$.

Under oscillatory shear the long-time distributions are considerably simpler when described in terms of $f(\kappa)$ than when described in terms of $\rho(\phi)$. As the flow oscillates, the orientation distribution $\rho(\phi, t)$ does not approach a steady-state value but is stretched and rotated with the flow in a complicated manner throughout each cycle, as indicated in figure 4.1c. For the sinusoidal shear with strain amplitude 1 shown in the figure, at the center of the cycle the distribution is almost isotropic, but is slightly distorted. As the suspension is sheared, the distribution is first stretched along the extensional axis by the term $\propto \boldsymbol{E}\cdot\boldsymbol{n}-\boldsymbol{n}(\boldsymbol{n}\cdot\boldsymbol{E}\cdot\boldsymbol{n})$ in equation 4.3, then rotated by the flow to be more closely aligned along the flow axis ($\Gamma(t) = 1$ curve). Reversing the flow first returns the distribution to its value at the center of the cycle before repeating the stretching and rotation in the opposite direction.

In contrast, at high Pe this picture is much simpler in terms of the phase-angle distribution $f(\kappa)$. The phase-angle distribution $f(\kappa)$ attains a steady-state form that is constant in time (upper portion of panel d) and is determined solely by $\mathfrak{D}(\kappa)$ through equations 4.7-4.8. From the definition of $\mathfrak{D}(\kappa)$, at moderate strain amplitudes, regions where the Jeffery orbit velocity is small correspond to regions where the phase-angle diffusivity $\mathfrak{D}(\kappa)$ is large, and vice versa. As a result, in figure 4.1d $f(\kappa)$ is enhanced at phase angles corresponding to particles which rotate rapidly with the Jeffery orbit (near $\kappa = 0, \pi$), and is suppressed at phase angles corresponding to particles which rotate slowly with the Jeffery orbit (near $\kappa = \pi/2, 3\pi/2$). This $f(\kappa)$, in conjunction with the initial centering of the trough in $\bar{u}/u$ about the peak in $f(\kappa)$, corresponds to the initially mostly-constant distribution $\rho(\phi)$. The stretching and rotation of $\rho(\phi)$ with time simply corresponds to the oscillation of the prefactor $\bar{u}/u$ about the peak in $f(\kappa)$. As the trough in $\bar{u}/u$ shifts slightly to either side of the peak in $f(\kappa)$, the overlap between

$f(\kappa)$ and $\bar{u}/u$ increases and $\rho(\phi)$ becomes more strongly peaked.

Motivated by the simple description for orientation dynamics at high Pe, we proceed to optimize the orientation distribution for a desired property. Equations 4.5, 4.7, and 4.8 completely determine the steady-state orientation distributions at long-times for an *arbitrary* shear waveform. Moreover, while in practice $\mathfrak{D}(\kappa)$ may be difficult to calculate analytically, it is extremely simple to calculate numerically – one integration determines $\mathfrak{D}(\kappa)$, which in turn determines the form of $f(\kappa)$ aside from a normalization constant. As a result, we can simply parameterize an arbitrary waveform and fit these parameters to optimize any desired property determined by the orientation distribution.

4.3 Maximizing Alignment

Strongly aligned particle orientations are crucial for engineering applications of nonspherical particle suspensions. For instance, a well-defined orientation strongly affects the mechanical stiffness [55] and thermal or electrical conductivity [120, 129, 144] of a fiber-reinforced composite, and orientation alignment determines the optical activity of a suspension [54]. For many processes, such as extruding fiber-reinforced composites, the alignment is desired at a specific moment in time, *e.g.* when the composite is cured or when the dichroism is measured, rather than over the entirety of the cycle. As such, rather than maximize the particle alignment averaged over a cycle, we instead maximize the alignment at one point in the oscillatory shear cycle, envisioning a situation where the suspension is rapidly cured into a solid matrix when the desired alignment has been achieved. Alternatively, a maximal alignment at one point in the cycle could be useful for calibrating

suspension characterizations such as flow dichroism, where the process of taking a measurement is rapid and a strong signal is desired. Most of these measured properties are determined through moments of the particle orientation, such as the standard rank-two liquid crystal order parameters $\boldsymbol{Q}$ and S_2 for dichroism and conductivity, where $\boldsymbol{Q}$ is the traceless, symmetric, second-order orientation tensor ($\boldsymbol{Q} = 2\langle \boldsymbol{nn} \rangle - \boldsymbol{\delta}$ in two dimensions) and S_2 is its maximal eigenvalue. For properties such as elasticity, higher-order tensorial parameters such as an analogous S_4 determine the material properties. The behavior of these order order parameters under flow are difficult to visualize, as they depend on integrals of the orientation distribution $\rho(\phi)$ over ϕ. Instead, we examine the largest value of $\rho(\phi)$, which is simpler to visualize. Empirically, the optimal waveforms that maximize $\rho(\phi)$ are identical to the optimal waveforms that maximize many of the more complex order parameters, including the rank-two and rank-four scalar liquid-crystal order parameters S_2 or S_4. The high symmetry of the Jeffery orbit prevents pathological distributions, such as a $\rho(\phi)$ with many large peaks along different directions, and ensures that maximizing $\rho(\phi)$ produces a highly-aligned distribution.

We maximize the largest value of ρ by first parameterizing the waveforms by 60 Fourier coefficients and optimizing over those coefficients. Without loss of generality, we optimize the value of ρ at the start of an oscillatory cycle. Likewise, there is a gauge freedom in selecting an overall offset for $\Gamma(t)$, corresponding to any transient shear done on the suspension infinitely far in the past; we choose $\Gamma(0) = 0$ throughout the paper. Surprisingly, the optimal waveforms for maximal alignment and for the other properties considered in this paper have extremely simple forms. As a result, both for maximizing ρ and for the rheology waveforms considered later, we first optimize using the 60 Fourier coefficients to find the simple optimal waveform, then re-optimize using the simpler waveform. The simple

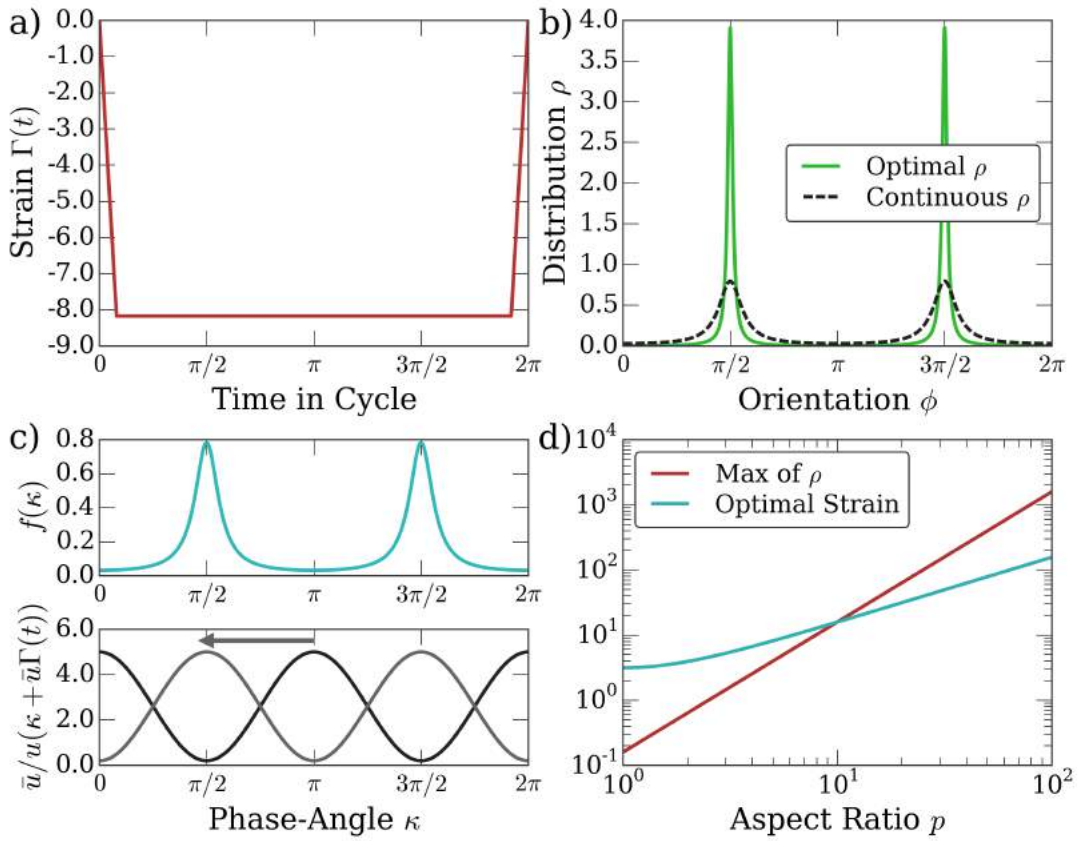

Figure 4.2: (a) The spike waveform that maximizes the maximum value of $\rho(\phi)$ for $p = 5.0$. The actual optimal waveform has a spike of zero width; panel a shows one of width $\pi/5$ for clarity. (b) The optimal $\rho(\phi)$ (green curve) is much more strongly peaked than the continuous-shear $\rho(\phi)$ (dotted-black curve), even at moderate $p = 5.0$. (c) $f(\kappa)$ (top) for the spike waveform. The prefactor $\bar{u}/u$ starts antialigned with $f(\kappa)$ (black curve), and translates to align its peak with that of $f(\kappa)$ (gray curve), as indicated by the arrow. (d) The maximal value of $\rho(\phi)$ (red) and the optimal strain (cyan), as a function of p.

optimal waveform always produces more extremal values of the desired property than the naive Fourier parameterization.

Figure 4.2a shows the waveform that maximizes the alignment in a dilute suspension of rods with aspect ratio $p = 5.0$. The waveform involves not shearing for almost all of the cycle, then straining by an amount $\Gamma = \pi(p + 1/p)/2 \approx 8.17$ that is precisely one-quarter of a Jeffery orbit. For the optimal waveform, the

duration of this spike goes to zero; panel a shows the spike at finite width for ease of viewing. Even for the moderate aspect ratio $p \approx 5.0$ this waveform produces an exceptionally strong alignment, as shown in panel b. The peak of the orientation distribution ρ for the optimal waveform (green curve) is $5\times$ greater than that for continuous shear (black dotted curve), even though the suspension is not being sheared for most of the optimal cycle!

Why is this alignment so strong compared to continuous shear? While the answer is not immediately obvious when examining the behavior of equation 4.4 in terms of $\rho(\phi)$, it is readily apparent in terms of $f(\kappa)$. There are two terms that determine the orientation distribution $\rho(\phi)$ in equation 4.5: a prefactor $\bar{u}/u$ that does not depend on the waveform but changes during a cycle, and the phase-angle distribution $f(\kappa)$ that depends on the waveform but does not change during a cycle. The prefactor $\bar{u}/u$ varies strongly with κ, having strong $\propto p$ peak at $\kappa + \bar{u}\Gamma(t) = \pi/2$. Under continuous shear, the particle phase angle is completely randomized – $f(\kappa) = 1/2\pi$ – and the alignment of ρ arises solely from the peaks in $\bar{u}/u$. Thus, from the standpoint of equation 4.5, continuous shear is a terrible way to align the distribution! Almost any other waveform will produce variations in $f(\kappa)$, and shifting the peak in $\bar{u}/u$ over a peak in $f(\kappa)$ will produce a more aligned distribution. To maximize the alignment, we should look for a waveform that creates the maximal peak in $f(\kappa)$, and then attempt to add a negligible motion on top of that waveform that will align the peak in $f(\kappa)$ with that in $\bar{u}/u$.

One waveform with a strongly-peaked $f(\kappa)$ is low-amplitude sinusoidal shear. As the amplitude of the sinusoidal shear approaches zero, the orientation distribution $\rho(\phi)$ becomes isotropic. Since $\rho(\phi) = \bar{u}/u \times f(\kappa)$, and since $\bar{u}/u$ is sharply peaked, the isotropic $\rho(\phi)$ implies that $f(\kappa)$ is strongly peaked with a magnitude

$\sim p$ as $p \to \infty$, as visible from equation 4.5. From the naive viewpoint of $\rho(\phi)$, zero-amplitude sinusoidal shear is a terrible way to align particles, as $\rho(\phi) = 1/2\pi$ is completely isotropic. But from the viewpoint of the phase-angle distribution, this is a great way to align the distribution, since $f(\kappa)$ is sharply peaked. The only slight problem is that, at zero strain, the prefactor $\bar{u}/u$ exactly cancels any peaks in $f(\kappa)$. However, this problem can be rectified by straining by an amount exactly 1/4 of a Jeffery orbit $\Gamma = \pi(p + 1/p)/2$, aligning the peak of $\bar{u}/u$ with that of $f(\kappa)$. Moreover, since $\mathfrak{D}(\kappa)$ and $f(\kappa)$ are determined by time-averages of the waveform (cf. equation 4.7), a rapid shift in strain will not affect the phase-angle distribution $f(\kappa)$.

This approach is precisely what the optimal waveform in figure 4.2 takes. Not shearing for most of the cycle creates the sharply-peaked $f(\kappa)$ shown in panel c which is the same as under low-amplitude shear, except for a shift resulting from our choice of $\Gamma(0)$. Exactly at the start of the cycle, the waveform shifts the peak of $\bar{u}/u$ to align with the peak of $f(\kappa)$, resulting in a strong alignment. Combining this shifted prefactor with the zero-shear $f(\kappa)$ gives an orientation distribution

$$\rho(\phi) = \frac{1}{2\pi} \frac{1}{p^2 \cos^2 \phi + \frac{1}{p^2} \sin^2 \phi} \quad . \tag{4.9}$$

Since the maximal value of the zero-amplitude $f(\kappa)$ is $p/2\pi$ and that of $\bar{u}/u$ is p for $p > 1$, the waveform produces a peak of height $p^2/2\pi$ in $\rho(\phi)$, as shown in panel d, as opposed to the $\sim p$ peak height from simple continuous shear. Aligning these peaks in $\bar{u}/u$ and $f(\kappa)$ requires a strain $\pi(p + 1/p)/2$ that is 1/4 a Jeffery orbit.

This mechanism has a simple explanation in terms of $\rho(\phi)$ and the velocity field of the Jeffery orbit. As the suspension is not sheared for most of the cycle, the orientation distribution is isotropic except for the duration of the spike. This isotropic distribution corresponds to orienting a sizeable fraction of the particles

near the gradient direction, where the Jeffery orbit rotates rapidly. The spike then rotates these particles by one-fourth of a Jeffery orbit, aligning them near the flow direction. The Jeffery orbit rotational velocity is suppressed by $\sim 1/p^2$ compared to the velocity near the gradient direction, resulting in the $\sim p^2$ bunching of particles visible in figure 4.2.

While the above argument shows that a $\sim p^2$ particle alignment is possible, it does not prove that the spike waveform in figure 4.2a is the optimal one nor divulge how robust it is to deviations from perfection. We can further understand the optimal waveform by delving deeper into the functional form of $\mathfrak{D}(\kappa)$. Expanding out the sines and cosines in equation 4.7 gives a simplified form for $\mathfrak{D}(\kappa)$:

$$\begin{aligned} \mathfrak{D}(\kappa)/D = &\frac{3}{8}(p-1/p)^2 + 1 - \frac{1}{2}(p^2-1/p^2)A_2\cos(2\kappa+\delta_2) \\ &+ \frac{1}{8}(p-1/p)^2 A_4 \cos(4\kappa+\delta_4) \quad , \quad \text{where} \\ A_n e^{i\delta_n} = &\frac{1}{T_{cyc}}\int_0^{T_{cyc}} e^{in\Gamma(t)/(p+1/p)}\,dt \end{aligned} \tag{4.10}$$

Both $\mathfrak{D}(\kappa)$ and $f(\kappa)$ are determined by the waveform $\Gamma(t)$ only through the four variables A_2, δ_2, A_4, δ_4, which in turn only determine the magnitude and phase of their $\cos(2\kappa)$ and $\cos(4\kappa)$ variations. In general, either $A_2 e^{i\delta_2}$ or $A_4 e^{i\delta_4}$ can take any values in the complex unit disk, although they cannot be varied completely independently of each other. For some simple oscillatory waveforms these coefficients can be calculated exactly – for example, for $\Gamma(t) = \Gamma_0 \sin(\omega t)$ the coefficients are $A_2 = J_0(2\Gamma_0/(p+1/p))$, $\delta_2 = 0$ and $A_4 = J_0(4\Gamma_0/(p+1/p))$, $\delta_4 = 0$, where J_0 is the zeroth-order Bessel function – but for a generic waveform these coefficients are not expressible analytically. Nevertheless, equation 4.10 still divulges much information about a generic waveform. Waveforms which only deviate from one another for a short time will have similar phase-angle distributions. Moreover, since $f(\kappa) \propto 1/\sqrt{\mathfrak{D}(\kappa)}$, an increasing A_2 and A_4 will increase the alignment in

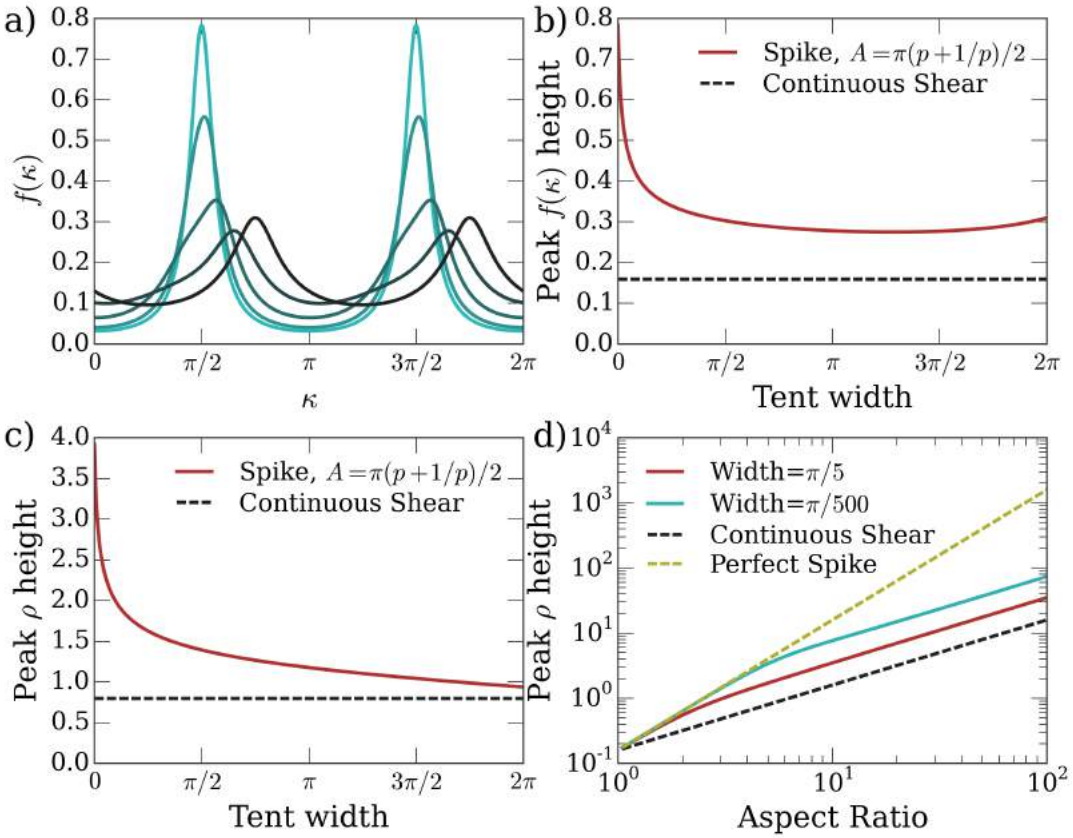

Figure 4.3: Numerical results for finite spike width on distribution alignment. (a) $f(\kappa)$ for a spike waveform, with spike widths of 0% (cyan), 1%, 10%, 50%, and 100% (black) of the triangle-wave limit of 2π, at fixed amplitude $\Gamma = \pi(p+1/p)/2$ and for a suspension with $p = 5$. (b) The peak height of $f(\kappa)$ as a function of the spike width; in general the peak height decreases as the spike width increases, but it always remains considerably greater than the constant $f(\kappa)$ for continuous shear (dashed line). (c) The maximum of $\rho(\phi)$ for a spike waveform as a function of the spike width, with the spike centered at $t = 0$. (d) The scaling of the maximal $\rho(\phi)$ as a function of aspect ratio for an infinitesimally fast spike (dashed yellow line), a spike of width $\pi/500$ (cyan), a spike of width $\pi/5$ like that in figure 4.2 (red), and continuous shear (dashed black line).

$f(\kappa)$.

The effect of a finite-spike width duration on particle alignment can be seen from its effects on the coefficients A_2 and A_4. For the optimal waveform in figure 4.2, the spike is of zero duration, and $A_2 = 1$, $A_4 = 1$, resulting in an $O(1)$

minimum in the otherwise $O(p^2)$ $\mathfrak{D}(\kappa)$, cf equation 4.10. Since $f(\kappa) \propto 1/\sqrt{\mathfrak{D}(\kappa)}$, cf. equation 4.8, and since $f(\kappa)$ is normalized, this $O(1)$ minimum in $\mathfrak{D}(\kappa)$ corresponds to an $O(p^2)$ peak in $f(\kappa)$. If the spike occupies a fraction τ of the cycle, then the phase of $\exp(in\bar{u}\Gamma)$ in equation 4.10 will be reduced by an amount $\propto \tau$, and A_2, A_4 will decrease by $\approx \tau$. Since the prefactors to both A_2 and A_4 scale as $\sim p^2$ as $p \to \infty$, a finite-width spike results in an $\sim \tau p^2$ increase in the minima of $\mathfrak{D}(\kappa)$, which decreases the maximum of $f(\kappa)$ by $\sim \tau p^2$. Thus, an $O(1)$ spike width will unfortunately produce an $O(p^2)$ decrease in the alignment. Physically, the spike duration needs to be $\lesssim 1/p^2$ due to diffusion. The optimal waveform creates a $\sim p^2$ alignment and therefore $\sim p^2$ gradients in $\rho(\phi)$. These enhanced gradients enhance the effect of diffusion by the same $\sim p^2$ factor, requiring an extremely brief spike duration before diffusion smooths out the distribution.

This behavior is shown in figure 4.3. Panel a shows $f(\kappa)$ for a particle with $p = 5.0$ for spike strains $\Gamma = \pi(p + 1/p)/2$ and widths varying from 0 (cyan) to 2π (*i.e.* triangle-wave shear, in black). Since a spike width of $\sim 1/p^2$ produces a significant decrease in the peak of $f(\kappa)$, even at moderate $p = 5.0$ a spike that occupies 1% of the duration of the cycle significantly decreases the peak value of $f(\kappa)$. This peak value decreases rapidly with increasing spike width (panels a and b), which correspondingly decreases the maximal value of $\rho(\phi)$ (panel c). Regardless of the spike width, however, the spike waveform always aligns $\rho(\phi)$ more than continuous shear does. As $f(\kappa) = 1/2\pi$ is constant for continuous shear, aligning the $\bar{u}/u$ prefactor with any peak in $f(\kappa)$ improves alignment over continuous shear. Panel d shows the scaling of the alignment with aspect ratio. While a spike of infinitesimal width creates a $\sim p^2$ orientational alignment, any fixed-width spike reduces the scaling to $\sim p$, as shown by the curves for a spike width of $\pi/5$ (the waveform in figure 4.2a) and of width $\pi/500$, although either

width always results in significantly more enhancement than continuous shear.

4.4 Maximizing and Minimizing Viscosity

Colloidal rods are a classic model system for exploring non-Newtonian rheological behaviors, with the first investigations dating back almost 100 years [73, 109]. Even dilute suspensions in simple shear flows can exhibit interesting non-Newtonian behavior such as shear-thinning, stress overshoots, and normal stresses [126, 26, 96, 41], arising from a combination of viscoelastic, flow-memory, and relaxation effects [80, 93, 67, 140, 29]. This non-Newtonian behavior arises because the particle orientations both couple to the flow and affect the suspension stress. As rodlike particle suspensions produce a wide array of rheological behaviors even for simple flows, we expect that we can strongly control their rheology under arbitrary-waveform oscillatory shear flows.

The stress at one instant in time in a suspension of rodlike particles is determined by the current strain rate and moments of the particle orientations:

$$\begin{aligned}\sigma =& 2\eta\mathbf{E} + 2\eta c\{2A_H(\mathbf{E} : \langle \boldsymbol{nnnn}\rangle - \delta\,\mathbf{E} : \langle \boldsymbol{nn}\rangle) \\ &+ 2B_H(\mathbf{E}\cdot\langle \boldsymbol{nn}\rangle + \langle \boldsymbol{nn}\rangle\cdot E - \frac{2}{3}\delta\,\mathbf{E} : \langle \boldsymbol{nn}\rangle) \\ &+ C_H\mathbf{E} + F_H D(\langle \boldsymbol{nn}\rangle - \frac{1}{3}\delta)\}\end{aligned} \tag{4.11}$$

where $\mathbf{E}$ is the rate-of-strain tensor of the fluid, δ the Kronecker-delta, η the suspending fluid viscosity, c the volume fraction of rods, and A_H, B_H, C_H, and F_H are shape-dependent hydrodynamic coefficients [11, 82, 67, 20]. At high Pe, the potentially elastic Brownian stress in the last term is negligible compared to the other terms, and the suspension stores no elastic energy.

For particles confined to the flow-gradient plane at high Pe, these equations simplify considerably. The increase in the effective shear viscosity due to the particles, per unit concentration and normalized by the fluid viscosity, is

$$(\sigma/2\eta - \mathbf{E})_{xy}/c = A_H\langle 1 - \cos 4\phi\rangle/8 + B_H + C_H \quad . \tag{4.12}$$

As a result, for particles orientations confined to the flow-gradient plane, controlling the shear stress in a suspension only involves controlling the $\langle \cos 4\phi \rangle$ moment of the distribution. As equations 4.11-4.12 show, at high Pe the suspension response is always proportional to the instantaneous strain rate and never has an elastic component. However, since the particle orientations change with time, the proportionality constant in equation 4.12 between the stress and the strain rate changes with time, producing a purely viscous but non-Newtonian response. We call this proportionality constant the instantaneous viscosity η_{inst}, as it can change during an oscillatory shear cycle. This non-Newtonian η_{inst} arises from the suspension's memory of the average waveform through $\mathfrak{D}(\kappa)$. At high Pe, the suspension has a negligible Brownian stress and hence no true viscoelasticity. While the theory of orientation dynamics at high Pe can describe relaxation effects due to diffusion [89], since we are considering the long-time rheology under rapid oscillations these transients have already decayed, and long-term relaxation effects no longer affect η_{inst}.

The instantaneous viscosity provides information about the particle properties through the hydrodynamic coefficients A_H, B_H, C_H, which depend on the particle shape. In a typical rheological measurement at high Pe all three coefficients are measured simultaneously. For idealized particle orientations confined to the flow-gradient plane, it is impossible to separately measure the coefficients B_H and C_H. However, the coefficient A_H can be measured from two separate waveforms that produce separate particle distributions, cf. equation 4.12. Ideally, these two

waveforms should produce an η_{inst} that is maximally different from one another. Motivated by this, we look for the waveforms that maximize and that minimize η_{inst}. For simple waveforms such as continuous shear or sinusoidal shear, the suspension viscosity η_{inst} is simply related to the suspension stress. For more complex waveforms, these two can differ dramatically, as the shear rate can be small or even zero when the viscosity is large. As a result, a waveform that extremizes the viscosity will not in general extremize the measured stress. However, an additional high-frequency, small-amplitude "probe" flow will measure the viscosity that is created by the "pump" waveform. The probe flow will not change the distributions, since $f(\kappa)$ and $\mathfrak{D}(\kappa)$ only depend on the average strain and not on the strain rate (cf. 4.7. Since the time-average value that the probe will measure is the time-average of the viscosity, we maximize and minimize the time-average of η_{inst}. In addition, the extremal η_{inst} waveforms are simple to analyze, as the viscosity depends only on the strain waveform and not directly on the strain rate.

As for the case with maximizing the distributions, extremizing the viscosity is simpler in terms of $f(\kappa)$. Since $f(\kappa)\,d\kappa = \rho(\phi)\,d\phi$ by construction, the average in equation 4.12 can also be taken in phase-angle space instead of orientation space: $\langle\cos(4\phi)\rangle = \int \cos(4\phi)\rho(\phi)\,d\phi = \int \cos(4\phi(\kappa + \bar{u}\Gamma))f(\kappa)\,d\kappa$. From this standpoint, the waveform $\Gamma(t)$ determines $f(\kappa)$, which does not change in time. Instead, during a cycle the strain shifts the position of $\cos(4\phi)$ in κ space, and the nonlinear transformation between ϕ and κ warps its shape. Maximizing or minimizing the viscosity then corresponds to selecting a waveform that maximizes or minimizes the overlap between $\cos(4\phi)$ and the $f(\kappa)$ that the waveform creates.

Figure 4.4a displays the waveform that maximizes η_{inst} for a suspension of particles with aspect ratio $p = 5.0$ (dashed red line). Similar to the waveform that

maximizes $\rho(\phi)$, during most of the cycle the suspension is not sheared. In contrast to the waveform in figure 4.2, however, the maximal-stress waveform spends an equal amount of time at two separate strains: at a strain $\Gamma = 0$ and at $\Gamma \approx 1.26$. Since the strain is relatively small, this waveform creates a well-peaked $f(\kappa)$ (dashed curve, upper portion of panel b) with the peak slightly offset from $\kappa = 0$. At $\Gamma = 0$, the peak in $f(\kappa)$ aligns with the peak at $\phi = -\pi/4$ in the stress term $(1 - \cos 4\phi)/8$ from equation 4.12. Increasing the strain to $\Gamma = 1.26$ aligns the second peak at $\phi = \pi/4$ with the peak of $f(\kappa)$. As a result, the viscosity is large and constant during the cycle, except for two small dips as the strain changes from $\Gamma = 0$ to $\Gamma = 1.26$, cf. panel c.

The waveform that minimizes η_{inst} is similar to the one that maximizes η_{inst}, as shown by the solid red line in figure 4.4a. The waveform is also a boxcar, alternating between a strain of $\Gamma = 0$ and $\Gamma \approx 8.17$. However, while this waveform is similar to the one that maximizes η_{inst}, their phase-angle distributions $f(\kappa)$ differ significantly. As the strain $\Gamma = 8.17$ is relatively large, $f(\kappa)$ no longer has a sharp peak, but is almost constant with small, $\cos(4\kappa)$ oscillations, as shown by the solid line in panel b. These oscillations create a minimum in $f(\kappa)$ at $\kappa = \pi$, near the double-peak of the stress term. The waveform then shifts this double-peak from the trough in $f(\kappa)$ at $\kappa = \pi$ to the trough at $\kappa = \pi/2$. As a result, the viscosity that is small and constant during a cycle, except for two small bumps as $\Gamma(t)$ changes from 0 to 8.17, cf panel c.

From this picture, we can understand the scaling with aspect ratio of the waveforms that maximize and minimize η_{inst} and their corresponding viscosities. The waveform that maximizes η_{inst} alternates between positioning either of the two closely-separated maxima of the stress term $(1 - \cos 4\phi)/8$, located at $\phi = \pm\pi/4$,

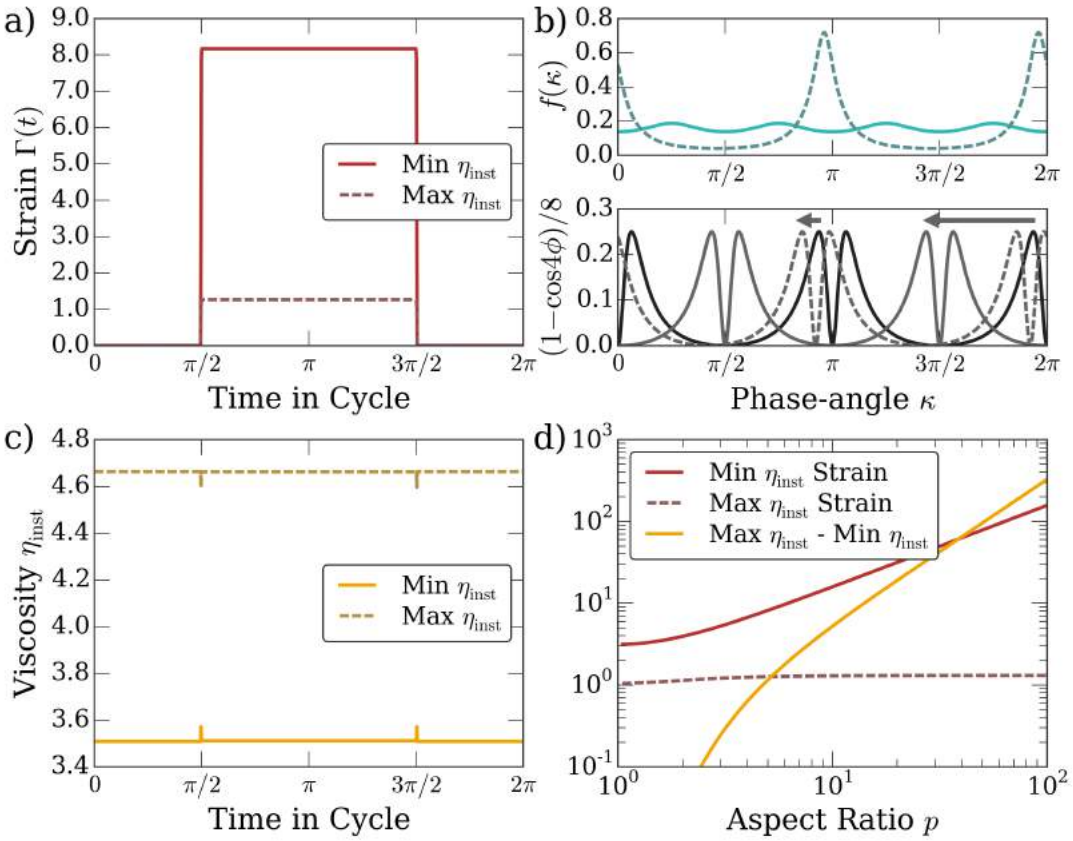

Figure 4.4: (a) The boxcar waveforms which maximize η_{inst} (dashed red line) and minimize η_{inst} (solid red line), for a suspension with $p = 5.0$. Both optimal waveforms have a ramp-width of zero, as shown in the figure. (b) Top panel: The phase-angle distributions which maximize (dashed) and minimize (solid) η_{inst}. The bottom panel shows the corresponding stress term at the start of the cycle (black), and its position at the middle of the cycle (dashed and solid gray lines). (c) The maximal and minimal viscosities, as a function of time in the cycle. (d) The scaling of the Γ that produces the maximal η_{inst} (dashed red line), the Γ for the minimal η_{inst} (solid red line), and the difference between the two viscosities (orange), as a funcion of p.

on the peak in $f(\kappa)$. As is visible from the coordinate relations between ϕ and κ in equation 4.1, the distance between these maxima is compressed in κ space, to a separation that scales $\sim 2/p$ as $p \to \infty$. Since $\bar{u}$ also scales $\sim 1/p$, alternating placement of the two peaks in the stress term to maximize η_{inst} requires fixed strain, independent of p. This asymptotic approach to a constant $\Gamma \approx 1.30$ at large p is visible in figure 4.4d. Likewise, the waveform that minimizes η_{inst} alternates between positioning the double-peaks in the stress term on the minima in $f(\kappa)$ at $\kappa = 0$ and $\kappa = \pi/2$. This $\pi/2$ shift in κ requires a strain $\Gamma = \pi(p+1/p)/2$, as shown by the minimal-η_{inst} strain in panel d. Moreover, this shift of $\Gamma = \pi(p+1/p)/2$ sets the coefficient $A_2 = 0$ in equation 4.10, leaving $f(\kappa)$ with the $\cos(4\kappa)$ modulation visible in the figure. Finally, we can estimate the scaling of the maximal and minimal η_{inst} with p. The expectation value of $(1 - \cos 4\phi)/8$ is always $O(1)$, as for the maximal viscosity $\langle 1 - \cos(4\phi)\rangle/8 < 1/4$ always and for the minimal viscosity $f(\kappa)$ never approaches zero. As a result, the difference between the maximal viscosity and the minimal viscosity will scale as a constant fraction of the hydrodynamic coefficient A_H in equation 4.12. The difference between the maximal and minimal viscosities in panel d reflects the $\sim p^2/\ln p$ scaling of the hydrodynamic coefficient A_H [82].

The waveforms which maximize and minimize the viscosity are robust to a finite ramp width even at large p, in contrast to the spike waveform which maximizes $\rho(\phi)$. Increasing the ramp width of the waveform to τ results in an $\sim \tau$ change in the coefficients A_2, A_4. However, neither A_2 nor A_4 equal 1 for the maximal or minimal strain waveforms. As a result, there are no sensitive minima in $\mathfrak{D}(\kappa)$, unlike the case for the maximal $\rho(\phi)$ waveforms, and $\mathfrak{D}(\kappa)$ changes proportional to an $O(\tau)$ factor everywhere, instead of $O(\tau p^2)$ in some locations. As a result, replacing the boxcar waveform by a trapezoidal waveform with a small ramp time

of duration τ changes the maximal and minimal viscosities change by a small $\sim \tau$ fraction. Plotting the difference between the viscosities for an infinitesimal ramp width and for a ramp width of $\pi/5$ results in a curve that is indistinguishable from the curve in figure 4.4d on the scale of the figure.

4.5 Maximizing Normal Stresses

The presence of hydrodynamic normal stresses is severely restricted by the linearity reversibility of Stokes flow. Since reversing time corresponds to changing the sign of the shear rate, the linearity Stokes flow implies that reversing time will change the sign of a the stress tensor. Thus, for an oscillatory flow, all stresses – including normal stresses – must time-average to zero, as an average value does not change sign upon reversing time. While in principle, a hydrodynamic normal stress difference can be nonzero at any instant of time, in practice any hydrodynamic normal stress difference is usually prevented by additional symmetries. For instance, in simple shear reversing time corresponds to reflecting the flow axis. If the suspension microstructure is symmetric under this reflection, then the normal stress difference will be identically zero by symmetry. This symmetry prevents hydrodynamic normal stress differences from arising in suspensions of rods both at infinite Péclet [66] and at zero Péclet.

As a result, most normal stresses in suspensions of nonspherical particles have a non-hydrodynamic origin, such as from Brownian motion and particle contacts [93, 110, 126, 100, 134, 80]. These non-hydrodynamic mechanisms can create normal stress differences either directly or through altering the suspension microstructure, creating a hydrodynamic normal stress created by non-hydrodynamic struc-

ture. Since the normal stresses can have non-hydrodynamic origins, there can be arbitrary normal stress differences, even those that do not time-average to zero under oscillatory or continuous shear.

While shear flows that vary simply in time usually do not give nonzero hydrodynamic normal stress differences, more complex waveforms can give rise to a nonzero first normal stress difference N_1 strictly from hydrodynamics. In general, reversibility of Stokes flow requires that N_1 time-average to 0. However, it is in principle possible to create complex waveforms that have a nonzero N_1 at any instant of time during the oscillation.

To understand the microstructural origins of N_1, we look at the normal stress components σ_{xx} and σ_{yy} of equation 4.11, where the x is the flow direction and y the gradient. Substituting $\boldsymbol{n} = (n_x, n_y, 0)$ and evaluating the dot products shows that the hydrodynamic normal stress difference $N_1 = \sigma_{xx} - \sigma_{yy}$ is again given by moments of the orientation distribution weighted by the hydrodynamic coefficient A_H, in the limit of large Pe:

$$N_1/\eta\dot{\gamma}c = \frac{1}{2}A_H\langle \sin 4\phi \rangle \quad . \tag{4.13}$$

An orientation distribution that is symmetric $\phi \to -\phi$ will always produce a hydrodynamic normal stress difference that is identically zero, which is why continuous shear and low-amplitude oscillatory shear have $N_1 = 0$. For a general waveform, however, $\rho(\phi)$ does not have this symmetry. The normal stress term $\sin(4\phi)$ has four equal maxima and minima, equally spaced in ϕ. However, the nonlinear transformation $\phi \to \kappa$ strongly warps the normal stress term, causing the maxima and minima to bunch together into two separate groups. As $\sin(4\phi)$ is odd in ϕ, the transformation creates a normal stress term that is also odd in $\kappa + \bar{u}\Gamma(t)$, in contrast to the shear stress term $(1 - \cos 4\phi)/8$ which is even in both ϕ and $\kappa + \bar{u}\Gamma(t)$.

The normal stress difference N_1 directly provides information about particle shape through the hydrodynamic coefficient A_H, like measurements of the shear stress. Measuring this coefficient with the normal stress difference would provide information on rodlike particle suspensions. Frequently, normal stress differences are measured in continuous shear at high Pe. These normal stress differences arise due to particle contacts, especially in the semi-dilute regime [143, 42, 46, 134]. However, in a more dilute suspension this measured N_1 could arise either directly, from contacts, or indirectly, through the effect of particle contacts on the orientation distribution. Measuring the normal-stress coefficient A_H would provide insight into the range of normal stress differences that could be expected from hydrodynamics alone and further elucidate the origins of normal stress differences in suspensions of Brownian rods.

In light of this, we look for a waveform that optimizes the magnitude of the normal stress viscosity $A_H\langle\sin(4\phi)\rangle/2$ from equation 4.13, imagining a measurement of this viscosity with a pump-probe experiment as for the shear viscosity. In contrast to the shear viscosities, due to reversibility of Stokes flow the average normal stress viscosity is always zero. Instead, we maximize the average of the absolute value of the normal-stress viscosity $|N_1/\eta c\dot{\gamma}|$, which will maximize the normal stress signal from a probe experiment at any given time. Moreover, maximizing the normal stress viscosity would facilitate a direct measurement of nonzero, hydrodynamic normal stress differences in a dilute suspension, as opposed to the usually non-hydrodynamic and/or semidilute regime normal stress differences that are currently measured [143, 110, 126, 78, 134].

Figure 4.5a displays the waveform that maximizes the signal from N_1 for a dilute suspension with $p = 5.0$. Like the waveforms that maximize and minimize the

viscosity, the strain $\Gamma(t)$ takes a boxcar shape, alternating between a strain $\Gamma = 0$ and a moderate strain $\Gamma \approx 3.77$. This moderate strain produces a moderately-peaked $f(\kappa)$, as shown in the upper portion of panel b. The waveform aligns one of the broad peaks in the normal-stress term $\sin(4\phi)/2$ with the peak of $f(\kappa)$, before translating to align the nearby broad trough with the peak of $f(\kappa)$ for the second half of the cycle. This produces a symmetric N_1 signal that averages to zero but has constant magnitude throughout the cycle, as shown in figure 4.5c.

Examining equation 4.13 in detail divulges the structure of this normal stress waveform. The normal stress term has four maxima corresponding to $\sin(4\phi) = 1$, at $\phi = (4n + 1)\pi/8$, and four minima at $\phi = (4n - 1)\pi/8$. Once again, the nonlinear $\phi \to \kappa$ transformation warps these equally-spaced maxima in ϕ into the bunches of maxima and minima visible in figure 4.5b. For instance, the close maximum/minimum pair near $\kappa = \pi$ are the image of the maximum at $\phi = 9\pi/8$ and the minimum at $\phi = 7\pi/8$. The Jeffery transformation in equation 4.1 places these at phase angles $\kappa + \bar{u}\Gamma = \pi - \tan^{-1}((\sqrt{2}-1)/p)$ and at $\pi + \tan^{-1}((\sqrt{2}-1)/p)$. Likewise, the broad outer extrema at $\kappa + \bar{u}\Gamma = \pi - \tan^{-1}((\sqrt{2}+1)/p)$ and $\kappa + \bar{u}\Gamma = \pi + \tan^{-1}((\sqrt{2}+1)/p)$ correspond to the maximum at $\phi = 5\pi/8$ and the minimum at $\phi = 11\pi/8$. This cluster of four extrema are separated from the other cluster by a large, $\sim \pi$ distance. One could try to maximize $|N_1|$ by aligning the peak of $f(\kappa)$ either with the inner set of extrema, at $\pi \pm \tan^{-1}((\sqrt{2} - 1)/p)$, or with the outer set of extrema, at $\pi \pm \tan^{-1}((\sqrt{2} + 1)/p)$. However, the peak of $f(\kappa)$ is at least of width $\sim 1/p$, so aligning the inner maximum with the peak of $f(\kappa)$ results in significant overlap of $f(\kappa)$ with the inner minimum. Instead, the optimal waveform aligns the outer, broad extrema with the peak of $f(\kappa)$. Since these extrema are separated by a distance of $\delta\kappa = 2\tan^{-1}((\sqrt{2} + 1)/p)$, and since $\bar{u} \sim 1/p$, the optimal waveform has a strain jump of $\Gamma \approx 2p\tan^{-1}((\sqrt{2} + 1)/p)$, which is ≈ 4.8

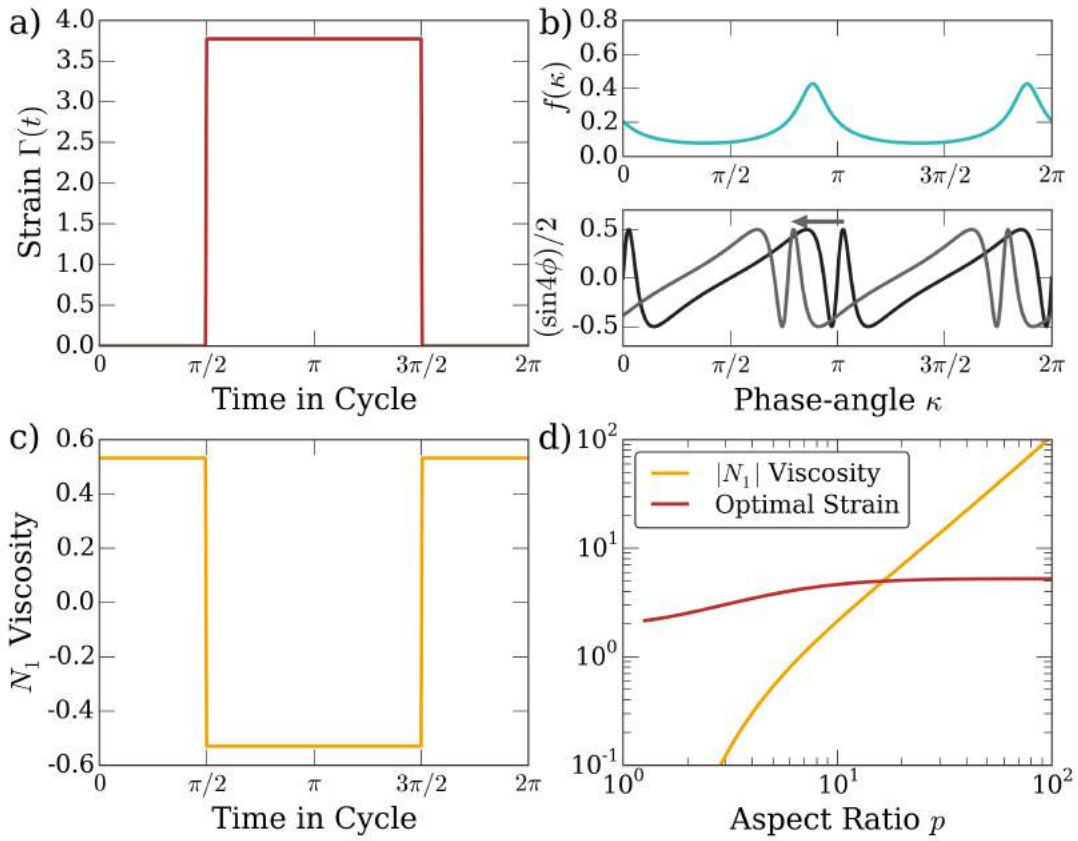

Figure 4.5: (a) The boxcar waveform which maximizes the average of the absolute value of the normal-stress viscosity, for a suspension with $p = 5.0$. The optimal waveform has a ramp-width of zero, as shown in the figure. (b) The corresponding $f(\kappa)$ (top panel). The bottom panel shows the corresponding normal stress term $\sin(4\phi)/2$ at the start of the cycle (black), and its position at the middle of the cycle (gray). (c) $N_1/\eta c\dot{\gamma}$ as a function of time in the cycle. $N_1/\eta c\dot{\gamma}$ is equal and opposite during the two halves of the cycle, averaging to zero. (d) The scaling of the maximal-$|N_1|$ viscosity (orange) and the corresponding strain (red), as a function of p. Note the slow approach with p to the asymptotic value of Γ.

for large p. Panel d shows that Γ asymptotically approaches a strain slightly higher than this value. By positioning the peak in $f(\kappa)$ slightly outside the skewed, broad extrema in the normal stress term, the optimal waveform reduces overlap with the nearby inner extrema. At moderate $p \lesssim 5$, the strain producing the maximal-$|N_1|$ approaches its asymptotic value slowly but still approximately follows the $\Gamma \sim 2p\tan^{-1}((\sqrt{2}+1)/p)$ scaling above. Like the case for the shear viscosity, $f(\kappa)$ for the normal stress waveform never approaches zero. As a result, the maximal and minimal values of the expectation $\langle\sin(4\phi)\rangle$ are always of order ± 1 independent of p, and the magnitude of the N_1 signal in figure 4.5d grows solely due to the growth of A_H with aspect ratio.

In this paper, we have explored the possibility of designing oscillatory shear waveforms to control suspensions of rodlike particles. Our approach to optimizing an oscillatory shear waveform is generic and can be implemented to optimize any desired property of a sheared suspension that depends on particle orientations, including for more practical cases than those considered here. While an exhaustive exploration of waveforms for any property is impossible, many simple properties will be optimized by waveforms similar to those shown here. For instance, while particle alignment determines suspension conductivity [120] and flow-dichroism [53], the relevant order parameter is not the maximum of ρ but the liquid-crystal order parameter S_2, which is the maximal eigenvalue of the traceless symmetric second-rank orientation tensor $\mathbf{Q} = \boldsymbol{nn} - \delta/2$. Likewise, the elasticity of a fiber-reinforced composite depends on fourth-order moments of the particle orientation, such as the analogous S_4. While these order parameters are different from the maximum of ρ, we find empirically that the waveform that maximizes ρ at the start of a cycle also maximizes S_2 and S_4. Alternatively, rather than maximize the particle alignment by maximizing $\rho(\phi)$, one might desire to *minimize* the particle

alignment along one direction. We find empirically that the waveform in figure 4.2 that maximizes particle alignment along one direction also most strongly minimizes the particle alignment – the strong enhancement of $\rho(\phi) \sim p^2$ at $\phi = \pi/2, 3\pi/2$ also results in a $\sim 1/p^2$ suppression of orientations at $\phi = 0, \pi$.

All of our analysis has necessarily been limited to orientations confined to rotate in the flow-gradient plane at high Pe, as there is no simple solution for fully-rotating particle orientations under arbitrary shear waveforms. Nevertheless, while the quantitative details of the results may change for fully three-dimensional orientations, the qualitative picture should remain the same. The ϕ dynamics of a freely-rotating particle in a simple shear flow are the same as one confined to the flow-gradient plane. Moreover, preliminary analysis [89] and experiments [88] suggests that the κ dynamics remain similar for freely-rotating orientations as for those confined to the flow-gradient plane. Since the results above have simple interpretations in terms of the particle phase angles κ, the optimal waveforms should be similar for real suspensions.

The waveform that maximizes particle alignment should remain the same for freely-rotating orientations. As most of the waveform involves zero shear, the particle distributions will remain isotropic except for the spike portion of the waveform. The spike in Γ would then not only bunch the particle orientations' ϕ values into a $\sim 1/p^2$ region, they would also bunch the orientations' θ values, as there is a $\sim 1/p$ "pinching" of the Jeffery orbits near the flow direction, cf. equation 4.1. In contrast, the waveforms that control the viscosity would likely change slightly. In equation 4.12 and equation 4.13 only A_H multiplies the particle orientations. For freely-rotating equations the hydrodynamic coefficient B_H also affects the shear stress through the particle orientations, entering as a term $\propto B_H \langle n_x^2 + n_y^2 \rangle$. As

a result, the difference between the maximal and the minimal viscosity will depend on both A_H and B_H, although N_1 is still only determined by A_H at high Pe. Moreover, this new expectation $\langle n_x^2 + n_y^2 \rangle$ depends on both κ and C. As a result of this additional degree of freedom, the waveform and distribution of phase angles and orbit constants that extremize η_{inst} might be slightly different from those in figure 4.4. Possessing a full solution to the orientation dynamics would allow for verification and investigation of these properties. More interestingly, a full solution would allow for the possibility of controlling shear flows where the principle axes of the strain change directions during the course of a cycle. Such waveforms could perhaps separately maximize the signal from all the hydrodynamic coefficients A_H, B_H, and C_H.

4.6 Appendix

Numerical methods To find the optimal waveforms, we parameterized the distributions by the lowest 60 real Fourier coefficients and optimized over those parameters using a BFGS algorithm as implemented in Python (scipy) [112]. As there are many local minima in this fit space – for instance, frequency-doubling a waveform produces almost the same distributions as the original waveform – we found the optimal values from 100 randomly-chosen initial guesses for the Fourier coefficients. Examining the best waveforms by eye quickly divulges what the correct simple, optimal waveform should be (*e.g.* the spike and boxcar waveforms). Using the realization that the optimal waveforms are simpler spikes or boxcars, we then re-optimize using the simpler waveform with several free parameters. For the spike waveform, we optimize the spike height, ramp time, and phase, and for the boxcar the boxcar height, boxcar width, and ramp time – since the optimized

viscosities are averages over the waveform, we do not optimize the boxcar phase. For the optimal distributions as well as the shear and normal stresses, the simple waveforms always produce a better value than any of the Fourier-parameterized waveforms. Finally, to evaluate the scalings with aspect ratio we only optimized over the simple waveform, at 100 aspect ratios logarithmically spaced from 1 to 100.

To evaluate distributions and stresses for a particular waveform, we evaluated the coefficients A_2, δ_2, A_4, δ_4 from equation 4.10 numerically and used those coefficients to reconstruct $\mathfrak{D}(\kappa)$ and a numerically-normalized $f(\kappa)$. Empirically it is necessary to use a somewhat high number of quadrature points (900 for $p = 5.0$ and up to 12000 for the $p = 100.0$ values shown in the scaling plots), as the waveforms discussed in this paper are somewhat pathological and not analytic, and a simple trapezoidal rule is therefore not exponentially convergent [112]. For the tent and spike waveforms, we choose the quadrature points to be only where the waveform is varying, while for the Fourier waveforms we used equally-spaced quadrature points.

4.7 Discussion & Future Work

In chapter 4 I have necessarily focused on optimizing only a select few properties of a suspension under oscillatory shear. As mentioned briefly in the text, many properties related to particle alignment and suspension rheology will be optimized by waveforms similar to those shown there (*e.g.* the waveform that maximizes particle alignment is also the waveform that minimizes particle alignment along one direction). Some additional simple properties are optimized by trivial waveforms –

for instance, minimizing the global alignment or minimizing an orientational order parameter such as S_2 can be done by simply not shearing. However, there are some interesting additional properties that can be extremized easily, which I have not put in the main text for space and for unity of theme.

4.7.1 Maximizing Normal Stress : Shear stress signals

In the text, I optimized shear and normal stress viscosities essentially because they are simple to understand and are a good heuristic for more physically reasonable stress signals. One reason I avoided optimizing stress signals is that empirically they either tend to depend on the details of the optimized metric, or they tend to result in trivial waveforms. For example, zero-amplitude shear minimizes dissipation over a cycle; infinite amplitude shear maximizes dissipation. Interestingly, maximizing the normal stress signal also results in an infinite-amplitude waveform, despite the lack of normal stresses in continuous shear. However it is difficult to tell if this is real or a numerical or parameterization artifact (for instance, frequency-doubling will double the stress signal without changing the distributions). Despite these complexities, in reality we almost always actually care only about the stress, so it is enlightening to examine the maximal stress.

One of the cleanest examples is maximizing the ratio of the normal stress signal to the shear stress signal. In general, N_1 will be easy to measure not so much when it is large but when it is large compared to other stresses in the suspension. To explore a waveform that would make it easy to measure N_1, I searched for a waveform that maximized the ratio of the L2 norm of N_1 to the L2 norm of the shear stress: $\sqrt{\int_0^{2\pi} N_1^2(t)\,dt}/\sqrt{\int_0^{2\pi} \sigma_{xy}^2(t)\,dt}$. These results are shown in figure 4.6, as fit with a parameterization of 20 Fourier coefficients (*i.e.* up to $\cos(10t)$).

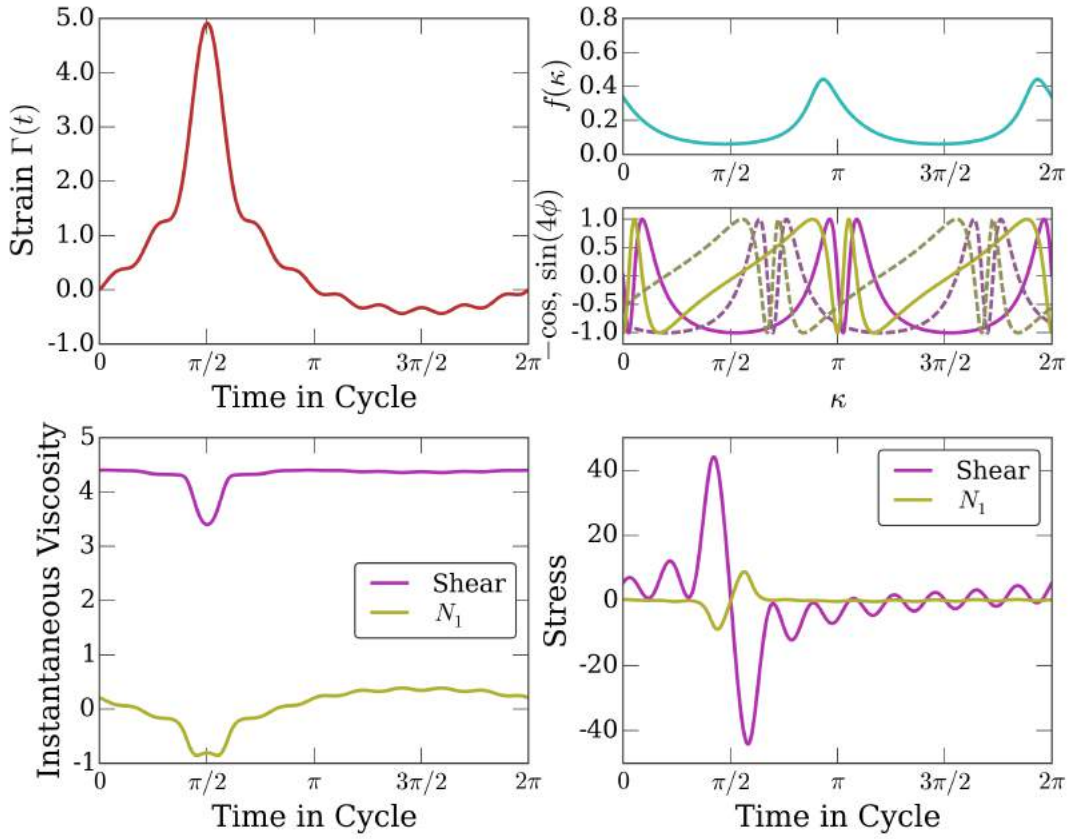

Figure 4.6: (a) The strain waveform that maximizes the ratio of the L2 norm of the normal stress to the L2 norm of the shear stress. (b) Top panel: The $f(\kappa)$ produced by the waveform. Bottom panel: $\sin(4\phi(\kappa + \bar{u}\Gamma))$ (yellow), which determines the normal stress, and $\cos(4\phi(\kappa+\bar{u}\Gamma))$ (magenta), which determines the shear stress, at two separate times in the cycle: the minimal strain (solid curves) and the maximal strain (dashed curves). (c) The instantaneous viscosity throughout the cycle, for both the normal stress (yellow) and shear stress (magenta). (d) The instantaneous stress throughout the cycle, for both the normal stress (yellow) and shear stress (magenta). Both the normal stress and the shear stress have two blips near the peak of the strain signal, where most of the shearing occurs.

Surprisingly, the waveform is comparatively simple – a sharp peak in the strain that gradually decays down to zero, like an isolated mountain with distributed foothills. This waveform is robust – fitting 100 different initial conditions at the same aspect ratio results in $\approx$ 70 of them converging to this waveform modulo phase shifts and inversions. Likewise, the same structure is present for aspect ratios of $p = 2.83$, 5.0, and 10.0. This waveform is also not a delta function or a spike – it is possible to get a much sharper spike with the amount of Fourier coefficients used, and a much sharper spike is achieved by the Fourier optimization of the maximal alignment waveforms. However, since the optimized parameters depend on both the strain and the strain rate, understanding why this waveform is optimal is not as simple as the ones in the main chapter text. For instance, by looking at the viscosity alone this waveform does not seem to be promising – there is only a small blip in the N_1 viscosity ("large" but negative for this waveform), and a small decrease in the shear viscosity. Since these two blips align with the region where the shear rate is highest, the relative signal is maximized. As a result, for this aspect ratio the L2 norm of the normal stress is $\approx 18\%$ of the L2 norm of the shear stress – small, but large compared to most waveforms and even compared to non-hydrodynamic normal stresses.

4.7.2 Extremizing Dynamics

While in chapter 4 I only discussed the long-time behavior of the particle orientations, the results in ref. [89] and chapter 3 provide an analytical solution to the orientation *transients* as well. As I show in chapter 3, the phase-angle distribution $f(\kappa)$ relaxes to its steady-state value by decaying with a spectrum of time scales $D_{\text{eff}}m^2$, for m an integer and D_{eff} a dresssed diffusive timescale that depends

on the oscillatory cycle through $\mathfrak{D}(\kappa)$. Each of these eigenvalues is associated with an eigenfunction which is $\exp(imz(\kappa))$, where $z(\kappa)$ is an allowable coordinate transformation defined through $\mathfrak{D}(\kappa)$. As a result, the dynamics are completely determined by two quantities: the scalar D_{eff} and the function $z(\kappa)$.

The simplest thing to optimize about the dynamics is D_{eff}. We could look for a waveform that either maximizes or minimizes D_{eff}, and we might expect that these waveforms have interesting properties. However, it so happens that both of these optimal waveforms are trivial. The waveform that minimizes D_{eff} is zero-amplitude shear, and the waveform that maximizes D_{eff} is continuous shear or equivalently triangle-wave shear [89] with amplitude $\Gamma = n\pi(p + 1/p)$, for n an integer. This result is somewhat easy to understand from equation 4.10 and equation 3.36, which can be recast to state:

$$D_{\text{eff}}/D = \left(2\pi / \int_0^{2\pi} (\mathfrak{D}(\kappa)/D)^{-1/2}\, d\kappa\right)^2 \tag{4.14}$$

Maximizing D_{eff} thus corresponds to minimizing the average of $1/\sqrt{\mathfrak{D}(\kappa)}$. As visible from equation 4.10, the waveform affects the variations in $\mathfrak{D}(\kappa)$ but not its mean value. Increasing these variations will make $\mathfrak{D}(\kappa)$ become closer to zero at certain values of κ, which will increase the average value of $1/\sqrt{\mathfrak{D}(\kappa)}$. Thus, the maximal value of D_{eff} should correspond to a constant $\mathfrak{D}(\kappa)$, which is precisely what continuous shear creates. Conversely, the minimal value of $\mathfrak{D}_{\text{eff}}$ should correspond to the maximally-varying $\mathfrak{D}(\kappa)$, with both $A_2 = 1$ and $A_4 = 1$, which is precisely what zero-amplitude shear creates. Optimizing over a Fourier parameterization of a waveform produces results that converge to these two limits.

4.7.3 Maximizing $\rho(\phi)$ via $f(\kappa)$

In the text, we sought to directly maximize ρ through one oscillatory shear waveform. We saw that $\rho(\phi)$ varies with time, but is always proportional to $\bar{u}/u \times f(\kappa)$, where $\bar{u}/u$ is a function that is independent of the details of the waveform and that translates with strain, and where $f(\kappa)$ is determined by averages of the strain waveform. We saw that, to maximize $\rho(\phi)$, the optimal strategy was to create a strong peak in $f(\kappa)$ and then align peaks in $\bar{u}/u$ with that peak in $f(\kappa)$.

This strategy suggests another approach – rather than maximize $\rho(\phi)$ directly, we could search for a waveform that instead maximizes $f(\kappa)$. Then, at the precise moment when alignment is desired, we could align $\bar{u}/u$ with this $f(\kappa)$, maximizing alignment. However, this strategy does not improve on the maximal $\rho(\phi)$. As alluded to briefly in the text, the waveform that maximizes $f(\kappa)$ is zero-amplitude shear. Furthermore, sufficiently rapid spikes – like the one that occurs in the optimal waveform – do not influence $f(\kappa)$, so this indirect strategy can be implemented via oscillatory shear alone. This approach is really what the waveform in chapter 4 achieves – it maximes $f(\kappa)$ by zero-amplitude shear, then aligns $f(\kappa)$ with a peak in $\bar{u}/u$ only when alignment is desired. The periodicity of this spike does not affect $f(\kappa)$ if it is sufficiently fast. However, this does suggest an alternative and equivalent way of maximizing alignmnet – do nothing, let $\rho(\phi)$ relax to isotropy, then rapidly strain by 1/4 of a Jeffery orbit to align the particles.

4.7.4 Wobbly Continuous Shear

The averaged equations derived in ref. [89] rely on periodicity in the rotational velocity experienced by this particle. Without this periodicity there would not be

an average equation, but it does not matter where this periodicity comes from – whether the periodic rotation of the Jeffery orbit or the periodic forcing of the flow. In chapter 3 I explored these two possibilities for the origins of periodicity.

There is a third option for creating periodicity in the particle's velocity field. Rather than having only a continuous shear and periodic orbits or only a periodic shear and orbits that return to their initial starting position, it is possible to combine these two. In the language of chapter 4 this corresponds to having $\Gamma(t)$ not be strictly periodic but having $\Gamma(t = 2\pi) = \pi(p+1/p)n$, where n is an integer. In other words, the strain waveform does not have to be strictly periodic but it can wind the particles around the sphere, as long as the particles wind by an integer number of half-Jeffery orbits during each period (it is half a Jeffery orbit because the rotational velocity is $\boldsymbol{n} \to -\boldsymbol{n}$ symmetric). Carrying through the derivation in ref. [89] results in the exact same equations as for oscillatory shear, including the simple description of $\mathfrak{D}(\kappa)$ in terms of A_2, δ_2, A_4, δ_4 in equation 4.10, but with the new, winding $\Gamma(t)$. For a fixed winding number, the space of waveforms is equal to the space of periodic waveforms – transform any periodic waveform $\Gamma(t) \to \Gamma(t) + n(p+1/p)/2 \times t$. The winding number n corresponds to the number of times that the strain winds around the unit disk in the complex plane for δ_2 in equation 4.10. Again, for simple waveforms $\mathfrak{D}(\kappa)$ can be calculated analytically – $A_k = J_n(k\Gamma_0/(p+1/p))$ for $\Gamma(t) = \Gamma_0 \sin(t)+n(p+1/p)/2\times t$ – but in general results are not calculable analytically. Wobbles that are a rational fraction of a Jeffery orbit period are easily included in this framework – if the period of the wobble is p/q Jeffery orbits, then after every q Jeffery orbits the wobble has repeated itself p times, so the p-repeated wobble winds around the disk correctly. While irrational periods are not included, the obvious argument of rational approximants suggests that they behave similarily.

Naively, one might think that allowing for wobbly continuous shear allows for a wider range of optimizable values than just for oscillatory shear. However, this is not the case. Since the coefficients A_2 etc. that determine $\mathfrak{D}(\kappa)$ are insensitive to rapid changes in strain, a winding waveform $\Gamma_w(t)$ that produces a given $\mathfrak{D}(\kappa)$ can be imitated by an oscillatory waveform $\Gamma_o(t)$ that tracks $\Gamma_w(t)$ exactly right until $t = 2\pi - \epsilon$, then rapidly reverses the shear to instantly return to the origin. Conversely, any oscillatory shear $\mathfrak{D}(\kappa)$ can be imitated by a winding waveform that tracks the oscillatory $\Gamma_o(t)$, then immediately spikes at $t = 2\pi - \epsilon$ to complete one winding.

However, there are optimizable properties that are unique to wobbly continuous shear. One such property is dissipation under continuous shear. One might try to wobble the shear, modifying the rod distribution and hence the suspension rheology, thereby decreasing the net dissipation throughout the cycle. While the actual dissipation depends on the particle volume fraction as well as on aspect ratio and details of the waveform, we could try to minimize just the dissipation produced by the particles. However, numerically exploring this shows that the waveform which minimizes particle-induced dissipation is simply continuous shear; the constant contribution to the suspension viscosity through B_H and C_H and its penalization of increases in the strain rate outweighs any change in the viscosity due to modifying the waveform.

CHAPTER 5

LIGHT MICROSCOPY AT MAXIMAL PRECISION

Microscopes provide an extraordinary vista into the dance of defects in atomically thin silica, the mesmerizing self-organization of active colloids into crystals, the intricate separation of chromosomes during mitosis. Tremendous effort has been put into improving both microscope design and imaging techniques over the past few decades, resulting in an enormous increase in image quality and resolution. Here, we show that a similarly large improvement can be achieved in the *analysis* of microscopy images. We demonstrate our approach on an image of colloidal particles, improving the measurement of object positions and radii in a microscope image by up to a factor of 100 over current methods. We measure object properties by fitting experimental images to a detailed model of the physics of image formation, a method we call Parameter Extraction from Reconstructing Images (PERI). This unprecedented resolution immediately opens a new window into colloidal science, which we illustrate by measuring interparticle potentials at the nanometer scale. Importantly, the ideas behind our technique can be readily applied to other imaging modalities such as brightfield microscopy or even STEM and STM.

Microscope technology has progressed to near perfection. Crisp images speak of precisely engineered microscope components – large-aperture and nearly aberration-free lenses, high-frame-rate and low noise cameras, powerful and uniform light sources. Nanometer-scale details boast of super-resolution techniques thought impossible mere decades ago – PALM [14], STORM [123], STED [65]. The continued development of more powerful techniques – SIM [84], Lattice-light sheet microscopy [28] – reassures that resolution will continue to improve.

However, our ability to extract *quantitative* information from microscopy images has not kept pace. Current methods rely on heuristic approaches, such as blob and centroid methods, for identifying feature locations and even for analyzing super-resolution images [121, 107, 59, 6, 133, 4]. While these methods rapidly provide information about structure in microscopy images, their simple nature necessarily ignores confounding physical attributes of image formation, such as illumination and point-spread functions that vary with location. As a result, systematic errors and inefficient estimates plague these techniques for all but the simplest images.

In this paper, we increase the precision of features extracted from standard confocal microscopy images by up to a factor of 100, without modifying the microscope or the image acquisition. Our method, dubbed parameter extraction from reconstructing images (PERI), creates a detailed model of the image that incorporates all the physics of image formation and fits the parameters in that model to find their correct values. In principle, this method measures parameters at the information-theoretic limit, determined by noise in the image. In practice, systematic errors arising from incomplete knowledge of the image formation eventually cut off the continued improvement of precision with decreasing noise. We illustrate

this approach using confocal images of dense suspensions of colloidal spheres. We measure each particle's position to within 2 nm and each particle's radius to within 3 nm – limited only by the incomplete description in the literature of the microscope's optics. Finally, we close by using this extreme precision to probe colloidal interactions at an unprecedented scale for simple microscopy.

How precisely can an object be located in an image? The fundamental limitation in locating an object arises from statistical noise in the image formation, not directly from diffraction or optical limitations [116]. This limit is determined through the interplay of the image signal and noise, as described by the Cramer-Rao Bound. Specifically, the Cramer-Rao Bound states that the covariance matrix of the estimated parameters is always larger than the inverse of the Fisher information matrix of the noise distribution [117]. For an image with Gaussian white noise of variance σ^2, sampled at points $\vec{x}_k$, the minimum uncertainty in the parameters $\vec{\theta}$ measured from the image is

$$\operatorname{cov} \theta_{ij} \geq \sigma^2 \left(\sum_k \frac{\partial \mathcal{I}(\vec{x}_k)}{\partial \theta_i} \frac{\partial \mathcal{I}(\vec{x}_k)}{\partial \theta_j} \right)^{-1} , \tag{5.1}$$

where $\mathcal{I}(\vec{x})$ is the image that would be measured in the absence of noise. We can use this equation to estimate the minimum uncertainty in measuring a colloidal particle's radius and position. For a particle of radius R blurred by diffraction over a width w, the derivatives with respect to particle radius in equation (5.1) are only nonzero on a shell at the particle's edge of approximately $4\pi R^2 w$ voxels. At the particle's edge, the intensity changes from a characteristic brightness $\approx I$ to ≈ 0 over a width $\approx w$, and the derivatives are thus of magnitude $\approx I/w$. Substituting these values gives a minimum uncertainty in a particle's radius as $\sigma_R \sim \sqrt{w/4\pi R^2}/\mathrm{SNR}$, where $\mathrm{SNR} = I/\sigma$ is the signal-to-noise ratio. Likewise, changing the particle's position only affects the edge voxels in the direction of

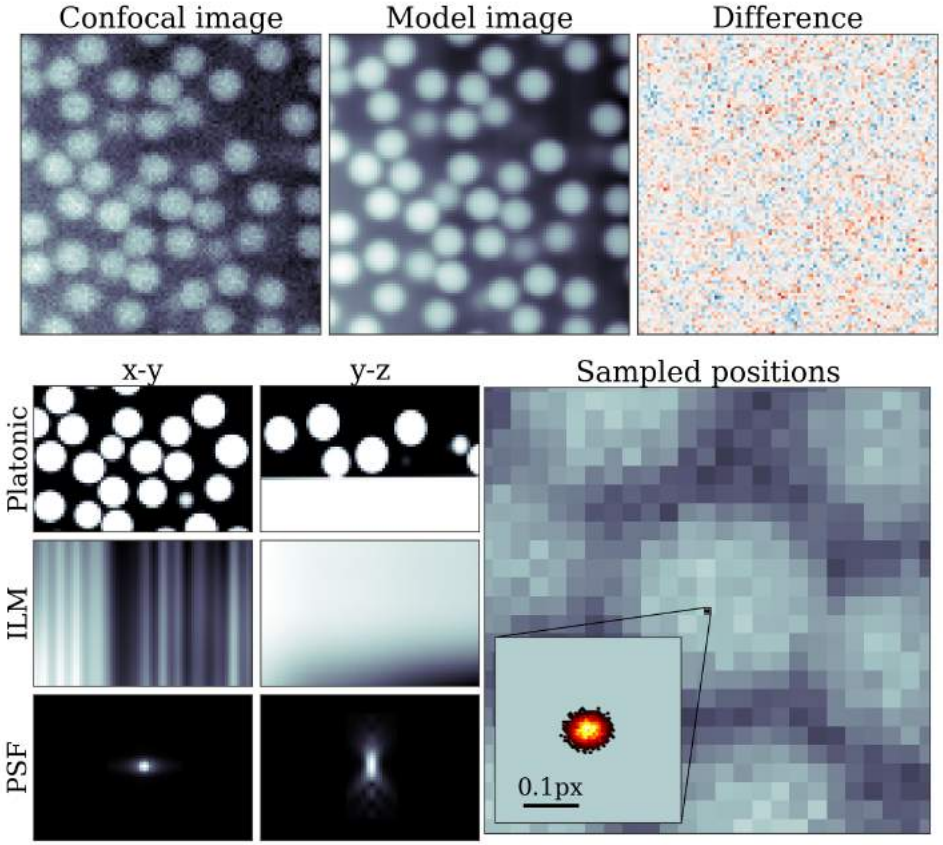

Figure 5.1: **PERI overview** – A demonstration of model information recovered from real confocal microscope images of $\langle a \rangle = 1.343(8)$ μm colloidal spheres at a volume fraction of $\phi = 0.130(5)$. On the top row, we compare (left) the true microscope image including CCD noise (middle) the reconstructed model image (right) the difference between the true image and model image. Notice that most of the structure in the difference image is uncorrelated white noise. In the lower left panels, we show reconstructed global parameters of the image along two different slices of the 3D confocal image, perpendicular to the scanning direction and including the scanning direction. We show the platonic (perfect) spheres as well as the coverslip (top), the spatially varying illumination field produced by the confocal scanning laser (middle), and the fitted point spread function of the microscope (bottom). Finally, in bottom right we show a histogram of x-y positions sampled from a single particle displaying a variance of 2 nm in each coordinate.

the particle's motion. The positional derivatives will thus be of magnitude $\approx I/w$ only on a shell of $\approx \pi R^2 w$ voxels, giving the minimal uncertainty in the particle's position as $\sigma_x \sim \sqrt{w/\pi R^2}/\text{SNR}$. For a colloidal particle of diameter 1 μm, imaged with a confocal microscope with voxel size of 100 nm and diffractive blur of $w \approx$ 200 nm at an SNR = 25, these uncertainties correspond to $\sigma_R \approx 1.5$ nm and $\sigma_x \approx 3$ nm, a fantastically high precision.

Actually achieving this localization without serious systematic errors requires a detailed knowledge of the image formation process. To incorporate this knowledge, we create a generative model of the microscope image based on the physics of the light interacting with the sample and with the microscope's optical train. We then fit every parameter in the model by comparing the image produced by the model to the experimental image. Our model describes the physics of image formation in the order that it occurs: (1) fluorescent dye is distributed unevenly throughout the sample, (2) the dyed sample is illuminated unevenly by the laser, (3) the resultant image is blurred due to diffraction, and (4) the final image is noisy.

Dye Distribution: To reconstruct the image, we start with the continuous distribution of the fluorescent dye in the sample. For the image in figure 5.1, the dye is distributed everywhere except in a slab, representing the glass cover-slip slide, and in a collection of spherical lacunae, representing the colloidal particles. To represent this continuous dye distribution on a pixelated grid, we draw these objects in real-space using a function that is tuned to match the exact Fourier representation of a sphere (see SI for an extensive discussion of this and the rest of the generative model). We call this correctly-aliased representation on a finite grid the Platonic image. While we focus on featuring only spheres in this work, PERI is flexible enough to include any parameterizable object in the generative

model, such as ellipsoidal [79, 102], rodlike [85], or polyhedral [60] particles.

Illumination field and background: This distribution of dye is illuminated by a scanned laser. Due to imperfections and dirt in the optics, the illumination is not uniform but instead varies in space. For instance, our line-scanning confocal's illumination field is highly striped, as any imperfections in the line illumination are dragged across the field of view. We describe this spatially-varying illumination as a continuous field that varies throughout the image. Empirically, we find that combining a Barnes interpolant along the scan direction and Legendre polynomials in the perpendicular directions accurately describes both the rapidly-varying stripes and the slowly-varying changes in the illumination of our line-scan confocal. Additionally, the microscope always registers a non-zero background signal, which we include in our model. We parameterize this background similarly to the illumination field.

Point spread function: Diffraction prevents the illuminated dye from being imaged exactly onto the detector. Instead, each dye molecule in the sample projects a comparatively large blur, known as the point-spread function (PSF), onto the imaging camera. As a result, the image captured on the camera is a convolution of the illuminated Platonic image with the PSF, and not simply the illuminated dye itself. While complicated, this PSF has been calculated exactly by many researchers for different geometries [63, 155, 158, 103, 34, 40, 156, 18]. For microscope samples with a refractive index different from what the optical train is designed for, the PSF worsens with depth, becoming significantly broader and more aberrated. We use an adaptation of these exact PSF calculations for a line-scanning confocal as our PSF model, optimizing over parameters such as the numerical aperture of the lens and the index mismatch of the sample to the optics.

Putting these three processes together, our model image $\mathcal{M}$ sampled at pixels $\vec{x}$ is described by

$$\mathcal{M}(\vec{x}) = B(\vec{x}) + \int \mathrm{d}^3\vec{x}' \; [I(\vec{x'})(1-(1-c)\Pi(\vec{x'}))]P(\vec{x}-\vec{x}';\vec{x}) \tag{5.2}$$

where I is the illumination field, B is the background, Π is the platonic image, and P is the PSF; we include a constant offset c to partially capture rapidly-varying variations in the background.

Noise: Finally, noise degrades the image recorded on the camera. We treat the noise using a Bayesian framework, and look for the maximum-likelihood model given the microscope data, complete with possible priors on parameter values. Since the noise is empirically Gaussian (see SI), the most likely model is the least-squares fit of the model to the microscope image.

As a result, we least-squares fit every parameter in our generative model to find the correct particle positions, radii, illumination field, and point-spread function. A typical confocal image contains a few times 10^3 particles, each with 4 fit parameters (x, y, z, R). In addition, there are a few hundred global parameters to optimize, such as the illumination and PSF parameters and the lens's z-step size along the optical axis, resulting in $\approx 10^4$ parameters per image – a daunting optimization problem. We begin with an initial guess for the Platonic image using standard particle locating techniques [36], and we simultaneously fit the particle positions and the global variables using a Levenberg-Marquardt algorithm modified for large parameter spaces [99, 147, 148, 149]. From here, we ensure that we have correctly identified every particle in the image by automatically adding and subtracting particles based on the the difference between the model and the microscope image. After finding the best-fit parameters, we sample from the log-likelihood using standard Monte Carlo techniques [104] to estimate the errors in

the image reconstruction. (See SI for a detailed description of the fitting method and numerical optimizations.) It is important to note that this fit is over all the pixels in the image – to get a meaningful extraction of parameters, every pixel must be described accurately. Imperfectly fit regions – due to e.g. deformed particles or PSF leakage from objects outside the image – can bias the extracted positions of particles in the region and even affect the entire image reconstruction through the influence on image-scale variables.

Using PERI to measure positions with nanometer accuracy requires rigorous checks on our method, with both generated and experimental data. We generate images with a detailed physical model, employing an exact, spatially-varying point-spread function [63], experimentally-measured spatially-varying illumination, dense collections of particles with varying radii, and a realistic amount of noise. PERI successfully fits these generated data, converging to the global fit minimum in the extremely large dimensional parameter space despite a host of possible numerical complications. From this fit, PERI extracts both the particle positions and radii at the Cramer-Rao bound ($\approx$2 nm and $\approx$1 nm, respectively). In contrast, current heuristic-based algorithms cannot measure the particle positions to better than 60 nm on realistically generated datasets. (See SI for a detailed comparison of PERI to other featuring algorithms.)

Emboldened by this success, we next test PERI on real experimental data. We take fast, three-dimensional movies of a suspension of $\approx$1.3 μm silica spheres suspended in a glycerol and water mixture (see SI) and feature these images using PERI. By analyzing each frame in the movie independently, we can extract systematic errors from PERI's featuring.

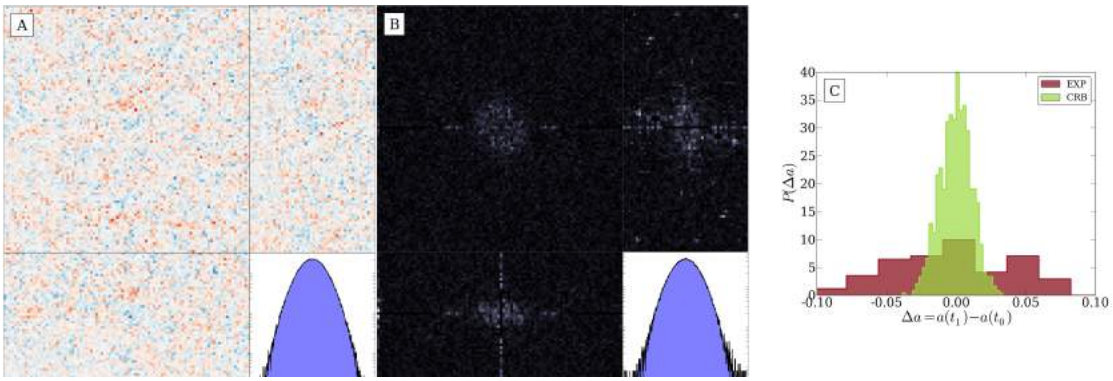

Figure 5.2: **Fitting the generative model to experimental data** – We experimentally verify our featuring algorithm by looking at the residuals in real and Fourier domains as well as comparing the radii of tracked particles between two different frames of a movie. (A) We plot three cross sections of the real space residuals showing nearly Gaussian white noise. The 'shadows' of spheres can be seen due to complications of the PSF. However, the probability distribution of all residuals (lower right) is very nearly Gaussian as shown as a quadratic on a logarithmic scale. (B) The Fourier power spectrum of the same residuals displayed along q_x, q_y, or $q_z = 0$. In all panels, excess power is visible at scales larger than the particles themselves but smaller than the features given by the ILM. These residuals are associated with the approximations we have made in the point spread function, particularly the difficulty in calculating the long tails of the PSF and the cutoff we employ to speed up numerical computations. The q-space histogram is also very nearly Gaussian with slight deviation from quadratic in the tails. (C) We plot the difference in radii across frames (red) as compared to the difference that we estimate using the radii CRB (green). The difference in peak high is proportional to the distance our experimental measurements are from the theoretic limit, roughly $3\times$ larger.

First, we analyze the residuals of our fits to the experimental data. Figure 5.2(a,b) shows these residuals in both real- and Fourier-space. If our fit to the experimental image were perfect, the residuals would be perfectly Gaussian. Instead, while the overall probability distribution is nearly Gaussian in both domains, in Fourier-space there are distinct wave vectors above the noise floor. Comprising roughly 10^{-5} of the power in the experimental image, the extremely small size of this remaining signal demonstrates the quality of our generative model. The deviations of our model from the experimental data occur at length scales slightly

larger than the particle diameter but smaller than typical illumination variations. These unexplained residuals most likely arise from approximations in models of line-scanning point spread function, excess aberrations in the microscope, and the artificially finite but large size we use in our PSF calculation to speed up optimization. Additionally, sharp peaks at high wave-vectors can be seen in one slice of the Fourier-space residuals, which arise from noise in the scanning of the lens and line illumination. The remaining question is how much these residuals affect the parameters of interest, the particle positions and radii.

We can use the extracted particle positions and radii to test the accuracy of PERI. Physically, the particle radii do not fluctuate in time and particles cannot overlap. Measuring any particle overlaps within a frame and individual radii fluctuations over time provides a model-independent measurement of errors in the particle positions and radii. In Fig. 5.2(c), we see a radius variation of 3 nm between consecutive images in the movie, corresponding to an error that is roughly $3\times$ the minimal error from the Cramer-Rao Bound. Additionally, in the samples in Fig. 5.1 and Fig. 5.2, we find an overlap only every few frames, which is consistent with the measured radii uncertainty. Combined, these measurements demonstrate that we are able to measure particle positions and radii to within 3 nm.

This extraordinary accuracy in locating object positions provides a method to measure interparticle interactions on an unprecedented scale for light microscopy. When silica particles are suspended in an aqueous solution, the particles charge, as the polar solvent dissociates ions on the particles' surface groups. This charge results in an electrostatic repulsion, which is in turn screened by counterions in the bulk. For a typical suspension, this screening length can be as short as 10 nm. In addition, dispersion forces create a slight attraction between the particles. The

combination of these two interactions, known as the DLVO potential, creates an interparticle potential that deviates from a hard-sphere potential only at nanometer separations. This potential ever so slightly biases the distribution of particle positions away from that expected for a hard sphere suspension.

We measure these nanometer-scale interactions using PERI by taking a large set of 600 images of 1.3 μm silica spheres suspended in a water-glycerol mixture. To prevent kinetic effects from confounding our measurements, we allow the sample to fully sediment for an hour. This produces the open layer of sediment approximately 2-3 particle layers deep that is shown in figure 5.3a. We then image this suspension repeatedly over the course of several hours, extracting simulation-level detail of $\approx$1200 particle positions and radii in each of the 1000 images. The particle interactions determine the structure of the suspension. We quantify this structure with the probability $P_s(\delta)$ of finding a pair of particles with surface-to-surface separation δ, accounting for radii polydispersity and sedimentation in a manner preferable to the usual pair-correlation function. To reconstruct the interparticle potential, we use the extracted particle radii and particle number from the data and we simulate the particle dynamics using Brownian dynamics, incorporating gravitational settling, interparticle van der Waals attraction, and interparticle Debye repulsion [122]. We then fit these parameters by simulating, reconstructing $P_s(\delta)$ from the simulation at each set of potential parameter values, and fitting these parameters to find the best $P_s(\delta)$ that matches experiment.

Figure 5.3b shows the experimental and best-fit simulation $P_s(\delta)$. The experimental $P_s(\delta)$ has some slight extra particle overlaps due to mis-featuring of particle positions and radii. Both the simulation and experimental $P_s(\delta)$ show a rapid but not instantaneous rise near contact, followed by a slow increase with oscillations.

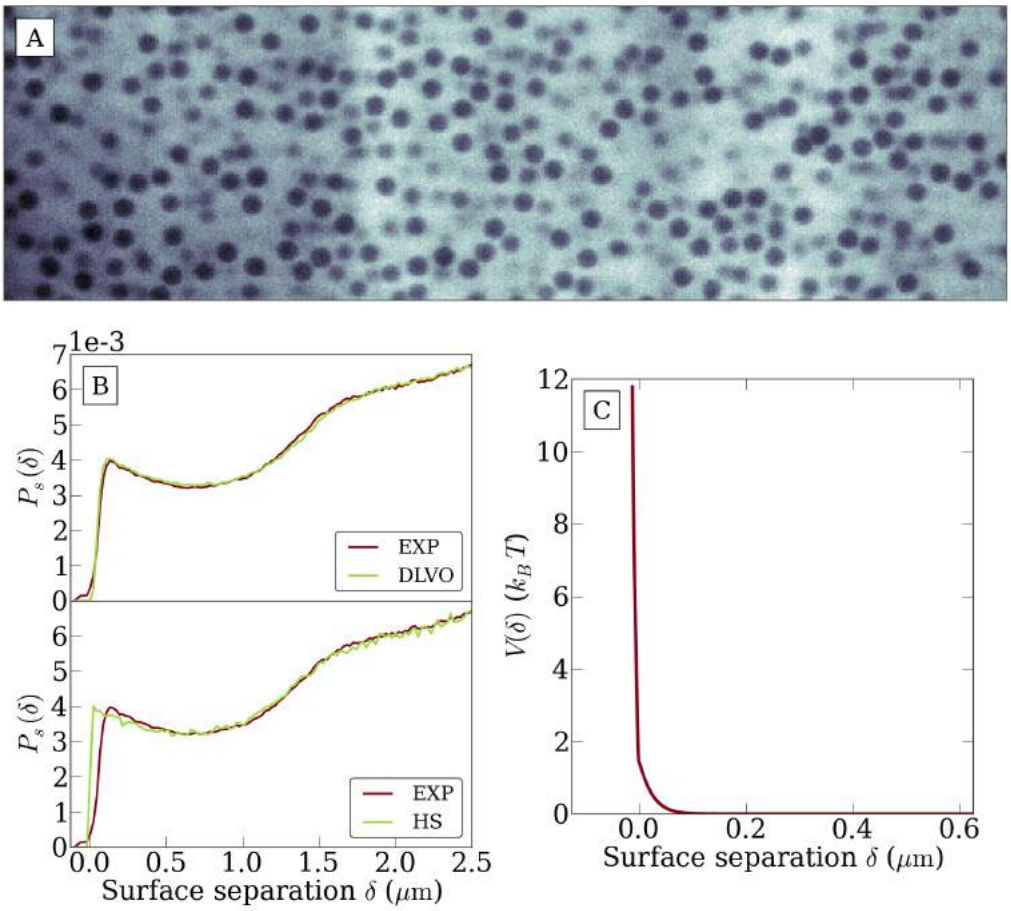

Figure 5.3: **Extracting Interparticle Potentials** (A) The dilute image of particles we use to extract interaction potentials. (B) The experimentally-measured distribution of particle separations $P_s(\delta)$ (red) and the best-fit simulation $P_s(\delta)$ (green, upper portion). While the best fit agrees excellently with experiment, the $P_s(\delta)$ for perfect hard spheres (green, lower portion) does not agree with experiment. (C) The best-fit interaction potential as a function of particle separation δ. Note the clear resolution of the screening length between 0 and $\approx$0.05 μm.

At long distances, the probability grows due to the increased volume where particles can be located; this growth is approximately linear and not quadratic because particle settling restricts particles to a quasi-two-dimensional region. From the excellent agreement of the simulation $P_s(\delta)$ with experiment, we can reconstruct the interparticle potential shown in panel c. Surprisingly, we find an extremely short 15 nm Debye screening length, in contrast to what is naively expected from the amount of salt from the added dye. This short screening probably arises due to salt impurities on the particle surfaces, in the fluorescent dye, and possibly in the deionized water. We also find a nonzero but extremely weak van der Waals interaction – 0.001 kT as opposed to the $\approx$ 1 kT Hamaker constant for silica particles in water. The weak attraction probably results from a combination of the index-matching of the spheres to the suspending fluid and retarded van der Waals interactions. These parameters reproduce the nearly hard-sphere potential shown in panel c. Our experimental data firmly constrains the possible potentials felt by the particles, strongly excluding both hard-sphere interactions and DLVO theory with naive van der Waals and electrostatic parameters, as shown by the disagreement between these simulated pair correlation functions and the experimental one in figure 5.3a. Importantly, both the hard-sphere potentials and the naive DLVO potentials are excluded by the values of $P_s(\delta)$ near contact. Without an accurate featuring method such as PERI, it is impossible to discern the potential at this accuracy.

Our technique and the ideas within it provide more than just a description of colloidal interactions. A nanometer accuracy in locating colloidal particle positions would revolutionize fields as diverse as the study of glassy systems to the measurement of biological forces in force-traction microscopy. Moreover, the principle of accurately reconstructing an image to extract parameters is applicable to

a wide range of fields. PERI could be easily extended to brightfield microscopy by implementing an accurate description of image formation in a brightfield microscope, which would greatly increase the applicability of PERI. Further applying these ideas to imaging modalities such as STEM or STM will usher in a new era of precision measurements, for objects whose sizes range from microns to angstroms.

CHAPTER 6

LIGHT MICROSCOPY AT MAXIMAL PRECISION: SUPPLEMENTARY INFORMATION AND DETAILS

6.1 Overview

In this supplemental material we describe the details of our method for extracting parameters from experimental confocal images at the highest resolution possible without modifying the microscope itself. To achieve maximal resolution, we build a generative model which aims to describe the value of every pixel in the experimental image. That is, we create simulated images by explicitly modeling every relevant aspect of image formation including particle positions and sizes, the location of dirt in the optics, amount of spherical aberration in the lens, and the functional form of the point spread function. We describe each of these model components in detail in Section 6.3 and how we decided on these particular components in Section 6.4. In order to fit this model to the experiment, we adjust all model parameters until the features present in the true experimental image are duplicated in the simulated one. We decide when the fit is complete and create a fair sample of the underlying parameters by using a traditional Bayesian framework which is described in general terms in Section 6.2. This high dimensional optimization is in general very difficult and so we describe our algorithmic improvements and particular techniques in Section 6.5. Finally, we assess the accuracy of this method in extracting underlying parameters and compare its performance with traditional featuring methods in Section 6.6.

Overall, this document is meant to provide a roadmap for other researchers to follow when adapting this technique to other types of microscopy and other

types of samples in order to extract the maximal amount of information from their experimental images.

6.2 Bayesian framework

When fitting a model to noisy data, it is useful to adopt a Bayesian framework in which we rigorously treat the noise as part of our model. In the case of our featuring method, we fit a model of each image pixel M_i to experimental data d_i, which can be described as a combination of signal and noise $d_i = S_i + \eta_i$. This noise is present due to the detection of a finite number of photons by the microscope sensor, noise in the electronics, etc. and can be well described for our system by uncorrelated $\langle \eta_i \eta_j \rangle = 2\sigma^2 \delta_{ij}$, Gaussian noise $\eta_i \sim \mathcal{N}(0, \sigma)$ (see Section 6.3).

In a Bayesian framework, the likelihood that an individual pixel is correctly described by our model is given by the Gaussian likelihood,

$$\mathcal{L}(M_i \mid d_i) = \frac{1}{\sqrt{2\pi\sigma_i^2}} e^{-(M_i - d_i)/(2\sigma_i^2)} \tag{6.1}$$

For uncorrelated pixel noise, the entire likelihood of the model given the image is given by the product over all pixels, $\mathcal{L}(\vec{M} \mid \vec{d}) = \prod_i \mathcal{L}(M_i \mid d_i)$. We are ultimately interested in the probability of the underlying parameters given the image we record. According to Bayes' theorem, we can write this as

$$\begin{aligned} P(\vec{\theta} \mid \vec{d}) &\propto P(\vec{d} \mid \vec{\theta}) P(\vec{\theta}) \\ &\propto \mathcal{L}(\vec{M}(\vec{\theta}) \mid \vec{d}) P(\vec{\theta}) \end{aligned}$$

where $P(\vec{\theta})$ are priors that allow us to incorporate extra information about the parameters $\vec{\theta}$. These priors can be as simple as the fact that the particle radius is positive definite or that a group of images share similar PSFs. For example, an

overlap prior $P_{\text{overlap}}(\vec{x}_i, \vec{x}_j, a_i, a_j) = \mathrm{H}(a_i + a_j - |\vec{x}_i - \vec{x}_j|)$, where H is the Heaviside step function, can be used to impose the physical constraint that particles cannot overlap. However, we found that the overlap prior only becomes relevant when the free volume of a particle is small compared to the average sampling error volume (when a particle is caged by ~ 1 nm on all sides) and so we ignore it most of the time.

We primarily work with the log-likelihood function $\log \mathcal{L}$ because the number of pixels in the image can be very large, on the order 10^7. For Gaussian noise, the log-likelihood is precisely the square of the L_2 norm between the model and the data. Therefore, we are able to maximize this log-likelihood using a variety of standard routines including linear least squares and a variety of Monte-Carlo sampling techniques. After optimizing, we use Monte-Carlo algorithms to sample from the posterior probability distribution to extract full distributions of the model parameters. In this way, any quantity of interest that is a function of particle distribution can be calculated using Monte-Carlo integration by

$$\begin{aligned} \langle \mathcal{O}(\vec{\theta}) \rangle &= \int \mathcal{O}(\vec{\theta}) P(\vec{\theta} \mid \vec{d}) \, \mathrm{d}\vec{\theta} \\ &= \frac{1}{N} \sum_{i}^{N} \mathcal{O}(\vec{\theta^i}) \end{aligned}$$

Here, $\vec{\theta^i}$ is a parameter vector sampled fairly from the posterior probability distribution and $\mathcal{O}(\vec{\theta^i})$ is an observable such as the pair correlation function, packing fraction, or mean squared displacement. Calculating higher-order moments provides estimated errors and error correlations on these observables. This is one of the more powerful aspects of this method – one can generate a probability distribution for each parameter and directly apply these distributions to any observable that can be inferred from the parameters.

Given this Bayesian framework, the main idea of this work is to create a full generative model for confocal images of spherical particles and provide algorithmic insights in order to implement the model on commodity computer hardware.

6.3 Generative model

Most of the difficulty in our method lies in creating a generative model that accurately reproduces each pixel in an experimental image using the fewest number of parameters possible. Our model is a physical description of how light interacts with both the sample and the microscope optics to create the distribution of light intensity that is measured by the microscope sensor and rendered as an image on the computer. In this section, we describe the model which we use to generate images similar to those acquired by line-scanning confocal microscopy of spherical particles suspended in a fluorescent fluid.

Our generative model aims to be an accurate physical description of the microscope imaging; it is not a heuristic. Creating this model requires a detailed understanding of image formation of colloidal spheres in a confocal microscope. In the simplest view, our samples consist of a continuous distribution of dye distributed throughout the image. If the fluid is dyed (as for the images in this work), due to diffusion the dye is uniformly distributed through the fluid. The fluid-free regions, such as those occupied by the particles, are perfectly dye-free. The sample is illuminated with a laser focused through an objective lens. This focused laser excites the fluorescent dye only in the immediate vicinity of the lens's focus. An objective lens captures the dye's emitted light, focusing it through a pinhole to further reject out-of-focus light. The collected light passes through a long-pass

or band-pass filter, which eliminates spurious reflected laser light before collection by a detector. This process produces an image of the sample at the focal point of the lens. Finally, rastering this focal region over the sample produces a three-dimensional image of the sample.

However, the actual image formation is more complex than the simple view outlined above. Excessive laser illumination can cause the dye to photobleach. Due to dirt and disorder in the optical train, the sample is not illuminated uniformly. Diffraction prevents the laser light from being focused to a perfect point and prevents the objective lens and pinhole from collecting light from a single point in the sample. Aberrations are present if the sample's refractive index is not matched to the design of the objective lens, broadening the diffractive blur deeper into the sample. Both the illuminating and fluorescing light can scatter off refractive index heterogeneities in the sample due to the particles.

Some of these complications can be eliminated by careful sample preparation. In practice, we eliminate photobleaching by using an excessive amount of dye in our samples and illuminating with a weak laser light. We eliminate scattering by matching the refractive index of the particles to the suspending fluid – it is fairly easy to match the refractive indices to a few parts in 10^3. Since the scattering is quadratic in the index mismatch, the effect of turbidity due to multiple-scattering is very weak in our samples. However, the rest of these complications must be accurately described by the generative model.

Based on this physical setup, we can describe the confocal images through three main generative model components:

- *Platonic image* $\Pi(\vec{x})$ – the physical shape of the dye distribution in the

sample (unmodified by perception of light).

- *Illumination field* $I(\vec{x})$ – the light intensity as a function of position, including both laser intensity variation from disorder in the optics and intensity attenuation into the sample.
- *Point spread function* $P(\vec{x};\vec{x}')$ – the image of a point particle due to diffraction of light, including effects from index mismatch and finite pinhole diameter.

plus three minor additional fit model components:

- *Image Background* c, $B(\vec{x})$ – the overall exposure of the image c and the background values corresponding to a blank image without dye, B.
- *Rastering Step Size* z_{scale} – the displacement distance of the lens as it rasters along the optical axis.
- *Sensor noise* σ – the noise due to shot noise from finite light intensity reaching the sensor or electronic noise at the sensor.

These components are combined to form the image through convolution

$$\mathcal{M}(\vec{x}) = B(\vec{x}) + \int \mathrm{d}^3x' \; [I(\vec{x'})(1-\Pi(\vec{x'})) + c\Pi(\vec{x'})]P(\vec{x}-\vec{x}';\vec{x}) \qquad (6.2)$$

which is sampled at discrete pixel locations to give the final image $M_i = \mathcal{M}(\vec{x}_i)$.

Here, we describe each part of our model in detail along with our explanations and motivations behind any simplifications. In subsequent sections we will also discuss other aspects of image formation which may result in other model choices and why we omit them from the final form of the model.

6.3.1 Platonic image

The Platonic image must accurately represent the continuous distribution of fluorescent dye in the sample on the finite, pixelated image domain. The colloidal sample consists of a collection of spherical particles embedded in the solvent, with either only the particles or only the solvent dyed. Our Platonic image should then consist of the union of images of individual spherical particles, with their corresponding radii and positions. Thus, if we have a method to accurately represent one colloidal sphere, we can easily construct the Platonic image in our generative model.

A naïve way to generate the Platonic image of one sphere would be simply to sample the dye distributions at the different pixel locations, with each pixel being either 0 (if it is outside the sphere) or 1 (if it is inside the sphere) with no aliasing. This method will not work, since a pixel value in the Platonic image can only change when a sphere's position or radii has shifted by one pixel. This method of Platonic image formation would produce a generative model that does not adequately distinguish between particle locations separated by less than 1 pixel or 100 nm! Simply multiplying the resolution and corresponding coarse-graining of the boolean cut by a factor of N in each dimension increases the resolution of this method to $1/N$ pixels. However, calculating these high resolution platonic spheres is computationally expensive, requiring 10^9 operations to draw spheres capable of determining positions within 0.01 px.

To find the correct representation of a Platonic sphere, we examine the mechanism of image formation in Eq. 6.2. The final image results from a convolution of the Platonic image with the point-spread function $P(\vec{x} - \vec{x'}; \vec{x})$. Thus, we need a representation of a sphere that will produce the correct image after being convolved

with the point-spread function. To do this, we recall that a convolution is a multiplication in Fourier space. However, creating the image of the sphere in Fourier space is problematic since there will be undesirable ringing in the Platonic image due to the truncation from the finite number of pixels (*i.e.* Gibbs phenomenon). Moreover, each update of one particle requires updating all the pixels in the image, which is exceedingly slow for large images.

Instead, we look for a functional form in real space that approximates the numerically-exact truncated Fourier series, where the truncation arises due to a finite number of pixels. For a sphere with radius a at position $\vec{p}$, this truncated Fourier series is given by$\tilde{\Pi}(\vec{q};\vec{p},a) = 4\pi a^3(j_1(q)/q)e^{i\vec{q}\cdot\vec{p}}$, where $\vec{q}$ is sampled only at frequencies in the image. We can view the truncation operation as a multiplication in Fourier space by a boxcar $\mathrm{H}(1-|q_x|)\mathrm{H}(1-|q_y|)\mathrm{H}(1-|q_z|)$, where $\vec{q}$ is the variable inverse to position, measured in px^{-1}. By the convolution theorem, this truncation corresponds to a convolution in real space with $\mathrm{sinc}(x)\,\mathrm{sinc}(y)\,\mathrm{sinc}(z)$, using the inverse Fourier transform of the boxcar as the sinc function. Thus, the numerically exact image of a sphere would be the analytical convolution of $\mathrm{sinc}(x)\,\mathrm{sinc}(y)\,\mathrm{sinc}(z)$ with a sphere of radius a at position p, represented on a discrete grid. However, the convolution with the sinc function is analytically intractable. To circumvent this, we approximate the sinc function by a Gaussian. This gives a representation of the correctly-aliased Platonic image $\Pi(x;\vec{a})$ of a sphere of radius a as

$$\Pi(\vec{x}) = \mathcal{S}(\vec{x}) * \left[\left(2\pi\sigma_x^2\sigma_y^2\sigma_z^2\right)^{-1/2} e^{-x^2/2\sigma_x^2} e^{-y^2/2\sigma_y^2} e^{-z^2/2\sigma_z^2}\right] \tag{6.3}$$

where $\mathcal{S}(\vec{x};\vec{p},a) = H(|\vec{x}-\vec{p}|-a)$ where $H(x)$ is the Heaviside step function, which is either 0 or 1 depending on whether $|\vec{x}-\vec{p}| > a$ or $< a$, and $*$ denotes convolution. The Gaussian widths σ should be approximately 1 px; however, if the ratio of the z pixel size to the xy pixel size $z_{\mathrm{scale}} \neq 1$, then σ_z will not be the same as σ_x and

σ_y.

While Eq. 6.3 does not generally admit a simple solution, there is a closed-form functional form for the symmetric case $\sigma_x = \sigma_y = \sigma_z$. In the symmetric case ($z_{\text{scale}} = 1$) Eq. 6.3 takes the form

$$\Pi(\vec{x}) = \frac{1}{2}\left[\text{erf}\left(\frac{a-r}{\sigma\sqrt{2}}\right) + \text{erf}\left(\frac{a+r}{\sigma\sqrt{2}}\right)\right] - \frac{1}{\sqrt{2\pi}}\frac{\sigma}{r}\left[e^{-(r-a)^2/2\sigma^2} - e^{-(r+a)^2/2\sigma^2}\right] \tag{6.4}$$

where r is the distance from the particle's center. The first bracketed group of terms corresponds to treating the sphere as a flat surface, and the second bracketed group corresponds to the effects the sphere's curvature on the integral. In each sub-grouping, the first term that depends on $r - a$ reflects the contribution due to the particle's nearer edge, and the second term that depends on $r + a$ reflects the contribution due to the particle's farther edge. We then fit σ in Eq. 6.4 to best match the exact Fourier space image of a sphere, giving a value $\sigma \approx 0.276$.

Although Eq. 6.3 does not admit a simple solution for $z_{\text{scale}} \neq 1$, we can use the exact form for $z_{\text{scale}} = 1$ to construct an approximate solution. Since both $\text{erf}(x)$ and e^{-x^2} approach their asymptotic values extremely rapidly, and since at the best fit $\sigma \approx 0.276$ $(a + r)/\sigma \gg 1$ for even moderately small radii, the terms $\text{erf}((a + r)/\sigma\sqrt{2}) \approx 0.5$ and $\exp(-(r+a)^2/2\sigma^2) \approx 0$ to an excellent accuracy. We then write the position vector in terms of its direction $\hat{x}$ and a vector $\vec{\delta x}$ as $\vec{x} \equiv a\hat{x} + \vec{\delta x}$, and replace $(a-r)/\sigma$ in Equation (6.4) by $\sqrt{(\delta x/\sigma_x)^2 + (\delta y/\sigma_y)^2 + (\delta z/\sigma_z)^2}$. Note that this approximation is exact in the limit of infinite sphere radii. Empirically, we find that this approximation works quite well, giving differences in the Platonic image of a few percent from a numerical solution to Eq. 6.3 as well as high resolution boolean cut real-space spheres (see Fig. 6.1).

While this implementation of the Platonic image correctly captures most of

the effects of finite-pixel size, there are still some minor details that need to be fixed to give unbiased images. By construction, Eq. (6.4) conserves volume – its integral over all space is $4/3\pi a^3$ since the Gaussian kernel is normalized. However, when $\Pi(\vec{x})$ is sampled on a pixelated grid, its sum is not exactly $4/3\pi a^3$ but is slightly different, depending on the position of the particle's center relative to a voxel's center. The slight change in volume is important for two reasons. First, the convolution with the PSF in our image generation (see next subsection) suppresses high-frequency portions of the image, but it does not affect the $\vec{q} = \vec{0}$ component, *i.e.* the image sum or the particle volume. Since we aim to create a Platonic image that accurately represents the final image, we need the $\vec{q} = \vec{0}$ component of the Platonic image to be correct. Secondly, as discussed in section 6.4 the real microscope image is actually an integral over a finite pixel area. As such, the image recorded on the detector preserves the particle's volume or the $\vec{q} = \vec{0}$ component of the image. To circumvent this issue of incorrect particle volume, instead of drawing the particle at its actual radius we draw it with a slightly different radius that preserves the particle's volume, which we accomplish with an iterative scheme. The results of this iterative scheme are shown in Fig. 6.1 along with the errors it introduces. Incidentally, the effects of image pixelation on image moments higher than $\langle 1 \rangle$, *e.g.* $\langle \vec{x} \rangle$ and its effects on the particle positions, are much smaller than the noise floor in our data at a moderate SNR (see section 6.4).

The representation in equation 6.4 is the best method for forming Platonic spheres on a pixelated grid that we have found. However, there are other, simpler methods which work almost as well as the Platonic sphere. Aside from the important curvature term, equation 6.4 is basically an erf() interpolation between particle and void at the particle's edge. Other interpolation schemes can provide similar results. For instance, the spheres could be constructed by ignoring the

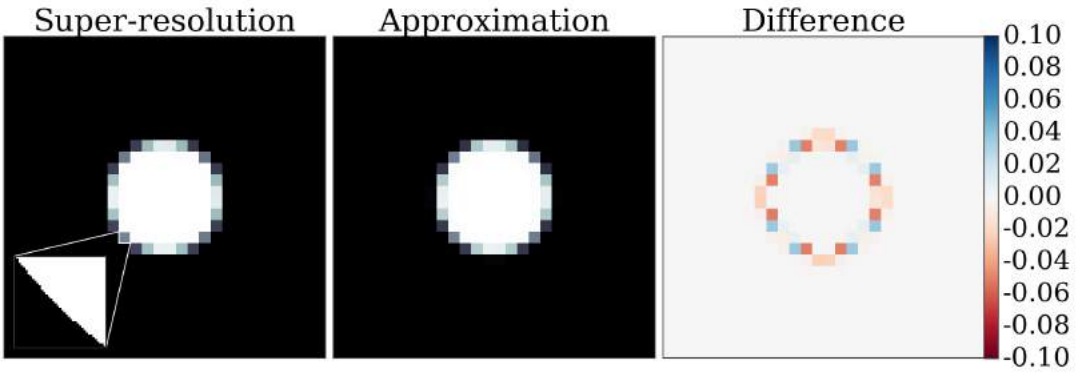

Figure 6.1: **Platonic sphere generation**. A comparison of our approximate platonic sphere generation method to a sphere created by performing a boolean cut $\Pi(\vec{x}) = \int_{\text{pixel}} \mathrm{d}\vec{x}' H(|\vec{x}-\vec{x}'-\vec{p}|-a)$ on a lattice $100\times$ higher in resolution in each dimension compared to the final image. On the left we show the super resolution sphere with fractional volume error $\delta V/V = 10^{-6}$ and an inset displaying the jagged edges caused by discrete jumps in distance. This is in contrast to the iterative approximate platonic sphere with volume error $\delta V/V = 10^{-16}$ drawn at an effective radius with change $\delta a/a = 2\times10^{-4}$. The differences between individual pixels along the center of the sphere (right panel) show a high frequency structure with a maximal relative value 0.08. These high frequency features are dramatically reduced later in the image formation process through the convolution with the point spread function.

curvature term and replacing the erf with a logistic $1/(1+\exp((r-a)/\alpha))$, a linear interpolation between particle and void at the pixel edge, or a cubic interpolation at the pixel edge. We have also implemented these methods for generating Platonic images of spheres, fitting the parameters to match the exact Fourier representation. For the logistic we fit α, for the linear interpolation we fit the slope, and for the cubic we fit one parameter and constrain the other two such that the Platonic image and its derivative are continuous. While all of these methods are functional, they are not significantly faster than the exact Gaussian approximation in equation 6.4 and result in slightly worse featuring errors (see table 6.1). As a result, we use the exact Gaussian approximation, but include these other options in our package for ease of use with more complicated shapes where the integral in equation 6.3 might not be analytically tractable.

The Platonic image needs to represent accurately all objects in the image, not just the spheres. In particular, when the solvent is dyed, the image usually contains a dark coverslip or its shadow from the point-spread function. We model this dark coverslip as a slab occupying a half-space. The slab is characterized by a z-position and by a unit normal $\hat{n}$ denoting the perpendicular to the plane. To capture accurately sub-pixel displacements of the slab, we use the image of a slab convolved with a Gaussian as above for a sphere; for the slab this gives a simple error (erf) function.

6.3.2 Illumination field

In order to illuminate the sample, confocal microscopes scan a laser over the field of view using several distinct patterns including point, line, and disc scanning. This illumination laser travels through the optics train and interacts with fluorescent dye in the suspension causing it to emit light in a second wavelength which is then detected. The intensity of this illumination pattern depends on the aberrations in the optics as well as dirt in the optical train which creates systematic fluctuations in illumination across the field of view. Accounting for these variations is important as they can account for most of the intensity variation in an image. In the case of our line scanning confocal microscope, these patterns manifest themselves as stripe patterns perpendicular to the scan direction, as the line-scan drags dirt across the field of view, overlaid on aberrations and optical misalignments which cause the corners of the image to dim.

Confocal microscopes image by rastering in z, illuminating each xy plane separately. Ideally, the microscope illuminates each plane identically. In practice, aberrations due to refractive index mismatches cause a dimming of the illumina-

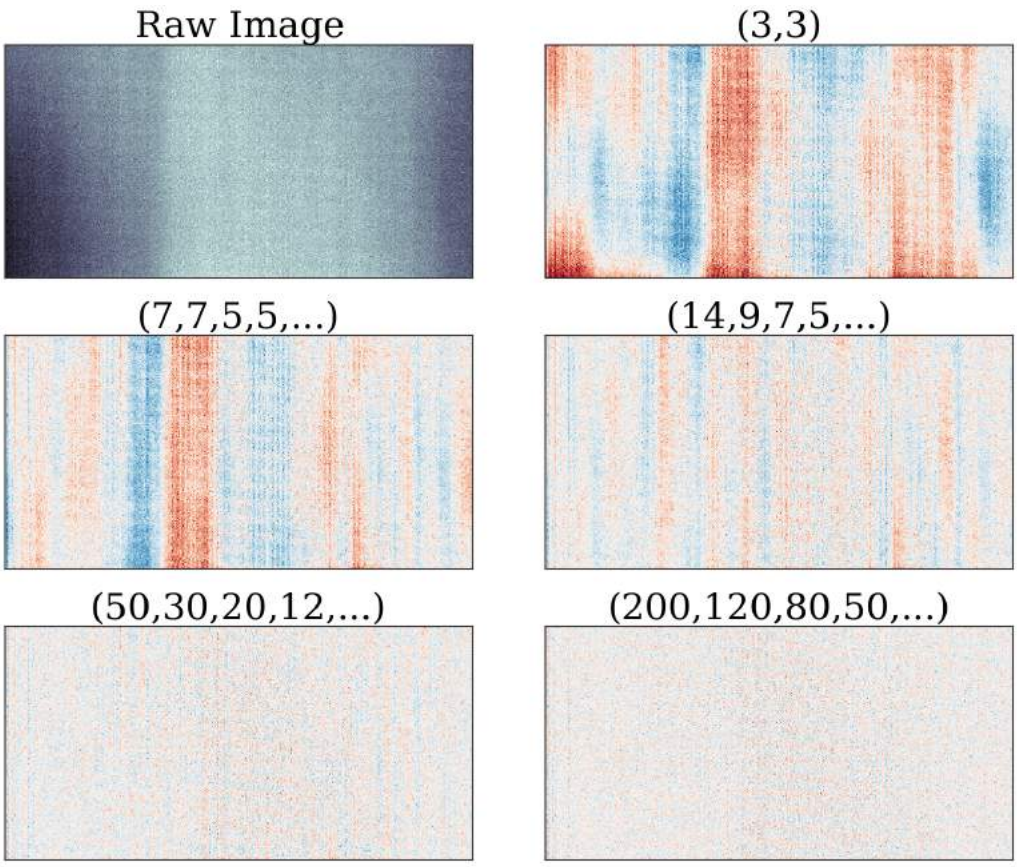

Figure 6.2: **Illumination field residuals**. A blank confocal image and its fit to the Barnes ILM in equation 6.7 over varying number of coefficients. Fitting the illumination with a low-order ILM of $(3, 3)$ Barnes points removes the large fluctuations over the image but clearly shows stripes in the image. The notation $(n_0, n_1, n_2, ...)$ corresponds to a Barnes ILM with n_0 coefficients in the expansion for $P_0(y)$, n_1 coefficients for $P_1(y)$, etc. Increasing the number of points to $(7, 7, 5, 5, 5)$ or $(14, 9, 7, 5, 5, 5)$ removes the overall modulation in y but leaves clear stripes in the image. Only at high orders of $(50, 30, 20, 12, 12, 12, 12)$ or $(200, 120, 80, 50, 30, 30, 30, 30, 30, 30, 30)$ do these stripes disappear. The residuals shown in the figure are all at the same scale and are averaged over the image z for clarity.

tion with depth into the sample [63]. Since this overall dimming only depends on the depth z from the interface and not on the xy position in the sample, it is natural to describe the illumination field as a product of an xy illumination and a z modulation:

$$I(\vec{x}) = I_{xy}(x, y) \times I_z(z) \quad . \tag{6.5}$$

Empirically we find that illumination fields of this form can accurately describe our real confocal images, without incorporating any coupling between xy and z.

We describe each of the separate functions I_{xy} and I_z by a series of basis functions. Since the modulation in z is fairly smooth [63], we describe $I_z(z)$ by a polynomial $P_z(z)$ of moderate order $\approx$ 7-11 for 50-70 z-slices; typically we use a Legendre polynomial as the orthogonality accelerates the fitting process. The in-plane illumination of a confocal is determined by its method of creating images. Our confocal is a line-scanning confocal microscope, which operates by imaging a line illumination parallel to the x axis and simultaneously collecting the line's fluorescent image. This line is then scanned across the image in y. As a result of this scanning, any dirt in the optics is dragged across the field of view, creating the illumination with stripes along the x-direction visible in figure 6.2. To model these stripes, we treat the variation along x and y differently. We write the xy illumination field as

$$I_{xy}(x,y) = \sum_k B(x;\vec{c}_k) \times P_k(y) \quad , \tag{6.6}$$

where $B_k(x;\vec{c}_k)$ is a Barnes interpolant in x and $P_k(y)$ a Legendre polynomial in y. Barnes interpolation is a method of interpolating between unstructured data using a given weight kernel [10], similar to inverse distance weighting, using a truncated Gaussian kernel to allow for strictly local updates to the high frequency illumination structure. We use an interpolant with equally spaced anchor points in x throughout the (padded, see section 6.3.3) image. The k^{th} Barnes interpolant has a large number of free parameters, described by the vector $\vec{c}_k$; the size of $\vec{c}_k$ is equal to the number of anchoring points in the Barnes. To account for the fine stripes in the image, we use a large number of points for the Barnes associated with low-order polynomials, and decrease the number of points for higher-order polynomials. For a typical image of size $(z,y,x) = (50,256,512)$

pixels, we use coefficient vectors of length $(\vec{c}_0, \vec{c}_1, \vec{c}_2, \vec{c}_3, \vec{c}_4, \vec{c}_5, \vec{c}_6, \vec{c}_7, \vec{c}_8, \vec{c}_9, \vec{c}_{10}) \approx (200, 120, 80, 50, 30, 30, 30, 30, 30, 30, 30)$. While this is a large number of coefficients, there are orders of magnitude fewer coefficients than pixels in the image. As a result, all of the ILM parameters are highly constrained (on the order of a few parts in 10^5, varying wildly with the parameter), and we do not overfit the image.

Putting this all together, we use an ILM given by:

$$\left[\sum_k B_k(x;\vec{c}_k)P_k(y)\right]\left[\sum_j d_j P_j(z)\right] \quad . \tag{6.7}$$

This ILM accurately describes measured confocal illuminations, as determined both from blank images and from images with colloidal particles in them. While the Barnes structure of this ILM is optimized for line-scanning microscopes, it can easily be changed. For ease of use for different microscopes or imaging modalities we have implemented various ILMs consisting of simple Legendre polynomial series, as functions $P_{xy}(x,y) \times P_z(z)$, $P_{xy}(x,y) + P_z(z)$, and as $P_{xyz}(x,y,z)$. Other illumination structures – such as a radially or azimuthally striped ILM for spinning-disk confocals – could also easily be incorporated into PERI's framework.

How well do these functional forms fit to experimental data for a line-scanning confocal microscope? We acquire blank images of a water-glycerol mixture as a function of depth and fit this data with Barnes illuminations of the form 6.7. As a function of the number of Barnes points in x and the polynomial degree in y, we look at the magnitude and patterns of the residuals. In Fig. 6.2, we see large scale structure in the ILM residuals, suggesting that high-order polynomials and Barnes interpolants with a large number of points are necessary. Fitting out the low-order background reveals the find stripes in x emerge due to the line-scan nature of our machine. Finally, at higher orders of interpolants and polynomials we are able to

adequately capture all illumination variation independent of depth into the sample.

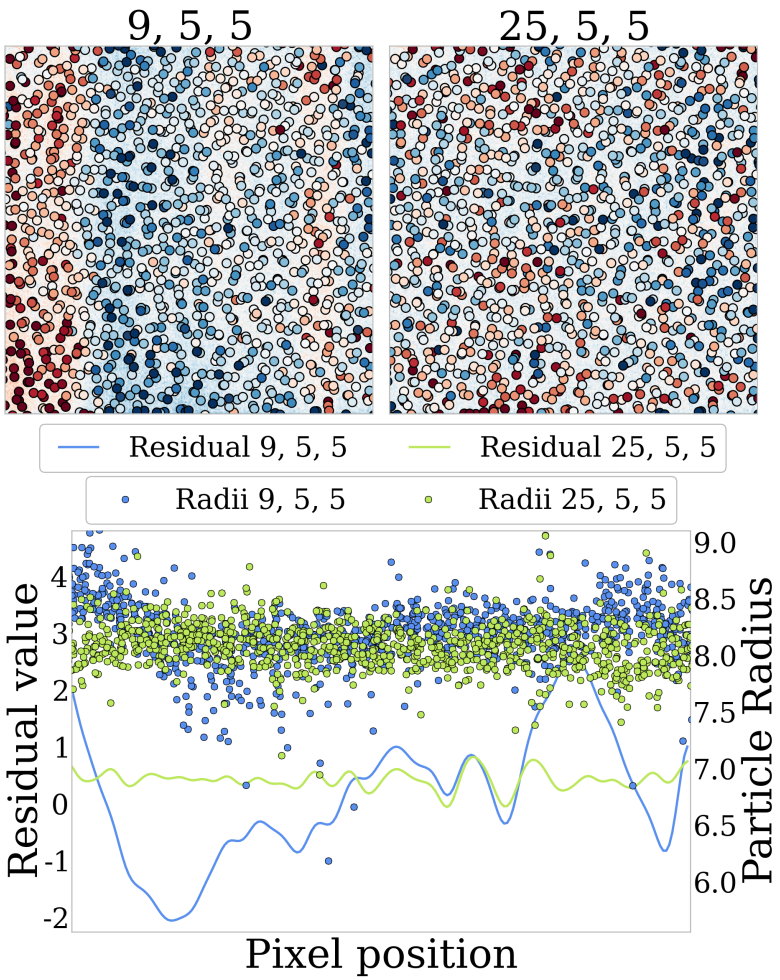

Figure 6.3: **ILM generated biases**. Using an incorrect illumination field results in significant biases. The upper left panel shows an image featured with a $(9, 5, 5)$ order polynomial in (x, y, z). In the foreground are the featured particle radii, color-coded according to their difference from the mean. In the background is the residuals of the featured image. Clear stripes are visible in both the featured radii and the residuals. The particles are systematically much larger on the left side of the image, before decreasing in size in the middle and increasing again in a small stripe on the image's right side. In contrast, when the image is featured with a higher-order $(25, 5, 5)$ degree polynomial, shown in the upper right, these systematic residuals disappear. The bottom panel shows the particle radii and image residuals for the two illumination fields as a function of the image x direction.

Fitting the ILM correctly is essential for finding the correct particle positions and radii. Fig. 6.3 demonstrates the effect of featuring a real confocal image with

an illumination field of insufficient order. In the left panel is an image featured with a high-degree polynomial illumination of 9^{th} order in the x-direction and of 5^{th} order in the y- and z- directions. While these polynomials are high-order, they are not high enough to capture all of the structure in the light illumination. There is a clear bias in the featured radii, with particle radii being systematically larger on the edge of the image and smaller in the middle. These biases arise from large stripes in the confocal illumination due to the line-scanning nature of our confocal. Using a higher-order 25^{th} degree polynomial in the x-direction (upper right panel) eliminates the effect of these stripes, as visible in the featured particle radii plotted as a function of x in the bottom panel. Note that the particle radii may be biased by as much as 1 px or 100 nm due to effects of the spatially varying illumination field.

6.3.3 Point spread function

Due to diffraction, the illuminating laser light focused from the microscope's lens and the detected fluorescent light collected from the sample are not focused to a single point. Instead, the light is focused to finite-sized diffraction-limited blur. To reconstruct an image correctly we need to account for the effects of diffraction in image formation.

A confocal microscope first illuminates the sample with light focused through the microscope lens. The lens then collects the light emitted from fluorophores distributed in the sample. As a result, the final image of a point source on the detector results from two separate terms: an illumination point-spread function P_{ilm} that describes the focusing of the incoming laser light, and a detection point spread function P_{det} that describes the focused fluorescent light collected from the

emitted fluorophores. Since a fluorophore is only imaged if it is both excited by the laser illumination and detected by the camera, the resulting point-spread function for a confocal with an infinitesimal pinhole is the product of the illumination and detection point-spread functions: $P(\vec{x}) = P_{\text{ilm}}(\vec{x})P_{\text{det}}(\vec{x})$. For a confocal with a finite-sized pinhole, this product becomes an convolution over the pinhole area. The two separate point-spread functions (PSFs) P_{ilm} and P_{det} can be calculated from solutions to Maxwell's equations in the lens train [63, 155, 158, 103]. The PSFs can be written as integrals over wavefronts of the propagating light.

An additional complication arises from the presence of an optical interface. Most microscope lenses are essentially "perfect" lenses, creating a perfect focus in the geometric optics limit. However, refraction through the optical interface destroys this perfect focus and creates an image with spherical aberration. In addition, the refracted rays shift the point of least confusion of the lens from its original geometric focus. For a confocal geometry, this spherical aberration and focal shift depend on the distance of the nominal focal point from the optical interface z_{int}.

All of these effects have been calculated in detail by many previous researchers [63, 155, 158, 103]. The PSFs depend on several parameters: the wave vectors of the incoming and outgoing light k_{in} and k_{out}, the ratio of the indices of refraction $n_{\text{sample}}/n_{\text{lens}}$ of the sample and the optical train design, the numerical aperture of the lens or its acceptance angle α, and the distance focused into the sample z_{int}. For completeness, we repeat the key results here. In polar coordinates, the illumination PSF $P_{\text{ilm}}(\rho, \phi, z)$ for illuminating light with wave vector k_{in} traveling

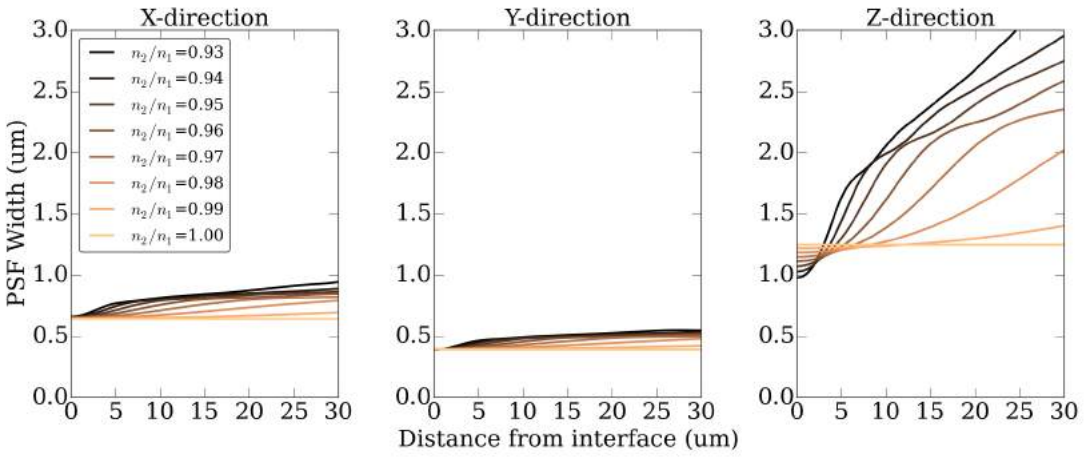

Figure 6.4: **PSF widths vs depth**. The x (left panel), y (center panel), and z (right panel) widths of the PSF as a function of distance from the interface, for various refractive index mismatches. The width of the point-spread function generally increases with depth and with index mismatch due to increased spherical aberrations. The width is broadest in the z (axial) direction, and is narrower in the y direction than along the x direction of the line illumination.

through a lens focused to a depth z_{int} from the interface is [63]

$$P_{\text{ilm}}(\vec{x}) = |K_1|^2 + |K_2|^2 + \frac{1}{2}|K_3|^2 + \cos 2\phi \left[K_1 K_2^* + K_2 K_1^* + \frac{1}{2}|K_3|^2\right] \quad \text{, where}$$

$$\begin{pmatrix} K_1 \\ K_2 \\ K_3 \end{pmatrix} = \int_0^\alpha \sqrt{\cos\theta'} \sin\theta' e^{-ik_{\text{in}} f(z,\theta')} \begin{pmatrix} \frac{1}{2}(\tau_s(\theta') + \tau_p(\theta')\cos\theta_2) J_0(k_{\text{in}}\rho\sin\theta') \\ \frac{1}{2}(\tau_s(\theta') - \tau_p(\theta')\cos\theta_2) J_2(k_{\text{in}}\rho\sin\theta') \\ J_1(k_{\text{in}}\rho\sin\theta')\tau_p(\theta')\frac{n_1}{n_2}\sin\theta' \end{pmatrix} d\theta'$$

$$f(\theta) = z_{\text{int}}\cos\theta - \frac{n_2}{n_1}(z_{\text{int}} - z)\sqrt{1 - \left(\frac{n_1}{n_2}\right)^2 \sin^2\theta} \tag{6.8}$$

Here $\tau_s(\theta')$ and $\tau_p(\theta)$ are the Fresnel reflectivity coefficients for s and p polarized light, J_n is the Bessel function of order n, and θ_2 is the angle of the refracted ray entering at an angle θ' ($n_2 \sin\theta_2 = n_1 \sin\theta'$). To derive this equation from equation (12) in Ref. [64], we used the additional assumption that all distance scales in the image (including z_{int}) are small compared to the focal length of the lens. The corresponding detection PSF P_{det} is identical to P_{ilm} except for the removal

of the $\sqrt{\cos\theta}$ and the replacement of k_{in} by the wave vector of the fluorescent light k_{out}. For an infinitesimal pinhole, the complete PSF is the product of these two point spread functions:

$$P(\vec{x}; z_{\text{int}}) = P_{\text{ilm}}(\vec{x}; z_{\text{int}}) P_{\text{det}}(\vec{x}; z_{\text{int}}) \quad . \tag{6.9}$$

The expressions in equations 6.8-6.9 are for a perfect pinhole confocal, whereas our confocal is a line-scanning confocal. While there have been several works describing line-scanning confocals [156, 40], these authors have treated where the line is focused onto the sample by a cylindrical lens. In our confocal, however, an image of a line is focused onto the sample through the large-aperture objective lens. As such, the illumination PSF in equation 6.9 is replaced by the integral of the detection PSF over a line in the x direction.

We use this model for a line-scanning point spread function with aberrations as our model for our exact PSF, fitting the paramters that enter into equations 6.8-6.9. These parameters are the acceptance angle α of the objective lens, the wavelength of the laser, the ratio of energies of the fluorescent light to the excitation light, the index mismatch n_1/n_2 of the sample to the optics, the position of the optical interface z_{int}, and the amount that the lens is moved as the scan is rastered in z. In principle, other details could be included – polychromaticity and distribution of the fluorescent light, finite pinhole width of the illuminating line, etc. – but we find that these parameters are both relatively unconstrained by the fit and have little impact on the other reconstructed parameters, such as particle positions and radii.

In addition, for initial featuring we occasionally use a Gaussian approximation to the PSF. Based on calculations of the exact PSF, $\approx 90\%$ of the function can be described by a Gaussian [158]. We verified this for PSFs calculated from Eq. 6.8,

and found that although the presence of aberrations from the interface worsens the Gaussian approximation, generally a Gaussian accounts for $\approx 90\%$ of the PSF except for in the most aberrated cases (large index mismatch imaging deep into the sample). Our simplest approximation of the PSF is as an anisotropic Gaussian with different widths in x, y, and z, with the widths changing with distance from the interface. We therefore parameterize the Gaussian widths as a function of depth,

$$P(\vec{x}; z) = \prod_i \frac{e^{-x_i^2/2\sigma_i^2(z)}}{\sqrt{2\pi}\sigma_i(z)} \tag{6.10}$$

where each width $\sigma_i(z)$ is described by a polynomial in z, typically a second order Legendre polynomial.

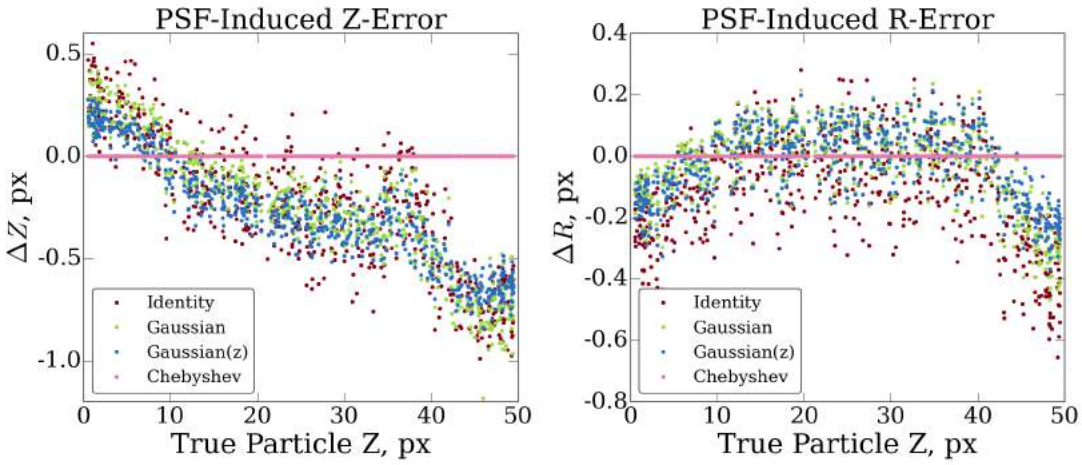

Figure 6.5: **PSF generated biases**. Using an incorrect point-spread function results in significant biases, as PSF leakage affects neighboring particle fits. Moreover, since the PSF gets significantly broader with depth, using a spatially constant PSF, there are systematic biases with depth in both the z positions (left panel) and a characteristic drift in the fitted radii errors with depth (right panel), as shown for the delta-function (identity), an (x, y, z) anisotropic Gaussian, and a depth-varying Gaussian point-spread function. In contrast, using the correct Chebyshev PSF eliminates the errors in both the radii and z positions.

Figure 6.5 shows the effects of ignoring these details about the point-spread function on the extracted positions. We generate confocal images using a simu-

lated, exact PSF with random distribution of particles up to a depth of 30 μm. Featuring this data using a 3D anisotropic Gaussian, we find a strong depth-dependent bias in the featured z position and radii measurements. Using a low order z-dependent Gaussian PSF decreases this bias only slightly. Interestingly however, ignoring the effects of diffraction completely and replacing the PSF with a Dirac delta-function does not cause significantly worse results than treating the PSF as a spatially-varying Gaussian. As shown by figure 6.5, an exact PSF is required to locate particle's positions and radii to within 20 nm (0.2 px). Therefore, we employ the full line-scan PSF calculation into our model.

The point-spread function defined in equations 6.8-6.9 decays extremely slowly with z and somewhat slowly in ρ. To accurately capture these long-tails of the PSF in our generative model, we calculate the PSF on a very large grid for convolutions, corresponding to $\approx 40 \times 25 \times 30$ px or $\approx 6 \times 3 \times 4$ μm in extent, which is considerably larger than the size of the 5 px radii particles. The long tails of the PSF bring information about structure far outside the image into the image region. As such, our generative model is defined not only in regions corresponding to the interior microscope image but also in an exterior padded region, which is cropped out when comparing to the model. For completeness, we still define the ILM and Platonic image (including exterior particles) in the exterior padded region; however parameters confined to this exterior region of the image are relatively unconstrained. We make up for this loss in speed due to the increased size by doing an extremely accurate but approximate convolution based on Chebyshev interpolation, as described in a future paper.

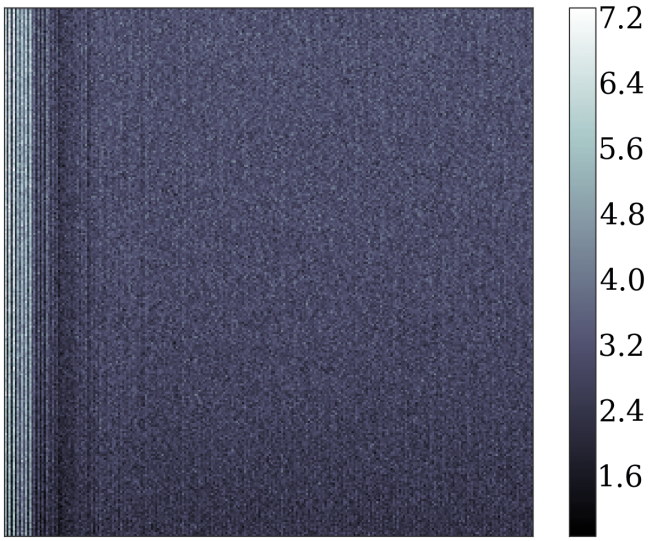

Figure 6.6: **Experimental background image**. The measured background from our line-scan confocal microscope captured by adjusting the exposure to a full brightness image, removing the sample, and capturing a set of images with no illumination including room lights. Note that the range of values is from 1 to 7 out of a maximum 255 given by the 8-bit resolution of the CCD. While only a variation of 3%, we have seen in the illumination field section that this can create a bias that significantly alters our inference as a function of the position in the field of view. To remove this bias we fit the background field to a low order polynomial and add it to our model image.

6.3.4 Background

Due to background, the detector CCD pixels always read a non-zero value even when there is no light incident on them. We incorporate this into our generative model by fitting a nonzero background level to the images. Ideally, this background would be constant at every pixel location. Empirically, however, we find from blank images that this background varies with pixel location in the detector (see Fig.6.6). For our confocal microscope, we find the background is slowly-varying in the optical plane, perhaps due to different dwell times for different regions of the line scan and different sensitivies of different pixels; the background does not vary in z. As a result, the background is well-modeled by a low-order polynomial in x

and y.

However, due to the long-tails of the PSF, the coverslip slab affects the image in a much larger z region than that of a typical particle. Rather than dealing with this by using an even larger point-spread function, we use the calculated point spread function to capture the effects of the PSF's moderate tails on the particles and slab, and fit a polynomial in z to capture the residual slab correction. This residual correction is mathematically the same as a background level in the detector. As a result, while the "true" background in the image is $P(x, y)$, our model uses a background $P(x, y) + P_{slab}(z)$, as the coverslip is usually oriented along the z direction.

6.3.5 Sensor noise

The last feature of the generative model is our understanding of the unrecoverable parts of the image: noise. To study the intrinsic noise spectrum of the confocal microscope, we subtract the long wavelength behavior from the blank image of Fig. 6.2. After removing the background we find that the noise appears white and is well approximated by a Gaussian distribution (see Fig. 6.7). There are, however, some highly localized non-Gaussian parts to the noise spectrum, arising due to the specific nature of our confocal. For instance, at high scan speeds slight intensity fluctuations in the laser's power couple to the dwell time on each stripe of line-scanned pixels. This produces periodic stripes across the image with a wavevector mostly parallel to the scan direction, but with a random noisy phase. How can we handle these sources of correlated noise and do they affect the quality of our reconstruction?

In principle, these correlated noise sources can be represented in the Bayesian model by introducing a full noise covariance matrix. That is, instead of writing that log-likelihood as the product of all pixel values, we can write

$$\log \mathcal{L}(\vec{M} \mid \vec{d}) = -\frac{1}{2}(M_i - d_i)\,\Lambda_{ij}^{-1}\,(M_j - d_j) \tag{6.11}$$

where Λ_{ij}^{-1} is the covariance matrix between each pixel residual in the entire image. In our optimization, we would form a low dimensional representation for this covariance matrix and allow it to vary until we find a maximum. In doing so, we would reconstruct the image and the correlated noise simultaneously. In practice, this introduces a large computational overhead due to the need for a full image convolution during each update as well as many new free parameters that need to be optimized.

Therefore, when desired we address the effect of correlated noise by working in reverse – we identify the several intense Fourier peaks in the confocal noise spectrum and remove them from the raw data before the fitting process. An example of this noise pole removal is given in Fig. 6.7. There, we can see that removing only 5 distinct poles (Fig. 6.7(d)) removes almost all visible correlated noise structure while changing the overall noise magnitude by a negligible amount. This small shift in estimated noise magnitude only affects the estimate of the errors associated with parameters such as positions and radii in a proportional way. Since these errors are very small and do not bias our inferred parameters, we often ignore the confocal's noise poles in our analysis entirely.

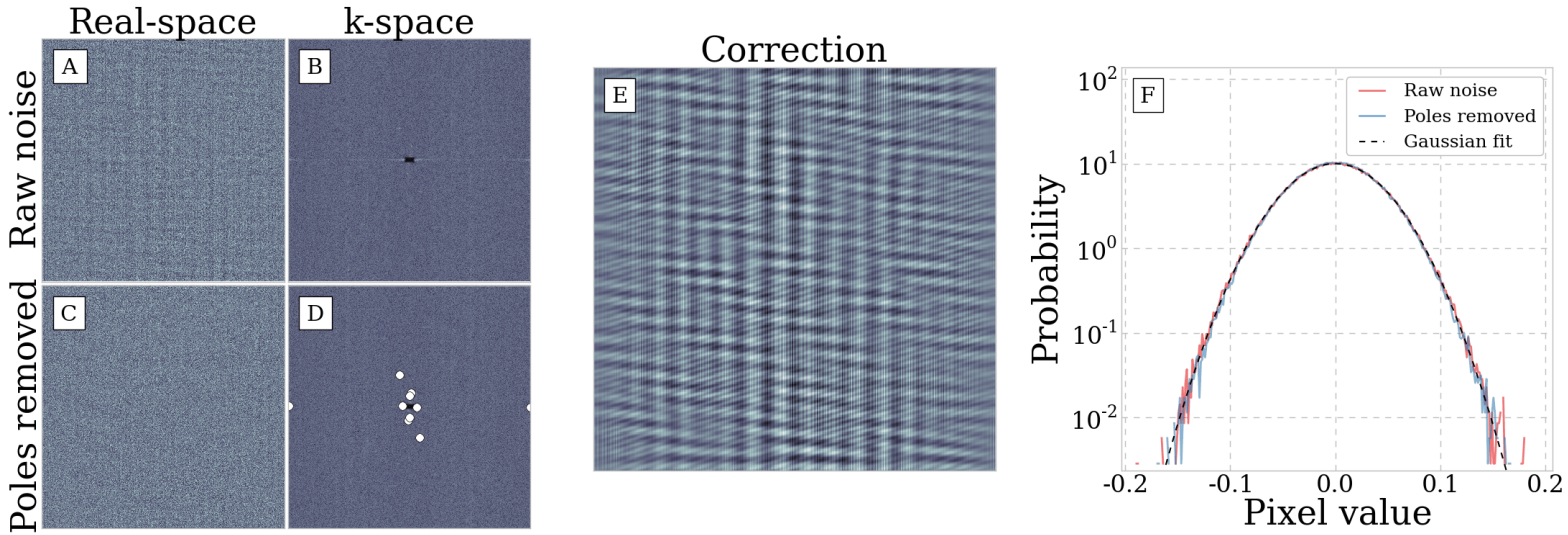

Figure 6.7: **Noise spectrum** (a) Real-space plot of residuals representing the intrinsic noises generated in line-scanning confocal microscopy. This noise spectrum was generated by subtracting the background from a blank sample as in Fig.6.2. Notice that while most of the signal appears to be white noise, there is a systematic modulation along the x coordinate and high frequency features in the y scan direction. (b) Fourier power of the noise spectrum given in (a). The high frequency modulation can now be seen as two small 'poles' in the Fourier power spectrum. Note the dark box in the center of the spectrum is created by subtracting the high order polynomial background from the blank image. In (c) and (d) we present the real and Fourier space noise after removing several discrete peaks in the Fourier intensity that represent correlated noise sources. The removed signal can be seen in (e) showing the stripes created by the scanning nature of the confocal microscope. In (f) we show the histogram of residuals from (a) and (c). In solid red we plot the data and in dashed black lines we plot a Gaussian fit to the residuals with a width $\sigma = 0.0398$, showing that the noise spectrum is well approximated by a Gaussian distribution after taking into account long wavelength background features.

6.4 Model considerations

Here, we investigate several complexities of image formation in confocal microscopes and systematically analyze whether or not it is necessary to include them in our generative model. In particular, we will first analyze how much complexity we must introduce into the model elements listed in the previous section, including the platonic image, illumination field, and point spread function. We will also look at elements of image formation which we have not explicitly included in our model. First, confocal microscopes build a 3D image by rastering in 1, 2, or 3 dimensions (see section 6.3) . There is noise in this rastering procedure that affects the image formation process. Second, The final image that comes from this scan is a cropped view of a much larger sample; the edges of this cropped image are influenced by the excluded exterior particles. Third, while the actual distribution of light intensity is a continuous field, the detector only measures a pixelated representation of this field. Fourth, while the exposure is made by the camera, particles undergo diffusional motion, blurring their apparent location. In this section, we address each of these image formation complexities and their effects on the inferred parameters.

We would like to systematically investigate at what level omitting a detail of the image formation from the model affects the fitted parameters. We can understand this quantitatively by examining the optimization procedure. Let us assume that the true image formation is completely described by a set of N parameters $\vec{\Theta}$. Then, near its maximum, the log-likelihood is approximately quadratic: $\log \mathcal{L} = \frac{1}{2} \sum_{ij} H_{ij} \Theta_i \Theta_j$, where the true value of the parameters is arbitrarily set to $\vec{\Theta} = 0$. Empirically, we find that with the starting parameter values provided by our initial featuring, the log-likelihood is extremely well-approximated by a quadratic.

If our model were complete, then the maximum of $\log \mathcal{L}$ would be exactly at the

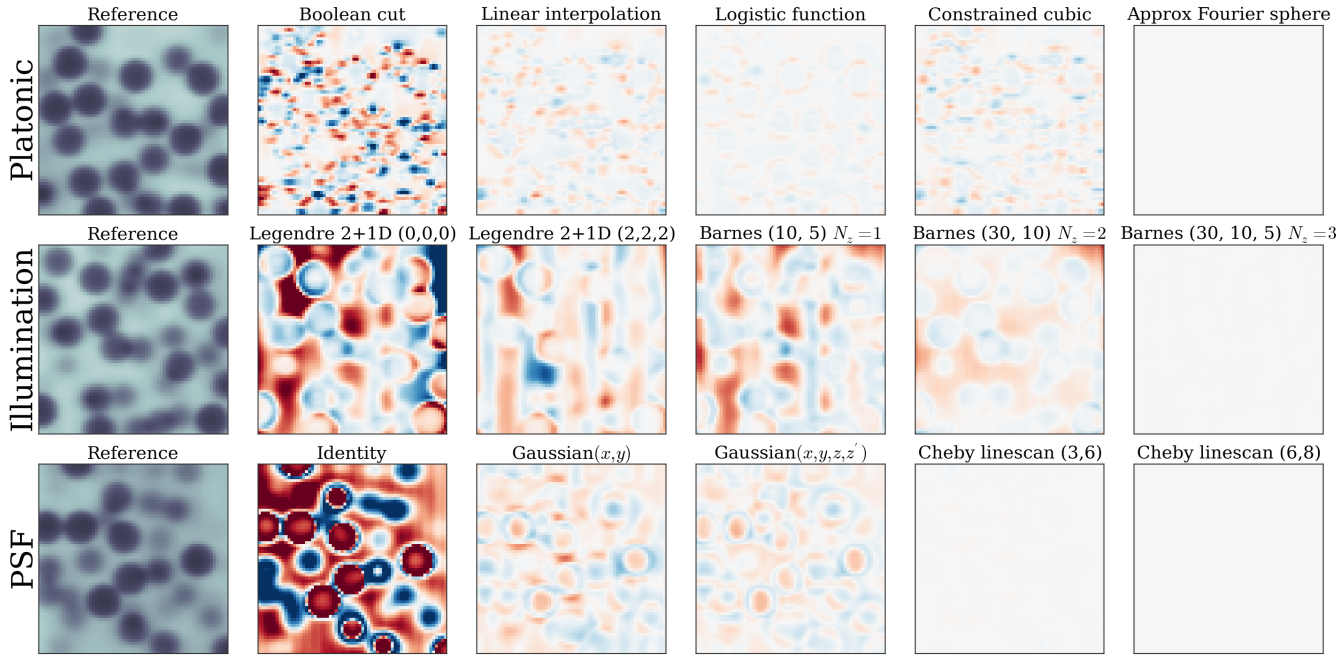

Figure 6.8: **Component complexity residuals**. Here we visually demonstrate the results of choosing between different forms of model components as well as different parameterizations of a single component. We generate simulated microscope images using the model components which we employ when fitting experimental data (left column) and fit them with different choices of platonic image (top row), illumination field (middle row), and point spread function (bottom row). Each choice is labeled above its panel showing the residuals and each row is on a common color scale. In the case of the platonic forms, the boolean cut, linear interpolation, and constrained cubic display higher order multipole errors while the logistic function's first correction is to the monopole (volume) term (as shown by the presence of rings). In the illumination field, stripes are present in the residuals until we use a Barnes interpolant with 30 control points. Past that, the ability to capture intensity as a function of depth is the remaining term which we are able to fit with a single extra Legendre polynomial in the z-direction. Finally, in the case of the PSF, we see hard boundaries transitioning to softer boundaries using a Gaussian PSF in both 3D and 3+1D. The residuals all but disappear when the image is fit with our exact line-scan confocal PSF model (Eq. 6.8) approximated by a Chebyshev polynomial in 3+1D.

true parameter values $\vec{\Theta} = 0$. However, our model is incomplete. This means that, instead of fitting all N parameters $\vec{\Theta}$, we only fit the first (say) M parameters, which for convenience we denote as $\vec{\theta}$. Thus we can write the log-likelihood as three separate terms:

$$\log \mathcal{L} = \frac{1}{2} \sum_{i,j=1}^{M} H_{ij}\theta_i\theta_j + \sum_{i=M+1}^{N} \sum_{j=1}^{M} H_{ij}\Theta_i\theta_j + \frac{1}{2} \sum_{i,j=M+1}^{N} H_{ij}\Theta_i\Theta_j \quad . \tag{6.12}$$

The first term, containing only the parameters $\vec{\theta}$ that we are fitting, is the quadratic in the reduced space, with a maximum at the true parameter values. The unimportant third term reflects the separate contribution to $\log \mathcal{L}$ of the unknown or ignored portions of the model, and is constant in the $\vec{\theta}$ space. However, the second term mixes both the fitted parameters θ and the unknown parameters Θ_j. This mixing results in a linear shift of $\log \mathcal{L}$ in the $\vec{\theta}$ space away from the true parameters, and causes a systematic bias due to an incomplete model. Minimizing $\log \mathcal{L}$ with respect to θ gives the fitted values of the parameters gives an equation for the best-fit incomplete model parameters $\vec{\theta}$:

$$\theta_j = \sum_{k=1}^{M} \bar{H}^{-1}_{jk} \sum_{i=M+1}^{N} H_{ik}\Theta_i \tag{6.13}$$

where $\bar{H}^{-1}$ is the inverse of the sub-block $\bar{H}$ of the Hessian matrix H that corresponds to the fitted parameters $\vec{\theta}$.

We can use equation 6.13 to estimate the effect on one of the estimated parameters θ_j, if we ignore one aspect of the generative model Θ_k. Ignoring the off-diagonal terms in H^{-1} to capture the scaling gives $\theta_j \approx H_{kj}\Theta_k/H_{jj}$. Thus, the error in the fitted parameter θ_j is proportional to both the coupling H_{kj} between that parameter and the ignored aspect of the generative model, and the magnitude of the error of the generative model Θ_k.

6.4.1 Component complexities

There are several choices one can make concerning the form and complexity of each of the components of our model image. As discussed in the Section 6.3, we have implemented many forms of the platonic image, illumination field, and point spread function and each one of these forms has a varying number of parameters with which to fit. How do we decide which form to use and at which complexity (number of parameters) to stop? To decide on a per-image basis, we could employ Occam's factor, which is a measure of the evidence that a model is correct given the data [98]. In practice, however, we are mainly concerned with how these models influence the underlying observables which we are attempting to extract. That is, we wish to use knowledge of the physical system to check which model best predicts the particle locations and sizes. To do so (as mentioned in the main manuscript), we often turn to particle sizes versus time as well as particle overlaps, both physical statements that assert almost no assumptions on our system.

We can also get a sense of the magnitude of the effect these choices have on inferred positions and radii by creating synthetic data and fitting it using a simpler model. In Fig. 6.8 we show the residuals of such fits for various simplifications made to the platonic form, illumination field, and point spread function. In the left columns of the figure we see the reference image formed using the most complex image model available and in each row the residuals for each choice with a description of that choice above the panel. For all but the last column, in which we fit the image with the exact model once again, we can see systematic errors in the fit. We compute how much these residuals influence the extracted positions and radii and report these errors in Table 6.1. In particular, most choices of platonic image aside from the naive boolean cut do not influence particle featuring below

	Fitting model type	Position error (px)	Radius error (px)
Platonic form	Boolean cut	0.03376	0.01577
	Linear interpolation	0.00778	0.00386
	Logistic function	0.00411	0.00352
	Constrained cubic	0.00674	0.00249
	Approx Fourier sphere	0.00000	0.00000
Illumination	Legendre 2+1D (0,0,0)	0.18051	0.13011
	Legendre 2+1D (2,2,2)	0.06653	0.03048
	Barnes (10, 5) $N_z = 1$	0.13056	0.06997
	Barnes (30, 10) $N_z = 2$	0.04256	0.02230
	Barnes (30, 10, 5) $N_z = 3$	0.00074	0.00022
PSF	Identity	0.54427	0.57199
	Gaussian(x, y)	0.47371	0.14463
	Gaussian(x, y, z, z')	0.34448	0.04327
	Cheby linescan (3,6)	0.03081	0.00729
	Cheby linescan (6,8)	0.00000	0.00000

Table 6.1: **Position and radii errors by model complexity.** Here we tabulate the position and radius errors associated with the model component choices made in Fig. 6.8. Note that while the components with the largest impact on determining underlying parameters are the ILM and PSF, the choice of platonic image cannot be ignored in order to reach the theoretical maximum resolution. Interestingly, in the case of PSF selection, Gaussian(x, y, z, z') (3+1D) is almost no better at extracting particle positions than Gaussian(x, y) (2D). However, its ability to extract particle sizes increases by 3 since it takes into account the variation of the PSF in space. Additionally, in the case of the ILM, capturing the stripes in the illumination using a 30 control point Barnes increases the resolution by 3 whereas capturing the illumination's dependence in depth causes the resolution to increase 10 fold.

an SNR of 30. However, the complexity of the illumination field always matters until all long wavelength structure is removed from the image. Finally, the choice of PSF is crucial, requiring the use of a calculated confocal PSF to even approach the CRB.

6.4.2 Scan jitter

Confocal microscopes operate by taking an image with the lens at a fixed z position to create one layer of the three-dimensional image, then moving the lens up a fixed amount to take the next layer. In our generative model, we assume that these steps of the lens (and the resultant image slices) are perfectly equally spaced by an amount which is fitted internally. However, a real confocal microscope will have some error in the vertical positioning of the lens. As a result, the actual image taken will not be sampled at exactly evenly spaced slices in z, but at slices that are slightly shifted by a random amount.

To test the effect of this z-scan jitter on our parameter estimation, we simulate images taken by a confocal microscope with imperfect z-positioning. Instead of sampling the image at a deterministic z position, we instead sampled the image at a z position shifted from the ideal position by an uncorrelated Gaussian amount of varying standard deviation. A representative image of a 5 px radius particle with a step positioning error of 10% is shown in Fig. 6.9(a). There is very little difference between this image with z jitter and the perfectly-sampled image, as shown by the difference image in panel b. We then fit an ensemble of these images at varying image SNR levels, over a random sampling of image noise, z-jitter noise, and random shifts of particle positions by a fraction of a pixel.

The results of these fits are shown in Fig. 6.9c, showing the actual error in the featured positions versus the size of the z-positioning noise. For our confocal which is equipped with a hyper-fine z-positioning piezo, we expect the z positioning error to be a few nm, or a few percent of a pixel. For a 3% error in positioning, the signal-to-noise ratio must be $\approx$ 100 for the effects of z-positioning jitter to be comparable to the theoretical minimum effect from the image noise. This small

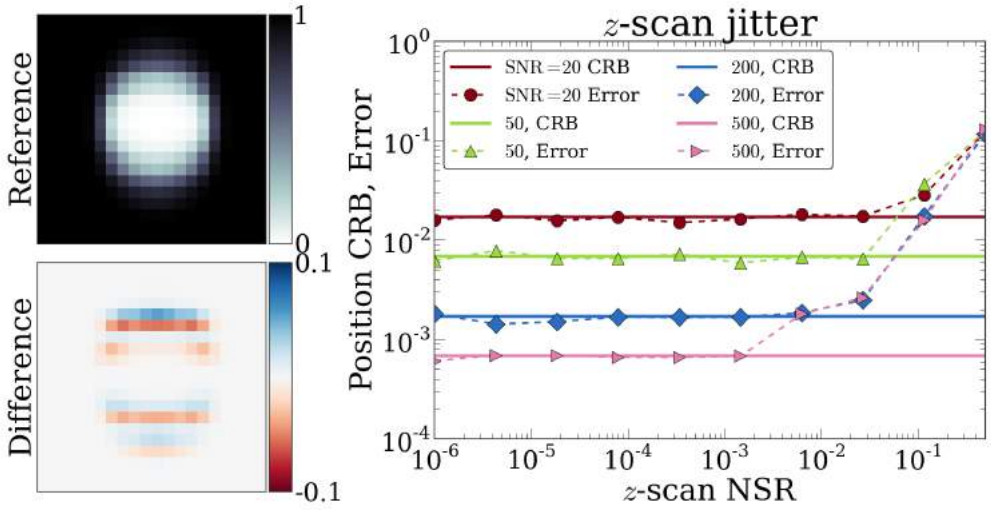

Figure 6.9: **Lens Positioning Jitter** (a) The xz cross-section of a simulated image of a 5 px radius colloidal particle taken with a 10% error in the lens positioning. (b) The difference between the image with positioning error and a reference image with zero positioning error. The differences between the images are both random and small, for this image no more than 7% of the perfect image intensity. (c) The effect of lens positioning error on featured particle positions, at signal-to-noise ratios of 20, 50, 200, and 500. The solid symbols and dashed lines show the position error for images with imperfect lens positioning, while the solid lines denote the Cramer-Rao bound for an image with no positioning error. At lens positioning errors of $\approx 10\%$ or larger, the error in featured positions from the z-slice jitter dominates that from the simple image noise, even for an SNR of 20. However, the featuring error due to a z jitter of $\approx 1\%$ is less than the error due to image noise, for any noise level than can be captured by an 8-bit camera.

effect of the error is partially due to the large size of our particle. If each z slice of the image is randomly displaced with standard deviation σ, then we expect roughly a $\sigma/\sqrt{N}$ scaling for the final error in the particle's z-position, where N is the number of z slices the particle appears in. A 5 px diameter particle with a 4 px axial point-spread function occupies ≈ 18 difference slices, decreasing the effect of scan noise by a factor of ≈ 4 and putting it below the CRB for our data.

As the error in z-positioning increases, however, the effect on the featured particle positions increases correspondingly. The error due to a $\approx 10\%$ z jitter is comparable to the CRB for image noises of $SNR = 20$. For exceptionally large

z-jitters of 40% the error due to the lens positioning dominates all other sources of error. However, even with this large error in lens positioning, the error in featured positions is still only 10% of a pixel, or about 10 nm in physical units.

6.4.3 Missing and Edge particles

The point spread function delocalizes the particle's image over a region larger than the particle's size. As a result, if two particles are close enough together, their images can overlap. This overlapping is a significant problem for heuristics such as centroid fitting, as the true particle centers do not coincide with the fitted centroid. In contrast, PERI's accuracy is negligibly affected by the presence of a second, close particle, since PERI correctly incorporates close particles in its generative model. The CRB of two touching, 5 px diameter particles increases by only $\approx 3\%$, and PERI finds particles to this accuracy when close.

However, large systematic errors can affect PERI when one of these particles is missing in the generative model. This situation is illustrated in its simplest form in Fig. 6.10. If one of the two touching particles is missing from the generative model, then the second particle will be enlarged and drawn into the first particle's void to compensate, as shown in panel b. As a result, the missing second particle will severely bias the fitted positions and radii of the first particle. Figure 6.10c shows the magnitude of this effect. For particles separated by 1 px or less, significant biases on the order of 0.4 px appear in the identified particle's featured position. These biases matter at essentially all values of the SNR, only being comparable to the CRB for SNR < 1. As a result, it is essential for PERI to identify all the particles in the image to return accurate results. For this reason, we take extra precaution and thoroughly search the image for missing particles before fitting, as

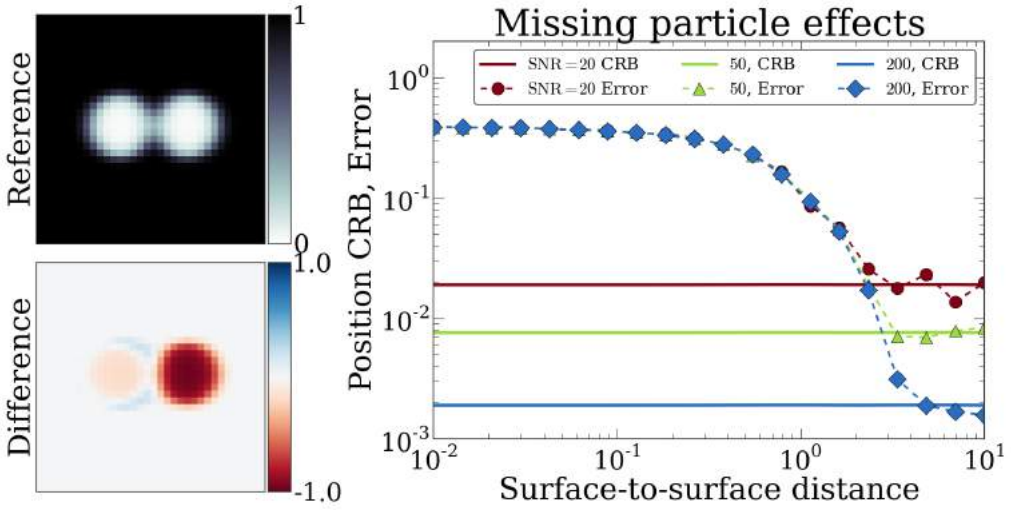

Figure 6.10: **Effect of missing particles**. (a) The xz-cross section of an image of two 5 px radius particles placed in contact. (b) The difference image for a bad generative model that includes only the particle on the left. To minimize the effect of the missing right particle, the left particle is drawn to the right and expanded in radius. This effect is visible as the red and blue ring on the right border of the left particle. (c) The error in position along the separation axis, as a function of true surface-to-surface distance, for a model with a missing particle. When the particles are separated by ≈ 10 px the featured particle is located correctly. However, as the particles get closer than ≈ 2 px significant biases start to appear. These biases saturate at a separation of ≈ 0.1 px, corresponding to a featuring error of ≈ 0.4 px.

detailed in section 6.5.

The biases caused by missing particles appear whether or not the missing particle is located inside or outside the image. As a result, accurately locating edge particles requires identifying all their nearby particles, even ones that are outside the image! We attempt to solve this problem by padding the Platonic and model images and the ILM by a significant portion, and including this padded extra-image region in both the add/remove and relaxation portions of the PERI algorithm. Nevertheless, it is extremely difficult to locate all the particles outside the image, for obvious reasons. As such, there is the possibility for moderate systematic errors to enter for particles located at or near the edge.

Nevertheless, if the exterior particle is identified, PERI correctly locates the interior particle, as shown in Fig. 6.11. To demonstrate this, we create simulated images of two particles near the boundary of an image. One particle is placed at $z = a$ so that its edge just touches the boundary while the other is placed at $z = -(a + \delta)$ on the other side of the border. We plot the CRB of the interior particle and the measurement errors of both PERI and trackpy as a function of the exterior particle's coordinate in Fig. 6.11. While the CRB only changes by a factor of 2 as the particles come within contact, the featuring errors grow drastically for traditional featuring methods due to biases introduced by the exterior particle. For this same data set, PERI featuring errors follow the CRB allowing precise unbiased featuring of particles at the edge of images.

This apparent conundrum of edge particles presents an interesting positive side-effect. Missing edge particles affect the fits because they contribute a significant amount to the image. As such, we might expect that a particle outside the field of view can still be located very precisely. This prediction is borne out by a calculation of the Cramér-Rao bound, as shown in Fig. 6.12. Until the particle and PSF fall off the edge of the image (distance $> 1R$), the CRB remains constant for all particle parameters. When the particle is centered on the image edge (distance of 0), the CRB is twice that of the bulk, intuitively corresponding to a loss of half of the information about the particle. As the volume of the particle leaves the image, the CRB decreases as $1/\delta^2$ until the particle is no longer part of the image. Interestingly, Fig. 6.12 shows that the PSF constrains the particle position to within 0.1 px even when the particle is entirely out of the image! If correctly seeded with a moderate guess for the particle position outside the image, PERI will locate the particle to a precision of the Cramér-Rao bound. However, in practice it is very difficult to seed these particles into PERI, as a slight change of the intensity

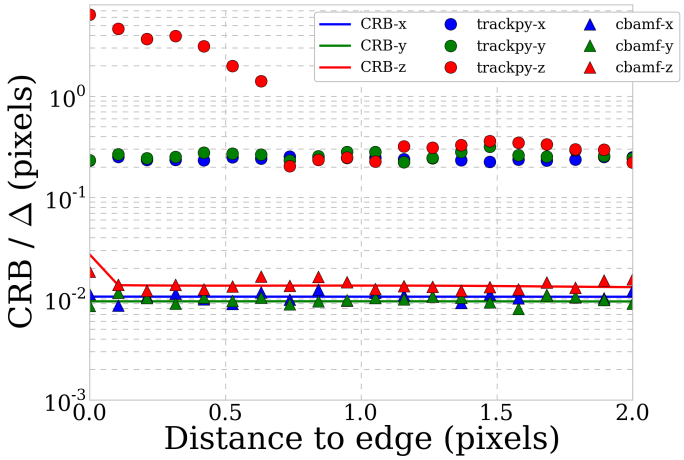

Figure 6.11: **Influence of particles outside of the image**. Here we place one particle at $x = a$ and a second particle at $x = -(a + \delta)$ so that one is completely inside the image and the other outside. We plot the CRB for the x, y, and z positions and radius a of the interior particle as well as measured errors for PERI in triangles and a centroid algorithm (trackpy) in circles as a function of the position of the second particle. When the exterior particle is further than a pixel outside the image we see that the measurements of the interior particle are constant. However, as the PSF of the exterior particle begins to overlap the interior particle the CRB and all measured errors increase dramatically. While PERI's measured error continues to follow the CRB, trackpy's error increases beyond pixel resolution. Note that pixel separations at the edge are generic in colloidal images especially in dense suspensions.

at the image edge could be either a missing particle outside the image or a slight variation in the ILM near the image edge. Nevertheless, PERI is very good at locating particles that are partially outside the image.

6.4.4 Pixel intensity integration

Our generative model considers the image formed on the camera as if the camera pixels had an infinitesimal size. In reality, the camera pixels have a finite extent. As a result, the image at each pixel on the camera is not a discrete sampling of

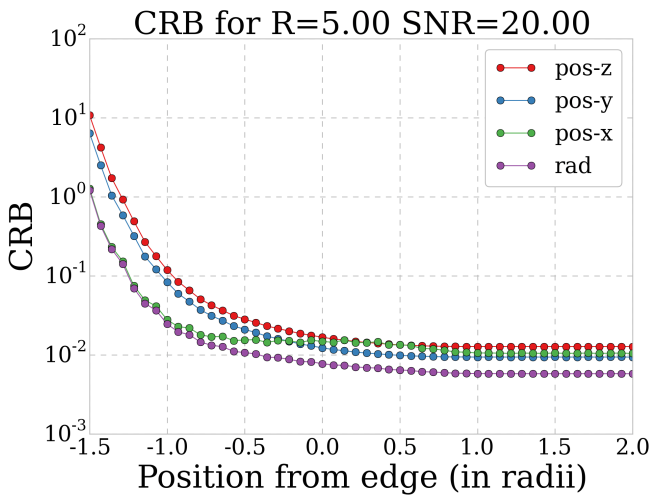

Figure 6.12: **CRB of edge particles**. Here we calculate the Cramér-Rao bound of the x, y, and z positions as well as radius (in red, blue, green, purple respectively) for an isolated particle as a function of its distance to the edge of the image. For positive displacement (inside the image) we see very little change with position as expected. As parts of the PSF leak out of the image (displacements close to zero, positive) we see that the expected error increases slightly since information is lost. Finally, as the particle itself leaves the image, information is lost more dramatically as indicated by a sharp rise in the CRB. However, note that even at a displacement of one radius a, the PSF allows us to locate the particle outside of the image to within a pixel. While in practice it is difficult to identify these particles systematically, their presence can greatly influence the measured positions of other edge particles.

the light intensity, as in our generative model, but is instead an integration in the detector plane over the pixel's size.

To check whether the effect of pixel integration matters, we generated images that were up-sampled by a factor of 8 in the xy-plane. We then numerically integrated these images over the size of each pixel. A representative image is shown in Fig. 6.13a. There is very little difference between the xy-integrated image and the generative model, as visible in panel b. We then fitted an ensemble of these xy-integrated pixel images, both over an ensemble of noise samples and over an ensemble of particle positions shifted by a random fraction of a pixel.

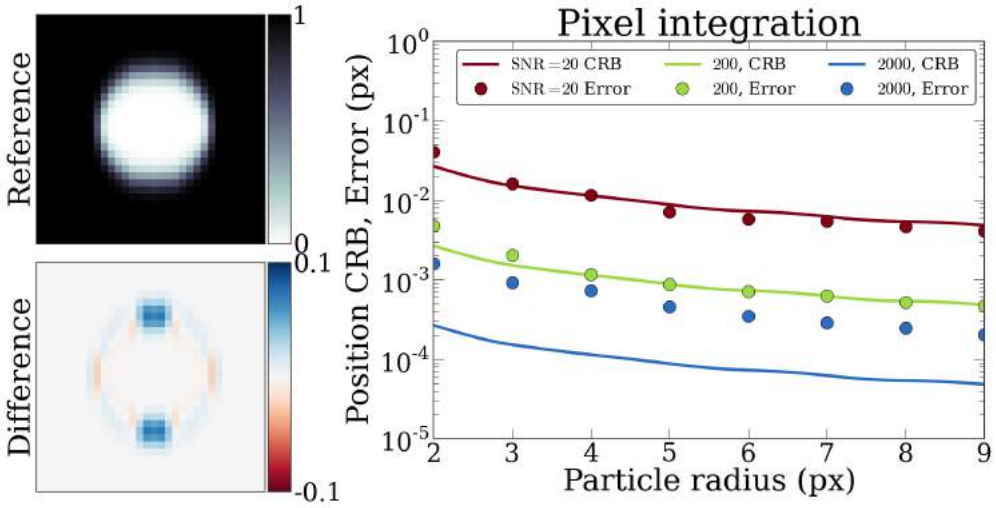

Figure 6.13: **Pixel Integration** (a) The xz cross-section of a simulated image of a 5 px radius colloidal particle, where each pixel contains the light intensity integrated over its area instead of sampled at its center. (b) The difference between the pixel-integrated image and a reference image sampled at the center of the pixels. The differences between the images are small (10%) and centered in a ring which has mean 0 and is positioned at the particle's edge. (c) The effect of pixel integration on featured particle positions as a function of particle radius, at signal-to-noise ratios of 20, 200, and 2000. The solid symbols and dashed lines show the position error for images generated with pixel integration and fit without, while the solid lines denote the Cramer-Rao bound for the images (without pixel integration). Integrating over a pixel area has no effect on the featured positions for any SNR compatible with an 8-bit depth camera. The effect of pixel integration only starts to matter for an SNR ≥ 400 (not shown).

The results are shown in Fig. 6.13c. We find that there is no discernible effect of pixel integration at a SNR of 200 or less. The error due to neglecting pixel integration becomes comparable to that due to noise only for $SNR \geq 400$, which is significantly higher than the maximum allowed by an ordinary 8-bit camera. Thus, the effect of integrating over a pixel size for a colloidal particle essentially always has a negligible effect on the fitted parameters.

6.4.5 Diffusional motion

A typical colloidal particle is not fixed in its location, but diffuses about due to Brownian motion. For an isolated colloidal particle, this Brownian motion results in a random walk with mean displacement $\langle \vec{x} \rangle = \vec{0}$ and a mean-square displacement $\langle x^2 \rangle = 6Dt$ that is linear in time, with a diffusion constant $D = kT/6\pi\eta R$ where η is the solvent viscosity and R the particle radius. As a result, the microscope takes an image not of a colloidal particle at a single position, but of an integrated image of the colloidal particle over the trajectory that it has diffused.

First, at what length- and time- scales is a colloidal particle de-localized due to Brownian motion by a scale that is larger than the resolution? For a 1 μm diameter particle in water to diffuse the 1 nm resolution provided by PERI takes a fantastically small time of $t = 1$ nm^2/D $\approx 10\mu$s. Even for our relatively viscous samples of $\approx 80\%$ glycerol and 20% water this time slows down to only $\approx 600\mu$s. These times are orders of magnitude faster than the $\approx$ 5ms required by our confocal to take a 3D image of the particle, corresponding to a 8 nm displacement. Thus, a freely diffusing particle has always diffused much more than the featuring errors than the uncertainty intrinsic to PERI.

However, this does not mean that the precision past 8 nm is empty. The particle's positions are Gaussian distributed about its mean value during the exposure time. While the extent of the distribution is much larger than the PERI featuring errors, the particle's mean position during the exposure time is well-defined. Moreover, the actual image on the camera from the diffusing particle is a convolution of the particle's trajectory with a single particle image. Since this convolution is like an averaging, we might expect that the small Brownian excursions are averaged out in the image formation, and that the image allows for accurate featuring of

the particle's mean position.

We can use the formalism of Eq. 6.13 to show that Brownian motion does not affect our featuring accuracies. Let the particle's mean position be $\vec{\bar{x}}_0$, and its Brownian trajectory be $\vec{x}_0(t)$. Then the actual image $I(\vec{x})$on the detector is

$$I(\vec{x}) = \frac{1}{t_{\text{exp}}} \int_0^{t_{\text{exp}}} I_0(\vec{x}_0(t))\, dt = I_0(\vec{\bar{x}}_0) + \frac{1}{t_{\text{exp}}} \int_0^{t_{\text{exp}}} I_0(\vec{x}_0(t)) - I_0(\vec{\bar{x}}_0)\, dt \quad (6.14)$$

where $I_0(\vec{x})$ is the image of one particle at position $\vec{x}$ and t_{exp} is the camera exposure time. As before, we view the actual image as $I(\vec{x}) = I_0(\vec{\bar{x}}_0; \theta) + (1 - \Theta)\Delta I$, in terms of a group of fitted parameters $\vec{\theta}$ and an additional parameter Θ describing the effects of Brownian motion ΔI. For the true image $\Theta = 0$ but for our model image $\Theta = 1$. Then equation 6.13 says the error will be $\theta_j \approx H_{kj}/H_{jj}$, where $H_{\Theta j} = \partial_\Theta \partial_{\theta_j} I = \partial_{\theta_j} \Delta I$. However, for small displacements the effect of Brownian motion on the image is

$$\Delta I = \frac{1}{t_{\text{exp}}} \int_0^{t_{\text{exp}}} \frac{\partial I(\vec{\bar{x}}_0)}{\partial x_i} (\vec{x} - \vec{\bar{x}}_0)\, dt = 0$$

since $\partial I(\vec{\bar{x}}_0)/\partial x_i$ does not depend on time. As a result, $\partial_{\theta_k} \partial_\Theta \Delta I = 0$ and there is no affect of Brownian motion on the image to first order in the displacements, *i.e.* when the particle displacement is moderately small compared to the radius.

Finally, in Fig. 6.14 we show empirically that the effect of Brownian motion is negligible for our exposure times. To create an image of a diffusing particle captured by a slow camera, we simulated a 200 point Brownian trajectory of a $R = 5$ px radius particle, generating an image for each point in the particle's trajectory. We then took the average of these images as the noise-free image captured by the microscope. One such image is shown in Fig. 6.14a. Once again, there is a slight difference (10%, as shown in panel b) between the slow image of a diffusing particle and the reference image taken of a particle at a single location. We then fitted an ensemble of these images, over a variety of both Brownian

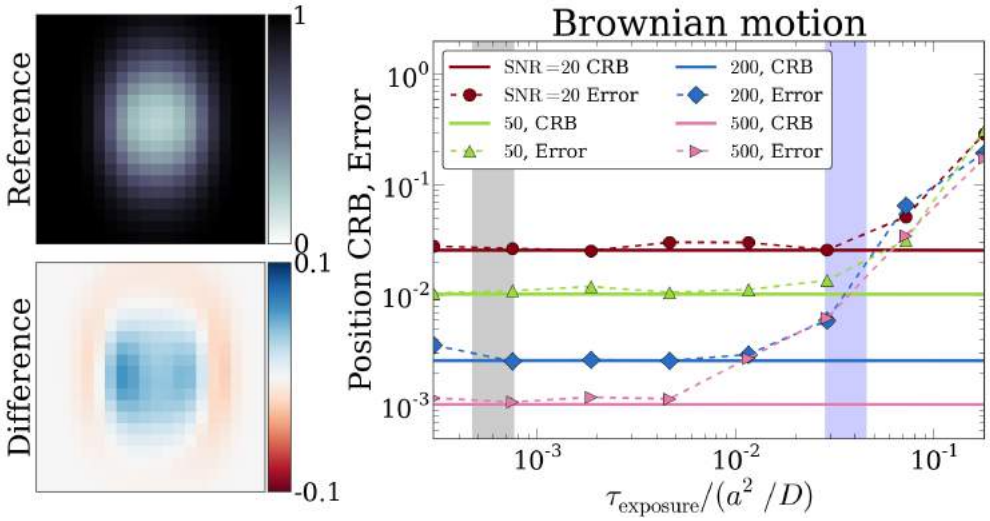

Figure 6.14: **Brownian Motion** (a) The xz cross-section of a simulated image of a 5 px radius colloidal particle undergoing strong Brownian motion $\tau_{\text{exposure}}/(R^2D) = 0.01$ during the image formation. (b) The difference between the diffusing-particle image and a reference image without diffusion. The differences between the images are small (10%) and are mostly in a ring with mean 0 at the particle's edge. (c) The effect of Brownian motion on featured particle positions as a function of exposure time, at signal-to-noise ratios of 20, 50, 200, and 500. The image exposure time for our camera is located in the shaded grey band for 20/80 water/glycerol and blue band for pure water. The solid symbols and dashed lines show the error between the fitted positions and the mean position in the particle's trajectory, while the solid lines denote the Cramer-Rao bound for the generated images. At our exposure times and SNR of 20, the effects of Brownian motion are small compared to those from noise in the image. Interestingly, for higher SNR or slower exposure times, Brownian motion starts to have a noticeable effect and must be incorporated into the image generation model.

trajectories and noise samples. Figure 6.14c shows the results of these fits as a function of the mean displacement during the collection $\tau_{\text{exposure}}/(R^2D)$, where τ_{exposure} is the exposure time of the camera and D the particle's diffusion constant. Brownian motion has a negligible effect on the featured positions for our experimental images of freely-diffusing particles (camera exposure time of 100 ms and $D = 0.007$ μm^2/s corresponding to a 1 μm particle in 80:20 glycerol:water, corresponding to $\tau_{\text{exposure}}/(R^2D) \approx 10^{-3}$). Interestingly, however, to achieve a higher localization accuracy at a higher SNR of ≈ 200, Brownian motion must be

correctly taken into account in the image formation. Incorporating Brownian motion at these high signal-to-noise ratios would allow the teasing out of information about the particle's trajectory from a single image.

6.5 Implementation

A typical confocal image is roughly 512 x 512 x 100 pixels in size and contains 10^4 particles meaning that the number of degrees of freedom in our fit is roughly 10^7 described by 10^5 parameters, a daunting space to optimize. On modern hardware using the highly optimized FFTW, the typical time for an FFT the size of a single image is $\sim$ 1 sec. Given this time, a single sweep through all parameters would take an entire week while a full optimization would consume a year of computer time. However, since particles have finite size, we are able to optimize most of these parameters locally with a small coupling to global parameters (ILM, PSF). Additionally, the finite intensity resolution of microscope sensors, typically 8 or 16 bits, allows us to make further simplifications to our model. Here we describe the practical algorithmic optimizations that we have made as well as the optimization schedule that we have devised to quickly reach the best fit model.

6.5.1 Partial image updates

First and foremost, we optimize our fitting procedure by working in image updates and only updating parts of the image that are required at any one time. In order to modify the position of one particle by a small amount, the number of pixels that are affected is simply $(2a + w)^3$ where a is the particle radius and w is the

PSF width, both in pixels. For a typical particle, the ratio of this volume to the entire image volume is typically 10^{-2} which represents a speed up of the same factor due to the roughly linear scaling of FFT performance with problem size ($N \log N$). In addition, since the PSF decreases with distance from a particle's center, a localized object produces only a weak signal in regions far away from it. For confocal microscope PSFs, the distance scale associated with this signal change is only a few tens of pixels. Therefore, we employ a technique common applied to inter-atomic potentials in molecular dynamic simulation – we simply cutoff the PSF at this distance scale allowing for exact partial updates. By cutting off the PSF, we are able to incrementally apply image updates in an exact procedure (up to floating point errors). For example, when moving a single particle from $\vec{x}_0$ to $\vec{x}_1$, we must simply calculate the local image change given by

$$\Delta\mathcal{M}(\vec{x}) = \int \mathrm{d}^3x' \; [I(\vec{x'})(1-c)(\Pi(\vec{x};\vec{x}_1) - \Pi(\vec{x};\vec{x}_0))]P(\vec{x}-\vec{x}';\vec{x}) \quad , \qquad (6.15)$$

cf. equation 6.2, then calculate $\mathcal{M} + \Delta\mathcal{M}$ only in a small local region around the particle being updated. We are able to use similar update rules for all variables except for those effecting the entire image such as the PSF, offset, z_{scale}, and estimate of the SNR.

Additionally, in our code, we generously employ the principle of "space-time trade-off" in which we cache intermediate results of all model components and reuse them later in the computation. In particular, we maintain a full platonic image and illumination field, which we update along with the model image. We also cache the calculated PSF so that we may utilize previous results until the PSF is sampled. In doing so, we are limited in our current implementation by the speed of the FFT, which takes 70% of the total runtime.

6.5.2 Optimization of parameters and sampling for error

Once an approximate initial guess is obtained by more traditional featuring methods [37], we optimize the parameters by fitting using a modified Levenberg-Marquardt routine. Our Levenberg-Marquardt algorithm uses previously-reported optimization strategies designed for large parameter spaces [149]. However, a Levenberg-Marquardt minimization requires the matrix $J_{i\alpha} \equiv \partial m(x_i)/\partial\theta_\alpha$, which is the gradient of each pixel in the model with respect to all the parameters. For the $\approx 10^5$ parameters and 10^7 pixels in our image, this matrix would be many thousand times too large to store in memory. Instead, we construct a random approximation to $J_{i\alpha}$ by using a random sub-section of pixels x_i in the image to compute J. This approach works well for the global parameters (PSF, ILM, etc) but fails for the particles, which appear in a relatively small number of pixels. For the particles, we instead fit small groups of adjacent particles using the full $J_{i\alpha}$ for the local region of affected pixels. As the global parameters and particle parameters are coupled, we iterate by optimizing first the globals, then the particles, and repeating until the optimization has converged.

Once the model is optimized, we use Monte Carlo sampling to estimate parameter errors. Our Monte Carlo sampler sweeps over each parameter and updates the particle position, accepting or rejecting based on the change in the log-likelihood of the model. We use slice sampling to produce highly uncorrelated samples, allowing an excellent error estimate from only a few sweeps. Our error sampling doubles as a check for convergence. If the log-likelihood increases after sampling, then the optimization has not converged and either more Monte Carlo sampling or more traditional optimization is needed. In practice, when desired we check with $\approx 5-10$ Monte Carlo sweeps, and ensure that the log-likelihood remains the

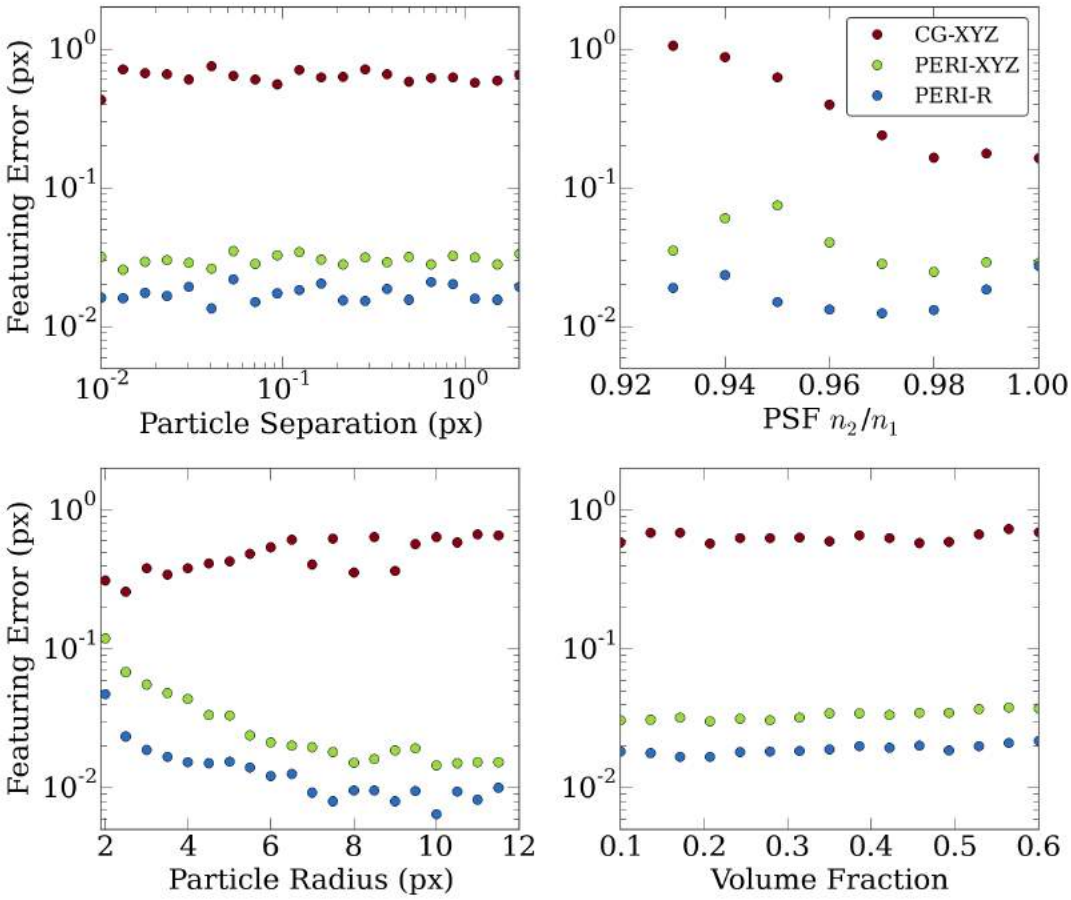

Figure 6.15: **Accuracy benchmark**. We compare the featuring errors of PERI and a traditional centroid (Crocker Grier or CG) featuring method with the optimal featuring parameters. The panels show the featuring errors vs. particle separation (upper left panel), vs PSF aberration through the index mismatch n_2/n_1 (upper right panel), vs. particle radius (lower left panel), and vs. the suspension volume fraction (lower right panel).

same or fluctuates by a few times $\sqrt{N}$, where N is the number of parameters in the model.

6.6 Benchmarks of featuring algorithms

We check our algorithm by benchmarking it against physically realistic image models, as shown in Fig. 6.15. For maximal realism, we generate these images with every model component in equation 6.2 as realistic as possible. We use our exact calculation for line-scanning confocal microscopes, with physical parameters expected from an experiment. From the structure of our fitted line-scan confocal images, we re-create a random illumination field that closely mimics the power spectrum of our actual confocal. We position the particles randomly, without placing them preferentially on the center or edge of a pixel. Since real images have particles that are also outside or partially inside the image, we generate the image on a large region before cropping to an internal region, resulting in edge particles and particles outside the field of view. [1]

We then fit these algorithms both with PERI and with traditional centroid-based featuring algorithms. When we fit these images with PERI we start with initial guesses that are not near the correct parameter values, to ensure that our method is robust to realistic initial guesses. For the centroid featuring methods, there are several algorithms and variants that can be used. We use the most commonly used of these versions, as implemented by Crocker and Grier [37] in the IDL language. All of these centroid algorithms require the user to select various parameters, such as a filter size for smoothing of the noisy image and a mask size for finding the centroid positions. As is well-known in the colloid community, using the incorrect parameters can result in significantly poorer results. To overcome

[1] Unless otherwise specified, we use an index mismatch $n_2/n_1 = 0.95$, a ratio of fluorescent light to excitation light energies of 0.889, an excitation wavelength of 488 nm, and a lens aperture acceptance angle of 1.173 corresponding to a 1.4 NA lens. The particles are 1 μm in diameter, with a pixel size used of 100 nm, and extend from a region from just above to ≈ 5 μm above the coverslip.

any possible limitation from using the incorrect parameters, we *fit* all the possible parameters[2] in the Crocker-Grier (CG) algorithm and use only the ones that produces the best global featuring of the data, as compared to the correct particle positions. (Centroid methods do not accurately find particle radii). Needless to say, an actual experimenter does not have access to the ground truth or to the optimal parameters for the featuring. Moreover, even with these optimal parameters, the centroid algorithm frequently misses a large fraction of particles, even in simple images. As such, we view the centroid featuring errors as unrealistically optimistic and probably not attainable with centroid methods even by experts. The results of these comparisons are shown in figure 6.15.

When two particles are close, their images overlap due to the breadth of the point-spread function. This overlap causes centroid methods considerable difficulty. To compare the effects of PSF overlap on both PERI and CG featured positions, we generate an ensemble of realistic images with isolated pairs of particles at random orientations and at a fixed particle edge-to-edge separations. The upper-left panel shows these results for edge-to-edge separations from 0.01 px to 2.0 px, with a fixed noise scale of about 0.05 of the illumination amount. As the randomly-generated illumination fields vary from image to image, and the illumination varies from region to region within an image, there is not truly a global SNR for all of the images; the fluctuations in this SNR from image to image are the origins of the fluctuations in featuring error throughout figure 6.15. PERI features particles at the Cramer-Rao bound regardless of their separation. In contrast, even at large separations of 2 px, CG has significant errors due to particle overlaps.

Aberrations due to index mismatch significantly affect image quality and ex-

[2]We fit the x, y, z bandpass sizes for both the lowpass and hipass filters, the centroid size or diameter, the particle mass size "masscut", the minimum particle separation, and a threshold below which pixels are ignored.

tracted particle locations. The upper right panel shows the effect of these aberrations on localizing isolated particles, as measured by the ratio between the index of refraction of the optics n_1 and of the sample n_2. Moving the ratio n_2/n_1 away from 1 increases aberration in the image. While increasing the aberrations in the lens negatively affects PERI's ability to feature particles, the localization accuracy always remains excellent. In contrast, CG methods perform poorly throughout, with extremely poor performance as the aberrations increase.

Since the CRB decreases with particle radius, we expect that increasing the particle radius should result in an increase in localization accuracy. The lower-left panel of figure 6.15 shows that PERI's precision improves with increasing particle radius. In contrast, the Crocker-Grier precision *worsens* with increasing particle radius. We hypothesize this arises due to the flat intensity profile near the center of a large particle, whereas a centroid method assumes that the intensity is peaked at the particle center. As a result, slight noise can significantly worsen a large particle's localization with centroid methods. Conversely, centroid algorithms improve for small particles, performing only $3\times$ worse than PERI's localization accuracy for particles with radius 2 px. For particles small to the PSF size, the image is essentially a single peak, which centroid methods work well for.

Realistic images taken with confocal microscopes consist of particles randomly distributed, occasionally close together and occasionally far apart. To examine the localization in these images, we use a Brownian dynamics simulation to create a random distribution of particles at volume fractions from $\phi = 0.1$ to $\phi = 0.6$. PERI localizes particle positions and radii excellently in all of these images, as visible in the lower-right panel. In contrast, centroid methods perform uniformly poorly, with localization accuracies of approximately half a pixel. Interestingly,

these centroid algorithms do not localize significantly worse for dense suspensions despite the presence of more close particles, although they do frequently fail to identify particles.

Finally, we check how the complexity of our synthetic data affects the accuracy of standard featuring methods. In Table 6.2 we see, surprisingly, that there is a non-monotonic relationship between positional error and image complexity, becoming optimal when there is significant striping in the image but little variation in depth. However, the rate of missing particles decreases significantly with simpler models and rising to as much as 40% for our most complex model images. The effective resolution of CG is never much smaller than a single pixel in these synthetic tests, most likely due to pixel edge biases.

6.7 Experimental Details

The microscope is a Zeiss LSM 5 Live inverted confocal microscope, used in conjunction with an infinity-corrected 100x immersion oil lens (Zeiss Plan-Apochromat, 1.4 NA, immersion oil with index $n = 1.518$). The LSM 5 Live confocals operate by line-scanning. Rather than rastering a single point at a time to form the image, a line-scanning confocal images an entire line at once. An image of a line is focused onto the sample, and the sample fluorescence is detected on a line CCD. Rastering this line allows images to be collected much faster. However, the different line-scanning optics worsen the point-spread function compared to a

Polydispersity	Illumination field	Point spread function	Position error	% Identified
0.0	Legendre 2+1D (0,0,0)	Identity	1.458	0.81
0.0	Legendre 2+1D (2,2,2)	Gaussian(x, y)	1.218	0.84
0.01	Barnes (10, 5), $N_z = 1$	Gaussian(x, y, z, z')	1.015	0.75
0.05	Barnes (30, 10), $N_z = 2$	Cheby linescan (3,6)	0.819	0.64
0.10	Barnes (30, 10, 5), $N_z = 3$	Cheby linescan (6,8)	1.085	0.64

Table 6.2: **Crocker-Grier featuring errors**. We show the effect of image complexity on position error and miss rate for the CG featuring method using synthetic data. Surprisingly, there is a non-monotonic behavior of error with complexity, hitting a maximum for highly striped images that don't vary strongly with depth. However, the featuring miss rate steadily decreases with complexity, reaching only 60% identified particles with our most realistic images.

point-scanning confocal and cause illumination imperfections such as dirt to be smeared out over one direction in the image. Importantly, our confocal is outfitted with a hyper-fine piezo scanner which gives precise z-positioning of the lens. This precise z-positioning is important for accurate reconstruction of images – with the less-precise standard positioning our image reconstruction and results suffer considerably. The data shown in the main text were taken at 108.1 in-plane frames per second.

Our experimental images consist of ≈ 1.3 μm silica particles (MicroPearl) suspended in a mixture of glycerol and water. The glycerol/water mixture is tuned to match the refractive index of the particles by minimizing the sample scattering. For these particles we find the optimal refractive index is $n \approx 1.437$ corresponding to $\approx 80\%$ glycerol and 20% water. We match the index of refraction of the spheres and the suspending fluid to within a few parts per thousand, resulting in practically zero scattering by the spheres of the laser or fluorescent light. The glycerol has the additional advantage of creating a very viscous suspension, slowing down the Brownian motion of the particles. We add fluorescein sodium salt to dye the suspending fluid. The fluorescein diffuses rapidly compared to the particles, and is effectively uniformly distributed throughout the regions occupied by the fluid. By using a considerable amount of dye and a low laser power, we minimize photobleaching during our experiments.

The samples used for determining interparticle interactions were prepared in a similar way. The suspending fluid was a mixture of glycerol and water. Since glycerol is hygroscopic, we controlled the concentration of glycerol and water by measuring the index of refraction. We tuned the index to $n = 1.437$ that matches the index of refraction of the silica particles; this corresponds to $\approx 76.4\%$ glycerol

and 23.6% water. To this we added fluorescein sodium salt dye, to a concentration of 0.4 mg/mL. Fluorescein sodium salt (molar weight 376.27) consists of two sodium ions bound to a dye molecule. As a result, this concentration of dye corresponds to ≈ 2 moles/mL of monovalent sodium ions and 1 mole/mL of divalent fluorescein ions. To this solution we added the 1.3 μm silica particles (MicroPearl) at a concentration of 6.8 mg particles per 1 mL of solution. These particles are placed in a 100 μm deep sample cell; since the particles sediment the experimental volume fraction is determined equally by settling and the sample cell height as compared to the density of particles in the original suspension. We allow the suspension to sediment for several hours to achieve equilibrium before taking any measurements. The data is collected over the course of a 1-2 hours; we do not observe any change in the $P_s(\delta)$ from the earlier samples to the later ones.

To extract the interparticle potential, we use Molecular Dynamics simulations to find $P_s(\delta)$ and vary the parameters to find the best-fit $P_s(\delta)$. Since we know the particles' positions and radii via PERI, we seed the simulation with the featured particle positions and radii and relax the particle positions thoroughly before sampling for $P_s(\delta)$. Using the extracted particle parameters enforces both the correct amount of particle radii polydispersity and the number density of particles. In the simulation we use a standard DLVO potential, consisting of non-retarded van der Waals attractions and Debye-Huckel repulsion [122], augmented by gravitational settling. The free parameters we fit are the strength of the attraction, the strength and screening length of the repulsion, and the settling strength; physically these correspond to the Hamaker constant, a combination of the particle zeta potential and salt concentration, and the average particle density. As mentioned in the text, we find that the potential is nearly hard-sphere, with a fitted Hamaker constant of 0.001 kT, a screening length of 15 nm, a maximal electrostatic repulsion strength

of 1 kT, and a gravitational settling height of about 0.45 μm. In contrast, if all the salt present in the suspension were due to the fluorescein dye, we would expect a huge screening length of 700 nm, which would be very easy to see even by eye. However, previous experiments have already shown that, even in suspensions where the ion concentration is carefully controlled by an ion exchange resin to be as dilute as possible, the screening length is usually much shorter ranged, around 100 nm [39]. As a result, we expect a short-ranged screening for our suspension without an ion exchange resin and with extra salt added via fluorescein dye. As is well known in the colloid literature, an increased electrostatic repulsion can be counteracted by an increased van der Waals attraction and vice versa; this tradeoff is also present in our fits. The reported numbers are the best-fit values from the simulation; however the uncertainties in these parameters are correlated so a range of similar potentials with different values is possible. This tradeoff in the fit landscape, along with possible featuring errors, may also explain some of the deviations of the parameters from those expected naively. However, we believe that these fitted values are relatively correct, and that deviations arise due to real, physical changes in the system such as index matching and other sources of ionic contaminants.

6.8 Discussion & Future Work

As mentioned in the text, currently PERI features particle radii to within 3 nm. While this is fantastically precise, for the data shown in the paper the Cramer-Rao Bound is approximately 1 nm, or even slightly smaller. WHile it is more difficult to measure accuracy to which particle positions are identified, given that the radii are not perfect I would imagine that, for sufficiently high SNR images,

the particle positions have some slight systematic errors at around 1 nm. In this section, I would like to briefly discuss what I think the reasons are for this current limitation. Incidentally, while Matt Bierbaum and I have discussed this extensively, these thoughts are my own, and while Matt may agree with some of them he may also disagree with some of them.

Featuring errors above the CRB can only arise from an incomplete model. Generally, there are two broad possibilities for an incomplete model: (1) The model equation used in PERI (e.g. equation 5.2 in the main text) is correct, but different components of the model are implemented correctly, or (2) The model equation used in PERI is wrong and the image formation process is actually a similar but distinct model. I will briefly address each of these two possibilities in order.

6.8.1 Incorrect Model Components

The residuals between the data and the model provide information about what is incorrect about the model. For the typical SNR ≈ 30 data shown in the paper, it is difficult to see structure in the residuals clearly, since the scale of the structure is about the same as the noise. In Fourier space there is a clear ring of residuals, shown in figure 5.2, that shows that the model is missing something on the scale of the particles. However, it would be easier to see the difference in real space. To this end, figure 6.8.1 shows an image of colloidal spheres in real space at a very high SNR ≈ 100, taken with a lot of fluorescent dye and a high laser power. In this image, rings are clearly visible around the particles. The rings are small in magnitude, but are delocalized over several pixels.

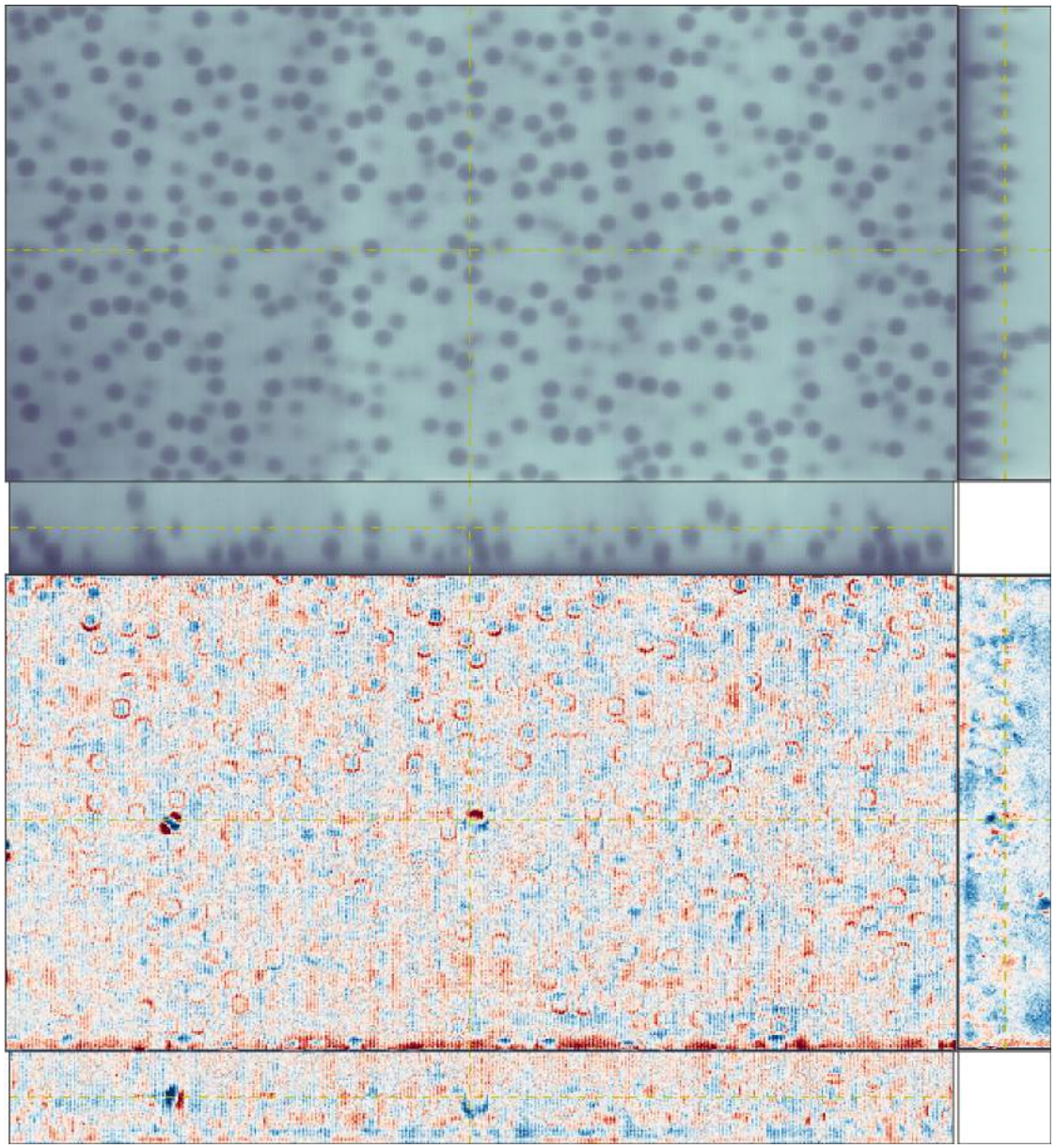

Figure 6.16: A high-SNR image of the 1.3 μm silica spheres as reconstructed with PERI. Upper panel: The raw data, in an xy (center), yz (right), and xz (lower) cross-section. Lower panel: The difference between the data and the best-fit model, at the same cross-sections; the scale in this image is 3$\times$ brighter than in the residuals in the text of chapter 5. At this high SNR, the rings around the particles due to an imperfect PSF are clearly visible. The region of strong residuals at the left-center of the image is from a small piece of "schmutz" in the sample and not from a regular particle.

This structure helps us determine what the issues could be with the model. If the model in equation 5.2 is correct, there cannot be a large problem with correctly aliasing the Platonic image, since this would produce residuals on the scale of one pixel. There cannot be a problem with the description of the illumination field or the background, as the residuals are always localized to near a particle. Only the PSF could be a problem. While the PSF we use is calculated exactly from the most realistic models in the literature of confocal point spread functions for large-aperture lenses, these models have some approximations and may not be completely correct.

Finite Focal Length: The focus of a lens arises due to constructive and desstructive interference. A perfect lens shapes the incoming wavefront to be equiphasal on a spherical cap surface, with the opening angle of the spherical cap equal to the acceptance angle of the lens. Since the center of this sphere is equidistant from each point on the surface, the secondary waves propagating from this spherical surface constructively interfere at the center, creating a bright focal spot. A point slightly off the center of the sphere is not equidistant from every point on the sphere, and the secondary waves will have some slight destructive interference at this point, creating a slightly dimmer intensity here. As a result, the intensity is brightest at the focus (the center of the sphere) and decreases (non-monotonically) with distance away from the focus. For a lens with aberrations, the light is not equiphasal on the spherical cap, and the structure of light near the focus is more complicated.

The intensity variation in the focal region depends on the pathlength difference traveled by light from different points of the spherical cap. In general, the pathlength difference depends on both the position of the point in the focal re-

gion, which we will parameterize by (x, y, z), and on the position on the spherical cap, which we will parameterize by spherical coordinates (f, θ, ϕ), where the constant f is the focal length of the lens or the spherical cap's radius of curvature. The intensity at a given point (x, y, z) is then determined by integrating over all the wavelets that leave each point (θ, ϕ). However, for positions near the focus $(x, y, z)/f \approx (0, 0, 0)$, basic geometry shows that the pathlength difference is independent of f. As a result, the intensity structure near the focus is independent of f, eliminating one parameter from the description of the PSF and considerably simplifying the intensity strucutre. This approximation is used in large-aperture lens confocal PSF calculations, and it is what is used in PERI. Without this, the PSF described by equation 6.8 would be considerably more difficult to implement.

However, empirically we find that PERI requires knowledge about the PSF relatively far from the focal point, especially along the optical axis direction. At these large distances, ignoring the finite size of f might not be a good approximation. From classic work done in the small-aperture limit [17], a finite f should tighten the focus of the lens, changing its behavior at the longest distances calculated by PERI. Ignoring this correction at long distances could bias the PSF at short distances, as it tries to trade off errors at different distances, providing the rings visible in figure 6.8.1. The effects could be included as a power series in $(x, y, z)/f$, but some analysis would be required to understand what the correct form is and to make it rapidly numerically calculable.

Residual Aberrations: Aberrations in the lens distort the cophasal surface from a spherical cap into something more complicated. These aberrations arise either from residual aberrations in the lens or from aberrations induced by index mismatch between the sample and the optics. Usually these aberrations are discussed

for low-aperture lenses, where the spherical cap is simple a flat disk. The wavefront aberration can depend not only on the position $\vec{x}_d$ on the disk, but also on the position $\vec{x}_i$ in the image space. For cylindrically-symmetric microscope optics which are the norm, symmetry dictates that the aberration can only depend on the invariant products x_d^2, x_i^2, and $\vec{x}_d \cdot \vec{x}_i$. As a result, usually the aberrations are described in power series in terms of these three variables. The lowest order aberration enters at quartic powers such as x_d^4; quadratic powers simply correspond to a change in the focal position.

Since PERI fits the index mismatch and the distance of the lens from the interface, PERI already includes some of the possible residual aberrations in the lens. However, the aberrations that PERI currently fits are only one combination of fourth- and sixth- order spherical aberration, corresponding to one term which is a combination of x_d^4 and x_d^6. Any other residual aberration in the lens is not fit, which would affect the PSF and bias the measurements. Due to some structure in the fit residuals, at one point I had guessed that including a different combination of fourth and sixth order aberrations could describe the PSF better. Spherical aberration is particularly simple to include, as it only depends on $|x_d|$ and thus the PSF does not change with in-plane position; the integrals in equation 6.8 simply change slightly. However, including this additional correction did not significantly improve the fit or the radii errors. Including other aberrations such as coma, say, is much more difficult. These other aberrations couple to the position in the image. As a result, the point-spread function at one point is not simply given by a one-dimensional integral like that in equation 6.8, but requires a two-dimensional integral over both θ and ϕ. Moreover, since the strength of the aberration changes with the position in the image, the PSF no longer describes a convolution in x and y but a spatially-varying convolution, which is much slower to implement

numerically. While the residual aberrations might be a problem, they should have a signal which is radii errors and fit residuals that are large away from the center of the image and that vary with position. We do not see significant errors like this in our fits, but since the effect we are looking for is small these aberrations may still be important.

6.8.2 Incomplete Model: two PSFs

The actual process of image formation is more complex than the simple model of equation 5.2. Light is focused through dirty optics onto the sample. This fluoresces a distribution of dye, which then travels back through the dirty optics but along a different path to be focused on the detector. Both of these focusing operations produce a separate point-spread function. For confocal microscopy with uniform illumination or with a pointwise-rastered collection, the combined effect of these PSFs is to simply create one PSF which is the product of a detection and illumination PSF, as discussed in chapter 5. However, for uneven illumination this is no longer the case. The sample should be modeled as illuminated with the dirty, uneven image of a line, and then that image propagated back onto the detector. This will result in a split-PSF model with two separate PSF convolutions – one to describe the illumination and one to describe the detection, rather than only one PSF that describes both illumination and detection.

The split-PSF and the single-PSF model should be equivalent for slowly-varying illumination that is uniform on the scale of the PSF. Likewise, any difference between these two models should arise as structure that is similar to the illumination scale. Figure 6.8.2 suggests that this might be the case. The figure shows the featured radii plotted versus each of the z, y, and x position of the particle, for

about 1.2 million particles.

The solid line is a fit of the radii to a polynomial of degree 5, 25, or 50, in the z, y, or x position, respectively. If there were no biases, these best fits would be completely flat, aside from a small amount of noise or perhaps some settling in z. As shown in the figure, the mean featured radii have slight systematic biases that are on the scale of the 3 nm errors in particle radius and are commensurate with the illumination stripes in the image. However, the residuals of the fit, averaged over the y and z directions, do not show this fluctuation (see figure 6.2). This suggests that the illumination is sufficiently well-fit and of high-enough order to capture the illumination flucutations, leaving a reason for this mismatch as the difference between the split-PSF and the single PSF. Implementing a second, complete ILM would be impractical, since the second ILM would be highly un-constrained as much of the fit power could be transferred between either of the two ILMs. However, the fit could be more constrained by requiring the incoming-light ILM and the detection-light ILM to be the same. The fit would still be much slower, as PERI would require a second set of convolutions. Alternatively, if the radii errors do result from an uneven illuminating line requiring a second PSF, another solution would be to thoroughly clean the optics. Decreasing the disorder should proportionally decrease the error in treating the illuminating line as disorder-free. Moreover, since this is a small effect, decreasing it by a factor of 2 or 3 would push it well below the CRB and make it negligible. In contrast, even for clean optics an ILM would still need to be fit, as it strongly couples to the particle positions and radii.

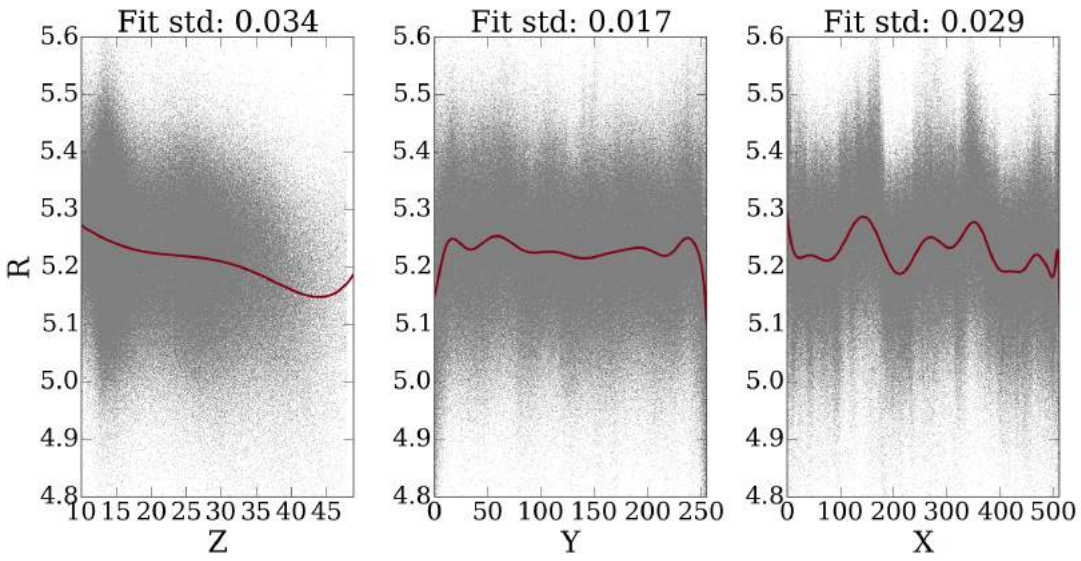

Figure 6.17: Particle radii as a function of position in images of size $(z, y, x) = (50, 256, 512)$. Each measured particle radius is plotted with a small gray dot; the plots contain approximately 1200 particles in 1000 separate different images, for about 1,200,000 different points. The red line is the best-fit polynomial curve. The particle radii are plotted vs z (left panel), y (right panel), and x (right panel). On the top of each plot is the standard deviation of the best-fit line, giving an idea of the radii featuring errors.

CHAPTER 7

EXPERIMENTAL APPARATI FOR IMAGING & SHEARING LIQUID CRYSTALS

Most imaging of liquid crystals is done using a set of crossed polarizers. This technique is a modification of a simple brightfield microscope. A polarizer is placed in the optical train immediately before the sample, causing the sample to be illuminated with polarized light. A second polarizer is placed immediately after the sample and aligned orthogonal to the first. If the sample is a simple material with an isotropic index of refraction, then the polarized light emitted from the first polarizer will be completely extinguished upon incidence with the second crossed polarizer. However, if the sample is birefringent, then the polarization direction of the light can be rotated relative to the first polarizer's direction, and some of the incident light can pass unabsorbed through the second polarizer. In general, the light will be rotated whenever the principle axes of the refractive index tensor are not aligned with polarizer angles, *i.e.* light will be transmitted when the in-plane projection of the molecular director's orientation is not aligned with either of the two polarizer directions. Since the contrast results from an extinguishing of rotated light between two crossed-polarized, the intensity at the detector for a perfectly aligned sample is proportional to $\cos^2\theta \sin^2\theta$, where θ is the angle between the director and any one of the crossed polarizers. A full analysis for spatially-varying three-dimensional director fields results in a more complicated expression [83].

Crossed-polarized microscopy has the advantage of being extremely simple to use – all that is required is the ability to place one polarizer in the optics train before the sample and one polarizer after the sample. However, the technique does not give detailed information about the sample. The crossed polarizers only

give information about the director averaged over the optical z axis, while in reality the director can vary freely in three-dimensions. Moreover, since all the transmitted light is extinguished when the director is aligned along either of the two polarizers axes, polarized light microscopy does not distinguish between a director configuration and that same configuration rotated by 90° about the optical axis. As such, better techniques are needed to measure more detailed properties of a liquid crystal director field.

One such technique is Fluorescence Confocal Polarizing Microscopy (FCPM) [132, 87]. FCMP works by impregnating the liquid crystal with a dilute amount of fluorescent dye. The dye is chosen so that it orients itself at a fixed orientation with respect to the director, usually with the dye's excitation axis parallel to the local director field but sometimes with the dye's axis perpendicular to the director. (Fluorescent dyes are usually well-modeled by a dipole; absorption occurs from the light parallel to the dipole axis and emission occurs as radiated by a dipole oscillating along the dye's axis, see *e.g.* [5, 75] for a very brief discussion of this.) The sample is then imaged with a confocal microscope, modified so that the excitation laser's polarization is controlled along a fixed axis. Only the portion of the excitation light that is polarized along the dye's orientation contributes to the dye's excitation, resulting in one factor of $\propto \cos^2\theta$ in the contrast. The dye then fluoresces, and this fluorescent light is then passed through a polarizer oriented along the same axis as the excitation polarizer before it is detected by the detector. This second extinction creates an additional factor of $\propto \cos^2\theta$ in the contrast, resulting in an overall $\propto \cos^4\theta$ intensity signal. There are several advantages to FCPM over cross-polarized microscopy. First, the $\cos^4\theta$ contrast is much greater than the ordinary $\cos^2\theta$ contrast from polarized light microscopy. Second, since dye excitation is essentially a local measurement, the

behavior of the collected signal is not complicated by a director field that varies along the optical axis direction. Third, since FCPM relies on excitation and not on rotation, FCMP can easily distinguish between 90° rotations of the director, in contrast to polarized-light microscopy. Fourth, and most importantly, since FCPM is a confocal technique, the image plane can be scanned throughout the sample to reconstruct a full, three-dimensional image of the director field instead of the z-averaged image taken from polarized light microscopy.

Outfitting a confocal microscope for FCPM normally requires a serious modification of the microscope. Here, I describe a plug-and-play modification for a Zeiss confocal microscope that instantly equips any confocal with FCPM capabilities. While I tested this design on a line-scanning confocal (5 Live), the apparatus should work on any confocal, including spinning disk or pinhole scanned confocals, as long as the microscope chassis is standard Zeiss chassis such as an AxioObserver Z1. The only determining factor is the physical dimensions of the slider slot in the beam path, which is the same on most of the Zeiss microscopes.

The Zeiss confocals operate by illuminating from one direction (the bottom) and collecting the fluorescent light from the same direction. As a result, the easiest way to outfit the microscope with an excitation and fluorescent polarizer is to use one polarizer, placed in a region of the beam path that both excitation and fluorescent light pass through. This setup also ensures that the excitation and fluorescent polarizers are always aligned. From the design of the microscope, the best place to place the polarizer is near the filter cube assembly, which is immediately before the objective lens in the excitation beam path. Ideally, the user should be able to rotate the polarization direction while collecting data. This creates a problem, however, since the intensity of the polarized incoming laser will be attenuated by

the rotating polarizer, confounding any quantitative measurements of the director direction. Placing a quarter-wave plate immediately in before of the polarizer fixes this problem. When properly aligned, the quarter-wave plate circularly polarizers the laser, and the sample is illuminated with the same intensity regardless of the polarizer orientation. After the detected light passes back through the polarizer, it will again be rotated in a random direction by the quarter-wave plate. However, since the detector detects the intensity independent of polarization, this second passage through the quarter wave plate will not affect the recorded intensity, aside from the possibility of slight polarization-dependent reflectivities within the optical path.

The challenge is implementing this fixed, calibrated quarter wave plate and rotating polarizer within the confined space of the microscope. Unless the filter cube is removed, the only viable location in the beam path is the slider position, a small gap about 12 mm high and 21 mm wide. This small height must contain both the polarizer and the quarter wave plate in series, mounted in such a way that the polarizer can easily rotate while the quarter wave plate remains rigidly fixed. To accomplish this, I designed and machined parts for a FCMP slider that fits in the slider section.

The FCPM slider is a modification of a Zeiss slider (Zeiss part number 4281030000000000), as shown in figure 7.1. The original slider consists of a slider body, which contains a set of mounts for a geared knob that is connected to a polarizer mount by a belt. The polarizer mount has an additional upper surface which mounts into a slight groove in the cover, ensuring that it rotates concentrically. The polarizer sits in the mount at a 4° angle to minimize complications due to scattered reflections, and is rotated by a belt (yellow).

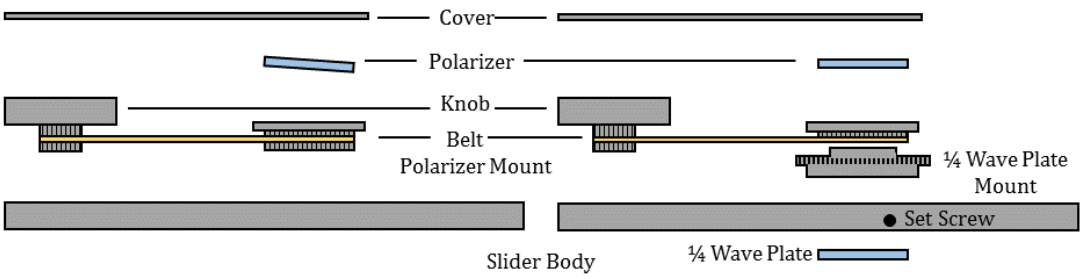

Figure 7.1: **Slider Design.** The modified Zeiss slider (right) as compared to the original (left). Note that this is a mock-up to illustrate the principles of the design and not a proper engineering schematic; parts are neither drawn to scale nor completely faithful to the actual machined material. There is an additional access hole on the opposite side of the slider from the set screw, to allow for turning of the 1/4 wave plate mount without disassembling the slider.

The modified slider differs from the original mainly in the rotating mount. The mount is re-machined, trimming off material on both the top and the bottom to allow for the quarter-wave plate mount to sit inside the slider as well. The polarizer's seat is also flattened, removing the 4° angle on the polarizer to allow for more space and remove some confounding reflections. The polarizer mount rotates on an "axle" on the upper surface of the quarter-wave plate mount itself, which projects far enough into the polarizer mount to allow it to rotate smoothly but not so far as to grind on the polarizer itself. Below this axle is a thin, wide plate on the quarter wave plate mount, which allows the mount to be fixed in place. A portion of this plate is notched to allow for rotation of the fixed quarter wave plate with a screwdriver via an access port; the rest of the plate is smooth to allow for a set screw to bite strongly onto the plate and fix it in place. The bottom of the quarter wave plate mount is machined to sit smoothly in the hole at the bottom of the slider body. The quarter wave plate itself is snugly snapped into the mount; in the final version both optics were also later glued. A printed grid with 2.5° marks is affixed on the bottom of the quarter wave plate mount to allow for precise rotation and alignment of the mount. The quarter wave plate mount

is machined of one piece of material. In addition to these parts, the body of the slider is modified slightly with an access port and with a tapped set screw hole.

The slider requires some initial calibration. The quarter wave plate is designed to be positioned at an arbitrary angle, since manually loading a quarter wave plate at the correct position to within a fraction of a degree is impossible. Calibration involves first setting the quarter-wave plate to the correct angle, then measuring the intensity variation across the field of view as a function of polarizer angle. (While the intensity should be uniform, even at the optimal quarter-wave plate position the intensity is not uniform and the variations in intensity change with polarizer angle.) To do the calibrations, a slide filled with a heavily dyed, isotropic liquid is placed on the microscope. In principle, the random isotropic distribution of the dye ensures that a perfectly aligned quarter wave plate will result in no change of the recorded intensity with polarizer angle. If the quarter wave plate is misaligned with respect to the polarization of the incoming laser beam, there will be a modulation of the intensity with polarizer angle. The quarter wave plate is rotated to the orientation that produces the minimum variation of transmitted laser intensity with changing polarizer angle, and fixed in place using the set screw.

While FCPM is an excellent technique for investigating the static structure of liquid crystals, the slow scanning nature of confocals means that FCPM is ill-suited for studying rapid dynamics. Here polarized light microscopy shines. The time resolution is only limited by the camera speed and the intensity of the light source, which are both easy to increase to well beyond confocal speeds. To that end, I re-machined a liquid-crystal cross-polarized shear cell for use with a microscope.

The design of the liquid crystal shear cell builds heavily on the design of the confocal rheometer in ref. [97]. Two plates are aligned carefully to a small gap

with a set of differential screws. The shearing motion is controlled by a piezo, allowing for precision control of complex, bi- or even tri-axial strain waveforms. A solvent trap isolates the sample from evaporation to the environment. The entire apparatus mounts on a microscope stage, allowing for simultaneous shearing and imaging.

However, the liquid-crystal shear cell differs in several key aspects from the shear cell in ref. [97]. First, porting the light through the apparatus for crossed-polarizing microscopy prevents the use of the Force-Measurement Device (FMD). There is instead a different top-plate portion that still contains a solvent trap. Second, the piezo stage is mounted on the top plate, not the bottom plate. The piezo then drives the top plate back and forth with a shearing motion, leaving the bottom plate stationary. This has the advantage of reducing the motion of the sample near the bottom plate, where the microscope images, and of preventing the bottom plate from possibly grinding against the lens. Third, since the base plate mounts directly on the lower mounting plate, the bottom coverslip height is positioned at the same height as an ordinary sample would be. As a result, the lens does not need to be lofted, in contrast to the ordinary shear cell. In addition to removing the need for an adapter that complicates the optical alignment, it also eliminates the possibility of smashing the delicate lens against the shear cell frame by accidentally selecting a different lens in the software and causing the microscope to automatically, rapidly rotate the lens turret; these accidents have damaged lenses in the past.

These differences are shown in figure 7.2. Both the upper and lower mounting plates are disks of the same size as in the original shear cell, with similarly machined mounts for both the thumbscrew posts and springs. In addition, the lower

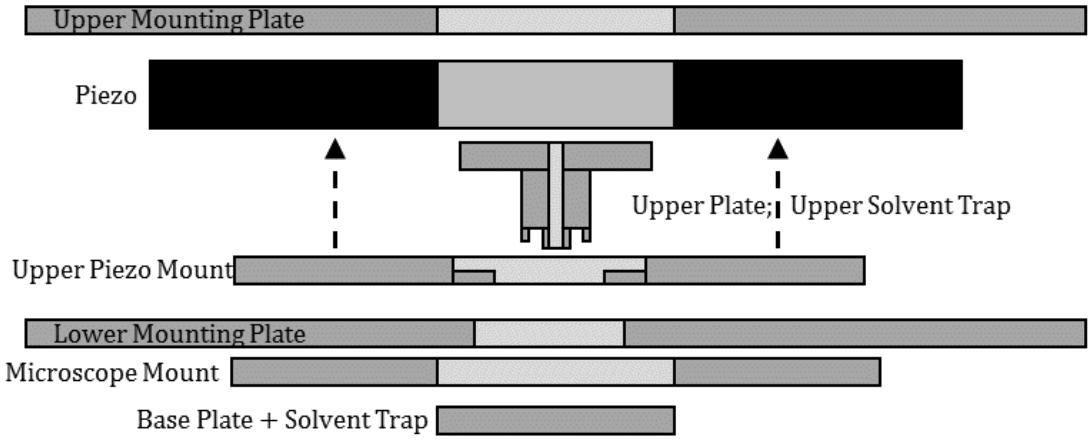

Figure 7.2: **Liquid-Crystal Shear Cell.** A rough schematic of the re-machined pieces and assembly of the liquid crystal shear cell. The view is a cross-section through the center of the roughly circularly symmetric apparatus. The dark gray corresponds to machined components which are solid in the cross-section; the light gray corresponds to circular or square holes which allow light to pass through.

mounting plate has the same set of screw holes to mount the microscope mount directly on the lower plate. Other than these features, the two mounting plates differ. The lower mounting plate is outfitted to directly mount the (standard) base plate and solvent trap, such that the bottom of the base plate sits flush with the bottom of the microscope mount. The top plate is machined with a square hole on the inside, of the same dimensions as the internal hole on the piezo; a rotating polarizer can be mounted in this square hole (not shown). In addition, there are screw holes to mount this piezo directly on the top plate. On the bottom of the piezo is mounted the upper portion of the top plate. This upper piezo mount has a large through hole and a large groove. After this upper piezo mount is mounted on the lower surface of the piezo, the rest of the upper plate and upper solvent trap is lowered through the piezo into the hole in the mount. The upper plate consists of a disk that bolts into the groove in the upper piezo mount; once the shear cell is assembled the top plate can be quickly changed by removing these bolts and the upper plate. Bolted to the disk is a cylinder with a through hole in

the center to allow the light to pass through. The bottom of this flat surface is not smooth. Instead, there are raised rings at the center and edge of the cylinder. On the center ring a small, 13 mm circular glass coverslip mounts and serves as the upper portion of the sample chamber. The outer ring serves as the upper portion of the solvent trap, penetrating into the pool of solvent in the base plate and solvent trap. To allow for small gaps without mechanical contact between the upper and base plates, the solvent trap ring is shorter than the coverslip ring. Finally, to prevent the sample from evaporating through gaps in the apparatus, the cylinder portion of the upper plate is machined from one piece of material. Thus, the only possibility for outside air to exchange with the sample when the solvent trap is filled is through improper gluing of the glass coverslips to the upper or base plates. This is in contrast to the normal shear cell, where air can exchange through the wiring path of the FMD; even when the FMD is sealed the normal shear cell chamber is quite large and can result in some temporary evaporation of the sample.

CHAPTER 8

CONCLUSIONS

Nonspherical colloidal particles have a wide variety of interesting behavior, even in the dilute limit. While their orientation dynamics are somewhat complicated, they can be simply understood in terms of the particle phase angle and orbit constant. Not only does this understanding allow for detailed control of a suspension (chapter 4), but it also has physically measurable consequences (chapter 2). While these experiments and theory were done in the dilute limit, their ideas and lessons should be applicable to at least semidilute suspensions. It would be interesting to explore the behavior of axisymmetric colloidal particle suspensions away from the dilute limit. Furthermore, the analysis and experiments in this thesis were done only for axisymmetric particles. While the rotational trajectories of some particles that are not axisymmetric is described by a Jeffery orbit [24], a particle that is not axisymmetric will in general have a more complicated rotational orbit – indeed, for non-axisymmetric particles the orientation is not even defined on a unit sphere. As shown by in ref. [157], the orientation dynamics of even weakly non-axisymmetric particles can be considerably richer than a simple Jeffery orbit, even when their symmetries are still ellipsoidal. As such, investigations of non-axisymmetric particles would be a fertile ground for exploring non-Newtonian suspension dynamics and physics far from equilibrium.

To what directions could these projects lead? One possible avenue of future research would be studying the orientation dynamics of particles confined to the flow-gradient plane as a rheological model system. While in practice confining orientations to the flow-gradient plane is difficult, this system is still a well-defined, physically reasonable rheological system which displays a host of rheological phe-

nomena. Importantly, there exists an analytical solution at arbitrary strain amplitudes and for arbitrary strain waveforms. At high Pe, the solution in chapter 3 includes both memory effects and relaxation effects, and the dynamics create rheological signals ranging from shear-thinning to normal stresses, with even some slight shear thickening or "amplitude" thickening. Extending the solution to finite Pe could allow for the exploration of viscoelastic effects as well, through the elastic Brownian stresses. By exploring this solution, more intuition could be built up for a realistic model system at strains large compared to unity.

Another possible direction for future research would be examining more complex flows than oscillatory simple shear, especially after a complete solution for the full orientation space is found. As I showed in chapter 4, even for particles confined to the flow-gradient plane it is possible to richly control the orientation dynamics. This control would be greatly extended using shear flows where not only the strain rate but also the strain axes change with time. Even for a flow controlled only by two parallel plates there is much flexibility here. For instance, the plate could be sheared along one direction of simple shear, say x, then along a second, orthogonal simple shear direction, say y, and also moved perpendicular to the plane to create an extensional flow. Coupling these motions together might allow for strong control of particle orientations. Since Stokes flow is reversible, any oscillatory cycle must not create a net drift of the particles orientations. However, it may be possible to create strong focusing of particle orientations when this cycle is coupled to diffusion, similar to the behavior seen in chapter 4. Furthermore, for multiaxial shear it may be possible to focus the particle orientations along more directions than just one flow direction, as the flow direction could rotate with time.

In this thesis I have also discussed reconstructing images to extract physical pa-

rameters. This method works because of an exhaustive attention to detail and the inclusion of the most-realistic physical models. As discussed in chapter 5, ignoring these tiny details or using heuristic physical models will not extract accurate parameters. However, this is as much an art as it is a science – some details may not need to be included, as discussed in section 6.4. Determining which aspects of the image formation matter and which do not can only be done through either trial and error or thorough analysis of the corresponding effects. Moreover, the model needs to be implemented in a numerically stable method to avoid getting the optimization stuck. As an example, we originally tried to vary the size of the calculated PSF, depending on the fitted parameters. However changing the PSF size by one pixel even for a large image can create serious discontinuities in the cost, preventing most algorithms from converging. While we found several methods to avoid some of this discontinuity, we found that the best method is simply not to vary the PSF's calculated size. Ignoring this and similar numerical details will result in a fit that will not converge, returning incorrect answers. Paying attention to these physical and numerical details will provide a method that allows for extremely precise localization of objects.

The apparatus of PERI is very flexible and could easily be extended to other imaging modalities. By accurately, quantitatively understanding the physics of the corresponding image formation, PERI could be extended to examine microscope imaging modalities such as brightfield, darkfield, differential image contrast, crossed polarized microscopy, or even a combination of these techniques examining the same sample. More exotically, PERI could be extended to analyze atomic positions in modalities such as Transmission Electron Microscopy (TEM), Scanning Transmission Electron Microscopy (STEM), or Scanning Tunneling Microscopy (STM). For imaging such as STEM or TEM the size of an atom is determined

mostly by the electron optics point-spread function. Measuring these point-spread functions using PERI could allow for better determination of optical aberrations in the electron beam, possibly allowing for better aberration corrections. In STM, the finite size of the atom's image is due to the delocalization of the wave function. As such, accurately measuring data with PERI could possibly allow for discrimination of details of atomic wavefunctions at the surfaces of condensed matter systems. But even in its current confocal form, PERI will provide us with an unprecedented view on colloidal science, from nanometer interparticle interactions to system-spanning networks in gels and force chains in glasses and jammed suspensions.

BIBLIOGRAPHY

[1] A. Acrivos, G. K. Batchelor, E. J. Hinch, D. L. Koch, and R. Mauri. Longitudinal shear-induced diffusion of spheres in a dilute suspension. *J. Fluid Mech.*, 240:651–657, 1992.

[2] A. Alizadeh, C. A. Nieto de Castro, and W. A. Wakeham. The theory of the taylor dispersion technique for liquid diffusivity measurements. *Int. J. Thermophys.*, 1:243, 1980.

[3] Y. Almog and I. Frankel. The motion of axisymmetric dipolar particles in homogeneous shear flow. *J. Fluid Mech.*, 289:243–261, 1995.

[4] Sean Andersson. Localization of a fluorescent source without numerical fitting. *Optics express*, 16(23):18714–18724, 2008.

[5] Pascal Anger, Palash Bharadwaj, and Lukas Novotny. Enhancement and quenching of single-molecule fluorescence. *Physical review letters*, 96(11):113002, 2006.

[6] S. M. Anthony and S. Granick. Image analysis with rapid and accurate two-dimensional gaussian fitting. *Langmuir*, 25:8152–8160, 2009.

[7] R. Aris. On the dispersion of a solute in a fluid flowing through a tube. *Proc. R. Soc. Lond. A*, 235:67, 1956.

[8] N. Bakhvalov and G. Panasenko. *Homogenisation: Averaging Properties in Periodic Media*. Kluwer Academic Publishers, Dordrecht, 1989.

[9] E. Balkovsky, G. Falkovich, and A. Fouxon. Intermittent distribution of inertial particles in turbulent flows. *Phys. Rev. Lett.*, 86:2790–2793, 2001.

[10] Stanley L Barnes. A technique for maximizing details in numerical weather map analysis. *Journal of Applied Meteorology*, 3(4):396–409, 1964.

[11] G. K. Batchelor. The stress system in a suspension of force-free particles. *J. Fluid Mech.*, 41:545–570, 1970.

[12] M. S. Bello, R. Rezzonico, and P. G. Righetti. User of taylor-aris dispersion for measurement of a solute diffusion coefficient in thin capillaries. *Science*, 266:773, 1994.

[13] T. H. Besseling, M. Hermes, A. Kuijk, B. de Nijs, T-S. Deng, M. Dijkstra, A. Imhof, and A. van Blaaderen. Determination of the positions and orientations of concentrated rod-like colloids from 3d microscopy data. *J. Phys. Condens. Matter*, 27:194109, 2015.

[14] E. Betzig et al. Imaging intracellular fluorescent proteins at nanometer resolution. *Science*, 313:1642–1645, 2006.

[15] M. A. Bibbo, S. M. Dinh, and R. C. Armstrong. Shear flow properties of semiconcentrated fiber suspensions. *J. Rheol.*, 29:905–929, 1985.

[16] R. B. Bird, H. R. Warner Jr., and D. C. Evans. Kinetic theory and rheology of dumbbell suspensions with brownian motion. *Adv. Polym. Sci.*, 8:1–90, 1971.

[17] M. Born and E. Wolf. *Principles of Optics*. Pergamom Press, Oxford, 6th ed. edition, 1980.

[18] Edward J Botcherby, Martin J Booth, Rimas Juškaitis, and Tony Wilson. Real-time slit scanning microscopy in the meridional plane. *Optics letters*, 34(10):1504–1506, 2009.

[19] A. Boustani and B. B. Maini. The role of diffusion and convective dispersion in vapour extraction process. *Journal of Canadian Petroleum Technology*, 40:68, 2001.

[20] H. Brenner. Rheology of a dilute suspension of axisymmetric brownian particles. *Int. J. Multiphase Flow*, 1:195–341, 1974.

[21] H. Brenner. Taylor dispersion in systems of sedimenting nonspherical brownian particles i: Homogeneous, centrosymmetric, axisymmetric particles. *J. Colloid and Interface Science*, 71:189–208, 1979.

[22] H. Brenner, A. Nadim, and S. Haber. Long-time molecular diffusion, sedimentation and taylor dispersion of a fluctuating cluster of interacting brownian particles. *J. Fluid Mech.*, 183:511–582, 1987.

[23] E. Bresler and G. Dagan. Solute dispersion in unsaturated heterogeneous soil at field scale: Ii. applications. *Soil Sci. Am. J.*, 43:467, 1979.

[24] F. P. Bretherton. The motion of rigid particles in a shear flow at low reynolds number. *J. Fluid Mech.*, 14:284–304, 1962.

[25] A. Brown, S. Clarke, P. Convert, and A. R. Rennie. Orientational order in concentrated dispersions of plate-like kaolinite particles under shear. *J. Rheol.*, 44:221–233, 2000.

[26] M. Chaouche and D. L. Koch. Rheology of non-brownian rigid fiber suspensions with adhesive contacts. *J. Rheol.*, 45:369–382, 2001.

[27] R. Chaudhuri and S. Paria. Core/shell nanoparticles: Classes, properties, synthesis mechanisms, characterization, and applications. *Chem. Rev*, 112:2373, 2012.

[28] Bi-Chang Chen, Wesley R Legant, Kai Wang, Lin Shao, Daniel E Milkie, Michael W Davidson, Chris Janetopoulos, Xufeng S Wu, John A Hammer, Zhe Liu, et al. Lattice light-sheet microscopy: Imaging molecules to embryos at high spatiotemporal resolution. *Science*, 346(6208):1257998, 2014.

[29] L.-Y. Chen, N. Goldenfeld, and Y. Oono. Renormalization group and singular perturbations: Multiple scales, boundary layers, and reductive perturbation theory. *Phys. Rev. E*, 54:376, 1996.

[30] X. Cheng, J. H. McCoy, J. N. Israelachvili, and I. Cohen. Imaging the microscopic structure of shear thinning and thickening colloidal suspensions. *Science*, 333:1276, 2010.

[31] D. Cioranescu and P. Donato. *An Introduction to Homogenization*. Oxford University Press, Oxford, 1999.

[32] H. J. H. Clercx and P. P. J. M. Schram. Brownian particles in shear flow and harmonic potentials: A study of long-time tails. *Phys. Rev. A*, 46:1942, 1992.

[33] B. G. Compton and J. A. Lewis. 3d-printing of lightweight cellular composites. *Adv. Mater.*, 26:5930–5935, 2014.

[34] José-Angel Conchello and Jeff W Lichtman. Theoretical analysis of a rotating-disk partially confocal scanning microscope. *Applied optics*, 33(4):585–596, 1994.

[35] L. Corté, P. M. Chaikin, J. P. Gollub, and D. J. Pine. Random organization in periodically driven systems. *Nature Physics*, 4:420–424, 2008.

[36] J. C. Crocker and D. G. Grier. Methods of digital video microscopy for colloidal studies. *J. Colloid and Interface Science*, 179:298, 1995.

[37] John C Crocker and David G Grier. Methods of digital video microscopy for colloidal studies. *Journal of colloid and interface science*, 179(1):298–310, 1996.

[38] S. Datta and S. Ghosal. Characterizing dispersion in microfluidic channels. *Lab on a Chip*, 9:2537–2550, 2009.

[39] Richard V Durand and Carl Franck. Surprisingly short-ranged interactions in highly charged colloidal suspensions. *Physical Review E*, 61(6):6922, 2000.

[40] E. Dusch, T. Dorval, N. Vincent, M. Wachsmuth, and A. Genovesio. Three-dimensional point spread function model for line-scanning confocal microscope with high-aperture objective. *Journal of Microscopy*, 228:132–138, 2007.

[41] A. Eberle, G. M. Vélez García, D. G. Baird, and P. Wapperom. Fiber orientation kinetics of a concentrated short glass fiber suspension in startup of simple shear flow. *J. Non-Newtonian Fluid Mech.*, 165:110–119, 2010.

[42] Aaron PR Eberle, Donald G Baird, Peter Wapperom, and Gregorio M Vélez-García. Obtaining reliable transient rheological data on concentrated short fiber suspensions using a rotational rheometer. *Journal of Rheology (1978-present)*, 53(5):1049–1068, 2009.

[43] A. Einstein. *Investigations on the Theory of the Brownian Movement*. Dover Publications, Mineola, NY, 1956.

[44] M. S. Fallon, B. A. Howell, and A. Chauhan. Importance of taylor dispersion in pharmacokinetic and multiple indicator dilution modeling. *Mathematical Medicine and Biology*, 26:263–296, 2009.

[45] J. Férec, M. Heniche, M. C. Heuzey, G. Ausias, and P. J. Carreau. Numerical solution of the fokker-planck equation for fiber suspensions: Application to the folgar-tucker-lipscomb model. *J. Non-Newtonian Fluid Mech.*, 155:20–29, 2008.

[46] Julien Férec, Gilles Ausias, MC Heuzey, and PJ Carreau. Modeling fiber interactions in semiconcentrated fiber suspensions. *Journal of Rheology (1978-present)*, 53(1):49–72, 2009.

[47] H. Fischer. Longitudinal dispersion and turbulent mixing in open-channel flow. *Annu. Rev. Fluid Mech.*, 5:59–78, 1973.

[48] F. Folgar and C. L. Tucker. Orientation behavior of fibers in concentrated suspensions. *J. Reinf. Plast. Compos.*, 3:98–119, 1984.

[49] A. Franceschini, E. Filippidi, E. Guazzelli, and D. J. Pine. Transverse alignment of fibers in a periodically sheared suspension: An absorbing phase transition with a slowly varying control parameter. *Phys. Rev. Lett.*, 107:250603, 2011.

[50] I. Frankel and H. Brenner. On the foundations of generalized taylor dispersion theory. *J. Fluid Mech.*, 204:97–119, 1989.

[51] I. Frankel and H. Brenner. Generalized taylor dispersion phenomena in unbounded homogeneous shear flows. *J. Fluid Mech.*, 230:147–181, 1991.

[52] I. Frankel and H. Brenner. Taylor dispersion of orientable brownian particles in unbounded homogeneous shear flows. *J. Fluid Mech.*, 255:129–156, 1993.

[53] P. L. Frattini and G. G. Fuller. Rheo-optical studies of the effect of weak brownian rotations in sheared suspensions. *J. Fluid Mech.*, 168:119–150, 1986.

[54] Paul L Frattini and Gerald G Fuller. The dynamics of dilute colloidal suspensions subject to time-dependent flow fields by conservative dichroism. *Journal of colloid and interface science*, 100(2):506–518, 1984.

[55] Shao-Yun Fu and Bernd Lauke. The elastic modulus of misaligned short-fiber-reinforced polymers. *Composites science and technology*, 58(3):389–400, 1998.

[56] W. H. Furry. Isotropic rotational brownian motion. *Phys. Rev.*, 107:7–13, 1957.

[57] S. J. Gason, D. V. Boger, and D. E. Dunstan. Rheo-optic measurements on dilute suspensions of hematite rods. *Langmuir*, 15:7446–7453, 1999.

[58] S. C. Glotzer and M. J. Solomon. Anisotropy of building blocks and their assembly into complex structures. *Nat. Mater.*, 6:557, 2007.

[59] Frederik Grüll, Manfred Kirchgessner, Rainer Kaufmann, Michael Hausmann, and Udo Kebschull. Accelerating image analysis for localization microscopy with fpgas. In *Field Programmable Logic and Applications (FPL), 2011 International Conference on*, pages 1–5. IEEE, 2011.

[60] Shani Guttman, Zvi Sapir, Moty Schultz, Alexander V Butenko, Benjamin M Ocko, Moshe Deutsch, and Eli Sloutskin. How faceted liquid droplets grow tails. *Proceedings of the National Academy of Sciences*, 113(3):493–496, 2016.

[61] Y. Han et al. Brownian motion of an ellipsoid. *Science*, 314:626, 2006.

[62] J. Happel and H. Brenner. *Low Reynolds number hydrodynamics: with special applications to particulate media*. Martinus Nijhoff Publishers, The Hague, 1983.

[63] S. Hell, G. Reiner, C. Cremer, and E. H. K. Stelzer. Aberrations in confocal fluorescence microscopy induced by mismatches in refractive index. *J. Microsc.*, 169:391, 1993.

[64] S Hell, G Reiner, C Cremer, and Ernst HK Stelzer. Aberrations in confocal fluorescence microscopy induced by mismatches in refractive index. *Journal of microscopy*, 169(3):391–405, 1993.

[65] S. W. Hell and J. Wichmann. Breaking the diffraction resolution limit by stimulated emission: stimulated-emission-depletion fluorescence microscopy. *Opt. Lett.*, 19:780, 1994.

[66] E. J. Hinch and L. G. Leal. The effect of brownian motion on the rheological properties of a suspension of non-spherical particles. *J. Fluid Mech.*, 52:683–712, 1972.

[67] E. J. Hinch and L. G. Leal. Time-dependent shear flows of a suspension of particles with weak brownian rotations. *J. Fluid Mech.*, 57:753–767, 1973.

[68] E. J. Hinch and L. G. Leal. Constitutive equations in suspension mechanics. part 2. approximate forms for a suspension of rigid particles affected by brownian rotations. *J. Fluid Mech.*, 76:187–208, 1976.

[69] P. S. Hubbard. Rotational brownian motion. *Phys. Rev. A*, 6:2421–2433, 1972.

[70] Y. Iso, C. Cohen, and D. L. Koch. Orientation in simple shear flow of semi-dilute fiber suspensions 1. weakly elastic fluids. *J. Non-Newtonian Fluid Mech.*, 62:115–134, 1996.

[71] Y. Iso, C. Cohen, and D. L. Koch. Orientation in simple shear flow of semi-dilute fiber suspensions 2. highly elastic fluids. *J. Non-Newtonian Fluid Mech.*, 62:135–153, 1996.

[72] Y. Ivanov, T. G. M. van de Ven, and S. G. Mason. Damped oscillations in the viscosity of suspensions of rigid rods i: Monomodal suspensions. *J. Rheol.*, 26:213–230, 1982.

[73] G. B. Jeffery. The motion of ellipsoidal particles immersed in a viscous fluid. *Proc. R. Soc. Lond. A*, 102:161–179, 1922.

[74] S. Jogun and C. Zukoski. Rheology and microstructure of dense suspensions of plate-shaped colloidal particles. *J. Rheol.*, 43:847–871, 1999.

[75] Timothy W Johnson, Zachary J Lapin, Ryan Beams, Nathan C Lindquist, Sergio G Rodrigo, Lukas Novotny, and Sang-Hyun Oh. Highly reproducible near-field optical imaging with sub-20-nm resolution based on template-stripped gold pyramids. *ACS nano*, 6(10):9168–9174, 2012.

[76] Y. Katayama and R. Terauti. Brownian motion of a single particle under shear flow. *Eur. J. Phys.*, 17:136, 1996.

[77] N. C. Keim, J. D. Paulsen, and S. R. Nagel. Multiple transient memories in sheared suspensions: Robustness, structure, and routes to plasticity. *Phys. Rev. E*, 88:032306, 2013.

[78] M Keshtkar, MC Heuzey, and PJ Carreau. Rheological behavior of fiber-filled model suspensions: effect of fiber flexibility. *Journal of Rheology (1978-present)*, 53(3):631–650, 2009.

[79] KM Keville, EI Franses, and JM Caruthers. Preparation and characterization

of monodisperse polymer microspheroids. *Journal of colloid and interface science*, 144(1):103–126, 1991.

[80] Aditya S Khair. On a suspension of nearly spherical colloidal particles under large-amplitude oscillatory shear flow. *Journal of Fluid Mechanics*, 791:R5, 2016.

[81] S. Kim and X. Fan. A perturbation solution for rigid dumbbell suspensions in steady shear flow. *J. Rheol.*, 28:117–122, 1984.

[82] S. Kim and S. Karrila. *Microhydrodynamics: Principles and Selected Applications*. Dover Publications, Mineola, NY, 2005.

[83] Maurice Kléman and Oleg D Lavrentovich. *Soft matter physics: an introduction*. Springer Science & Business Media, 2007.

[84] P. Kner, B. B. Chhun, E. R. Griffis, L. Winoto, and M. G. L. Gustafsson. Super-resolution video microscopy of live cells by structured illumination. *Nat. Methods*, 6:339–342, 2009.

[85] Anke Kuijk, Alfons van Blaaderen, and Arnout Imhof. Synthesis of monodisperse, rodlike silica colloids with tunable aspect ratio. *Journal of the American Chemical Society*, 133(8):2346–2349, 2011.

[86] H Lamb. *Hydrodynamics*. Dover Publications, Mineola, NY, 1932.

[87] OD Lavrentovich. Fluorescence confocal polarizing microscopy: Three-dimensional imaging of the director. *Pramana*, 61(2):373–384, 2003.

[88] B. Leahy, X. Cheng, D. C. Ong, C. Liddell-Watson, and I. Cohen. Enhancing rotational diffusion using oscillatory shear. *Phys. Rev. Lett.*, 110:228301, 2013.

[89] Brian D Leahy, Donald L Koch, and Itai Cohen. The effect of shear flow on the rotational diffusion of a single axisymmetric particle. *Journal of Fluid Mechanics*, 772:42–79, 2015.

[90] L. G. Leal. The slow motion of slender rod-like particles in a second-order fluid. *J. Fluid Mech.*, 69:305–337, 1975.

[91] L. G. Leal. Particle motions in a viscous fluid. *Annu. Rev. Fluid Mech.*, 12:435–476, 1980.

[92] L. G. Leal and E. J. Hinch. The effect of weak brownian rotations on particles in shear flow. *J. Fluid Mech.*, 46:685–703, 1971.

[93] L. G. Leal and E. J. Hinch. The rheology of a suspension of nearly spherical particles subject to brownian rotations. *J. Fluid Mech.*, 55:745–765, 1972.

[94] S. H. Lee, S. J. Gerbode, B. S. John, A. K. Wolfgang, F. A. Escobedo, I. Cohen, and C. M. Liddell. Synthesis and assembly of nonspherical hollow silica colloids under confinement. *J. Mater. Chem.*, 18:4912, 2008.

[95] D. T. Leighton. Diffusion from an initial point distribution in an unbounded oscillating simple shear flow. *Physicochem. Hydrodyn.*, 11:377–386, 1989.

[96] W Letwimolnun, Bruno Vergnes, Gilles Ausias, and Pierre J Carreau. Stress overshoots of organoclay nanocomposites in transient shear flow. *Journal of non-newtonian fluid mechanics*, 141(2):167–179, 2007.

[97] Neil YC Lin, Jonathan H McCoy, Xiang Cheng, Brian Leahy, Jacob N Israelachvili, and Itai Cohen. A multi-axis confocal rheoscope for studying shear flow of structured fluids. *Review of Scientific Instruments*, 85(3):033905, 2014.

[98] David JC MacKay. *Information theory, inference and learning algorithms*. Cambridge university press, 2003.

[99] D. W. Marquardt. An algorithm for least-squares estimation of nonlinear parameters. *J. Soc. Indust. Applu. Math.*, 11:431–441, 1963.

[100] J. Mewis and N. J. Wagner. *Colloidal Suspension Rheology*. Cambridge University Press, Cambridge, UK, 2012.

[101] M. San Miguel and J. M. Sancho. Brownian motion in shear flow. *Physica A*, 99:357, 1979.

[102] Ali Mohraz and Michael J Solomon. Direct visualization of colloidal rod assembly by confocal microscopy. *Langmuir*, 21(12):5298–5306, 2005.

[103] M. J. Nasse and J. C. Woehl. Realistic modeling of the illumination point spread function in confocal scanning optical microscopy. *J. Opt. Soc. Am. A*, 27:295–302, 2010.

[104] R. M. Neal. Slice sampling. *Ann. Stat.*, 31:705–767, 2003.

[105] A. Okagawa, R. G. Cox, and S. G. Mason. The kinetics of flowing dispersions vi: Transient orientation and rheological phenomena of rods and discs in shear flow. *J. Colloid and Interface Science*, 45:303–329, 1973.

[106] A. Okagawa and S. G. Mason. The kinetics of flowing dispersions vii: Oscillatory behavior of rods and discs in shear flow. *J. Colloid and Interface Science*, 45:330–358, 1973.

[107] R. Pathasarathy. Rapid, accurate particle tracking by calculation of radial symmetry centers. *Nat. Methods*, 9:724–726, 2012.

[108] F. Perrin. Mouvement brownien d'un ellipsoide - i. dispersion diélectrique pour des molécules ellipsoidales. *J. Phys. Radium*, 5:497–511, 1934.

[109] Anton Peterlin. Über die viskosität von verdünnten lösungen und suspensionen in abhängigkeit von der teilchenform. *Zeitschrift f ur Physik*, 111(3):232–263, 1938.

[110] M. Petrich, C. Cohen, and D. L. Koch. An experimental determination of the stress-microstructure relationship in semi-concentrated fiber suspensions. *J. Non-Newtonian Fluid Mech.*, 95:101–133, 2000.

[111] C. Pozrikidis. Orbiting motion of a freely suspended spheroid near a plane wall. *J. Fluid Mech.*, 541:105, 2005.

[112] William H Press. *Numerical recipes 3rd edition: The art of scientific computing*. Cambridge university press, 2007.

[113] S. Pujari, S. S. Rahatekar, J. W. Gilman, K. K. Koziol, A. H. Windle, and W. R. Burghardt. Orientation dynamics in multiwalled carbon nanotube dispersions under shear flow. *J. Chem. Phys.*, 130:214903, 2009.

[114] X. Qiu, H Daniel Ou-Yang, D. J. Pine, and P. M. Chaikin. Self-diffusion of interacting colloids far from equilibrium. *Phys. Rev. Lett.*, 61:2554, 1988.

[115] M. Rahnama, D. L. Koch, and E. S. G. Shaqfeh. The effect of hydrodynamic interactions on the orientation distribution in a fiber suspension subject to simple shear flow. *Phys. Fluids*, 7:487–506, 1995.

[116] S. Ram, E. S. Ward, and R. J. Ober. Beyond rayleigh's criterion: A resolution measure with application to single-molecule microscopy. *Proc. Natl. Acad. Sci. U.S.A.*, 103:4457–4462, 2006.

[117] C Radhakrishna Rao. Information and accuracy attainable in the estimation of statistical parameters. *Bull Calcutta. Math. Soc.*, 37:81–91, 1945.

[118] N. Krishna Reddy, J. Pérez-Juste, I. Pastoriza-Santos, P. R. Lang, J. K. G. Dhont, L. M. Liz-Marzán, and J. Vermant. Flow dichroism as a reliable method to measure the hydrodynamic aspect ratio of gold nanoparticles. *ACS Nano*, 5:4935–4944, 2011.

[119] M. W. Reeks. The transport of discrete particles in inhomogeneous turbulence. *J. Aerosol Sci.*, 14:729–739, 1983.

[120] A Rocha and A Acrivos. On the effective thermal conductivity of dilute dispersions general theory for inclusions of arbitrary shape. *The Quarterly Journal of Mechanics and Applied Mathematics*, 26(2):217–233, 1973.

[121] Salman S Rogers, Thomas A Waigh, Xiubo Zhao, and Jian R Lu. Precise particle tracking against a complicated background: polynomial fitting with gaussian weight. *Physical Biology*, 4(3):220, 2007.

[122] W. B. Russel, D. A. Saville, and W. R. Schowalter. *Colloidal Dispersions*. Cambridge University Press, Cambridge, UK, 1989.

[123] M. J. Rust, M. Bates, and X. Zhuang. Sub-diffraction-limit imaging by stochastic optical reconstruction microscopy (storm). *Nat. Methods*, 3:793, 2006.

[124] J. A. Sanders, F. Verhulst, and J. Murdock. *Averaging Methods in Nonlinear Dynamical Systems*. Springer, 2nd ed. edition, 2000.

[125] H. A. Scheraga. Non-newtonian viscosity of solutions of ellipsoidal particles. *J. Chem. Phys*, 23:1526–1532, 1955.

[126] Maryam Sepehr, Pierre J Carreau, Michel Moan, and Gilles Ausias. Rheological properties of short fiber model suspensions. *Journal of Rheology (1978-present)*, 48(5):1023–1048, 2004.

[127] E. S. G. Shaqfeh and G. H. Fredrickson. The hydrodynamic stress in a suspension of rods. *Phys. Fluids A*, 2:7–24, 1990.

[128] E. S. G. Shaqfeh and D. L. Koch. The effect of hydrodynamic interactions on the orientation of axisymmetric particles flowing through a fixed bed of spheres or fibers. *Phys. Fluids*, 31:728–743, 1988.

[129] Eric SG Shaqfeh. A nonlocal theory for the heat transport in composites containing highly conducting fibrous inclusions. *Physics of Fluids (1958-1988)*, 31(9):2405–2425, 1988.

[130] M. L. Shofner, K. Lozano, F. J. Rodríguez-Macías, and E. V. Barrera. Nanofiber-reinforced polymers prepared by fused deposition modeling. *J. Appl. Polym. Sci.*, 89:3081–3090, 2003.

[131] V. Singh, D. L. Koch, and A. D. Stroock. Rigid ring-shaped particles that align in simple shear flow. *J. Fluid Mech.*, 722:121, 2013.

[132] Ivan I Smalyukh, SV Shiyanovskii, and OD Lavrentovich. Three-dimensional imaging of orientational order by fluorescence confocal polarizing microscopy. *Chemical Physics Letters*, 336(1):88–96, 2001.

[133] C. S. Smith, N. Joseph, B. Rieger, and K. A. Lidke. Fast, single-molecule localization that achieves theoretically minimum uncertainty. *Nat. Methods*, 7:373–375, 2010.

[134] Braden Snook, Levi M Davidson, Jason E Butler, Olivier Pouliquen, and

Elisabeth Guazzelli. Normal stress differences in suspensions of rigid fibres. *Journal of Fluid Mechanics*, 758:486–507, 2014.

[135] E. J. Stancik, G. T. Gavranovic, M. J. O. Widenbrant, A. T. Laschitsch, J. Vermant, and G. G. Fuller. Structure and dynamics of particle monolayers at a liquid-liquid interface subjected to shear flow. *Faraday Discuss.*, 123:145–156, 2003.

[136] W. Stasiak and C. Cohen. Multiple-time scale approach to stress growth in suspensions of rodlike macromolecules. *J. Non-Newtonian Fluid Mech.*, 25:277–287, 1987.

[137] C. I. Steefel and K. Maher. Fluid-rock interaction: A reactive transport approach. *Reviews in Mineralogy and Geochemistry*, 70:485, 2009.

[138] W. E. Stewart and J. P. Sorensen. Hydrodynamic interaction effects in rigid dumbbell suspensions. ii. computations for steady shear flow. *Transactions of The Society of Rheology*, 16:1–13, 1972.

[139] C. A. Stover and C. Cohen. The motion of rodlike particles in the pressure-driven flow between two flat plates. *Rheol. Acta*, 29:192–203, 1990.

[140] S. S. Strand, S. Kim, and S. J. Karrila. Computation of rheological properties of suspensions of rigid rods: Stress growth after inception of steady shear flow. *J. Non-Newtonian Fluid Mech.*, 24:311–329, 1987.

[141] A. D. Stroock, S. K. W. Dertinger, A. Ajdari, I. Mezić, H. A. Stone, and G. M. Whitesides. Chaotic mixer for microchannels. *Science*, 295:647–651, 2002.

[142] G. Subramanian and D. L. Koch. Inertial effects on fibre motion in simple shear flow. *J. Fluid Mech.*, 535:383–414, 2005.

[143] RR Sundararajakumar and Donald L Koch. Structure and properties of sheared fiber suspensions with mechanical contacts. *Journal of Non-Newtonian Fluid Mechanics*, 73(3):205–239, 1997.

[144] RR Sundararajakumar and Donald L Koch. Electrical conductivity of isotropic fibre suspensions. *Proceedings of the Royal Society of London A: Mathematical, Physical and Engineering Sciences*, 455(1985):1923–1930, 1999.

[145] G. Taylor. Dispersion of soluble matter in solvent flowing slowly through a tube. *Proc. R. Soc. Lond. A*, 219:186–203, 1953.

[146] G. Taylor. Conditions under which dispersion of a solute in a stream of solvent can be used to measure molecular diffusion. *Proc. R. Soc. Lond. A*, 225:473–477, 1954.

[147] Mark K Transtrum, Benjamin B Machta, and James P Sethna. Why are nonlinear fits to data so challenging? *Physical review letters*, 104(6):060201, 2010.

[148] Mark K Transtrum, Benjamin B Machta, and James P Sethna. Geometry of nonlinear least squares with applications to sloppy models and optimization. *Physical Review E*, 83(3):036701, 2011.

[149] Mark K Transtrum and James P Sethna. Improvements to the levenberg-marquardt algorithm for nonlinear least-squares minimization. *arXiv preprint arXiv:1201.5885*, 2012.

[150] P. T. Underhill, J. P. Hernandez-Ortiz, and M. D. Graham. Diffusion and spatial correlations in suspensions of swimming particles. *Phys. Rev. Lett.*, 100:248101, 2008.

[151] E. Vadas, R. G. Cox, H. L. Goldsmith, and S. G. Mason. The microrheology of colloidal dispersions ii. brownian diffusion of doublets of spheres. *J. Colloid and Interface Science*, 57:308–326, 1976.

[152] K. A. Valiev and E. N. Ivanov. Rotational brownian motion. *Sov. Phys.-Usp.*, 16:1–16, 1973.

[153] T. G. M. van de Ven and S. G. Mason. The microrheology of colloidal dispersions: V primary and secondary doublets of spheres in shear flow. *J. Colloid and Interface Science*, 57:517, 1976.

[154] D. Velegol and J. L. Anderson. Probing the structure of colloidal doublets by electrophoretic rotation. *Langmuir*, 12:675, 1996.

[155] T. D. Visser and S. H. Wiersma. Electromagnetic description of image formation in confocal fluorescence microscopy. *J. Opt. Soc. Am. A*, 11:599–607, 1994.

[156] R Wolleschensky, B Zimmermann, R Ankerhold, and M Kempe. High-speed scanning confocal microscope for the life sciences. In *European Conference on Biomedical Optics 2005*, pages 58600N–58600N. International Society for Optics and Photonics, 2005.

[157] A. L. Yarin, O. Gottlieb, and I. V. Roisman. Chaotic rotation of triaxial ellipsoids in simple shear flow. *J. Fluid Mech.*, 340:83, 1996.

[158] B. Zhang, J. Zerubia, and J-C. Olivo-Marin. Gaussian approximations of fluorescence microscope point-spread functions. *Appl. Optics*, 46:1819–1829, 2007.